Constraining CO emission estimates using atmospheric observations

Pim Hooghiemstra

ISBN:

Cover: *South American biomass burning observed from space*, by Ineke Tesselaar and Pim Hooghiemstra

Optimizing CO emission estimates using atmospheric observations

Optimaal schatten van CO emissies met behulp van observaties in de atmosfeer

(met een samenvatting in het Nederlands)

PROEFSCHRIFT

ter verkrijging van de graad van doctor aan de Universiteit Utrecht op gezag van de rector magnificus, prof. dr. G. J. van der Zwaan, ingevolge het besluit van het college voor promoties in het openbaar te verdedigen op

maandag 25 juni 2012 des middags te 12.45 uur

door

Pim Benjamin Hooghiemstra

geboren op 10 februari 1984 te Bergschenhoek

Promotoren: Prof. dr. T. Röckmann
Prof. dr. M. C. Krol

This research has been sponsored by the SRON User Support Program 2006-2010 on project number GO-AO/05, with financial support from the Netherlands Organization for Scientific Research, NWO.

No mountain too high...

...to climb by bike.

Contents

Contents i

Samenvatting v

1 Introduction 1

1.1 Scientific relevance of CO . . . 1

1.2 Sources of CO . . . 2

1.2.1 Surface sources . . . 2

1.2.2 Oxidation sources . . . 5

1.3 Sinks of CO . . . 7

1.4 Trends and inter annual variability in atmospheric CO . . . 9

1.4.1 Trends . . . 9

1.4.2 Inter annual variability . . . 11

1.5 Estimating emissions of CO . . . 15

1.5.1 Bottom-up approach . . . 15

1.5.2 Top-down approach . . . 17

1.6 CO observations . . . 17

1.6.1 Surface observations . . . 17

1.6.2 Aircraft observations . . . 18

1.6.3 Satellite observations . . . 18

1.7 Research questions and outline . . . 22

2 Inverse Modeling **25**

2.1 Introduction . . . 25

2.2 Technical framework . . . 25

2.2.1 Synthesis inversion . . . 26

2.2.2 Variational approach . . . 27

2.3 Toy model example . . . 27

2.3.1 Overdetermined problem . . . 28

2.3.2 Underdetermined problem . . . 30

2.4 Historical overview . . . 31

2.5 4D-Var: Assumptions and challenges . . . 33

2.5.1 Outliers in the observations . . . 33

2.5.2 Separation of sources . . . 34

2.5.3 State vector representation . . . 34

2.5.4 Spin-up and spin-down . . . 35

2.5.5 Multiple datasets . . . 35

2.5.6 Coding the adjoint, an example . . . 38

3 Optimizing global CO emission estimates using a four-dimensional variational data assimilation system and surface network observations **41**

3.1 Introduction . . . 42

3.2 Description of the four dimensional variational data assimilation system . . . 43

3.2.1 The chemical transport model TM5 . . . 44

3.2.2 Specification of a priori state . . . 44

3.2.3 Specification of a priori uncertainties . . . 45

3.2.4 Atmospheric observations . . . 46

3.2.5 Inversion specifics . . . 47

3.3 Inversion results . . . 48

3.3.1 Comparison of modeled and observed CO mixing ratios . . . 48

3.3.2 Posterior emission estimates . . . 50

3.3.3 Validation with independent NOAA aircraft observations and MOPITT total columns . . . 53

3.3.4 Comparison with recent inverse modeling results . . . 55

3.4 Discussion . . . 56

3.4.1 Separating CO emission categories . . . 56

3.4.2 Observation error settings . . . 57

3.5 Sensitivity analysis . . . 59
3.5.1 Sensitivity study GFED3 . . . 60
3.5.2 Sensitivity study OH . . . 60
3.5.3 Sensitivity study FVERT . . . 61
3.6 Conclusions . . . 61

4 Comparing optimized CO emission estimates using MOPITT or NOAA surface network observations 65

4.1 Introduction . . . 66
4.2 Method . . . 67
4.2.1 Chemistry Transport Model TM5 . . . 68
4.2.2 Prior Information and Error Structure ($\mathbf{x}_b$, $\mathbf{B}$) . . . 68
4.2.3 Observations Assimilated in 4D-Var ($\mathbf{y}, \mathbf{R}$) . . . 69
4.2.4 Observations Used for Validation . . . 77
4.3 Results and Discussion . . . 78
4.3.1 Emission Increments and the Fit to the Observations . . . 78
4.3.2 Comparison with Recent Studies . . . 83
4.3.3 Validation of Posterior Emission Estimates with Independent Observations . . 85
4.4 Sensitivity Studies . . . 87
4.5 Summary and Conclusions . . . 92
4.6 Appendix A: Derivation of $\tilde{\mathbf{A}}$ . . . 93

5 Interannual variability of carbon monoxide emission estimates over South America from 2006 to 2010 95

5.1 Introduction . . . 96
5.2 Inverse Modeling . . . 98
5.2.1 TM5 model . . . 98
5.2.2 Prior state and uncertainties . . . 99
5.2.3 Observations . . . 100
5.2.4 Bias correction . . . 102
5.3 Results . . . 104
5.3.1 Fit with assimilated observations . . . 104
5.3.2 Interannual variability of CO emissions over South America . . . 106
5.3.3 Validation with independent observations . . . 113
5.4 Discussion . . . 114
5.4.1 GFED3 . . . 115

5.4.2 IAV in biomass burning emissions . . . 115
5.4.3 Expansion of sugar cane plantations . . . 116
5.5 Summary and conclusions . . . 117
5.6 Appendix A: Sensitivity studies . . . 118
5.7 Appendix B: Comparison with recent work . . . 121

6 Conclusions and Outlook **123**
6.1 Introduction . . . 123
6.2 Conclusions . . . 123
6.3 Outlook . . . 126

Bibliography **129**

Dankwoord **139**

Curriculum Vitae **141**

Samenvatting

Dit proefschrift gaat over koolstofmonoxide (ook wel koolmonoxide genoemd, afgekort als CO). CO is een kleurloos en reukloos gas dat bij hoge concentraties schadelijk is voor mensen. CO concentraties die over een periode van meerdere uren boven de 1500 ppm (1500 deeltjes CO per 1 miljoen deeltjes lucht) komen zijn dodelijk voor mensen. Gemiddelde CO concentraties in de atmosfeer zijn gelukkig veel lager, zo rond de 100 ppb (dus 100 deeltjes CO per 1 miljard deeltjes lucht). CO is een belangrijk gas in de atmosfeer doordat het reageert met het hydroxyl radicaal (OH). Dit radicaal is de zogenoemde stofzuiger van de atmosfeer en door te reageren met CO (waarbij het broeikasgas CO_2 wordt gevormd), is er minder OH beschikbaar om andere stoffen, zoals het broeikasgas methaan (CH_4), te oxideren. Wanneer er naast CO ook hoge concentraties stikstofoxiden (NO_x) aanwezig zijn, dan kan dit leiden tot vorming van fotochemische smog, een mengsel van schadelijke stoffen waaronder ozon en fijnstof.

In het algemeen wordt CO in de troposfeer gevormd door onvolledige verbrandingsprocessen en verdwijnt het weer na reactie met OH, door opname aan de grond of door transport naar de stratosfeer. De bronnen en putten van CO zijn bekend. Op het noordelijk halfrond is er met name uitstoot (emissie) aan de grond door het verkeer (in Noord Amerika, Europa en Azië) en door verbranding van hout en mest om op te koken of het huis van te verwarmen (met name in Zuid-Oost Azië). Ook tijdens branden in de boreale bosgebieden van Canada en Alaska, Europa en Siberië wordt er CO uitgestoten. In de tropen zijn bos- en savanne branden de grootste oppervlaktebron van CO. Een deel van deze branden wordt door mensen aangestoken, bijvoorbeeld om een stuk land vrij te maken voor landbouw. Andere stoffen in de atmosfeer zijn ook een bron van CO. Oxidatie van CH_4 leidt bijvoorbeeld tot ongeveer een kwart van de jaarlijkse CO productie in de troposfeer. Andere niet-methaan vluchtige organische stoffen (NMVOS) leiden uiteindelijk ook tot productie van CO na een keten van chemische reacties in de atmosfeer. Zoals reeds vermeld is de reactie met OH de grootste put voor CO (90%) en de overige 10% wordt deels opgenomen door de bodem en een klein deel wordt getransporteerd naar de stratosfeer.

Hoewel de bronnen en putten bekend zijn, is de grootte van elke afzonderlijke bron onzeker. In de wetenschappelijke literatuur lopen de schattingen van CO emissies uit de verschillende bronnen ver uiteen. In het algemeen zijn met name de CO emissies uit bos- en savanne branden (hierna kortweg branden genoemd) en de productie uit NMVOS, onzeker. In het algemeen zijn er twee

manieren om de emissies te schatten: *bottom-up* en *top-down*. Om bijvoorbeeld de jaarlijkse CO emissie van het verkeer in een bepaald land te berekenen gaat de bottom-up aanpak uit van bekende statistieken. Zo wordt de hoeveelheid benzine die er gebruikt is gecombineerd met de CO emissie per verbruikte liter benzine. Maar aangezien deze methode is gebaseerd op statistieken, zijn de geschatte CO emissies ook direct afhankelijk van de juistheid en nauwkeurigheid van deze statistieken. Men kan zich voorstellen dat eenzelfde exercitie voor het bepalen van een bottom-up emissie schatting van branden nog onzekerder is.

De top-down methode is een onafhankelijke methode om CO emissies te schatten. Deze methode gebruikt een *a priori* set van emissies, integreert deze in een chemie-transport model tot gesimuleerde CO waarden (in mixing ratios, CO moleculen ten opzichte van lucht, parts per billion [ppb]) die vervolgens vergeleken worden met gemeten CO mixing ratios. Tijdens een iteratief proces worden de emissies zodanig aangepast dat ze voldoende dicht in de buurt blijven van de a priori set en het verschil tussen de gesimuleerde en gemeten mixing ratios geminimaliseerd wordt. In wiskundige termen zijn de optimale CO emissies ($\hat{x}$) de oplossing van het volgende minimalizatie probleem:

$$\begin{aligned} \hat{x} &= \arg\min \mathcal{J}, \\ \mathcal{J}(x) &= \frac{1}{2}\left(x - x_b\right)^\top \mathbf{B}^{-1}\left(x - x_b\right) + \frac{1}{2}\sum_{i=1}^{N}\left(H(x)_i - y_i\right)^\top \mathbf{R}_i^{-1}\left(H(x)_i - y_i\right), \end{aligned}$$

met x_b de a priori emissie set, $\mathbf{B}$ de a priori error covariantie matrix, N het aantal meettijdstippen, H het gediscretizeerde chemie-transport model TM5, y de observaties, $\mathbf{R}$ de observatie error covariantie matrix, $\top$ de matrix getransponeerde operator en $\mathcal{J}$ heet de kostenfunctie.

In hoofdstuk 3 optimaliseren we maandelijkse CO emissies op de TM5 model resolutie (6°x4°) die begrensd worden door metingen van het grond netwerk van NOAA (National Oceanic and Atmospheric Administration) voor 2003 en 2004. We onderscheiden drie emissie categorieën, te weten antropogeen (i.e., CO emissies als gevolg van verbranding van fossiele- en bio brandstoffen), branden (in bos en savanne) en natuurlijk (CO emissie uit planten en de oceaan). Daarnaast optimaliseren we een maandelijkse schalingsfactor voor de productie van CO uit methaan en een schalingsfactor voor de productie uit NMVOS. Met name de antropogene bron in Europa en Azië wordt verhoogd door de inversie, met een factor 1.5 en 2, respectievelijk. Vervolgens onderzoeken we hoe goed het systeem in staat is om de verschillende bronnen van elkaar te onderscheiden. Immers, de observaties geven alleen informatie over de totale CO bron, maar onderscheiden van de bronnen is in potentie mogelijk door verschillen in de a priori emissie schattingen en hun onzekerheden op te leggen. Het blijkt moeilijk om de antropogene bron van de NMVOS bron te scheiden omdat beide bronnen gedurende het hele jaar CO emitteren en de emissiepatronen elkaar deels overlappen. Juist omdat CO emissies uit branden de dominante bron zijn op het zuidelijk halfrond en bovendien deze emissies alleen plaatsvinden in het droge seizoen (van Juni tot November), blijkt het goed mogelijk om deze emissies te scheiden van de andere in het systeem als we naar de emissies kijken op een jaarlijkse schaal. Extra inversies om de gevoeligheid van het systeem, voor bijvoorbeeld de opgelegde maandelijkse OH verdeling of de verticale verdeling van de emissies uit branden, te testen, geven aan dat het systeem behoorlijk gevoelig is voor deze model aannames. Dit wordt verklaard door het kleine hoeveelheid metingen in verhouding tot het grote aantal onbekenden dat we proberen op te lossen met dit systeem.

Voor de studie beschreven in hoofdstuk 4 hebben we het systeem aangepast. Uit de resultaten in hoofdstuk 3 bleek dat de oplossing sterk afhankelijk was van de keuze van de onzekerheid voor de NMVOS a priori. Het leek ook niet helemaal eerlijk om deze bron slechts globaal te kunnen schalen met een parameter, terwijl andere emissie categorieën worden geoptimaliseerd op de modelresolutie en dus veel meer vrijheidsgraden hebben om de metingen te kunnen fitten. We hebben dus de

NMVOS bron toegevoegd aan de natuurlijke bron, waarbij we de verticale verdeling van deze emissies hebben opgeslagen. We optimaliseren derhalve een volume bron met een constante hoogteverdeling. In deze studie hebben we twee losse inversies met elkaar vergeleken: De eerste gebruikte alleen observaties van het NOAA grond netwerk, de tweede gebruikte satelliet metingen van het MOPITT (Measurements Of Pollution In The Troposphere) instrument. Hoewel we een vernieuwde bottom-up schatting van de antropogene emissies hebben gebruikt in deze studie, hebben we opnieuw gevonden dat de antropogene emissies in zowel Europa als Azië onderschat worden, in dit geval beide met een factor 2. Opvallend genoeg was de onzekerheidsreductie over Europa groter voor de inversie gebaseerd op de NOAA observatie dan voor de MOPITT inversie. Dit was onverwacht omdat we dachten dat de satelliet observaties de emissies veel beter zouden begrenzen. In de realiteit is de dichtheid van het NOAA grond netwerk in Europa en Noord-Amerika heel goed en bovendien is de onzekerheid op de metingen veel kleiner in vergelijking met de satelliet observaties. Daarnaast hebben we alleen MOPITT observaties tussen breedtegraden 65°N en 65°S gebruikt, omdat de metingen rond de polen van lagere kwaliteit zijn wat ook leidt tot minder observaties boven het Europese continent. Een groot verschil tussen beide inversies kwam naar voren voor de tropen. De inversie gebaseerd op NOAA observaties resulteerde in veel hogere CO emissies uit branden, terwijl de MOPITT inversie juist op veel hogere emissies uit NMVOS uitkwam vergeleken met de a priori emissies. Een eerste oorzaak voor dit verschil is het verschil in dekking door de observaties voor de tropen. De NOAA meetstations zijn gecentreerd op het noordelijk halfrond en er zijn maar een klein aantal stations in de tropen en op het zuidelijk halfrond. MOPITT observaties begrenzen de emissies dus veel beter (wat ook naar voren kwam in een grotere onzekerheids reductie). Een tweede oorzaak is de verticale gevoeligheid van beide datasets. Het MOPITT instrument is met name gevoelig voor CO in de vrije troposfeer met een piekgevoeligheid tussen 4 en 7 km. Gegeven dat de NMVOS emissies met bijhorende verticale verdeling met name in dit deel van de atmosfeer worden geëmitteerd levert een groot verschil op met de NOAA inversie. De geoptimaliseerde emissies van beide inversies zijn verder gevalideerd met onafhankelijke vliegtuig- en FTIR (Fourier Transform Infrared) kolomdata. Hieruit komt een positieve bias in MOPITT kolommen naar voren, met name op het zuidelijk halfrond.

In hoofdstuk 5 hebben we het systeem zo aangepast dat de emissies begrensd worden door zowel NOAA grond waarnemingen als MOPITT observaties. Een correctie schema voor de positieve bias in MOPITT (geïdentificeerd in hoofdstuk 4), is gebruikt om beide observationele datasets goed te kunnen fitten. Dit systeem hebben we vervolgens toegepast om de emissies boven Zuid Amerika over de periode 2006-2010 te kwantificeren op een model resolutie van 1°x1°. In het droge seizoen, tussen juli en oktober, worden de CO emissies gedomineerd door de emissies uit branden. De inversies over 5 jaren geven een iets kleinere interjaarlijkse gang in vergelijking met de a priori emissie set uit GFED3 (Global Fire Emission Database, versie 3). Daarnaast laten de resultaten zien dat in de droge jaren 2007 en 2010 de CO emissies als gevolg van branden, geassocieerd met ontbossing van het Amazone gebied, te groot zijn in GFED. Daarentegen zijn de emissies in de overige jaren juist te laag, met name de emissies in de Braziliaanse *Cerrado*, de gras en savanne landschappen ten oosten van het tropisch regenwoud. Een ander opvallend resultaat was de pertinente onderschatting van de CO emissies in de staat São Paulo in Brazilië. In deze staat zijn 60% van de suikerriet plantages in Brazilië gevestigd waarvan de oogst gebruikt wordt voor het produceren van suiker en de biobrandstof ethanol. Deze plantages worden voor de oogst afgebrand, om de handmatige oogst te vereenvoudigen. De CO emissies voor deze staat kwamen voor ieder jaar 50-100% hoger uit dan in de a priori emissie set. Tenslotte hebben we met het fitten van zowel grond metingen van NOAA als satelliet metingen van MOPITT een bias correctie gefit die een duidelijk positieve bias in de MOPITT kolommen weerspiegelde van maximaal 5 ppb tussen 30 en 50 graden zuiderbreedte.

In het laatste hoofdstuk van dit proefschrift worden de belangrijkste resultaten en conclusies nog eens onder elkaar gezet. Daarnaast doe ik aanbevelingen voor toekomstig onderzoek aan CO inverse modelleren. Ten eerste is duidelijk geworden uit mijn onderzoek dat het onderscheiden van de ver-

schillende CO emissie categoriën een lastige taak is. Een manier om dit probleem aan te pakken is een inversie te doen waarin we meerdere stoffen tegelijk optimaliseren, zoals bijvoorbeeld CO en formaldehyde (een voorloper van CO uit oxidatie van methaan en NMVOS). Hoewel zulke systemen al bestaan (Pison et al. (2009) en Fortems-Cheiney et al. (2011)), zouden zowel CO als formaldehyde begrensd moeten worden met hoge resolutie satellietobservaties.

Ten tweede is de maandelijkse tijdsresolutie waarop de CO emissies worden geoptimaliseerd onderwerp van discussie. Met name bos- en savanne branden variëren op een veel kleinere tijdschaal, van enkele uren tot dagen, waardoor de aanname van maandelijkse CO emissies tot fouten in de oplossing leidt. Het nieuwste TM5-4D-Var systeem voor CO is in staat om emissies op dagelijkse schaal te optimaliseren en wordt in een eerste toepassing gebruikt om de CO emissies uit de bosbranden rond Moskou in de zomer van 2010 te optimaliseren.

CHAPTER 1

Introduction

1.1 Scientific relevance of CO

Carbon monoxide (CO) is a gas consisting of a carbon and an oxygen atom. This gas is odorless and colorless, and it is toxic to humans when present in high concentrations. Such high concentrations can be generated for example by old heaters or old cars without catalytic converters. CO concentrations may rise to harmful concentrations in an enclosed space (e.g., a non-ventilated room). Concentrations of CO are denoted in units of mixing ratios. That is, the concentration is given as the ratio of the number of molecules of CO per number of molecules of air in a volume (e.g., 50 CO molecules per 10^9 molecules of air is denoted as 50 parts per billion (ppb)). Levels of CO exceeding 100 ppm (parts per million) are harmful to humans. Moreover, if CO mixing ratios are persistently above 1500 ppm, death occurs within a couple of hours. However, in a normal house, CO mixing ratios are often much lower, ranging from 0.5 to 5 ppm.

CO is also present in the atmosphere, but at significantly lower mixing ratios. For example, the mean background CO mixing ratios is around 100 ppb and hence, 1000 times lower than levels that are harmful to humans. However, close to emission hotspots, due to forest fires or urban pollution, atmospheric CO mixing ratios can be much higher. For instance, during the large fires in Russia in July-August 2010, atmospheric CO concentrations of over 10 ppm were measured in Moscow (Konovalov et al., 2011).

In atmospheric chemistry (Jacob, 1999), CO is an important trace gas for three reasons:

- The reaction of CO with the hydroxyl radical OH is the main sink of OH (Spivakovsky et al., 2000), accounting for 38% of annual OH loss (Huijnen et al., 2010). Hence, variability in CO directly affects OH concentrations since OH is the so-called cleansing agent of the atmosphere (Logan et al., 1981). It thus influences the oxidizing capacity of the atmosphere. For example, a consequence of reduced OH in the atmosphere is a longer methane lifetime. Since methane is a very strong greenhouse gas (with a global warming potential of 25 over the next 100 years compared to CO_2 (IPCC, 2007)), CO can have an indirect effect on global warming.
- In the presence of high NO_x concentrations, e.g., in cities where NO_x and CO are emitted in large quantities by cars (European Commission and Netherlands Environmental Assessment Agency, 2010), CO is a precursor of ozone. Ozone in the lower troposphere is a toxic gas-phase compound that is harmful for crops and humans at high concentrations.
- CO is a perfect tracer of pollution transport in the atmosphere. With a lifetime of approximately 2 months, plumes with enhanced CO mixing ratios (e.g., due to extensive biomass

burning in the Southern Hemisphere) can be detected and traced with respect to background CO mixing ratios. For example, by analyzing satellite derived CO columns, Gloudemans et al. (2006) found that enhanced CO mixing ratios over Australia were partly originating from fires in South America and Southern Africa that were transported to the south-east and rapidly transported eastwards by the westerlies. Thus, CO can be used to investigate long range atmospheric transport of pollutants.

A large part of this thesis deals with the modeling of the CO distribution and more specifically, optimizing CO emission estimates using inverse modeling. This modeling framework will be discussed in detail in Chapter 2. In the coming sections however, we first introduce the sources (Sect. 1.2) and sinks (Sect. 1.3) of CO and trends and interannual variability in atmospheric CO (Sect. 1.4). Two methods for estimating CO emissions are detailed in Sect. 1.5. Surface, aircraft and satellite CO observations are discussed in Sect. 1.6 and this introduction ends with the formulation of research questions and an outline for the rest of the thesis (Sect. 1.7).

1.2 Sources of CO

In oxygen rich air, combustion of carbon containing fuels leads to formation of CO_2. However, in the absence of enough oxygen, incomplete combustion releases CO. CO is also produced in the atmosphere due to the oxidation of carbon containing compounds (Sect. 1.2.2). A table presenting estimates of the current budget of CO in the troposphere is given in Chapter 2.

1.2.1 Surface sources

Fossil fuel and biofuel combustion emit large quantities of CO. This emission category is referred to as the anthropogenic category in this work. Fossil fuels such as coal, oil and natural gas are the main source of energy and are typically used for ground transport and in the industry. Biofuels such as bioethanol and biodiesel are an alternative fuel for car engines and also a source of CO. Domestic cooking is another large source of CO to the atmosphere, in particular in Asia, where people are used to cook on old stoves or open fires indoors (Naeher et al., 2000). Wood, dung and crop residues are used as fuels for either cooking or heating the house.

Estimates of the dominant CO emissions from different processes are shown in Figure 1.1. The top four panels show the estimates (in g m^{-2}month^{-1}) for the industry, ground transport, residential cooking and heating, and agriculture for 2004 from the Emission Database for Global Atmospheric Research (EDGAR) version 4.1 (European Commission and Netherlands Environmental Assessment Agency, 2010). The bottom panel shows the total CO emissions from all processes together. The numbers in the titles represent the annual total emissions in Tg CO/yr for each process (1 Tg = 10^{12}g). It is clear that India and China are the main emitters of CO, with a large contribution from the residential sector and the industry. For India, also the agricultural sector is a large source of CO. For Europe and North America, the main CO emissions are due to ground transport. Africa and South America show only small emissions. However, in southeastern Brazil, a clear emission signal from agriculture is present which is due to burning of the agricultural waste from sugar cane plantations. Indeed, before harvesting the cane, residual crops are burned to facilitate the harvesting, emitting loads of CO to the atmosphere (Cardoso et al., 2012). Although this burning source should be added to the biomass burning category discussed below, in this work it is part of the anthropogenic source category.

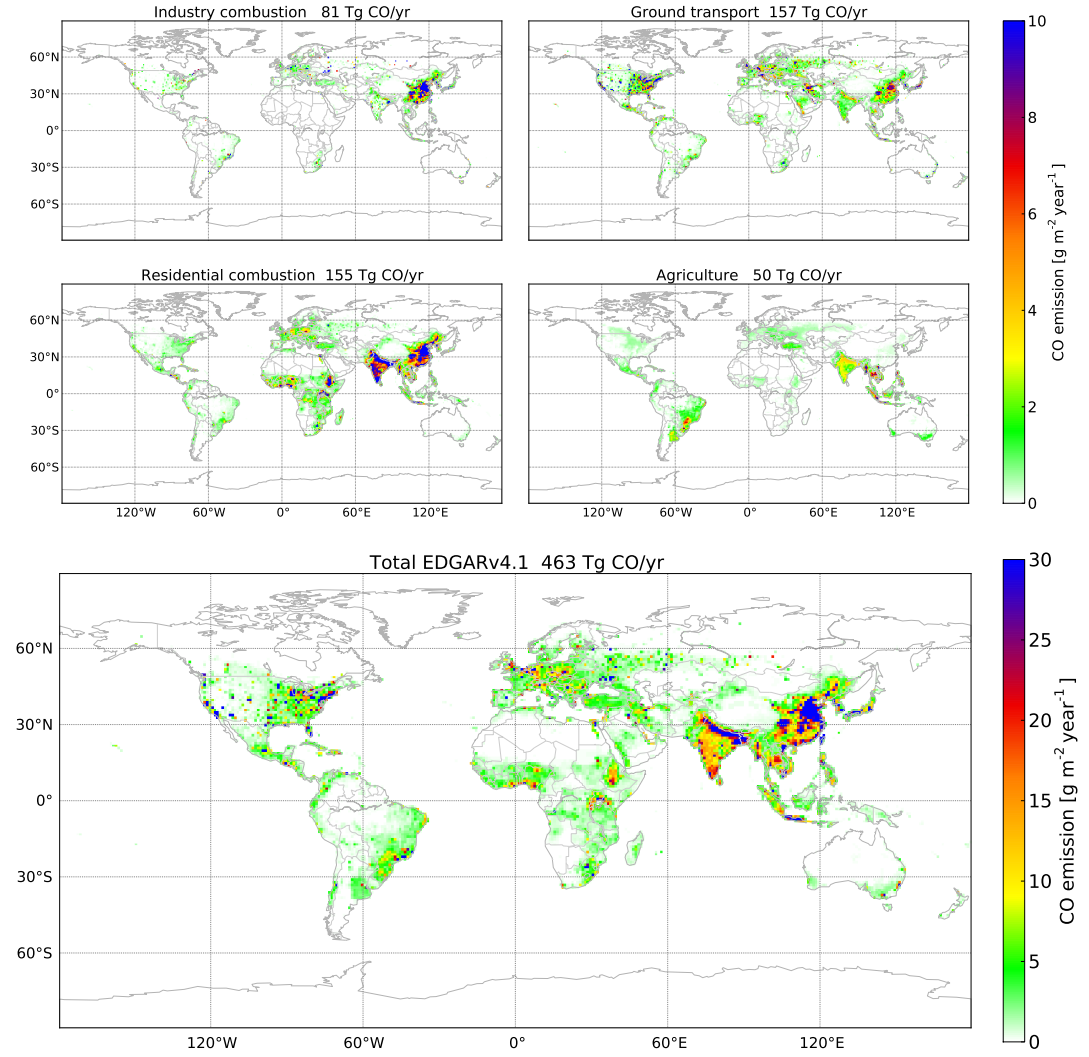

Figure 1.1: *Top: CO emissions from fossil fuel and biofuel combustion sources in EDGARv4.1 for 2004. Numbers in the titles represent total annual emissions from that source category. Bottom: Total CO emissions from fossil fuel and biofuel combustion from EDGARv4.1 for 2004.*

Biomass burning is also a large source of CO, mainly in the Tropics and in the boreal forests of North America and Russia. Boreal forest fires are typically triggered by lightning or human induced. In North America, crown fires are the dominant fire type, burning less area but consuming higher fuel loads and therefore emit relatively more CO per unit area compared to surface fires which are the dominant fire type in Russia (Wooster and Zhang, 2004). Hence, although the number of fires and the total burned area in Russia is much greater compared to North America each year (Wooster and Zhang, 2004), the difference in CO emissions for these regions is much smaller.

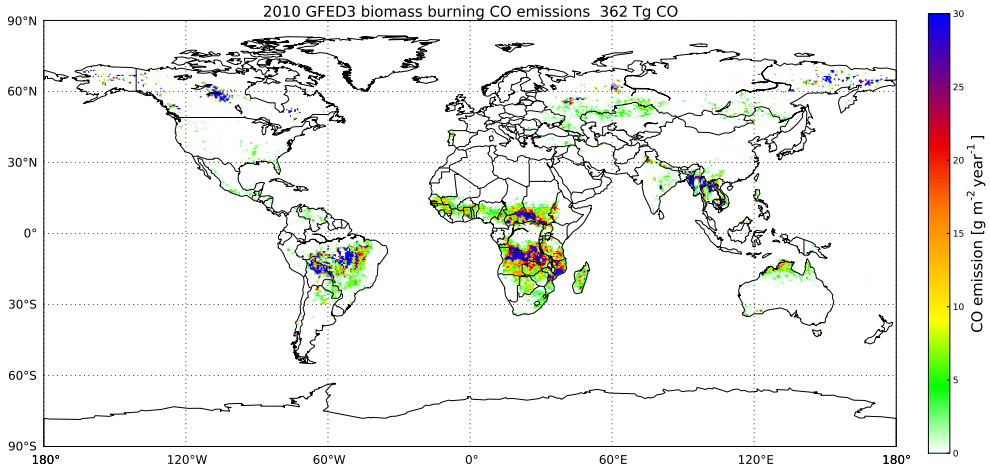

Figure 1.2: *Biomass burning CO emissions from GFED3 for 2010. Numbers in the title represent the global annual total emission in Tg CO.*

In the Tropics, forest fires are mainly human induced. For example, land-use change practices in South America and Indonesia convert forest to pasture or croplands. The remaining biomass debris is piled up and ignited multiple times (even in the years after clearing of the land), emitting large amounts of CO, CO_2 and other fire pollutants. In the dry season of South America and Southern Africa (roughly from June to October in Southern Africa and from August to October in South America (Torres et al., 2010)), savanna fires cause smoke layers that can be transported over the oceans and even arrive in Australia. Biomass burning is thought to be the main driver of inter annual variability (IAV) in CO emissions in the Tropics. Firstly, climatic conditions seem very important as the link between precipitation and fire counts is very strong (Aragão et al., 2008; Torres et al., 2010). Secondly, socio economic factors may play a role. For example, varying market demands for soy, beef, palm oil and sugar cane, can trigger land-use changes in the Amazon forest and in Indonesia because large landholders clear the forest to start new plantations (Laurance, 2007).

The Global Fire and Emission Database (GFED) (van der Werf et al., 2010) is a biomass burning inventory for carbon containing trace gases, including CO. The most up-to-date GFED version 3 global biomass burning CO emission estimates for the year 2010 are shown in Fig. 1.2. The Tropical and in particular African emissions stand out in this figure. African biomass burning CO emissions peak during December to February for Northern Hemisphere Africa, whereas emissions for Southern Hemisphere Africa peak from June to October. Emissions in South America are also clearly visible and were anomaliously high in 2010 due to a once-in-a-century drought that struck the Amazon region (Lewis et al., 2011). Boreal forest fire emissions are also visible in Alaska and Canada. The severe drought in Russia in the summer of 2010 emitted enormous amounts of CO to the atmosphere with estimates ranging from 10 to 30 Tg CO (Yurganov et al., 2011; Witte et al., 2011). Surprisingly, GFED3 reported only 6.7 Tg CO biomass burning emissions in July and August 2010.

Living vegetation also emits CO, but the mechanism is unclear (Tarr et al., 1995). Tarr et al. (1995) estimate a global CO source for living vegetation of 50-200 Tg CO/yr. Dead vegetation also emits CO during an abiotic process, depending on temperature and UV radiation (Zepp et al., 1996; Schade

et al., 1999; Schade and Crutzen, 1999b; Derendorp et al., 2011), leading to a global emission estimate of 50-179 Tg CO/yr (Schade and Crutzen, 1999b). Additional CO is emitted by the oceans, totaling to about 20 Tg CO/yr.

1.2.2 Oxidation sources

Apart from direct surface sources of CO, the photochemical source of CO consists of the oxidation of volatile organic compounds (VOCs) in the atmosphere. In general a separation is made between CO produced from methane oxidation and CO from *non-methane* VOCs (NMVOCs). Approximately 90% of the NMVOCs are of biogenic origin and the most important NMVOCs for CO production include isoprene (C_5H_8), monoterpenes ($C_{10}H_{16}$), methanol (CH_3OH) and acetone (C_3H_6O) (Duncan et al., 2007).

Methane oxidation

Methane is mainly oxidized by the OH radical and consists of the following reactions (Seinfeld and Pandis, 2006):

$$CH_4 + OH \overset{O_2}{\Rightarrow} CH_3O_2 + H_2O \tag{1.1}$$

The formed methyl peroxy radical (CH_3O_2) can react with NO, NO_2, HO_2 and itself, but the most important reactions are with NO and HO_2 :

$$CH_3O_2 + NO \overset{O_2}{\Rightarrow} HCHO + HO_2 + NO_2 \tag{1.2}$$

$$CH_3O_2 + HO_2 \overset{O_2}{\Rightarrow} CH_3OOH + O_2 \tag{1.3}$$

The produced methyl hydroperoxide (CH_3OOH) may photolyze (i.e., decompose due to radiation) or react with OH. Both of these reactions lead to production of formaldehyde (HCHO). Formaldehyde may either photolyse or react with OH to form CO:

$$HCHO + h\nu \overset{2O_2}{\Rightarrow} 2HO_2 + CO \tag{1.4}$$

$$\Rightarrow H_2 + CO \tag{1.5}$$

$$HCHO + OH \overset{O_2}{\Rightarrow} HO_2 + CO + H_2O \tag{1.6}$$

The highest methane mixing ratios are observed over emission hotspots such as wetlands, biomass burning regions, industrialized regions and rice paddies (Bergamaschi et al., 2007, 2009). However, since most OH is present in the Tropics (Spivakovsky et al., 2000) and the reaction rate constant for the reaction of methane with OH is temperature dependent, CO production from methane is typically highest in the Tropics. Annual CO from methane oxidation amounts to approximately 800-900 Tg CO/yr (Bergamaschi et al., 2000; Hooghiemstra et al., 2011).

Oxidation of non-methane volatile organic compounds

The chain of reactions for the oxidation of NMVOCs is more complex than the oxidation of methane and a large list of intermediate species is formed. Moreover, only some intermediate species oxidize to CO since a large fraction of the organic compounds become less volatile and are taken up by aerosols. The reaction chain for VOCs is illustrated in Fig. 1.3. Consider for example the oxidation

of isoprene (C_5H_8) by OH. Here, the radical R in Fig. 1.3 is C_5H_7. The OH molecule abstracts the hydrogen atom to form water. The radical R quickly reacts with oxygen and forms RO_2. In the presence of NO_x, the next step is a reaction with NO, forming NO_2 and RO. In this step, tropospheric ozone is formed as the NO_2 molecule is photolyzed and the resulting oxygen atom forms ozone by reaction with an oxygen molecule. Alternatively, RO_2 reacts with a hydroperoxide radical (HO_2) producing an organic peroxide (ROOH) which may photolyze to RO or reacts with OH to either recycle the RO_2 molecule or to produce a carbonyl product. The RO radical reacts with oxygen to produce a carbonyl product and HO_2, which may form ozone again in subsequent reactions if NO_x is available. The carbonyl product may be taken up in an aerosol or is oxidized further, in the end forming formaldehyde which in turn will result in production of CO (Eq. (1.4) - (1.6)). However, as mentioned before, intermediate species may be lost by forming secondary organic aerosols. For isoprene, it is typically assumed that only one of the five carbon atoms will result in a CO molecule and hence, the CO yield from isoprene is 0.2 (Duncan et al., 2007). However, for larger NMVOCs the CO yield is more uncertain and hence, CO production from the oxidation of NMVOCs is a rather uncertain term in the CO budget.

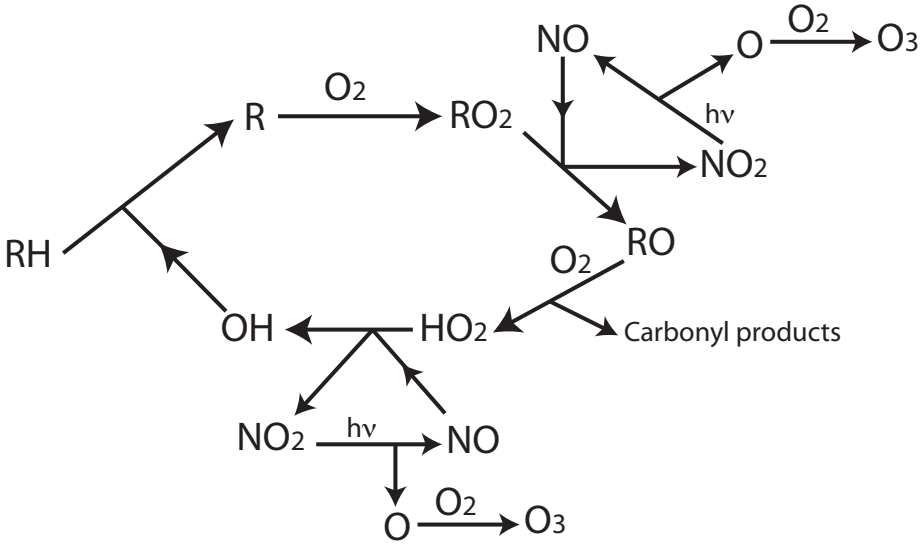

Figure 1.3: *Oxidation pathway of a volatile organic compound (Seinfeld and Pandis, 2006), denoted here as the molecule RH, in which R is a radical. Note that only in the presence of NO_x, ozone is produced.*

In their model study, (Huijnen et al., 2010) have shown that approximately 95% of all chemically produced CO in the troposphere is due to oxidation or photolysis of formaldehyde. Figure 1.4 shows an annual CO production field due to oxidation of NMVOCs, derived from a full-chemistry model simulation (Myriokefalitakis et al., 2008), which has been scaled to produce 400 Tg CO/yr (Hooghiemstra et al., 2011). Additionally, emissions from vegetation and the oceans (totalling to 115 Tg CO/yr (Houweling et al., 1998)) have been added to this figure. Although these emissions are a three-dimensional volume source, the two-dimensional CO production (the sum of the columns) is shown here. Note that in the model simulation used in this thesis, a fixed vertical distribution is applied to release CO emissions from this source higher up in the troposphere. Highest CO production is in the Tropics which is associated with isoprene emissions from vegetation. However, the strength

of this source is rather uncertain.

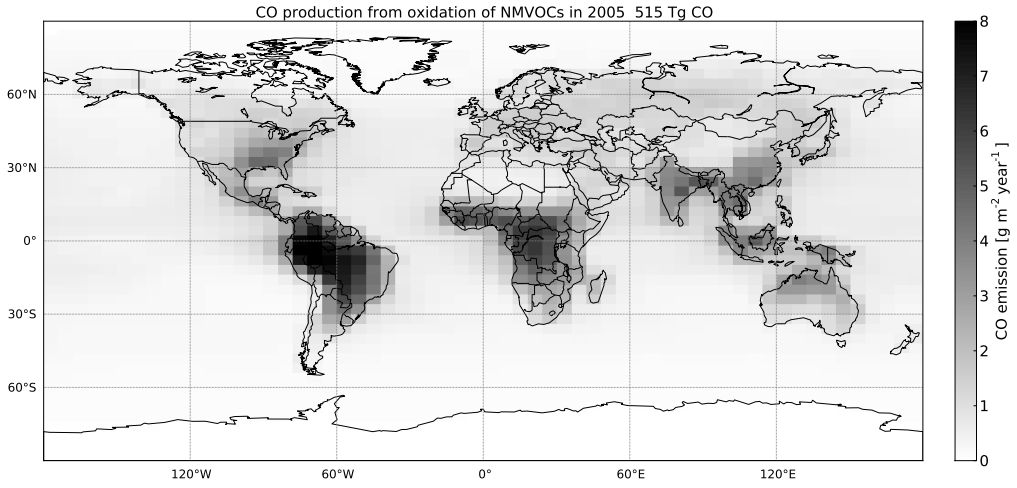

Figure 1.4: *CO emissions from oxidation of NMVOCs, scaled to emit 400 Tg CO/yr. Additional direct emissions from vegetation and the oceans have been added, amounting to 115 Tg CO/yr.*

1.3 Sinks of CO

The hydroxyl radical (OH) is the main sink of CO and accounts for approximately 90% of CO removal. OH is formed in the troposphere following photolysis of ozone, and is highly reactive. However, OH is also regenerated during many catalytic loops. Annual mean tropospheric OH concentrations are currently estimated at around 10^6 molecules cm^{-3}. This number can be inferred from measurements of trace gases that have OH as their prime sink, such as methylchloroform (CH_3CCl) (Krol and Lelieveld, 2003; Prinn et al., 2005; Bousquet et al., 2005; Montzka et al., 2011), ^{14}CO (Krol et al., 2008) and carbon tetrachloride (IPCC, 2007). The global mass balance equations for a trace gas define the rate of change in the burden G to equal the difference between emissions E and removal L. Assuming that the removal of the gas is a first order reaction with OH with reaction rate constant k, the removal term $L = k[\mathrm{OH}]\mathrm{G}$ and one derives (Montzka et al., 2011):

$$\frac{dG}{dt} = E - k[\mathrm{OH}]\mathrm{G} \Rightarrow \mathrm{k[OH]} = \frac{\mathrm{E}}{\mathrm{G}} - \frac{\mathrm{dG/dt}}{\mathrm{G}}. \tag{1.7}$$

Recently Montzka et al. (2011) inferred small year-to-year variations in OH based on methylchloroform measurements of 2-3%. Earlier studies reported larger IAV in OH up 10% (Prinn et al., 2005; Bousquet et al., 2005). Differences are found to be mainly caused by reduced uncertainties in methylchloroform measurements and bottom-up emission estimates.

Although global annual OH concentrations and IAV can be determined, it is much more difficult to calculate regional OH concentrations and seasonal variations based on methylchloroform observations, because this gas has a long lifetime of approximately 4.9 years and it is only measured at a few sites.

Therefore, ^{14}CO measurements might be used for more regional OH concentration calculations, since this gas has a much shorter lifetime. However, the observational network of measurements is small and since the main source of this gas (cosmic rays) is in the upper atmosphere and the measurements at the surface, model errors may lead to biased OH results (Krol et al., 2008).

Nevertheless, (Spivakovsky et al., 2000) constructed an OH climatology for the troposphere, as a function of 3-D distributions of OH precursors such as ozone, nitrogen oxides, CO and hydrocarbons. The resulting OH field has a mean annual OH concentration of 1.16 x 10^6 molecules cm^{-3} and a North-South ratio of 1, i.e., the mean hemispheric OH concentrations are nearly equal. It was found by (Huijnen et al., 2010) that this OH field had to be scaled by a factor 0.92 to be consistent with methylchloroform observations in the atmospheric chemistry and transport model TM5 (Krol et al., 2005) for the period 2000 - 2007. Huijnen et al. (2010) also computed an OH field using a full-chemistry simulation of TM5, which results in a mean annual OH concentration of 1.05 x 10^6 molecules cm^{-3}. Moreover, this OH field has a more pronounced North-South ratio. Further differences between these OH fields are lower OH concentrations over tropical land masses in the Huijnen et al. (2010) OH field, but higher OH concentrations in the NH Tropics and midlatitudes as can be seen in Fig. 1.5, in which the differences between the two OH fields is shown (as Huijnen et al. (2010) - Spivakovsky et al. (2000)).

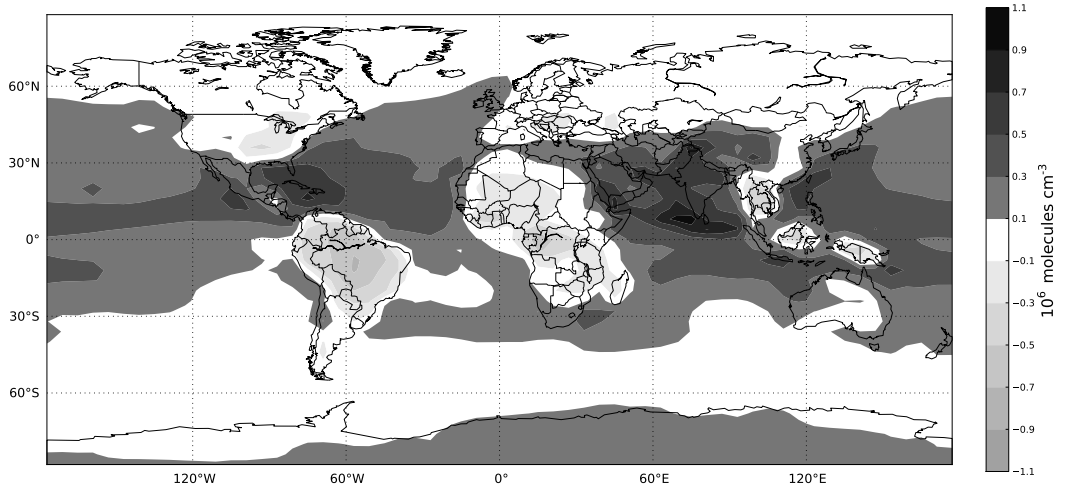

Figure 1.5: *Vertically integrated mass- and rate constant (k_{CO}) weighted OH difference field (Huijnen et al. (2010) - Spivakovsky et al. (2000)) in units of 10^6 molecules cm^{-3}.*

The reaction CO + OH results in CO_2, which is the number one anthropogenic greenhouse gas. Assuming annual CO emissions of 2000-3000 Tg CO/yr, this results in 0.9-1.3 Pg C/yr which is 10-15% of the 9 Pg C/yr CO_2 emitted from fossil fuel combustion. Current models often emit this source directly as CO_2 at the surface and neglect the vertical distribution and the lifetime of CO. Other sinks of CO are dry deposition and loss to the stratosphere, but these sinks are relatively small ($< 10\%$.)

1.4 Trends and inter annual variability in atmospheric CO

1.4.1 Trends

Measurements of CO from the NOAA surface network (from the end of the 1980's to present) have been used to analyze trends and inter annual variability in atmospheric CO (Novelli et al., 1998, 2003) for the 1990's. Figure 1.6 shows the observed CO mixing ratio at 6 stations from the NH high-latitudes via the Tropics to the SH high-latitudes. A clear seasonal cycle is observed, which is caused by seasonal variations in OH (e.g., minimum OH levels coincide with maximum CO levels and vice versa). Moreover, the seasonal cycle on the SH is opposite to the seasonal cycle on the SH.

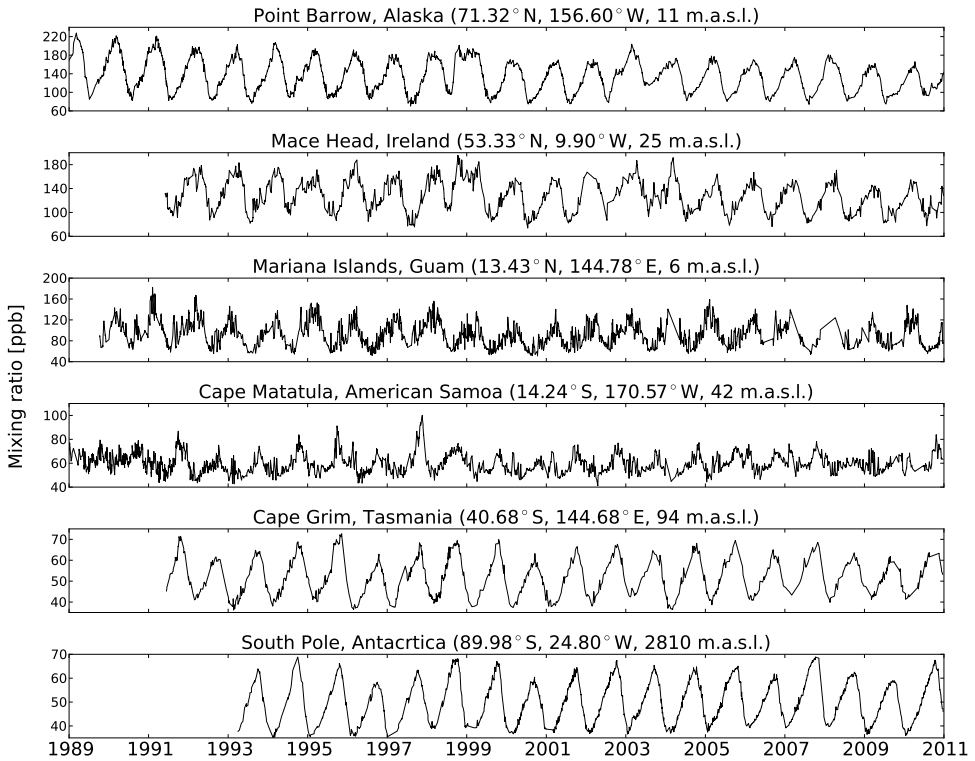

Figure 1.6: *Time series of CO mixing ratios measured by the NOAA surface network for six stations from different latitudinal regions.*

A negative trend in NH CO mixing ratios of -0.52 ppb/yr was found to be due to a decline in CO emissions from fossil fuel use. The atmospheric CO measurements at Barrow, Alaska (Fig. 1.6, top panel) show that this negative trend continued also in the 21st century, most likely due to a decrease in

European emissions (Duncan et al., 2007; Duncan and Logan, 2008). This station is mainly sensitive to anthropogenic CO emissions from Europe and North America. However, enhanced CO from fires in Russia in 1998 (due to the strong El Niño Southern Oscillation of 1997/1998) and 2002, is also observed at this station.

Figure 1.7 shows the time series of annual, anthropogenic CO emission estimates from the EDGAR inventory. Although Asian emissions have been steadily increasing since the early 1970's (dashed line) due to increased emissions from industry, residential cooking and road transport, this increase is counter-balanced by a decrease in CO emissions in North America (dotted line), Europe and Russia (dash-dotted line). The decrease in emissions in Eastern Europe and Russia is attributed to a contraction of the economy in Russia after the collapse of the formal Sovjet Union. The decrease in North America and Western Europe is associated with regulatory measures for road vehicles (Duncan et al., 2007; Duncan and Logan, 2008).

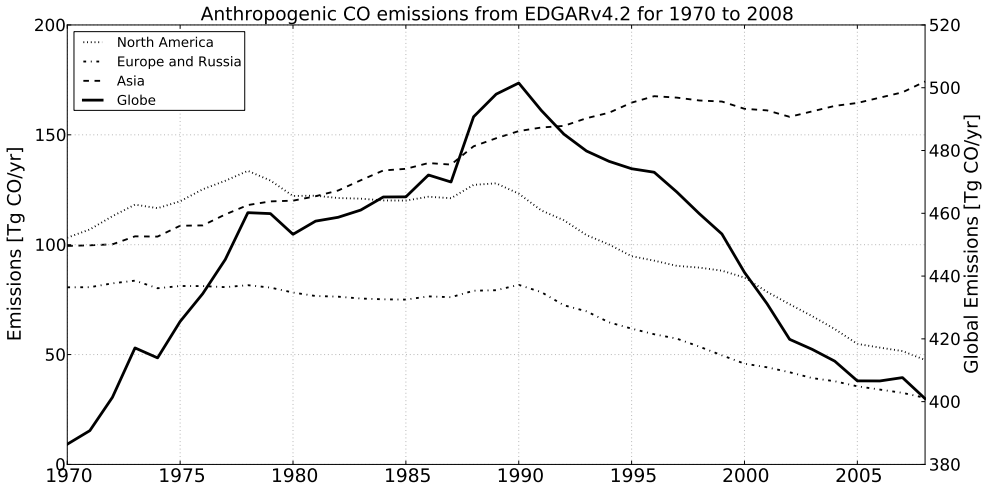

Figure 1.7: *CO emissions from different anthropogenic sources (road transport, residential cooking, industry and agriculture) as estimated in the EDGARv4.2 inventory for the period 1970-2008. Dashed and dotted lines represent CO emissions from NH continental regions (numbers on the left axis), the solid line represents the global CO emission estimate (numbers on the right axis).*

For the European surface stations, the decrease in CO emissions from fossil fuel use are often masked by other processes. For example, measurements of CO at Mace Head, Ireland (Fig. 1.6, second panel) are only slightly sensitive to CO emissions from the continent since the prevailing wind direction is from the west. Moreover, the North Atlantic Oscillation (NOA) influences climate variability in Europe and may also mask the reduction of European emissions. However, for total column observations at the Jungfraujoch station in the Alpes, Duncan et al. (2007) found a small negative trend in observed CO columns in the period 1988-1997.

The negative trend in global anthropogenic emissions (solid line in Fig. 1.7) is further explained by the fact that European emissions typically take place more northwards compared to emissions in Asia. Therefore, air with enhanced CO may be transported towards the Arctic, where it is trapped during the winter due to low OH concentrations and the CO lifetime is much higher than the average 2

months. In contrast, Asian CO emissions may be transported southwards in direction of the Tropics, where the higher OH concentrations will remove CO much faster from the atmosphere.

As observed in Fig. 1.6, there is no discernible trend in the Tropics and SH CO mixing ratios. CO mixing ratios in this region are dominated by CO emissions from biomass burning which do not show a trend, although they vary largely from year to year, especially over South America and Indonesia. For example, the strong El Niño Southern Oscillation (ENSO) event in 1997/1998 led to a severe drought in the Amazon region and Indonesia. A large pulse of biomass burning CO perturbed the CO mixing ratios at American Samoa in summer 1997 and resulted in enhanced CO at the South Pole station in both 1997 and 1998 due to transport of pollution plumes.

1.4.2 Inter annual variability

Inter annual variability in atmospheric CO mixing ratios in the Tropics, the SH and the boreal forests of North America and Eurasia are due to year-to-year variations in biomass burning (Duncan et al., 2007). Several studies investigated IAV in carbon emissions. For example, van der Werf et al. (2006) found a difference of more than 250 Tg CO/yr (approximately 10% of the current CO budget, see Table 2.3) between 1998 and 2000. Influences from climate such as the ENSO have a pronounced influence on biomass burning CO emissions leading to IAV. For example, in an El Niño year, droughts in South East Asia, Indonesia and South America may lead to more slash-and-burn practices in agricultural regions: forest is cut, the slash allowed to dry and ignited. The remaining ash fertilizes the soil and crops can be planted on the burned area. However, due to the extreme drought, the fires may easily run out of control destructing large parts of intact forest. The strongest El Niño event of the 20^{th} century in 1997/1998 led to an excess of biomass burning CO emissions of 225-400 Tg CO which is an enhancement of 45-80% of normal biomass burning CO emissions (Novelli et al., 2003).

IAV in atmospheric CO columns due to biomass burning was also observed from space by the MOPITT and SCIAMACHY instruments (Edwards et al., 2006b; Gloudemans et al., 2009). In their work, Edwards et al. (2006b) focussed on the first 5 years of MOPITT observations from 2000 to 2005. Although the largest CO columns were found to originate from biomass burning CO emissions in Africa and South America, IAV in biomass burning CO was in particular large for the Maritime continent (Indonesia plus Malaysia) and was closely linked to the ENSO precipitation index (Edwards et al., 2006b). Gloudemans et al. (2009) studied inter annual variability in CO total columns retrieved from the SCIAMACHY satellite instrument for 2003 to 2007. For the Martime continent they found highest CO columns for autumn in 2004 and 2006, coinciding well with the warm phases of El Niño in the period 2003-2007 and hence, extensive biomass burning in this region. For the Amazon region, highest CO columns were measured in October 2004, 2005 and 2007 whereas 2004 and 2006 showed somewhat lower columns.

Other fire characteristics and fire pollutants such as aerosols also show IAV. For example, Aragão et al. (2008) linked hot pixel counts (a measure for fire occurrence) to precipitation for the Amazon region for the years 1998 to 2006 and found very good anti correlations between the number of hot pixel counts and rainfall. Torres et al. (2010) found a similar relation between rainfall and fire counts and these in turn correlated well with OMI observed aerosol optical depths for the period 2005-2009. However, low aerosol loading over the Amazon region in 2008 (compared to previous years) could not be explained by excessive rainfall as the rainfall deficit in 2008 was comparable to 2005 for which high aerosol loadings were measured. Torres et al. (2010) speculated that socio-economic factors such as the global demand for beef or soy could play a role or perhaps regulatory measures from the Brazilian government to reduce deforestation (see below). Inter annual variability of biomass burning CO emissions from South America will be investigated in detail in Chapter 5.

Deforestation

Deforestation is the term used to describe the removal of forest or trees in a region after which the land is converted. Currently, deforestation occurs mainly in tropical regions in Africa, South East Asia (including Indonesia) and South America. However, large forests used to cover for example Europe in the past. An increasing demand for wood, due to the growing population and demands for wood in the ship industry (used for colonization and naval warfare), the forests of Europe were deforested in the 15^{th} century (Williams, 2003). In this work we focus on deforestation in the Amazon region in South America. This Tropical rain forest region spreads out over several countries (e.g., Brazil, Bolivia, Peru, Ecuador, Colombia, Venezuela, Guyana, Suriname and French Guiana, see Fig. 1.8), but the largest part (62% according to Malhi et al. (2008) and even 70% according to Kirby et al. (2006)) is in Brazil. Deforestation was initiated in the 1960, likely due to the paving of two highways through the Amazon to connect the North Western states of Brazil to the rest of the country (Kirby et al., 2006). Before that time, access to the forest was restricted. Other unpaved roads through the Amazon made the region accessible and governmental incentives encouraged colonization of the Amazon (Fearnside, 2005; Kirby et al., 2006). Clearing forest to pastures was widely used, but deforestation for mining, timber extraction and hydroelectirc energy was also started.

Later, with an increasing world wide demand for soy (for biofuels and cattle feed) from the mid-1990's, another threat to the Amazon emerged: soybean plantations (Fearnside, 2001). Large areas in the Cerrado grasslands were converted to croplands to produce soy on a large scale. In addition, land clearing in the forest was used to convert more land to croplands. Moreover, the steadily growing cattle herd in Brazil (Brasileiro de Geografia e Estatistica, 2009), led to more forest conversions to pasture lands also triggers deforestation and this is still ongoing. For example, Laurance (2007) describes how a change of crop in the USA (from soy to corn) increases deforestation in the Amazon: Due to the lower production of soy in the USA, soy prices increase which stimulates large landholders to start more soy plantations in the Amazon. Either new forest is converted to croplands or cattle pastures are further converted to croplands, effectively pushing the ranchers further into the forest (leading to deforestation again). Soy plantations are more harmful to the Amazon region compared to the traditional cattle ranching because effective infrastructure has to be build to transport the soy to the ports for export. This infrastructure again leads to deforestation to pave (rail)roads.

The global demand for biofuels to reduce our dependency on fossil fuels is the next threat to the Amazon. Apart from soy, used to generate biodiesel and livestock feed, in particular sugar cane is used to produce ethanol. In 2008, Brazil produced 27.6 billion l ethanol of which roughly 80% was used as fuel in so-called flex-fuel vehicles (Rovere et al., 2011). Flex-fuel vehicles were developed in 2003 and the owners can decide what combination of gasohol (gasoline combined with 20-25% ethanol) and ethanol they want to buy at the station. Currently, over 30% of the Brazilian fleet consists of flex-fuel vehicles (Walter et al., 2011). The remaining 20% sugar cane ethanol was exported (making Brazil the largest exporter of sugar cane ethanol (Walter et al., 2011)). Traditionally, sugar cane plantations are located in the state of São Paulo (see Fig. 1.8), close to the port (Cardoso et al., 2012). However, with the growing international demand, the plantations are extended to other states. The majority (90%) of the plantations are started on pasture lands, previously used for cattle ranching. Hence, no direct deforestation is needed for these plantations (Lapola et al., 2010). However, as outlined above, indirect land-use changes may as well lead to deforestation in the Amazon forest. With a growing cattle herd, ranchers are pushed further into the Amazon. It is estimated that indirect deforestation could largely offset the benefits from biofuel production due to the amount of greenhouse gases emitted by the deforestation process (Lapola et al., 2010).

Deforestation by small farmers is typical for the state of Rondônia in Brazil (Fearnside, 2005). Small parts of the forest are cleared and the cleared biomass is dried during the dry season (July - October). At the end of the dry season, the biomass is burned. In contrast, large landholders use mechanized land clearing to convert forest to pastures or croplands (van der Werf et al., 2009). The biomass is

Figure 1.8: *Map of South America in which the borders of the Amazon region are given by the black line. Important states in Brazil with respect to deforestation or sugar cane plantations are denoted by white acronyms: PA = Pará, RO = Rondônia, MT = Mato Grosso and SP = São Paulo. Colors on the map indicate the enhanced vegetation index. Greenish colors refer to tropical forest whereas brownish colors refer to sparse vegetation (e.g., in the Andes mountain range). This figure has been downloaded from http://earthobservatory.nasa.gov/Features/AmazonEVI/ on February 16, 2012. We only added the state markers (PA, RO, MT and SP).*

piled up and ignited several times in the same year or spread out over several years. The latter means that it is difficult to map annual deforestation rates onto CO emissions. For example, if the fuel is extensively dried, biomass debris is burned at the end of the dry season and emits CO_2 and CO to the atmosphere, which can then be linked to the area deforested. However, in a wet year like 2009, ignition of the wet fuels may be difficult and removal of the biomass by fire may be postponed to the next year, which obviously makes the connection between annual deforestation and emissions more difficult. This is shown in Fig. 1.9, where we compare statistics of deforestation with CO emissions from GFED3 and observed CO columns. Indeed, the National Institute for Space Research (INPE) shows a steady decrease in deforestation from 2005 onwards, but CO emissions over the Amazon region do not show a similar behavior (in particular in the last 5 years), indicating that deforestation and CO emissions are difficult to connect. CO emissions seem to match observed CO column-averaged mixing ratio much better. These observations will be used in the inverse modeling approach (see below) to estimate inter annual variability in CO emissions over South America (Chapter 5).

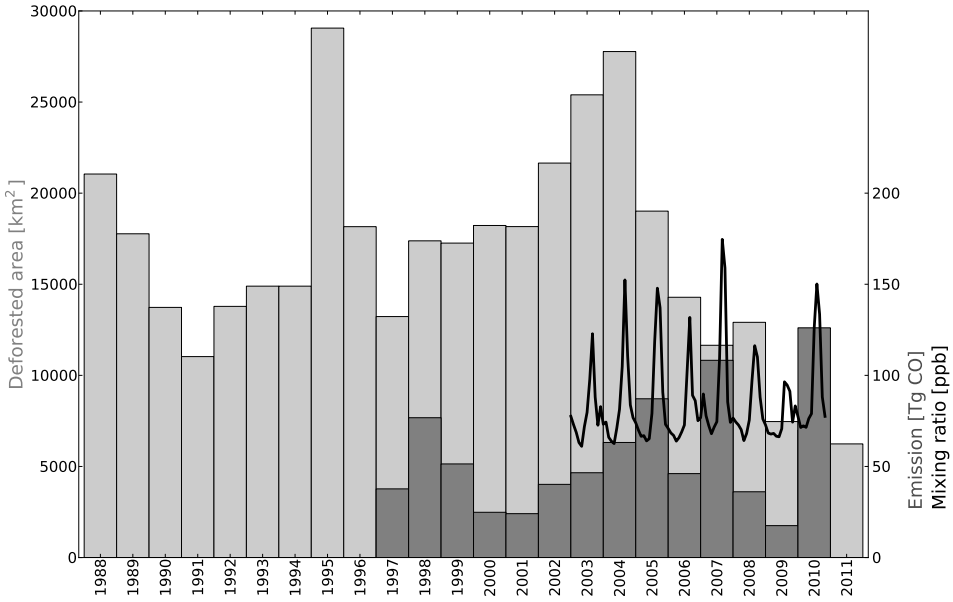

Figure 1.9: *Deforestation statistics (light gray) from the Brazilian National Institute for Space Research (INPE) from 1988 to 2011 (numbers on the left axis represent annual deforested area in km^2). Annual biomass burning emissions (in Tg CO) from GFED3 (dark gray) for South America from 1997 to 2010 are taken from van der Werf et al. (2010) with numbers on the right axis. The black line represents monthly mean column-averaged CO mixing ratios from the MOPITT instrument from 2003 to 2010 (also with numbers on the right axis).*

1.5 Estimating emissions of CO

Although the various mechanisms of CO formation are relatively well understood (Sect. 1.2), the exact magnitude of the emissions and their temporal variations are less certain. The approach to estimate emissions from the underlying emission processes is called the 'bottom-up' approach. In contrast, emissions can be estimated by using atmospheric measurements, the so-called 'top-down' approach.

1.5.1 Bottom-up approach

The bottom-up approach basically uses statistics of fuel usage combined with information on CO emission per unit of fuel combusted. For example, annual emissions from fossil fuel combustion by road transport in the EDGAR inventory (European Commission and Netherlands Environmental Assessment Agency, 2010) are typically estimated per country. Statistics on the amount of fuel (per fuel type) used is derived from the International Energy Agency. Because different vehicle types may emit different amounts of CO per unit of fuel burned, an estimate of the amount of heavy duty vehicles, light duty vehicles, passenger cars, motorcycles etc. per country is derived from the International Road Federation. Finally, emission factors (from the EMEP/EEA Air Pollutant Emissions Inventory Guidebook) are needed to compute the emission of CO per unit of fuel combusted for each vehicle type. CO emissions derived in this way may carry uncertainties. For example, although the fuel use statistics in the Western world are rather well-known, this is certainly not the case for the developing world (Africa, Asia and South America). Moreover, uncertainties in CO emission factors may also play a role.

Typically CO emissions from fossil fuel combustion inventories are presented on annual scales without seasonal or daily variation. However, recent inverse modeling studies have shown that CO emission estimates on the NH (mainly from this emission category) do vary throughout the year. Kopacz et al. (2010) and Fortems-Cheiney et al. (2011) reported much higher CO emission estimates in winter than in summer with differences up to a factor two for North America, Europe and Asia. Kopacz et al. (2010) reported that vehicle cold-start CO emissions may be underestimated in current inventories. Day-to-day variation in emissions and emission peaks during rush hours in the morning and evening are typically not included in bottom-up inventories, but may be important for accurate modeling of the CO concentrations in emission regions.

Fewer statistics are available on CO emissions from residential fuel use, mostly in India and China (Fig. 1.1). For this source the bottom-up approach and the emission factors depend heavily on the fire types used (e.g., open fire and wood-burning stoves (Naeher et al., 2000)).

Estimating biomass burning CO emissions proofs to be even more difficult because (1) unlike fossil fuel usage, there are hardly statistics on fuel usage, (2) fires may not be detected or burn beneath the surface and (3) emission factors are highly uncertain. The Global Fire Emission Database (GFED) inventory employs satellite based burning information combined with biogeochemical modeling and laboratory experiments to come up with biomass burning carbon emissions for the period 1997 - 2010 (van der Werf et al., 2003, 2006, 2010). From the carbon emissions, the emissions of trace gases (CO, CO_2, CH_4 etc.) are derived. Here we summarize the main features of the latest release, GFED3 (van der Werf et al., 2010) for CO.

The amount of carbon emitted from fires (per unit of time) is computed as the product of burned area (in m^2), fuel loads $\left(\frac{gC}{m^2}\right)$ and combustion completeness $\left(\frac{1}{m^2}\right)$. For CO an additional multiplication with the CO-specific emission factor (the amount of carbon emitted as CO in $\frac{gCO}{gC}$) is performed.

Burned area

After the occurrence of a large fire, a burn scar remains, which is visible from space (Giglio et al., 2010). The new GFED3 product uses the updated burned area product at a very high resolution of 500 m as described in Giglio et al. (2010). The largest burned area was found for savannas (36.6%), followed by woody savannas (28.8%), open shrublands (11.1%) and grasslands (9.2%). Forest fires (both Tropical and boreal) are responsible for only 5% of the burned area, but due to the higher fuel load per area (see below), forest fires typically emit more CO per unit area compared to savannas and grasslands.

Fuel loads and combustion completeness

In the GFED3 inventory, fuel loads and combustion completeness are estimated using the CASA (Carnegie-Ames-Stanford-Approach) biogeochemical model (van der Werf et al., 2010). Fuel loads specify the amount of biomass (above and below ground) available as fuel in a fire. In the past, biome-averaged values of fuel loads have been used, but explicitly modeling of the fuel loads takes the heterogeneity of the different biomes into account and have been shown to result in more realistic estimates of fuel loads (van der Werf et al., 2010).

Since not all available biomass is burned during a fire, combustion completeness (CC) is used to quantify the fraction of the fuel load that is actually burned. CC depends on the fuel type (grass will burn more completely compared to a tree), but also on moisture content of the fuel (dry fuels burn more completely than moist fuels). Moreover, CC typically changes throughout the year as the moisture content may change in the dry season due to extensive drying of the fuels.

Emission factors

The CASA biogeochemical model yields carbon emission estimates. However, since not all fuels are combusted completely, CO, methane and other trace gases are co-emitted with CO_2. Emission factors are used to estimate the amount of a trace gas emitted per unit of emitted carbon. In GFED3 biome averaged emission factors are used based on the work by Andreae and Merlet (2001). However, since emission factors (like combustion completeness), also depend on the type of fuel, fuel moist, temperature and fractional tree cover (van Leeuwen and van der Werf, 2011) this approximation brings large uncertainties to the CO emission estimates.

Apart from the GFED inventory, there are a few other CO emission inventories which were recently compared by Stroppiana et al. (2010). This study again showed the large uncertainties still existing in bottom-up inventories for biomass burning. For example, global estimates of biomass burning CO emission for the year 2003 ranged from 365 to 770 Tg CO. On continental scales, differences were also large. For South America estimates ranged from 35 to 122 Tg CO, which underscores the need for a better quantification of biomass burning emissions.

Given the large uncertainties in current bottom-up inventories for biomass burning, a different approach to estimate the amount of fuel combusted is by monitoring the radiative energy released by fires from space. Wooster et al. (2005) showed that approximately 15% of the energy released by fires can be measured by nadir-viewing mid-infrared instruments. Wooster et al. (2005) also report that fire radiative power (FRP) correlates well with the combustion rate and the fire radiative energy (FRE, the total energy radiated by a fire) correlates well with the fuel mass combusted during a fire. Within the MACC (Monitoring atmospheric composition and climate) project, a first biomass burning emission product based on satellite derived FRP, GFASv1.0 (Global Fire Assimilation System), has become available recently (Kaiser et al., 2012). CO emissions [gCO $s^{-1}m^{-2}$] are computed as the product of the dry matter combustion rate $f(DM)$ with the CO emission factor [gCO kg^{-1}DM]. The dry matter combustion rate $f(DM)$ [kg DM $s^{-1}m^{-2}$] is derived directly from the fire radiative power using a conversion factor depending on land cover type (Kaiser et al., 2012).

The uncertainties in bottom-up CO emission inventories are also obvious when these emissions are simulated in global chemistry and transport models. These simulations are compared to observed CO mixing ratios and typical findings are (1) too low emissions from Asia (Kasibhatla et al., 2002; Shindell et al., 2006), (2) an underestimate of the winter-spring CO maximum on the NH (Kopacz et al., 2010; Fortems-Cheiney et al., 2011) due to seasonality in fossil fuel and biofuel combustion on the NH and (3) biomass burning emissions are claimed to be too low (Liu et al., 2010; Kopacz et al., 2010) and the peak month of SH CO (due to biomass burning) is shifted one month compared to observations. However, the chemistry transport models are not perfect either and different models give different results even when the same emissions are applied (Shindell et al., 2006).

1.5.2 Top-down approach

The top-down approach is an independent approach to determine estimates of trace gas emissions. The available atmospheric measurements (see below), combined with an atmospheric chemistry and transport model are used to find a statistically optimal set of (posterior) emissions. On the one hand, the resulting simulated CO mixing ratios fit the measurements while on the other hand the optimized emissions remain close to the starting set of (prior) emissions. More information about the top-down methods as well as an historical overview of CO inverse modeling will be given in Chapter 2.

1.6 CO observations

Atmospheric measurements of CO are a key ingredient to validate the outcome of model simulations and are even more important for inverse modeling, since the emissions are being tuned to fit these measurements. CO observations can be separated in three types: surface observations, aircraft observations and satellite observations.

1.6.1 Surface observations

The largest and most well-known network of surface observations of CO is maintained by the National Oceanic and Atmospheric Administration Earth System Research Laboratory (NOAA/ESRL) Global Monitoring Division (GMD). Paired flask samples are taken every week at approximately fifty locations worldwide. Originally, the stations locations were chosen to represent background conditions and therefore, the stations are often located in remote places (e.g., station Barrow, Alaska or South Pole station). However, some stations in Europe, North America and Asia are located in strong emission regions (e.g., station Tae-ahn Peninsula, Republic of Korea).

The flask samples are analyzed centrally in the NOAA laboratory in Boulder, Colorado, USA (Novelli et al., 1998, 2003). The measurements are made using gas chromatography and calibrated to the GMD/WMO 2004 CO scale. In this way, high precision measurements of CO became available with an uncertainty of approximately 0.5 - 1 ppb. In Chapter 5 the recently revised NOAA data are used (Novelli and Masarie, 2010). Differences with earlier data releases are typically very small except for the remote SH.

Other institutes also measure CO at surface stations. For example the Advanced Global Atmospheric Gases Experiment (AGAGE), performs continuous in-situ observations of CO at 11 stations worldwide (some at the same location as the NOAA sites). CO mixing ratios are provided at an hourly time resolution at these sites and hence result in a dataset with a much finer temporal resolution. However,

in comparison with the NOAA surface network, the spatial density of the AGAGE network is much lower.

A completely different type of CO observations performed from the ground, are made by the Network for the Detection of Atmospheric Composition Change (NDACC) Infrared Working Group (IRWG). This comprises a network of over twenty stations where high resolution spectrometers make measurements of total column CO, i.e., the amount of CO molecules in a certain column that reaches from the surface to the top of the atmosphere. In contrast to many satellite instruments measuring CO currently (see Sect. 1.6.3), these measurements are typically sensitive to the whole column. Since this network was originally developed for stratospheric observations, many observations are taken at high-altitude locations. Also, their spatial density is very low.

1.6.2 Aircraft observations

Surface flask observations of CO are mainly sensitive to boundary layer CO. Due to the remote locations of the surface sites, in particular background CO levels are being measured. Some stations are sensitive to pollution plumes, transported from high emission regions (e.g., station Ascension Island). These transport patterns of CO can also be detected using aircraft measurements of CO. In the past, many aircraft campaigns were organized to monitor particular regions and events. For example, the distribution of trace gases over the Southern Pacific, was studied during the Pacific Exploratory Mission (PEM-Tropics B) (Blake et al., 2001). In addition, Asian outflow over the Northern Pacific due to emissions from Asia was studied during the Transport and Chemical Evolution over the Pacific (TRACE-P) aircraft mission (Jacob et al., 2003). These aircraft campaigns are of short duration (in the order of 1 month).

Since the beginning of the 21st century, however, two programs measure trace gases on commercial aircraft. The Measurement of OZone and water vapour by AIrbus in-service airCraft (MOZAIC) and Civil Aircraft for the Regular Investigation of the atmosphere Based on an Instrument Container (CARIBIC) programs use a fleet of passenger aircraft to measure in-situ CO with high resolution on the main flight routes from Europe to North America and from Europe to the Middle East and Asia. Unfortunately, only a few flights head to the SH continents resulting in coverage of mainly the NH.

Apart from these programs, the NOAA aircraft program yields regular CO observations (up to 8 km altitude) over selected sites, mainly in North America.

1.6.3 Satellite observations

Both aircraft and surface observations do not provide global coverage of CO. However, satellites do. The first space based pictures of CO were made in the 1980's during the Measurement of Air Pollution from Satellites (MAPS) program. This instrument onboard of a space shuttle measured global CO levels for short periods in November 1981, October 1984 and in April and October 1994. This pioneering instrument showed for the first time that high concentrations of CO are found in the Tropics (apart from the polluted NH). In a later flight, the importance of biomass burning CO emissions on enhanced CO levels in the SH was observed. Note that since there were people on board of the space shuttle, they were able to observe also the smoke from the fires over Brazil, Southern Africa and Indonesia.

Satellite observations using the thermal infrared

In the years following the last MAPS flight in 1994, the Measurements of Pollution in the Troposphere (MOPITT) was developed and scheduled for launch on the NASA satellite Terra. The Terra satellite

was launched on December 18, 1999 in a sun-synchronous orbit, approximately 705 km above the Earth's surface and with Equator crossing times of 10.30 and 22.30 h. First measurements from MOPITT date from March 2000. MOPITT is a nadir-looking instrument with a spatial resolution of approximately 22 km x 22 km resulting in global coverage every 3 days. MOPITT measures CO in the thermal infrared (TIR) and the shortwave infrared (SWIR). Recently, the MOPITT version 5 product was released which utilizes both the TIR and SWIR channels of the instrument. However, since we only use the TIR data from MOPITT in this thesis, we describe the TIR measurements of MOPITT below.

The TIR channel of MOPITT operates at a wavelength of 4.7 µm and measures upwelling thermal radiation from the Earth's surface and the atmosphere. The instrument was designed to measure the CO profile and total column with an accuracy of 10% (Pan et al., 1995). Gas correlation spectroscopy was used to maximize the CO signal, and minimizing the signal from other trace gases. The MOPITT instrument utilizes a series of correlation cells (Length Modulated or Pressure Modulated) with different amounts of CO in each cell. All cells sample a specific part of the spectral line, leading to the identification of different altitude ranges. In this way, it is possible to measure the CO profile. However, the signal of these correlation cells depends not only on the trace gas amount, but also on temperature variations. Since the temperature difference between the surface and the atmosphere is often very small near the surface, the MOPITT instrument sensitivity peaks in the free troposphere, typically between 4 and 7 km altitude. If the temperature contrast between the surface and the lowermost atmosphere is large enough, MOPITT has also sensitivity to the surface. Night time conditions (when thermal contrast between the surface and the atmosphere is very weak or even negative) result in even less sensitivity to CO in the lower troposphere. Moreover, night-time observations turn out to be biased (Emmons et al., 2007, 2009) and are not used in this work. In the TIR-only MOPITT product used in this thesis (MOPITT V4, (Deeter et al., 2010)), the CO profile is retrieved at ten pressure levels: A floating surface level and nine equidistant pressure levels from 900 to 100 hPa. The retrieval algorithm is based on the maximum a posteriori (MAP) solution, a specific type of the optimal estimation technique (Rodgers, 2000). Like the inverse modeling technique described in Chapter 2, this approach is based on measurements (radiances) a model (the radiative transfer model) and an a priori profile (Deeter et al., 2003).

The sensitivity of the instrument towards each level in the profile is given by the averaging kernel (Fig. 1.10). The averaging kernel is a dimensionless quantity that is defined as the dependence of retrieved CO on true CO mixing ratios. Hence, for a MOPITT retrieval on 10 atmospheric layers, the averaging kernel is a matrix of dimensions (10×10). Each row of this matrix describes how the true CO mixing ratios profile contributes to the retrieved CO mixing ratio at a specific level. Figure 1.10 clearly shows that the averaging kernel peaks at the free tropospheric levels (at 400 and 700 hPa) indicating maximum sensitivity at this altitude range.

The spatial distribution of CO as measured by MOPITT for March and September 2004 is illustrated in Fig. 1.11. Highest CO column (expressed in 10^{18} molecules cm^{-2}) are generally found on the NH in March. The typical hotspot from CO emissions in South-East Asia is clearly visible and transported to the east also affecting CO levels over the North Pacific ocean and the North American continent. In contrast, peak CO levels are observed on the SH in September. Emissions associated with biomass burning in South America, Africa and Indonesia are transported over the Atlantic and Pacific oceans. Note that mountain ranges (over which the air columns are small) such as the Himalaya, the Rocky Mountains and the Andes are visible.

Other space-borne satellite instruments that also measure CO in the thermal infrared in the 4.7 µm band are the Atmospheric Infrared Sounder (AIRS), the Tropospheric Emission Spectrometer (TES) and the Infrared Atmospheric Sounding Interferometer (IASI). Details of the characteristics of these instruments can be found in the literature (McMillan et al., 2005, 2011; Rinsland et al., 2006;

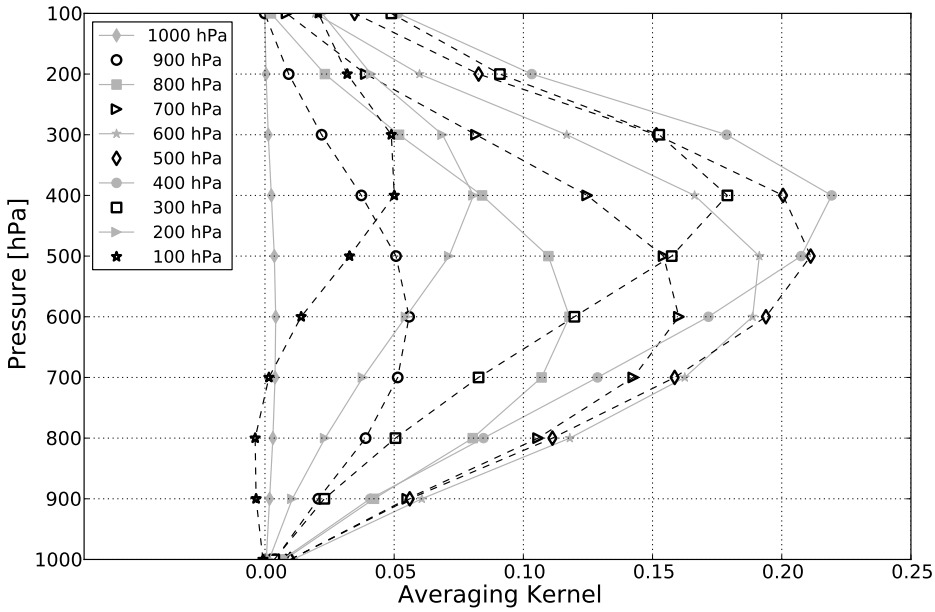

Figure 1.10: *Typical MOPITT averaging kernel for a retrieval on 10 atmospheric levels (assuming a surface pressure of 1000 hPa). The lines show the relative contribution of 'true' CO to retrieved CO for a specific retrieval level.*

Turquety et al., 2009; George et al., 2009) and in Table 1.1[1] The TIR-based satellite instruments have been extensively validated with aircraft data and ground based Fourier-Transform Infrared Spectrometer (FTIR) data. In addition, the satellite observations have been mutually compared. For example, the early MOPITT V3 product was positively biased (+20% in 2006) in comparison with aircraft observations (Emmons et al., 2009), but the first validation for MOPITT V4 showed much better comparison with this data (Deeter et al., 2010). AIRS observations have also been shown to be positively biased with respect to aircraft profiles (+9%) (McMillan et al., 2011) and even larger differences were found on the SH (Yurganov et al., 2010). IASI was compared to the other three TIR instruments and was found to be within 7% on the NH and around 10% lower than MOPITT and AIRS on the SH (George et al., 2009).

Satellite observations using the shortwave infrared

A drawback of the thermal infrared sounders discussed above is their low sensitivity to surface CO. Hence, to be able to effectively constrain surface CO emissions using TIR-based satellite data, model vertical transport should be resolved correctly. However, shortwave infrared (SWIR) sounders are sensitive to the entire atmospheric column, including the boundary layer. SWIR sounders measure CO at a wavelength of 2.3 μm using reflected solar radiation. Currently, the SCIAMACHY and MOPITT instruments permit retrieving CO in this wavelength band. For SCIAMACHY, several instrument and calibration issues are present such as the growing of an ice layer on the detectors

[1] This table has been copied from George et al. (2009).

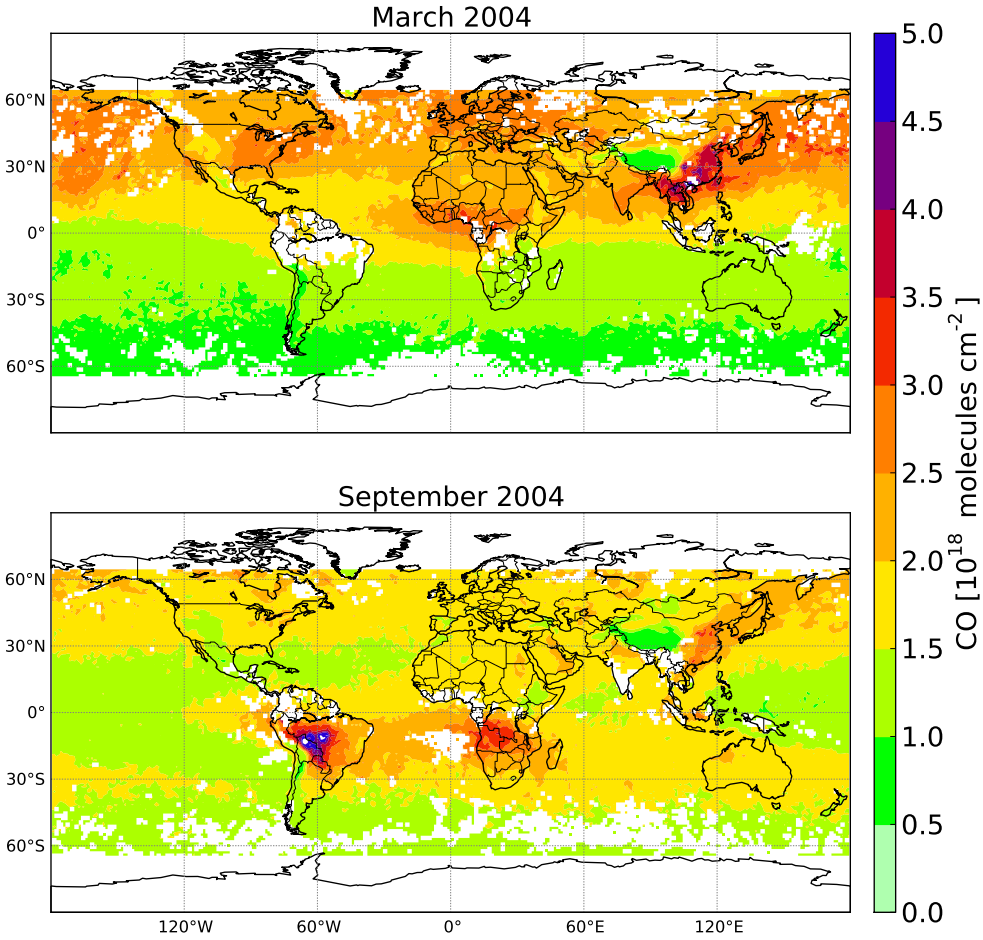

Figure 1.11: *Monthly averaged total column CO as observed by MOPITT for March (top) and September (bottom) 2004.*

and an increasing number of bad and dead pixels due to cosmic radiation (Gloudemans et al., 2005). Although these issues have been corrected for in the operational retrieval code, the signal-to-noise ratio of the retrievals is much smaller compared to the TIR-based retrievals due to their dependence on surface albedo and solar zenith angle (de Laat et al., 2006). This leads to large random errors in individual retrievals of 10-100% and hence, the retrievals have to be averaged over large spatial regions and long temporal windows, which may make these observations less useful in an inverse modeling approach.

In contrast, the follow-up of SCIAMACHY and OMI, the upcoming TROPOMI mission (scheduled

Table 1.1: *Characteristics of current thermal infrared satellite instruments. This table has been copied and adjusted from George et al. (2009).*

Mission/Platform Agency Launch date	Platform altitude Equator crossing time (d/a orbit)[a] Instrument type	Spectral coverage Pixels size, Spatial coverage Spectral resolution
MOPITT/Terra	705 km	2140-2192, 4265-4305
NASA (EOS)	10:30, d	22x22 km, swath 640 km
December 1999	Gas correlation radiometer, 3 bands	0.04 cm^{-1} (effective)
AIRS/AQUA	705 km	650-1136, 1216-1613, 2170-2674
NASA (EOS)	13:30, a	13.5x13.5 km x 9 pixels, swath 1650 km
May 2002	Grating spectrometer, 2378 channels	$\approx$ 1.8 cm^{-1} (2170-2200 cm^{-1})
TES/AURA	705 km	652-919(2B1), 923-1160(1B2), 1090-1339(2A1) and 1891-2251(1A1)
NASA (EOS)	10:45, a	0.53x8.3 km x 16 pixels
July 2004	FTS, 40540 channels, OPD 8.45 cm	0.10 cm^{-1} (apodized)
IASI/MetOP	817 km	645-2760
EUMETSAT/CNES	09:30, d	12 km diam x 4 pixels, swath 2200 km
October 2006	FTS, 8461 channels, OPD 2 cm	0.5 cm^{-1} (aposdized)

[a] descending and ascending orbits, respectively

for launch in 2015), will also measure CO in the 2.3 μm band and will have (1) a much smaller footprint of approximately 7x7 km so that cloud contamination will occur less often and (2) much higher signal-to-noise ratio which will reduce the need to average observations. In addition, the MOPITT version 5 product combines the TIR and SWIR channels of the instrument to have the best of both worlds. Figure 1.12 shows the main differences between the new joint product and the TIR-only product for the months March and September 2010. Due to enhanced sensitivity to the lowermost atmosphere, the joint product results in larger CO columns in particular in the mid- to high-latitudes of the NH in March and for biomass burning CO in Brazil in September. However, the differences are generally within 10% of the monthly averaged CO columns.

1.7 Research questions and outline

From the previous paragraphs, it is clear that large uncertainties still exist in current CO emission estimates. Numerical techniques may help to constrain the emissions further since the available (MOPITT) and upcoming (TROPOMI) high resolution satellite observations provide detailed information on CO mixing ratios throughout the troposphere. However, atmospheric models should be able to ingest the data.

In this thesis the top-down approach is used to provide an estimate of CO emissions on the global scale. The overarching research questions of this thesis are:

1. How do CO observations constrain the CO emissions on global and regional scales?
2. What is the added value of TIR satellite measurements, compared to surface network observations, in particular for monitoring biomass burning emissions and their variability?

The observation-based emission estimates are obtained by employing the TM5-4D-Var system which is described in Chapter 2. Previous studies with the same system focused on CH_4 (Meirink et al.,

2008a,b; Bergamaschi et al., 2009, 2010). Although CO and CH_4 share the same atmospheric sink (oxidation by OH), the lifetime of CH_4 (ten years) is much longer than the lifetime of CO (two months). Therefore, the system has to be characterized for CO. This is the subject of Chapter 3. Using measurements of the surface network only, we address the more technical issues like:

- Is the system capable to substantially reduce the uncertainty in our prior CO emission estimates?
- Can independent information be obtained about different emission categories that have distinctly different spatial and temporal emission distributions?
- What is the effect of model errors on the inferred CO emission estimates?

In Chapter 4 the system is extended such that it can ingest also MOPITT satellite data. Emissions estimates obtained by using the NOAA surface network will be compared with inferred emission estimates from the assimilation of MOPITT data only. Specifically, the following questions are addressed:

- How do optimized emission estimates using either NOAA surface or MOPITT satellite data compare?
- How does the treatment of the NMVOC-CO emissions in the modeling framework influence the solution?

In Chapter 5 the system is improved again. Surface and satellite data can be simultaneously assimilated in the system. It appears to be necessary to implement a bias correction scheme to obtain emission estimates that are consistent with both observational datasets. We apply this system to the 2006-2010 period to optimize CO emissions over South America on high spatial resolution, in particular in the dry season. In this chapter, we focus on the following questions:

- Can we infer a bias in MOPITT observations, and how does this bias vary from year to year?
- Is it possible to quantify the IAV in biomass burning CO emissions from South America? And consequently, can we use the inferred emission estimates to validate bottom-up estimates?
- Which factors drive this IAV?

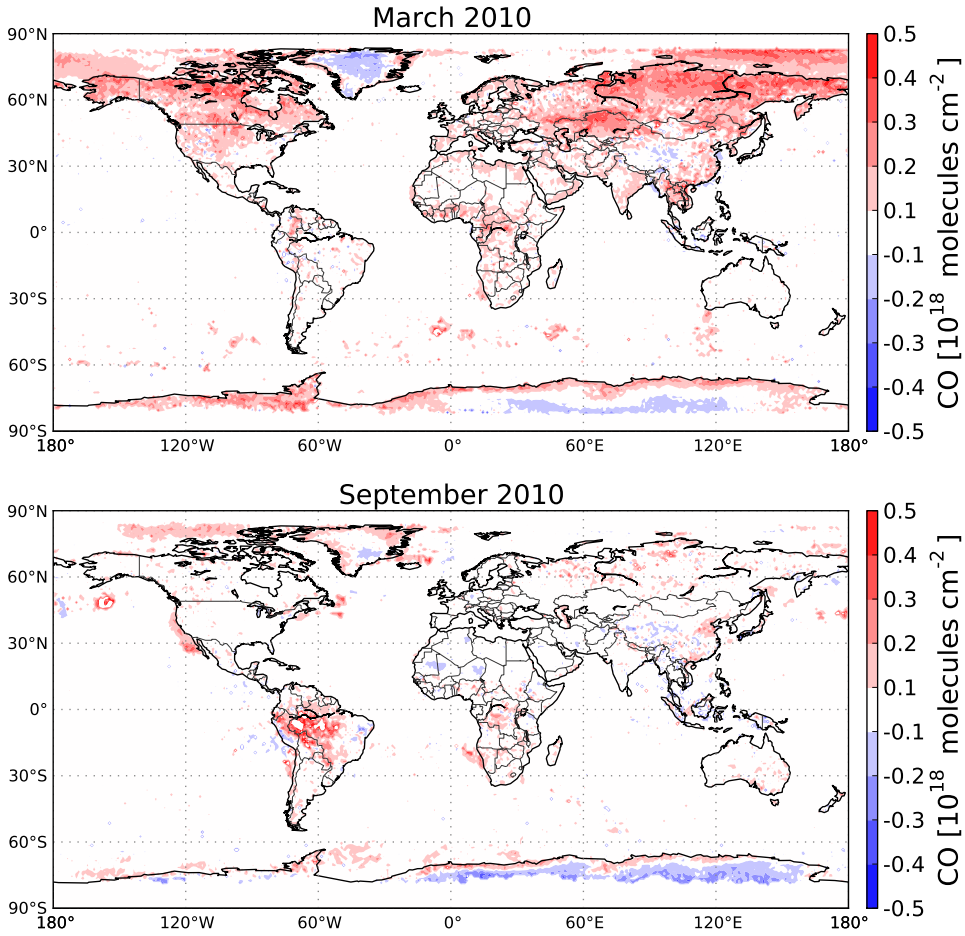

Figure 1.12: *Monthly averaged total column CO differences (in 10^{18} molecules cm^{-2}) for MOPITT defined as (V5-Joint minus V5-TIR-only) for March (top) and September (bottom) 2010.*

CHAPTER 2

Inverse Modeling

2.1 Introduction

As outlined in the previous chapter, the bottom-up approach to estimate emissions results in a gridded emission product (e.g., GFED or EDGAR inventories). These emissions are subsequently used in model simulations and integrated over space and time to provide CO mixing ratios. However, discrepancies between modeled and observed CO mixing ratios exist (Shindell et al., 2006). The idea of data assimilation is to use the atmospheric measurements to learn something about the emissions. In general however, the dimension of the unknown (true) emission vector is much larger than the dimension of the observation vector (or more strictly formulated: the number of independent observational constraints). Hence, the optimization problem is underdetermined and does not have a unique solution.

The traditional Bayesian inversion uses a priori information (usually from these bottom-up inventories) about the emissions and tunes the emissions to fit the observations, while staying close to the prior state. This is the method of choice in this work. The number of variables (i.e. unknown emissions) that can be constrained by assimilating atmospheric observations depends on the number of measurements, their associated measurement error and the locations at which these measurements are performed. Hence, increasing the number of measurements (e.g., by including satellite observations) has the potential to lead to better constrained emission estimates. However in the Bayesian inversion approach their is no objective way to give weight to different data streams and the prior information remains an important ingredient. The geostatistical method (e.g., Michalak et al. (2004)) is another inversion method which does not use prior information on the emissions themselves, but models the prior correlations between the emissions such that the information in the observation can be optimally exploited to infer the emissions.

2.2 Technical framework

Consider a set of prior emissions x_b with corresponding error covariance matrix $\mathbf{B}$. Similarly, suppose we have a vector of measurements y with an error covariance matrix $\mathbf{R}$. The idea of inverse modeling is to obtain optimal emissions $\hat{x}$ that (after simulation by the atmospheric chemistry and transport model) are as close as possible to the observations. However, due to the underdetermined nature of the problem we also require the optimal emissions to stay close to the prior state x_b. If one would like to obtain $\hat{x}$ in a least squares sense, the formal mathematical equations are given by:

$$\hat{x} = \arg\min \mathcal{J} \tag{2.1}$$

$$\mathcal{J}(x) = \mathcal{J}_b(x) + \mathcal{J}_{obs}(x) \tag{2.2}$$

$$= \frac{1}{2}\left(x - x_b\right)^\top \mathbf{B}^{-1}\left(x - x_b\right) + \frac{1}{2}\sum_{i=1}^{M}\left(H(x)_i - y_i\right)^\top \mathbf{R}_i^{-1}\left(H(x)_i - y_i\right), \tag{2.3}$$

where $\mathcal{J}$ is called the cost function (with $\mathcal{J}_b$ and $\mathcal{J}_{obs}$ the background and observational parts, respectively), H the (non) linear chemistry transport model, M the number of time steps with observations and $\top$ the transpose operator. The analytical minimum of the cost function can be found if the chemistry transport model is linear. Indeed, by setting $\nabla\mathcal{J}(\hat{x}) = 0$, one can show that

$$\hat{x} = x_b + \mathbf{K}\left(y - \mathbf{H}x\right), \tag{2.4}$$

where $\mathbf{H}$ is the tangent linear model corresponding to H (Bouttier and Courtier, 1999). This formula is often referred to as the Best Linear Unbiased Estimator (or BLUE analysis). The matrix $\mathbf{K}$ is called the gain matrix and is defined as

$$\mathbf{K} = \mathbf{BH}\left(\mathbf{HBH}^\top + \mathbf{R}\right)^{-1}. \tag{2.5}$$

Working out the details of $\nabla\mathcal{J}(\hat{x}) = 0$ further, one can show that the posterior error covariance matrix $\mathbf{A}$ is equal to

$$\mathbf{A} = \left(\mathbf{B}^{-1} + \mathbf{H}^\top\mathbf{R}^{-1}\mathbf{H}\right)^{-1}. \tag{2.6}$$

For problems with a state vector with a low dimension, the analytical BLUE analysis can be applied since the matrices in Eq. (2.5) and (2.6) are small enough for direct inversion. However, when the dimensions of the vector and matrices are large, direct inversion is no longer feasible. This gave rise to two distinct approaches of finding optimal emissions. In the next two paragraphs we discuss the so-called synthesis (Bergamaschi et al., 2000; Pétron et al., 2002; Kasibhatla et al., 2002; Arellano et al., 2004; Jones et al., 2009) and variational approach (Stavrakou and Müller, 2006; Pison et al., 2009; Kopacz et al., 2009, 2010; Fortems-Cheiney et al., 2011).

2.2.1 Synthesis inversion

In a synthesis inversion the idea is to keep the number of parameters to be estimated (the elements of the state vector) limited. For example, if we assume that the emission distribution for each category (e.g., fossil fuel and biofuel combustion and biomass burning) per continent is known in advance and only the strength of the continental emissions is uncertain, the state vector consists of a number of scale parameters. Given a low-dimensioned state vector only low CPU costs are needed to obtain the Jacobian $\mathbf{H}$ of the corresponding chemistry transport model H. Suppose the state vector has dimension n. Then the Jacobian matrix $\mathbf{H}$ is of dimension $n \times m$ with m the number of measurements. Each column $\mathbf{H}(:, i)$ of this matrix is computed by simulating the transport model H for an emission vector e_i (which is zero everywhere except for element i which is 1). Given the prior emissions x_b and the corresponding error covariance matrix $\mathbf{B}$ as well as the observations y and their corresponding covariances in the matrix $\mathbf{R}$, one directly computes the optimal emissions and their errors by using Eq. (2.4) and (2.6).

2.2.2 Variational approach

A large drawback of the synthesis approach is that the method is only feasible for a relatively small amount of variables in the state vector: Firstly, to construct the Jacobian of the transport model $\mathbf{H}$, for each variable a model simulation needs to be performed. Secondly, for large state vectors, the corresponding matrices (in Eq. (2.5) and (2.6)) become too large to invert. Moreover, the assumption of known spatial patterns in the prior emissions may lead to erroneous results. For example, if the spatial pattern is completely wrong, the system will never be able to obtain realistic emissions. Moreover, due to aggregation errors (Kaminski et al., 2001), the calculated posterior error is underestimated (Meirink et al., 2008b). Therefore, the four-dimensional variational data assimilation (4D-Var) approach aims to optimize the emissions on the resolution of the underlying transport model. Since direct application of Eq. (2.4) to find the optimal emissions is no longer feasible, the cost function (Eq. 2.3) is minimized iteratively. Nowadays mainly two distinct optimizers are used for iterative minimization of the cost function in the 4D-Var franework: the conjugate gradient method (CONGRAD) and a quasi Newton method (m1qn3, Gilbert and Lémarechal (2006)). For a given state x, both methods require the evaluation of the cost function $\mathcal{J}(x)$ and its gradient $\nabla\mathcal{J}(x)$. The gradient of the cost function is calculated by running the adjoint model. The adjoint of the transport model TM5 used in this thesis has been developed and applied in a number of studies (e.g., Krol et al. (2008), Meirink et al. (2008a,b), Bergamaschi et al. (2009, 2010)). The construction of the adjoint to incorporate satellite observations is illustrated in Sect. 2.5.6. The quasi Newton method m1qn3 has the large advantage that it can be used even if the model is non linear. This occurs for example, if one wants to optimize emissions and the OH field simultaneously (Pison et al., 2009; Fortems-Cheiney et al., 2011). However, the convergence rate of this optimizer is often poorer compared to CONGRAD. Also, with this method it is not possible to obtain an estimate of the posterior errors. A workaround for this is to use a Monte Carlo approach (Chevallier et al., 2007). However, in this work the CONGRAD method is used to minimize the cost function.

The CONGRAD method combines the conjugate gradient method (Hestenes and Stiefel, 1952) with the Lanczos iteration (Lanczos, 1950) to obtain both the minimum of $\mathcal{J}$ and, after N iterations, the N leading eigenvalues and eigenvectors of the Hessian of the cost function. In general, the convergence rate of CONGRAD is slow due to large differences in magnitude of individual partial derivatives of $\mathcal{J}$. However, using a preconditioner, the convergence rate may be largely improved. Ideally, one would take the square root of the Hessian of the cost function as a preconditioner (as the iterative process would converge in 1 iteration), but this matrix is not known. Therefore, the preconditioner is defined as the matrix $\mathbf{L}$, such that $\mathbf{L}\mathbf{L}^\top = \mathbf{B}$. Note that since the Hessian of $\mathcal{J}$ ($\mathcal{J}''$) is equal to the inverse of the posterior error covariance matrix $\mathbf{A}^{-1}$ (Eq. 2.6) (Meirink et al., 2008b), the N leading eigenvalues λ_i and eigenvectors ν_i result in an estimate of the posterior error covariance matrix:

$$\mathbf{A} \approx \mathbf{B} + \sum_{i=1}^{N} \left(\frac{1}{\lambda_i} - 1 \right) (\mathbf{L}\nu_i)(\mathbf{L}\nu_i)^\top. \tag{2.7}$$

2.3 Toy model example

In this section we illustrate the 4D-Var concepts using an example model. Consider a simple 1-D model that transports air around ten grid boxes with circular boundary conditions (concentration outflow from box 10 enters box 1). We assume a 'true' initial concentration of 10 in box 1 and a 'true' emission of 0.3 per time step in box 4 (units are not specified for simplicity). The transport is assumed to be constant over time and transports 10% of the grid box concentration to the right neighbor per time step. Figure 2.1 shows the modeled concentration time series for all grid boxes.

The concentration pulse in box 1 is quickly transported to the right. In addition, the emission in box 4 enhances concentrations downwind of this box. After approximately 100 time steps, the starting pulse is smoothened out over all grid boxes and concentrations increase steadily due to the constant emission in box 4 and associated transport.

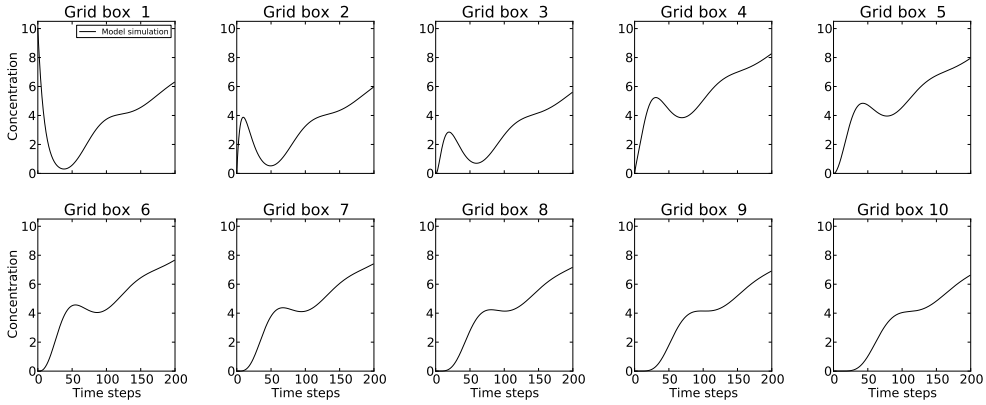

Figure 2.1: *Simulated concentration for all grid boxes given an initial concentration of 10 in box 1 and an emission of 0.3 per time step in box 4. Concentrations have been simulated for 200 time steps.*

In the next step we sample from the concentration time series shown in Fig. 2.1 and perturb these 'pseudo-observations' with random noise to mimic observational uncertainty. Now the question is: With this set of measurements and some prior information on the initial concentration and the emissions, how well can we retrieve the 'true' state using a 4D-Var system? In this example the prior initial concentration is chosen equal to the 'true' state, but the prior emission is put in grid box 5. In addition, the prior error covariance matrix $\mathbf{B}$ and the observation error matrix $\mathbf{R}$ are assumed diagonal. In the following we discuss the performance of the inversion system for (1) an overdetermined system, i.e., there are more observations available than unknown variables in the state vector and (2) a more realistic system in which the number of observations is limited. Since we know the true state, we can investigate the quality of the inversion directly by comparing the posterior state to the true state. The specific objective is to investigate the dependence on the errors specified by the matrices $\mathbf{B}$ and $\mathbf{R}$, the position of the observations and the fit with the measurements.

2.3.1 Overdetermined problem

If the number of available observations is larger than the number of unknown state vector elements, the minimization problem is overdetermined. Consider a model simulation consisting of 10 time steps with observations in each grid box. The number of measurements in this example is 100 (10 observations in all 10 grid boxes), compared to a state vector length of 20. For the base inversion the standard deviation of the prior state vector elements is assumed to be 100% of the corresponding state vector element, with a minimum error of 0.02. The uncertainty in the observations is assumed to be constant, 0.5.

The initial concentration is inferred by the system quite easily but finding the correct emission is more difficult. For non-perturbed observations (inversion NP in Table 2.1), the system finds the best

solution, an emission in box 4 of 0.27, even though we deliberately assigned the prior information of the emission to the wrong box 5. The cost function is strongly reduced from 40.3 to 2.2, because the measurements represent the 'true' state. The system can not retrieve the 'true' emission of 0.3 in box 4 as a result of the balance the system seeks between the information in the prior state and in the observations. Note that even with perturbed observations (inversion Base), the system is capable to retrieve the emission (of 0.26) in box 4. But in this inversion, the cost function reduction is smaller due to the noise we added to the measurements. The uncertainty reduction (ur), defined as

$$\mathrm{ur} = \left(1 - \frac{\sigma_\mathrm{a}}{\sigma_\mathrm{b}}\right) \times 100\%, \tag{2.8}$$

where σ_a (σ_b) is the standard deviation corresponding to the posterior (prior) estimate, is a measure for the information content of the observations. For example, without assimilation of any observations, $\sigma_a = \sigma_b$ and hence, no uncertainty reduction is achieved. For the base inversion, uncertainty reductions for the retrieved concentration in box 1 and the emission in box 4 are 86% and 67%, respectively.

We perform two sensitivity inversions in which the uncertainty in the prior or the observations is altered: for sensitivity S1, the minimum standard deviation of the prior state vector elements is reduced from 0.02 to 0.005, effectively increasing our trust in the prior estimate. In sensitivity S2 the error on the observations is increased by a factor 2, reducing the constraints of the observations on the emissions. For both sensitivity inversions the retrieved emission decreases to 0.21 since we either put more trust in the prior information (S1) or reduce our confidence in the observations (S2), leading to a system that has more difficulties to find the correct answer. This is also observed by inspection of the cost function. For S1, the penalty for departing the prior state has doubled compared to the base inversion, even though the solution remains closer to the prior. For S2, the prior cost function is already decreased by a factor 4 compared to the base. Although the posterior cost function for this inversion (1.3 + 3.8) is small, the solution is less accurate compared to the base inversion. Relaxing the observational constraints typically also leads to a smaller uncertainty reduction. For the sensitivity inversions, the uncertainty reduction is significantly smaller since the confidence in the observations has been reduced in comparison with our trust in the prior estimate. This illustrates that inversions of this kind have to find a balance between two terms of the cost function: (1) a part that is driven by observations, and (2) a background term, that specifies the information of the prior.

Table 2.1: *Results from the inversions using the toy model in overdetermined mode. Only two out of 20 state vector elements are given for the prior and the posterior (NP, Base and sensitivity S1 and S2). The value of the cost function is also given. Note that $\mathcal{J}_b(x_b) = 0$ and thus the prior cost function consists of the observational part only. The uncertainty reduction is defined as $\left(1 - \frac{\sigma_a}{\sigma_b}\right) 100\%$, where σ_a (σ_b) is the standard deviation corresponding to the posterior (prior) estimate.*

	Prior	Posterior				Uncertainty reduction			
		NP	Base	S1	S2	NP	Base	S1	S2
Concentration box 1	10	10	10.2	10.2	10.2	90%	89%	90%	81 %
Emission box 4	0.3	0.27	0.26	0.21	0.21	69%	68%	47%	47%
$\mathcal{J}_{apri}$	-	40.3	54.8	54.8	13.7				
$\mathcal{J}_{apos} = \mathcal{J}_b + \mathcal{J}_{obs}$	-	2.0+0.2	2.2+13.4	4.9+15.2	1.3+3.8				

2.3.2 Underdetermined problem

In a typical 4D-Var atmospheric inversion, the number of state vector elements is much larger than the 20 elements in the above example. In our inversions (reported in Chapters 3 to 5), the length of the state vector ranges from 37000 to almost 200000. Moreover, the number of available observations is often significantly smaller than the number of unknowns leading to an underdetermined minimization problem. Here we discuss the complications that arise when we have to deal with such a problem in the framework of the example model defined in the previous section.

In this example, the number of measurement stations is reduced from 10 to 3 and the number of observational time instances is reduced from 10 to 5, leading to 15 observations to estimate 20 unknown variables. The measurements are taken in grid boxes 4, 5 and 8. Since we sample in the grid box of the 'true' emission and in the grid box down wind of this box, this situation is favorable to constrain the emission (in contrast to the NOAA-CO sampling network that samples on background locations).

The base inversion shows directly that a decrease in the number of observations (compared to the previous section) has a large effect on the systems' capability to solve for all individual state vector elements. The emission in box 4 is estimated at 0.18 (compared to a 'true' emission of 0.3). The cost function is reduced from a prior value of 11.1 to a posterior value of 3.5 (see Table 2.2).

Apart from the sensitivity inversions (S1 and S2) we performed in the previous section, here we also investigate the influence on the measurement station locations. Therefore, in sensitivity study S3, observations are performed in boxes 3, 7 and 9 (on background stations). Finally, the effect of a very wrong prior is investigated in sensitivity study S4, where the 'true' initial concentration of 10 in box 1 is spread out equally over all grid boxes and similar for the emission of 0.3 in box 4.

Table 2.2: *Results from the inversions using the toy model in underdetermined mode. The concentration in box 1 and the emission in box 4 are given for the prior and the posterior (base and sensitivity studies S1-S4). Default stations are positioned in boxes 4, 5 and 8. Default prior state is given in the text. Spread indicates that the true initial concentration and emission are spread out evenly over all grid boxes.*

	Base	S1	S2	S3	S4
Stations	default	default	default	3, 7 and 9	default
Prior	default	default	default	default	spread
Concentration box 1	10.1	10.1	10.0	10.2	1.0
Emission box 4	0.18	0.08	0.08	0	0.07
$\mathcal{J}_{apri}$	11.1	11.1	2.8	2.4	25.6
$\mathcal{J}_{apos} = \mathcal{J}_b + \mathcal{J}_{obs}$	1.2+2.3	1.1+3.8	0.4+1.0	0.2+1.8	1.7+1.8

With stricter errors on the prior estimate (S1) the solution deteriorates: an emission of 0.08 is found in box 4. In addition, the system puts an emission of 0.01 in box 3 and a negative emission (-0.05) in box 5. Increasing the observation error (S2) results in a similar solution. The value of the cost function in these two inversions is quite different as discussed before.

Although the number of observations is smaller than the number of unknowns, the system is capable to retrieve an emission in box 4 given that the observations are located in boxes 4, 5 and 8. However, if the observation locations are changed to boxes 3, 7 and 9, no emission is retrieved in box 4 and the initial concentration is increased to 10.2. Two important aspects of typical atmospheric inversions follow from this example:

1. The capability of the system to retrieve correct emissions depends strongly on the density of the measurements in both space and time. Measurements that are not sensitive to emissions will not constrain the emissions. This issue will be discussed further in Chapters 3 and 4.
2. The fit with the measurements may be good for the wrong reasons. In this example, the system is capable to fit the measurements without retrieving a positive emission, because the available measurements are not sensitive to the 'true' emission. Another possibility is that the system fits the measurements by increasing the initial concentration only, without inferring a positive emission. This effect is also observed for real atmospheric inversions. For example, if multiple emission categories are optimized it is possible that increases in one emission category are compensated by decreasing emission from another category. This issue will be discussed in paragraph 2.5.2 below and in Chapters 3 and 4.

Finally, the effect of a uniform prior estimate is very large in this example. With few measurements, the system cannot retrieve the initial concentration in box 1 anymore and finds an emission in box 4 of 0.07, which is much smaller than the true emission. The inversion also increases the emission in box 3 to 0.05 and finds a negative emission of -0.06 in box 5. This indicates that a state-of-the-art prior emission estimate is a necessary ingredient for a successful inversion. This will be discussed further in Chapter 5.

To finish this example we examine the prior and posterior modeled time series for the base inversion. Figure 2.2 shows for each grid box the time series generated using the 'true' settings (i.e., initial concentration of 10 in box 1 and an emission of 0.3 in box 4) as a solid black line, the time series corresponding to the prior emissions (solid gray line) and the time series corresponding to the posterior emission estimates (dashed black line). The observations in box 4, 5 and 8 are also shown with their 1-σ errors. The 'true' concentration in grid boxes 1 to 3 is well reproduced by the system due to the correctly inferred initial concentration of 10 in box 1 that is transported to the right over time. For box 4 and 5, where we have measurements, the posterior simulation is closer to the truth compared to the prior simulation, indicating that the information content of the observations has been used to update the prior emissions. The concentration in grid boxes 6, 7 are only slightly constrained by the observations down wind in box 8, but the posterior simulation is much closer to the truth compared to the prior. Negative posterior emissions in grid boxes 7 and 8 (not shown) result in negative concentrations in boxes 9 and 10 which are not constrained by the observations in this example. The posterior simulation drifts away from the truth over time, which underscores the need for observations in these grid boxes to keep the solution physically realistic.

2.4 Historical overview

Since the first inversion study for CO using a 3-D atmospheric chemistry transport model (Bergamaschi et al., 2000), approximately twenty inversion studies have been published in the last decade. Improvements in the modeling framework, mainly due to higher computer power, include:

- The spatial model resolution has improved from a global resolution of 10°x10° in TM2 (Bergamaschi et al., 2000) to a much finer resolution of 3.75°x2.75° (Chevallier et al., 2009) for the LMDZ-INCA model and a 2°x2.5° for the GEOS-Chem model (Jiang et al., 2011). The model used in this thesis, TM5 (Krol et al., 2005), is even capable to zoom in to a 1°x1° resolution regionally, which is employed in the inversions as described in Chapter 5.
- The temporal resolution of the models (from 1 day to only a couple of minutes).

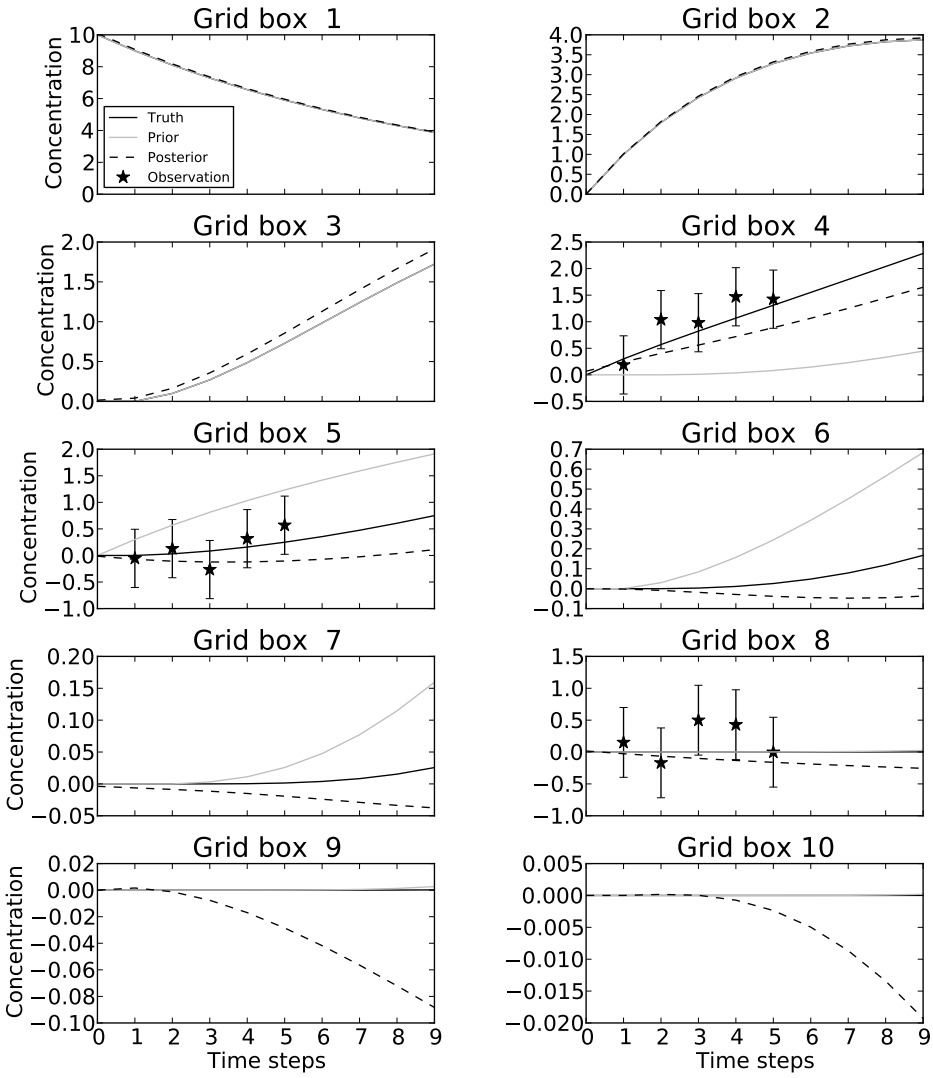

Figure 2.2: *Time series of the prior (solid gray line), posterior (dashed black line) and truth (solid black line) simulation for the base inversion discussed in Sect. 2.3.2 for the first 9 time steps. Observations in grid boxes 4, 5 and 8 during the first 5 time steps are also shown with 1-σ errors.*

- The spatio-temporal resolution of the emissions to be optimized. Note that this resolution is typically larger than the spatio-temporal resolution of the observations. In the past, time-independent emissions were optimized on monthly time scales e.g., Arellano et al. (2004). The next step was time-dependent optimization (still on a monthly resolution, e.g., (Arellano et al.,

2006)), and currently, emissions can be optimized per week (Pison et al., 2009; Fortems-Cheiney et al., 2011). A current study with TM5 is underway using a daily resolution.

- The observations used as constraints in the inverse modeling framework were initially only surface network measurements (Bergamaschi et al., 2000; Kasibhatla et al., 2002; Pétron et al., 2002), that were averaged over monthly time scales. Currently in TM5, flask observations are assimilated in 3 hour windows and continuous measurements are averaged to obtain one measurement per day. This is somewhat different for satellite observations. The first CO inversion exploring satellite measurements was performed by Arellano et al. (2004), using MOPITT columns. These columns were binned to the model resolution (4°x5°) and averaged over the month. Currently in TM5, MOPITT columns, binned on a 1°x1° grid are assimilated on a daily basis to infer as much information as possible from these measurements.

An overview of these studies is given in Tables 2.3 and 2.4. Since several studies use different emission categories (for example, separating fossil fuel combustion from biofuel combustion), we have chosen to aggregate the emissions to four main categories: anthropogenic (consisting of fossil fuel and biofuel combustion), biomass burning (forest and savanna fires in the Tropics and the Boreal forests), natural (direct emissions from plants, the ocean and the secondary production of CO by oxidation of NMVOCs) and CO produced by oxidation of methane (see Table 2.3). In Table 2.4 the total emission estimates (aggregating all categories together) for continental regions are given.

The large range of estimates given in these two tables represents the still large uncertainties in current CO emission estimates. Note that the emission estimates are for different years in which the true emissions may have been different. The remaining differences between the studies are likely caused by different assumptions. For example, the chosen OH field (either from a climatology (Spivakovsky et al., 2000) or calculated on-line in the model simulation) has a large effect on derived emissions (see Chapter 3). In addition, the use of different meteorological fields for a fixed year yields different results as shown by Liu et al. (2010). Other differences include the choice of aggregation region, the treatment of the observations in the assimilation systems, and the transport models themselves (Shindell et al., 2006).

2.5 4D-Var: Assumptions and challenges

Some assumptions and challenges in the 4D-Var approach were already illustrated using the toy model in Section 2.3. Here we summarize additional problems one encounters when dealing with atmospheric inversions.

2.5.1 Outliers in the observations

As outlined before, the 4D-Var system adjusts the emissions iteratively to fit the observations. Hence, outliers, i.e. observations due to local pollution events, measurement failure or observations that can not be reproduced due to the coarse model resolution, may influence the inversion results. Therefore, we apply an outlier filter in this work by performing the inversions assimilating surface network observations in two cycles. In cycle 1, all observations are assimilated leading to posterior emissions. The posterior simulation is compared to the observations and all observations outside a 3σ range of the modeled CO mixing ratio are flagged an not used in the second inversion cycle (Bergamaschi et al., 2010). This filter is considered to be not necessary in case we assimilate satellite observations, because (1) the huge number of satellite observations prevents single outliers to influence the solution (as compared to a NOAA-based inversion) and (2) the assigned observation errors (σ) associated

with these observations are typically large and the simulated model mixing ratios all fall within 3σ of the observations. For a NOAA-based inversion the effect of outliers on the inferred emissions can be significant, up to 20% for continental scale emissions (see Chapter 3).

2.5.2 Separation of sources

In the iterative 4D-Var process, the prior simulation is compared to the observations, leading to a model-data mismatch. Since atmospheric observations only constrain the total CO burden, separation of the different emission categories depends completely on the information supplied in the prior (that is, both the magnitude of the emissions and their associated errors and error correlations). For example, suppose that given a prior model underestimate, emissions have to increase in a certain region, then there are two possibilities:

1. If there is only one emission category present in that region, it is obvious that the emissions in this category are increased.
2. If there are multiple emission categories prescribed in the prior for this region, the dominant emission category (associated with the largest error) is increased to keep the background of the cost function small. However, if emissions of several categories are of the same order of magnitude, there may be multiple possible increments all with the same background cost. In that case, the system has difficulties separating the source categories.

By inspection of the posterior error covariance matrix (**A** in Eq. (2.7)), it is possible to quantify if emission categories can be separated by the system. On the one hand, posterior correlations for two emission categories close to zero, indicate that the sources can be separated. On the other hand, correlations significantly larger than 0 indicate that compensation effects occur: an emission going up to compensate for another emission going down. Consider for example a prior model underestimate for station South Pole. To match the observations, CO emissions from biomass burning might increase, possibly leading to a mismatch on some other stations. It may turn out that it is cheapest to compensate the enhanced biomass burning emission by a reduction in for example NMVOC-CO emissions on the SH. This kind of behavior typically leads to negative correlations between emission categories and will be discussed in more detail in Chapter 3.

2.5.3 State vector representation

In this work, the emissions are optimized on a monthly resolution for 3 emission categories (except in Chapter 5 where we optimize total CO emissions only) on the model resolution. With a model grid spacing of 6° in the longitudinal direction and 4° in the latitudinal direction (the coarse grid of TM5), the total number of surface grid boxes is 2700. Suppose we perform an inversion for 15 months (including 1 month spin-up and 2 months spin-down, see Sect. 2.5.4), the length of the state vector becomes 3 x 15 x 2700 = 121500. Note that when we optimize extra parameters (e.g., to optimize the initial concentration field as in Chapter 3 or to fit a bias as in Chapter 5), extra elements are added to the state vector. Here, the order of the elements is according to category, month, and horizontally grid. The prior error covariance matrix (**B** in Eq. 2.3) describes the variances of the grid-scale emissions and the covariances between these emissions. Spatially, correlations are assumed Gaussian and two grid boxes at a distant d apart have a correlation of $\exp\left(-\left(\frac{d}{L}\right)^2\right)$, where L is the spatial correlation length (1000 km, except in Chapter 5 where it is only 100 km). Emissions are also correlated in time and the correlation for two emissions t months apart is given by $\exp\left(-\frac{t}{T}\right)$, with T the temporal correlation length (generally 3 months for the seasonally varying biomass burning

category and 9.5 months for the other categories, which are known to vary only slightly from month to month). No correlations between emission categories are assumed.

Note that for a large state vector of dimension n it is not feasible to store the matrix $\mathbf{B}$ of dimension $n \times n$ in memory. Therefore, the matrix is decomposed as $\mathbf{B} = \mathbf{GCG}$, where $\mathbf{G}$ is a diagonal matrix consisting of the standard deviation of the prior emissions and $\mathbf{C}$ is a correlation matrix (with unit diagonal) storing the spatial and temporal correlations. The matrix $\mathbf{C}$ is further decomposed in a spatial $\mathbf{C}_h$ and a temporal part $\mathbf{C}_t$ such that $\mathbf{C} = \mathbf{C}_t \otimes \mathbf{C}_h$ as outlined in Meirink et al. (2008b).

2.5.4 Spin-up and spin-down

In general, a model simulation starts from a certain 3-D CO distribution, known as the initial concentration field. However, since the true emissions are not known before hand, deficiencies in the initial field may be projected on the emissions in the first months of the inversion. This problem is resolved by using a spin-up time of several times the lifetime of CO (i.e., 6 to 10 months, given a CO lifetime of 2 months). The emissions are optimized during the spin-up period, but not interpreted. This way, the observations in the target period do no longer 'see' the initial concentration field. One drawback of this method is the CPU time needed to simulate the additional months. In this work, given the CO lifetime of 2 months, we have chosen to use a spin-up time of one month, but only optimize the initial concentration field in Chapter 3. This is in contrast with methane inversion studies (e.g., Bergamaschi et al. (2010)) in which the initial concentration field is always optimized. However, our choice is justified due to the relative short lifetime of CO copmared to the methane lifetime of approximately ten years. In later chapters, we found that by using a sufficiently accurate initial concentration field, there is no need to further optimize it: sensitivity studies in which we did/did not optimize this field showed only small differences in the derived emission estimates.

To constrain the emissions of the last month of the target period, a spin-down period of two months is used. Indeed, it has been shown that due to the short CO lifetime, observations more than two months in the future do not longer constrain the emissions significantly (Pétron et al., 2002).

2.5.5 Multiple datasets

To optimally constrain CO emissions, it is important to have accurate observations. However, the spatial and temporal resolution of these observations is also important. Therefore, in an ideal case, one would assimilate both high precision flask observations from the NOAA surface network (possibly combined with high temporal resolution continuous surface measurements e.g., from AGAGE (Advanced Global Atmospheric Gases Experiment)) in combination with high spatial and temporal resolution satellite measurements which are also sensitive to CO at higher altitudes. However, due to the large difference in data density between surface and satellite measurements, it appears to be difficult to give correct weights to each dataset.

We illustrate this with an example, shown in Fig 2.3 and 2.4. Figure 2.3 shows the prior simulation for the year 2010 sampled at station Ascension Island (for the west coast of Africa in the Atlantic Ocean) and the observations from the NOAA surface network at this site. The mismatch between the simulation and the observations leads to a contribution to the cost function. In this case, the observations at Ascension Island lead to a cost of 480 for the period April to December. For comparison, we calculate the contribution of MOPITT observations to the cost function by binning all observations within 10° of Ascension Island. The prior and observed column-averaged mixing ratios for this region (averaged over the same period) is shown in the top panel of Fig. 2.4. If we assume an uncertainty of 10% in the MOPITT observations (MOPITT was developed to measure CO columns

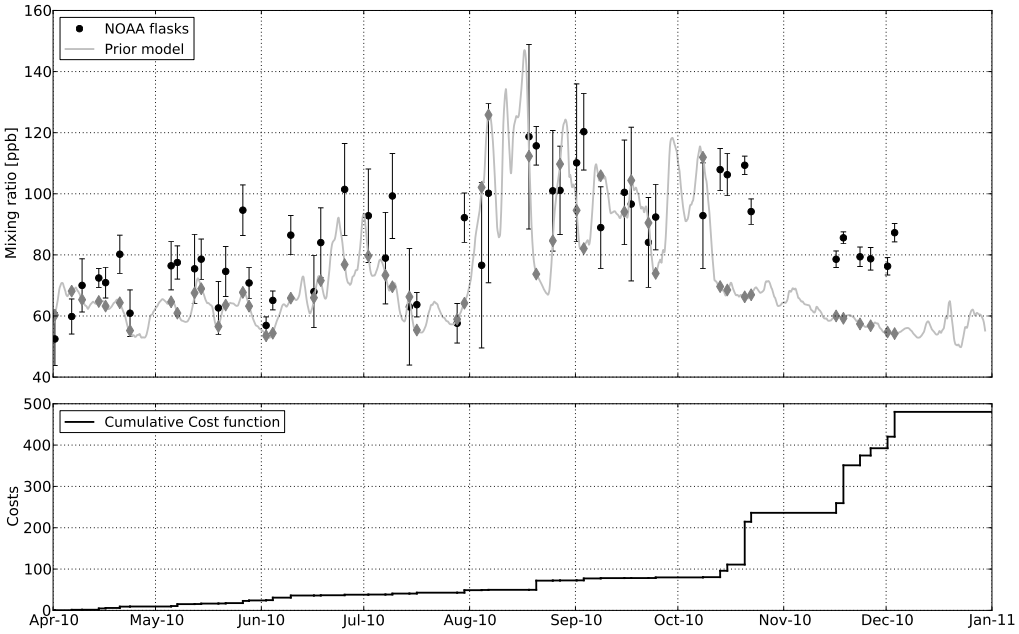

Figure 2.3: *Top: Prior simulation (grey) and flask observations (black) from the NOAA surface network for station Ascension Island. The observation error (black bars) include a constant measurement error of 3 ppb and a varying model error component. Bottom: Cumulative cost function per observation. The mismatch between the prior simulation and the NOAA flask observations leads to a contribution of 480 to the observational part of the cost function.*

with 10% accuracy (Pan et al., 1995)), the model underestimate leads to a contribution to the cost function of 19824. One could imagine that in an actual inversion, the MOPITT mismatch completely drives the emission changes, since obviously the most cost reduction can be found in reducing this mismatch. In order to give the NOAA observations more weight in the cost function, the uncertainty in the MOPITT observations has been artificially increased by a factor $\sqrt{50}$ (see Chapter 4 for more details). With the enhanced errors, the same MOPITT observations now lead to a cost function contribution of 573 (Fig. 2.4, bottom-right panel), which is much closer to the contribution of the NOAA site Ascension Island.

Hence, we stress that it is very important to have a balanced cost function. This balance is twofold, since (1) the background and observational part of the cost function should be balanced to prevent either overfitting of the observations (see Chapters 4 and 5) or a posterior emission estimate that is not very different from the prior and (2) when multiple datasets are assimilated, the observational costs corresponding to each dataset should be balanced (Chapter 5). As can be read throughout this thesis, the results of the inversion can be very sensitive to the error settings and tuning these settings is an important aspect of inverse modeling.

An additional difficulty lies in the consistency between datasets. One could imagine that if the prior simulation underestimates one observational dataset but overestimates a different set of observations, the 4D-Var system will seek for a compromise in which both datasets are fitted as good as possible

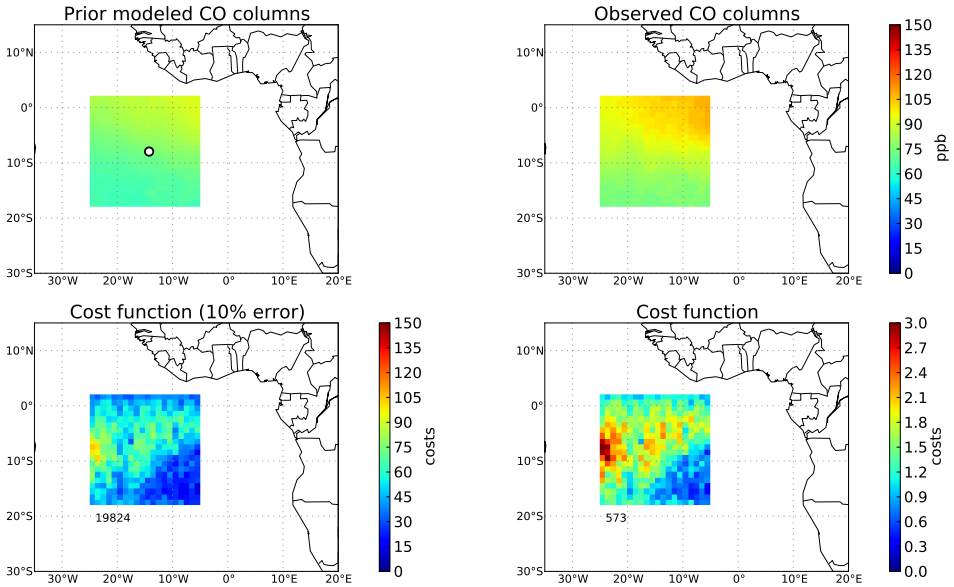

Figure 2.4: *Top: Column-averaged CO mixing ratio for the prior simulation (averaged over the period April to December 2010) for a rectangular region over the NOAA site Ascension Island (left). The location of the Ascension Island site is also indicated. The corresponding observed column-averaged CO mixing ratios from MOPITT are shown in the right panel. Bottom: Cumulative cost function on the grid for the period April to December 2010. In the left panel we have used an uncertainty of 10% of the observed columns (the MOPITT measurement requirement (Pan et al., 1995)), leading to a total cost function value for this region of 19824. In the right panel, the error on the MOPITT observations has been inflated by a factor* $\sqrt{50}$*, resulting in a contribution to the cost function of 573.*

given their uncertainties. For CO, a clear inconsistency has been found previously on the SH. Inversion studies assimilating satellite observations (mainly from the MOPITT instrument) infer emissions that, once simulated and translated to atmospheric mixing ratios, do not agree with surface network observations on the high latitudes of the SH (Arellano et al., 2006; Kopacz et al., 2010; Fortems-Cheiney et al., 2011). It seems that the satellite observations are biased high on the SH and hence, a scheme to correct for this bias should be developed such that surface and satellite observations can be jointly assimilated (see Chapter 5). For methane inversions, Meirink et al. (2008a) and Bergamaschi et al. (2009) used a latitudinal, polynomial bias correction based on 4 parameters that are optimized in the 4D-Var system. This resulted in emission estimates that are in agreement with both NOAA surface observations of methane and the bias-corrected total columns of methane as derived from SCIAMACHY retrievals. It should be stressed that bias-correction is a widely-applied mechanism in weather forecasts, which heavily rely on (biased) satellite data (e.g., Auligné et al. (2007)).

2.5.6 Coding the adjoint, an example

As mentioned before, a large advantage of using an adjoint model, is that it is not necessary to calculate the Jacobian matrix $\mathbf{H}$ of the atmospheric chemistry transport model with a series of (expensive) model simulations. Instead, the sensitivity of the emissions to a certain model-data mismatch is calculated by one adjoint simulation. However, implementation of the adjoint model is often complex. In this project, the adjoint of the transport model TM5 was already developed (Krol et al., 2008; Meirink et al., 2008b). However, the assimilation of MOPITT observations in the forward and adjoint model had to be implemented. As an example, we write out the steps for the adjoint of MOPITT assimilation.

The TM5 model is co-sampled with a MOPITT observation, leading to a modeled CO mixing ratio profile (in this case on 25 levels, x_0). To compare the model with the column observation we have to construct a function $F : \mathbb{R}^{25} \rightarrow \mathbb{R}$. According to Deeter et al. (2010), the following steps are needed to obtain a 'pseudo column' (z_3) based on the TM5 model column. In this example, we assume that the MOPITT observation is given on 10 vertical layers and the MOPITT retrieved surface pressure is sufficiently close to the TM5 modeled surface pressure.

1. Redistribute (using mass-conserving interpolation) the CO mixing ratio profile given on 25 layers to the 10 MOPITT layers, $F_1 : \mathbb{R}^{25} \rightarrow \mathbb{R}^{10}$
2. Apply the MOPITT prior profile $\in \mathbb{R}^{10}$ and the MOPITT averaging kernel[1] $\in \mathbb{R}^{10\text{x}10}$, $F_2 : \mathbb{R}^{10} \rightarrow \mathbb{R}^{10}$
3. Calculate a column-averaged CO mixing ratio from the profile, $F_3 : \mathbb{R}^{10} \rightarrow \mathbb{R}$

The pseudo model column is given by $z_3 = F(x_0)$, with $F = F_3 \circ F_2 \circ F_1$. Given a MOPITT observation y_{mop} and associated uncertainty σ_{mop}, the contribution of this observation to the cost function is

$$\mathcal{J}(x_0) = \frac{1}{2}\left(\frac{F(x_0) - y_{\text{mop}}}{\sigma_{\text{mop}}}\right)^2 = \frac{1}{2}\left(\frac{z_3 - y_{\text{mop}}}{\sigma_{\text{mop}}}\right)^2. \tag{2.9}$$

The gradient of the cost function is given by

$$\nabla\mathcal{J}(x_0) = \frac{\partial F(x_0)}{\partial x_0}\frac{(z_3 - y_{\text{mop}})}{\sigma^2_{\text{mop}}}. \tag{2.10}$$

In this case, the function F is linear and hence, the gradient can be written as

$$\nabla\mathcal{J}(x_0) = \mathbf{F}^\top \text{adz}_3 = \mathbf{F}_1^\top \mathbf{F}_2^\top \mathbf{F}_3^\top \text{adz}_3, \tag{2.11}$$

where adz_3 represents the departure (Giering and Kaminski, 1998) corresponding to the model-data mismatch. In general, the function F might be nonlinear, but the tangent linear matrices (Bouttier and Courtier, 1999) can be used in the last equation to compute the gradient of the cost function.

The correctness of the implementation can be checked by verifying that the following equality holds up to machine precision (Krol et al., 2008; Meirink et al., 2008b):

$$x^\top \text{adx} = \text{y} \cdot \text{ady}, \tag{2.12}$$

where x is a random vector $\in \mathbb{R}^{25}$, $y = F(x)$, ady is a random number and $\text{adx} = \mathbf{F}^\top \text{ady}$.

[1] The variability in the MOPITT V4 CO mixing ratio is modeled using log-normal CO mixing ratios (Deeter et al., 2010). Application of the averaging kernel required the use of logarithms which results in a nonlinear model. For simplicity, we have linearized the averaging kernel to keep the equations linear. The linearization procedure is extensively described in Chapter 4.

Table 2.3: *Overview of global annual CO emission estimates (in Tg CO/yr) for a series of literature studies. CO emissions are subdivided in several categories. We summarize the numbers in the three emission categories defined in this thesis: anthropogenic, natural and biomass burning.*

Study	Bergamaschi et al. (2000)		Pétron et al. (2002)		Kasibhatla et al. (2002)		Jones et al. (2003)		Arellano et al. (2004)	
Source	Prior	Posterior	Prior	Posterior	Prior	Posterior	Prior	Posterior	Prior	Posterior
Anthropogenic	660	1021	677	958	600	920	585	640	610	850
Biogenic (direct/secondary)	500	332	820	-	400	470	-	-	460	195[b]
Biomass burning	850	700	437	460	430	540	530	470	670	890
Methane	830	830	735	1701[a]	808	949	1350	1150[a]	-	-
Total	**2840**	**2883**	**2669**	**3044**	**2238**	**2879**	**2465**	**2260**	**1740**	**1935**[c]

Study	Müller and Stavrakou (2005)		Arellano et al. (2006)		Stavrakou and Müller (2006)		Hooghiemstra et al. (2011)[d]	
Source	Prior	Posterior	Prior	Posterior	Prior	Posterior	Prior	Posterior
Anthropogenic	571	730	604	785	571	664	531	871
Biogenic (direct/secondary)	967	849	492	394	914	1032	927	521
Biomass burning	409	356	501	563	467	450	404	409
Methane	876	825	-	-	796	761	885	883
Total	**2823**	**2760**	**1597**	**1742**[c]	**2748**	**2907**	**2747**	**2684**

[a] Estimate of CO emissions from vegetation + NMVOCs + methane.
[b] Estimated as the mean of the reported range 150-240 Tg CO.
[c] CO from methane production has been presubtracted.
[d] These results are derived in Chapter 3.

Table 2.4: *Overview of total CO emissions reported in the literature. CO emissions (in Tg CO/yr) are specified per continent. The global source of CO from oxidation of NMVOCs and methane (also in Tg CO/yr) is given if available.*

Study	Pétron et al. (2002)		Jones et al. (2009)[b]		Pison et al. (2009)		Kopacz et al. (2010)		Fortems-Cheiney et al. (2011)	
Region	Prior	Posterior	Prior	Posterior	Prior	Posterior	Prior	Posterior	Prior	Posterior
North America	193	197	135	146	137	188	57	71	137	199
Europe	163	160	110	111	103	128	78	95	108	137
Asia	395	686	367	531	296	539	389	660	307	506
South America	202	171	113	141	146	131	119	183	151	184
Africa	296	335	234	303	264	317	214	343	246	283
Oceania	31	31	69	185	96	88	23	40	96	117
NMVOC	638	-	-	-	-	-	853	-	-	-
CH_4	735	1701[a]	1215[a]	1344[a]	1212[a]	1179[a]	426	1290[a]	1257[a]	1176[a]
Total	**2648**	**3044**	**2243**	**2761**	**2271**	**2592**	**2159**	**2682**	**2320**	**2617**

[a] Estimate of CO emissions from vegetation + NMVOCs + methane.
[b] We report the estimates from the MOPITT inversion.

CHAPTER 3

Optimizing global CO emission estimates using a four-dimensional variational data assimilation system and surface network observations

We apply a four-dimensional variational (4D-Var) data assimilation system to optimize carbon monoxide (CO) emissions for 2003 and 2004 and to reduce the uncertainty of emission estimates from individual sources using the chemistry transport model TM5. The system is designed to assimilate large (satellite) datasets, but in the current study only a limited amount of surface network observations from the National Oceanic and Atmospheric Administration Earth System Research Laboratory (NOAA/ESRL) Global Monitoring Division (GMD) is used to test the 4D-Var system. By design, the system is capable to adjust the emissions in such a way that the posterior simulation reproduces background CO mixing ratios and large-scale pollution events at background stations. Uncertainty reduction up to 60 % in yearly emissions is observed over well-constrained regions and the inferred emissions compare well with recent studies for 2004. However, with the limited amount of data from the surface network, the system becomes data sparse resulting in a large solution space. Sensitivity studies have shown that model uncertainties (e.g., vertical distribution of biomass burning emissions and the OH field) and the prior inventories used, influence the inferred emission estimates. Also, since the observations only constrain total CO emissions, the 4D-Var system has difficulties in separating anthropogenic and biogenic sources in particular. The inferred emissions are validated with NOAA aircraft data over North America and the agreement is significantly improved from the prior to posterior simulation. Validation with the Measurements Of Pollution In The Troposphere (MOPITT) instrument version 4 (V4) shows a slight improved agreement over the well-constrained Northern Hemisphere and in the tropics (except for the African continent). However, the model simulation with posterior emissions underestimates MOPITT CO total columns on the remote Southern Hemisphere (SH) by about 10 %. This is caused by a reduction in SH CO sources mainly due to surface stations on the high southern latitudes[1].

[1]This chapter has been published as P. B. Hooghiemstra et al. (2011) *Optimizing global CO emission estimates using a four-dimensional variational data assimilation system and surface network observations*, Atmospheric Chemistry and Physics, 11, 4705–4723, 2011.

3.1 Introduction

Understanding the budget of carbon monoxide (CO) is important, because by reaction with the radical OH, CO influences the oxidizing capacity of the atmosphere significantly (Logan et al., 1981). Enhanced CO concentrations reduce OH concentrations and this has a feedback on the concentration of methane, the second most important anthropogenic greenhouse gas. CO is also a precursor of tropospheric ozone under high NO_X($NO + NO_2$) conditions (Seinfeld and Pandis, 2006). CO is emitted into the atmosphere by incomplete combustion of fossil fuels, biofuels and during biomass burning events. In addition, CO is produced throughout the atmosphere by oxidation of methane and non-methane volatile organic compounds (NMVOCs). The main sink of CO is the reaction with the OH radical. Deposition of CO on the Earth's surface is a minor sink, accounting for 5–10 % of the total sink strength (Sanhueza et al., 1998; Pétron et al., 2002).

The magnitude of CO emissions from different source categories is not well quantified. In particular, emissions from biomass burning (most importantly forest and savanna fires) carry large uncertainties partly due to the variability of fires in both space and time. In addition, bottom-up inventories like the widely used Global Fire Emission Database (GFED) (van der Werf et al., 2004, 2006, 2010) come with substantial uncertainties due to insufficient knowledge about burned area, fuel load, and emission factors (van der Werf et al., 2006). Uncertainties in biomass burning emission estimates are largest in deforestation regions (e.g. South America and Indonesia) and regions where organic soils burn (e.g. Indonesia and the Boreal region).

One way to better constrain emissions of CO is inverse modeling (Enting, 2002). In short, atmospheric measurements, a chemistry transport model (CTM) and a priori information about the emissions are used to optimize the emission in such a way that the mismatch between simulated and observed CO concentrations is minimized. The a priori emission estimates are taken from bottom-up inventories. Throughout the literature there are basically two inversion methods used for CO inversions: synthesis Bayesian inversions (e.g., Bergamaschi et al., 2000; Kasibhatla et al., 2002; Pétron et al., 2002; Palmer et al., 2003, 2006; Arellano et al., 2004, 2006; Heald et al., 2004; Jones et al., 2009) and adjoint inversions (e.g., Müller and Stavrakou, 2005; Yumimoto and Uno, 2006; Stavrakou and Müller, 2006; Chevallier et al., 2009; Kopacz et al., 2009; Fortems-Cheiney et al., 2009; Tangborn et al., 2009; Kopacz et al., 2010). The synthesis inversion optimizes CO emissions over large geographical regions with a preset CO emission distribution in each region, whereas the adjoint inversion technique is able to derive optimized CO emissions on the grid-scale of the underlying CTM, through an iterative approach used to minimize the mismatch between model and observations. Adjoint inversions reduce the risk of aggregation errors and are in particular suited for assimilation of large observational (satellite) datasets (Meirink et al., 2008b; Bergamaschi et al., 2009).

In the current study we apply a 4D-Var system for CO based on the earlier work for methane (Meirink et al., 2008a,b; Bergamaschi et al., 2009). Although this system is designed to assimilate large observational datasets, it will be tested in this first study by only assimilating surface observations from a limited number of NOAA stations to optimize monthly mean CO emissions for a period of two years. This approach is followed to obtain a benchmark characterization of the system for future assimilation of satellite data. Firstly, we focus on the capability of the system to estimate annual continental emissions by inspecting the reduction of the prior errors assigned to the sources. The optimized emissions will be validated by comparing model results to independent aircraft data from NOAA and satellite data from the Measurements Of Pollution in The Troposphere (MOPITT) instrument (Deeter et al., 2003, 2007, 2010). Secondly, we will investigate the influence of prior settings and model errors on the inversion results by performing sensitivity studies.

This paper is organized as follows: the 4D-Var system is described in Sect. 3.2. Section 3.3 presents the optimized (posterior) emissions and their uncertainty reduction for 2003 and 2004 as well as a

validation with independent aircraft and satellite data. The results are discussed in Sect. 3.4 and the performance of the 4D-Var system is further investigated by performing sensitivity studies (Sect. 3.5). Finally we give conclusions in Sect. 3.6.

3.2 Description of the four dimensional variational data assimilation system

The 4D-Var modeling system for CO is based on the TM5-4D-Var system originally developed for methane (Meirink et al., 2008b; Bergamaschi et al., 2009). Given a set of atmospheric observations y and a chemistry transport model H it is possible to optimize a set of fluxes x (the state vector) using the Bayesian technique (Rodgers, 2000). The a posteriori vector x is found by minimizing the mismatch between the model forward simulation $H(x)$ and the observations (y) weighted by an observation error covariance matrix $\mathbf{R}$, while staying close to a set of a priori fluxes x_b, weighted by the a priori error covariance matrix $\mathbf{B}$. Mathematically this problem can be written as the following minimization problem:

$$\begin{aligned} \hat{x} &= \text{Arg}\min\ \mathcal{J} \\ \mathcal{J}(x) &= \frac{1}{2}\left(x - x_b\right)^\top \mathbf{B}^{-1}\left(x - x_b\right) + \frac{1}{2}\sum_{i=1}^{M}\left(H_i(x) - y_i\right)^\top \mathbf{R}_i^{-1}\left(H_i(x) - y_i\right), \end{aligned} \tag{3.1}$$

where the index i refers to the time step, M is the number of time steps with observations and T is the transpose operator. Observations y_i are assimilated in the 4D-Var system at time i. The classic Bayesian approach determines the a posteriori solution $\hat{x}$ (Rodgers, 2000):

$$\hat{x} = x_b + \mathbf{K}(\mathbf{H}x - y), \tag{3.2}$$

with $\mathbf{K} = \mathbf{B}\mathbf{H}^\top\left(\mathbf{H}\mathbf{B}\mathbf{H}^\top + \mathbf{R}\right)^{-1}$ and $\mathbf{H}$ is the Jacobian matrix corresponding to the CTM H (Arellano et al., 2004). The a posteriori error covariance matrix $\mathbf{A}$ can be written as

$$\mathbf{A} = \left(\mathbf{H}^\top\mathbf{R}^{-1}\mathbf{H} + \mathbf{B}^{-1}\right)^{-1}. \tag{3.3}$$

When the number of state vector variables is large, it is not possible to compute the inverse matrices in the above equations directly. Hence an iterative minimization algorithm is required. The conjugate gradient method (Hestenes and Stiefel, 1952) can be used to minimize the cost function (Eq. 3.1) if the CTM is linear. In general, the CTM H is nonlinear with respect to the state vector x since the CO emissions perturb OH concentrations and hence the CO sink term. However, for tropospheric CO, Pétron et al. (2002) have shown that to a reasonable approximation, the system can be linearized by using fixed OH fields. In this case the cost function $\mathcal{J}$ is quadratic and we use the same minimization algorithm as in the European Centre for Medium-Range Weather Forecasts (ECMWF) 4D-Var (Fisher and Courtier, 1995): the cost function $\mathcal{J}$ is minimized and the leading eigenvalues λ_i and eigenvectors ν_i of the Hessian of the cost function are derived. The a posteriori error covariance matrix (Eq. 3.3) describing the uncertainty in the optimized state vector $\hat{x}$, equals the inverse Hessian of the cost function. Hence, the a posteriori error covariance matrix is approximated by a finite combination of the leading eigenvalues and eigenvectors of the Hessian of the cost function added to the a priori error covariance matrix $\mathbf{B}$ (Fisher and Courtier, 1995):

$$\mathbf{A} \approx \mathbf{B} + \sum_{i=1}^{N}\left(\frac{1}{\lambda_i} - 1\right)(\mathbf{L}\nu_i)(\mathbf{L}\nu_i)^\top, \tag{3.4}$$

where $\mathbf{L}$ is the preconditioner explained below. The approximation converges to the true posterior error covariance matrix as the eigenvalues converge to 1 if the number of iterations is large enough. The rate of convergence of the minimization is in general quite slow, but a preconditioner can be used to speed up the convergence rate. Fisher and Courtier (1995) have shown that the matrix $\mathbf{L}$ such that $\mathbf{L}\mathbf{L}^\top = \mathbf{B}$ is a suitable preconditioner when used in this 4D-Var approach. However, due to the large number of state vector elements, the preconditioner is too large to be stored. The approach of Meirink et al. (2008b) is therefore adopted to reduce the required storage. In our study, we consider the minimum of the cost function reached when the norm of the gradient of the cost function is reduced by 99 %. Typically, less than 30 iterations are needed to achieve this reduction. Although the eigenvalues have not yet converged to 1 by this time, the errors on the scale of a continent seem reasonably converged after a limited number of iterations as shown in Fig. 3.3.

The chemical transport model H, the prior state x_b with uncertainty $\mathbf{B}$ and the observations y with their uncertainty $\mathbf{R}$ will be described in more detail in the following sections.

3.2.1 The chemical transport model TM5

The CTM (also called the forward model) used in this study to relate CO emissions to atmospheric CO mixing ratios is the two-way nested chemical transport model TM5 (Krol et al., 2005). TM5 is an offline model driven by 3-hourly meteorological fields (6-hourly for 3-D input fields) from the ECMWF. Here we do not use the full-chemistry TM5 model, but the so-called TM5 CO-only model (svn-version 3197). This model, running on a coarse $6° \times 4°$ horizontal grid with 25 vertical layers in this study, deviates from the full-chemistry version by employing simplified CO-OH chemistry. In order to keep the model linear, a monthly OH climatology is used (Spivakovsky et al., 2000), which is scaled by a factor 0.92 based on methyl chloroform simulations performed for 2000–2006 (Huijnen et al., 2010). The annual mean OH concentration for 2004 amounts to 1.1×10^6 molecules cm^{-3}. The corresponding tropospheric lifetime of methyl chloroform is 4.8 yr.

3.2.2 Specification of a priori state

The state vector (x in Eq. 3.1) consists of the variables to be optimized by the inversion. Here we distinguish between monthly surface CO emissions, monthly varying parameters that scale the chemical production of CO from oxidation of methane and NMVOCs, and the initial 3-D CO mixing ratio field. The emissions are divided in three categories: anthropogenic (combustion of fossil fuels and biofuels), natural sources (direct CO emissions from vegetation and the oceans) and biomass burning (open vegetation fires, both natural and human induced).

The a priori anthropogenic emissions are taken from the Emission Database for Global Atmospheric Research (EDGARv3.2) inventory (Olivier et al., 2000, 2003) compiled for the year 1995. The distribution of natural CO emissions (Houweling et al., 1998) is scaled to emit 115 Tg CO yr^{-1} which is well within the range of the estimate by Schade and Crutzen (1999a) (50–170 Tg CO yr^{-1}). Biomass burning emissions are taken from GFED2 (van der Werf et al., 2006). Biomass burning CO is distributed over the vertical model grid as follows: 20 % is released in the layers 0–100 m, 100–500 m and 500–1000 m. The remaining 40 % is released between 1000–2000 m in accordance to Labonne et al. (2007). The sensitivity of the optimized emissions with respect to the chosen injection height is discussed further in Sect. 3.5.

The chemical production of CO from oxidation of methane and NMVOCs requires monthly 3-D CO production fields. Constant methane mixing ratios of 1800 parts per billion (ppb) are used throughout

the atmosphere. Methane is oxidized by the OH climatology using a temperature dependent reaction rate constant (Seinfeld and Pandis, 2006)

$$k = 2.45 \times 10^{-12} \exp(-1775/T). \tag{3.5}$$

The CH_4 to CO conversion yield is taken as unity. We acknowledge the possibility of introducing a bias by neglecting the significant N-S gradient in tropospheric CH_4 and the vertical gradient in stratospheric CH_4. The observed 10 % N-S gradient in tropospheric methane would result in a 10 % gradient in CO produced from methane oxidation. Since in our approach, about 880 Tg CO is produced annually from CH_4 oxidation (Table 3.2), this leads to an overestimate of 45 Tg CO yr^{-1} on the SH and a similar underestimate on the NH. Although such a bias is small compared to the global CO emissions and chemical production, we will improve the CH_4 oxidation scheme in the next version of the 4D-Var system.

A full-chemistry model run using TM4 (Myriokefalitakis et al., 2008) yields monthly 3-D CO fields produced by oxidation of biogenic and anthropogenic hydrocarbons including CH_4-CO. The total prior CO source from methane and NMVOCs is scaled to 1600 Tg CO yr^{-1} within the range of values used in the literature (1279–1644 Tg CO yr^{-1}) (e.g., Bergamaschi et al., 2000; Müller and Stavrakou, 2005; Duncan et al., 2007; Kopacz et al., 2010). We construct the monthly NMVOC-CO (CO from NMVOCs) source by subtracting the monthly CH_4-CO described above from the total fields. The 3-D CH_4-CO and NMVOC-CO fields themselves will not be optimized: instead a monthly scaling factor with unit a priori value is optimized. Hence, for these sources we apply a traditional synthesis inversion in the sense that the prior spatial emission patterns are constant and only the global total magnitude of CH_4-CO and NMVOC-CO is optimized.

A forward model simulation with these a priori emissions has been performed for the years 2002–2005 and daily mean CO mixing ratios have been archived. The a priori initial CO mixing ratio field is taken from this archive and further optimized by including the initial 3-D field in the state vector. This approach has been adopted from previous methane 4D-Var studies (e.g., Meirink et al., 2008b). Also, when optimizing the initial CO mixing ratio field in this way, a long spin up time is not necessary saving up to 50 % of computertime. The approach outlined here yields similar emission estimates compared to an inversion starting from a posterior field from a previous simulation that is not further optimized.

3.2.3 Specification of a priori uncertainties

3.2.3.1 Emissions

The prior emission grid-scale errors are set in such a way that in combination with prior correlations (see below), the prior emission errors aggregated to continental regions are in a realistic range. The prior anthropogenic emission inventory used in this study (EDGARv3.2) is compiled for the year 1995. Inverting for the years 2003/2004, we expect large emission increments due to rapid economic development, particularly in Asia. Hence we assign large errors to this region. In contrast, for the Western developed world (North America, Europe and Australia) we expect that the 2003/2004 anthropogenic emissions are close or somewhat smaller compared to 1995. Therefore, we apply grid-scale errors of 250 % of the corresponding grid-scale emission for the developing world (Asia, Africa and South America) and 50 % for the Western developed world. With these settings, realistic continental-scale errors are computed for the developing world (65–75 %) and the Western developed world (20–48 %) in the range previously used by Stavrakou and Müller (2006).

The grid-scale prior emission errors for biomass burning and the natural source are set to 250 % of the corresponding grid-scale emission, since both inventories bear large uncertainties. For both source categories this leads to prior continental emission errors in the range of 40–100 % (Table 3.2).

Emission uncertainties are correlated in time and space resulting in a reduction of the effective number of variables to be optimized. For the three emission categories we use a Gaussian spatial correlation length of 1000 km as in Meirink et al. (2008b). An e-folding temporal correlation length of 9.5 months (0.9 month-to-month correlation) is chosen for anthropogenic emissions. This month-to-month correlation is justified because the prior inventory suggests no seasonal cycle. Due to the variable nature of fires in time, the temporal correlation length for biomass burning emissions is set to 0.62 months (0.2 month-to-month correlation). For natural emissions the temporal correlation length is set to 9.5 months.

3.2.3.2 Initial concentration field and additional parameters

The grid-scale prior initial concentration error is 5 % of the corresponding prior initial concentration. The initial concentration field is correlated in space by a Gaussian correlation length of 1000 km as in Meirink et al. (2008b). The a priori errors on the monthly scaling factors for CO production from methane and NMVOCs are set to 2 % and 8 %, respectively. The scaling factors are correlated in time with a correlation length of 3 months (0.7 month-to-month correlation). This tight error setting is chosen because the NMVOC-CO source is only 1 state vector element per month whereas the other emission categories have a state vector element for each grid box.

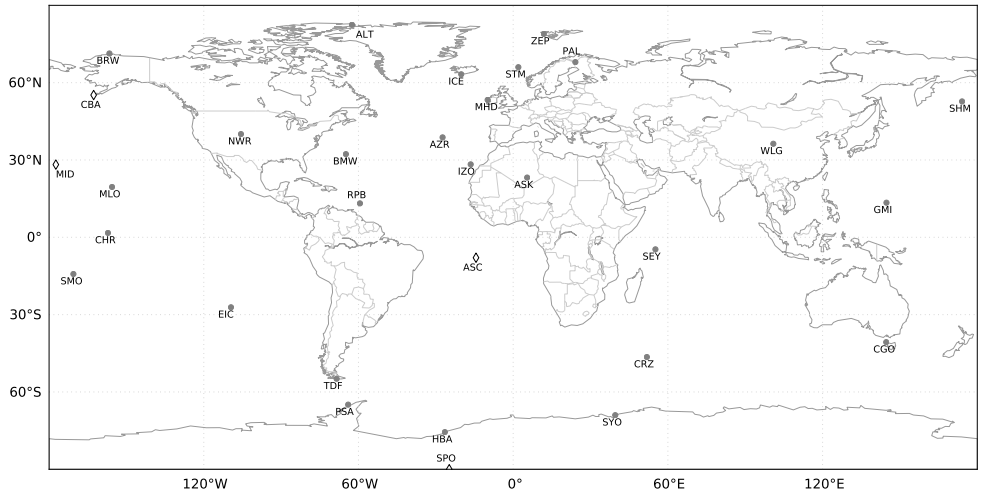

Figure 3.1: *Location of 31 NOAA surface sites. Stations for which prior and posterior simulations will be shown (Sect. 3.3.1) are represented by diamond markers.*

3.2.4 Atmospheric observations

In this first TM5 CO inversion study, only surface observations from NOAA/ESRL GMD are assimilated in the 4D-Var system. The NOAA surface network provides CO observations from a globally distributed network of stations (Novelli et al., 1998, 2003). A subset of 31 stations, mainly remote

stations and stations at larger distances from continental source regions are used in the inversions. Stations close to source regions as well as other stations for which we expect large model errors due to the coarse model resolution are left out. The selected stations are shown in Fig. 3.1. The observation error consists of the measurement error and the model error. The measurement error is set to 1.5 ppb (Novelli et al., 1998). We estimate the model error using the same approach as described in Bergamaschi et al. (2010). First, the impact of local emissions on the simulated CO mixing ratio is accounted for by a simple emission model for observations in the boundary layer. Second, to account for sub-grid variability that can not be resolved, the vertical component of the model error is calculated from the modeled CO mixing ratios in adjacent grid cells. Third, the temporal standard deviation of the modeled CO mixing ratios within a 3 h window is added to the representation error. With this advanced representation of the model error, we do not account for possible other model uncertainties in vertical transport or the OH field. This will be discussed further in Sects. 3.4 and 3.5.

The model error is usually much larger than the measurement error for stations close to or downwind of emission regions (e.g., Fig. 3.7). In remote areas in the SH, however, the measurement error is the dominant term in the observational error. No correlations between the observations are set resulting in a diagonal observational error covariance matrix $\mathbf{R}$.

3.2.5 Inversion specifics

Although we apply an advanced model error and thus increase the observation error, it is still not expected that the model is capable of simulating all measured pollution events and in particular the transition from polluted to very clean conditions. To account for this and to prevent possible biases due to a few single outliers, the inversion is done in two cycles: after the first inversion we reject all data points that are outside a 3σ error range of the model simulation (Bergamaschi et al., 2010) (see also Fig. 3.7). Then the second inversion cycle is performed. In the CH_4 inversion of Bergamaschi et al. (2010), typically 3 % of the data were rejected, but the a posteriori emissions for both inversion cycles did not differ very much in general. However, in the current study, focusing on the shorter-lived CO, approximately 15–20 % of the data from the first inversion are rejected. Inferred continental emissions in the second cycle are within 15 % of the emissions in the first cycle for most sources/regions and show a similar pattern of adjustments. The effect of rejecting data on inferred CO emissions will be discussed in more detail in Sect. 3.4.

The years 2003 and 2004 are inverted separately because the inversions are computationally demanding. The inversions use a one month spin up, in which the emissions are optimized already, but not analyzed, and 2 months spin down to supply enough observations to optimize the emissions in the last months of the year. Given a lifetime of about 2 months for CO, it has been investigated that to optimize emissions of month m, it is sufficient to use observations for months m, $m+1$ and $m+2$ (not shown). Observations at later times will not significantly influence the emissions in month m, because the emission signal is sufficiently diluted and chemically removed by that time. It should be borne in mind, however, that emissions in month m are influenced by emission estimates in surrounding months $(m-3, \ldots, m+3)$ via the prior temporal correlation length.

The length of the state vector is 189 030, that is (15 months $\times$ 3 source categories + 25 vertical layers of the initial concentration field) $\times$ (60 $\times$ 45 grid boxes) + 15 months $\times$ 2 scaling factors. In contrast, the total number of observations is only about 1400 per year. By introducing a non-diagonal prior error covariance matrix, the number of "true" unknowns is greatly reduced to approximately 25 000, but the problem still remains underdetermined (data sparse and hence strongly dependent on a priori knowledge of the emissions). Nevertheless, a grid-scale inversion is performed here to reduce the risk of aggregation errors, which often occur in a big region approach (Stavrakou and Müller, 2006; Meirink et al., 2008b) and to prepare for future ingestion of large amounts of satellite data.

3.3 Inversion results

3.3.1 Comparison of modeled and observed CO mixing ratios

In this section we will discuss the capability of the current 4D-Var system to adjust the state vector in such a way that background CO mixing ratios as well as observed large scale pollution events are adequately captured. Figure 3.2 shows the prior and posterior simulation of CO mixing ratios and surface observations for a subset of four stations used in the inversion (diamond markers in Fig. 3.1). All panels show that the model simulation with a priori settings (yellow) is capable to simulate the seasonal cycle and some pollution peaks even though the simulations are performed on a coarse $6° \times 4°$ grid. However, differences with the observations (red) up to 50 ppb are observed. In contrast, the posterior simulation (blue) fits the observations at all four stations rather well. This better fit is obviously caused by combined changes in the surface emissions and in the global source of CO from methane and NMVOCs. A quantitative analysis for all assimilated stations is shown in Table 3.1 for 2004. Here we present the bias per station for the prior and posterior simulation of the two inversion cycles. A value for the goodness of fit parameter χ^2/n is also given in this table. A χ^2/n value close to 1 indicates that the system is behaving well.

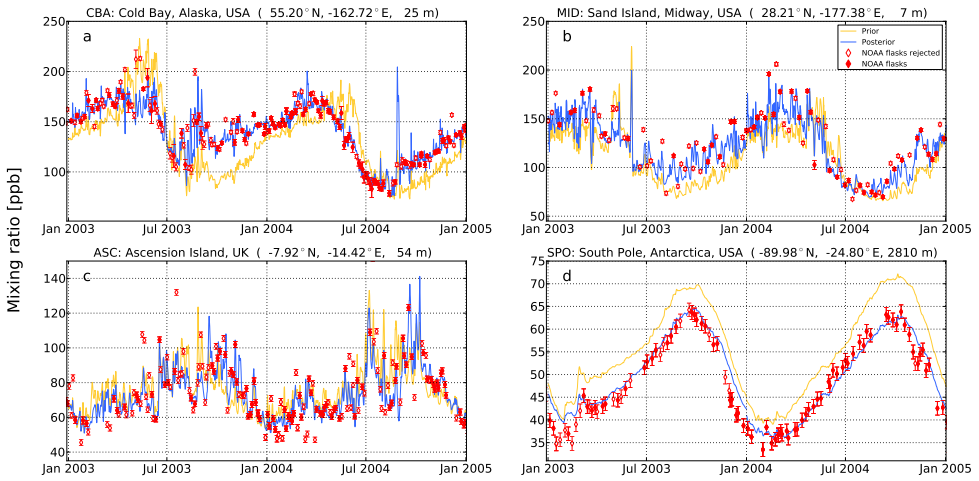

Figure 3.2: *Comparison of modeled and observed CO mixing ratios at* **(a)** *Cold Bay, Alaska,* **(b)** *Sand Island, Midway,* **(c)** *Ascension Island and* **(d)** *South Pole station from the NOAA surface network. Red dots correspond to NOAA observations, red open markers represent rejected data from inversion cycle 1 to cycle 2. Model simulations using prior (posterior) settings are shown in yellow (blue).*

For station Cold Bay, Alaska (Fig. 3.2a), representing the high latitude NH, the prior simulation underestimates observed CO mixing ratios up to 50 ppb, in the period September 2003 to February 2004 and from September 2004 to January 2005. For the year 2003, the inversion decreases biomass burning emissions from Russia in spring, but emissions are increased in summer. The posterior annual biomass burning emission estimate for Russia in 2003 is 97 ± 28 Tg CO (compared to the

prior estimate of 75 ± 77 Tg CO), well within the range reported by Kasischke et al. (2005) (55–139 Tg CO yr^{-1}). This shows that Russian fires account for 60 % of the total CO emissions from biomass burning in Asia in 2003 (158 Tg CO, Table 3.2). In contrast, in 2004 the inversion increases the Alaskan and Canadian biomass burning emissions in summer, from a prior emission estimate of 16 ± 19 Tg CO from June to August to 36 ± 9 Tg CO as posterior emission estimate. Similar values were also reported by Pfister et al. (2005) and Turquety et al. (2007), and these numbers are in closer correspondence to 30 Tg CO as estimated in the recently released updated GFED3 (van der Werf et al., 2010). Pfister et al. (2005) inferred CO emissions using satellite observations and reported a posterior emission estimate of 30 ± 5 Tg CO. Turquety et al. (2007) constructed a daily biomass burning emission inventory taking into account the emissions from peat burning. They estimated a total of 30 Tg CO from June to August 2004 for North America. Outside the biomass burning season, the inversion attributes increased CO levels to enhanced anthropogenic emissions in East Asia. From Table 3.1 it is observed that for station Cold Bay the prior bias decreases from -9.7 ppb in the first inversion cycle to -4.3 ppb in the second inversion cycle due to rejection of observations that are not reproduced by the model, likely due to an underestimated model error for this station (see Sect. 3.4.2). This rejection improves the a posteriori χ^2/n diagnostic for this station from 2.7 to 1.15. The posterior bias is reduced to nearly zero.

Table 3.1: *Statistics of the fit for the stations used in the inversion. Bias is defined as the mean difference between observed (y^o) and modeled (y^m) CO mixing ratio: $\frac{1}{n}\sum_{i=1}^{n}(y_i^o - y_i^m)$, where n is the number of observations per station and σ_i the observation error for observation y_i^o. The χ^2/n defines the goodness of fit defined as $\frac{1}{n}\sum_{i=1}^{n}\left(\frac{y_i^o - y_i^m}{\sigma_i}\right)^2$. A χ^2/n value close to 1 indicates that the system is behaving well.*

					Inversion cycle 1				Inversion cycle 2			
		lat	lon	alt	Bias [ppb]		χ^2/n		Bias [ppb]		χ^2/n	
ID	station name	[°]	[°]	[m.a.s.l.]	prior	posterior	prior	posterior	prior	posterior	prior	posterior
ALT	Alert, Nunavut, Canada	82.45	−62.52	210.0	0.94	−1.97	6.94	3.01	2.78	0.40	7.29	1.16
ASC	Ascension Island, UK	−7.92	−14.42	54.0	3.20	0.17	5.97	3.03	3.77	−0.34	4.89	1.22
ASK	Assekrem, Algeria	23.18	5.42	2728.0	−3.94	1.21	4.22	1.64	−5.26	−1.14	3.86	0.91
AZR	Terceira Island, Azores, Portugal	38.77	−27.38	40.0	−8.10	−0.86	7.84	4.69	−6.67	−1.01	6.62	1.22
BMW	Tudor Hill, Bermuda, UK	32.27	−64.88	30.0	1.66	−1.06	3.78	1.48	1.98	−2.03	3.11	0.99
BRW	Barrow, Alaska, USA	71.32	−156.60	11.0	−0.52	16.65	6.78	3.05	−1.09	−0.24	6.77	0.91
CBA	Cold Bay, Alaska, USA	55.20	−162.72	25.0	−9.65	0.06	9.04	2.70	−4.33	−0.01	6.96	1.15
CGO	Cape Grim, Tasmania, Australia	−40.68	144.68	94.0	9.18	1.97	1.24	0.37	9.18	2.20	1.24	0.34
CHR	Christmas Island, Republic of Kiribati	1.70	−157.17	3.0	8.79	0.54	4.02	1.58	9.45	0.34	3.86	1.13
CRZ	Crozet Island, France	−46.45	51.85	120.0	5.84	−0.28	3.87	1.14	5.52	−0.20	3.69	0.91
EIC	Easter Island, Chile	−27.15	−109.45	50.0	−9.03	−9.07	5.64	5.26	0.73	−3.07	0.46	1.92
GMI	Mariana Islands, Guam	13.43	144.78	6.0	−8.19	−4.07	4.30	3.23	−1.74	−0.49	2.80	1.32
HBA	Halley station, Antarctica, UK	−75.58	−26.50	33.0	6.93	0.04	4.33	0.65	6.93	0.09	4.33	0.57
ICE	Heimay, Vestmannaeyjar, Iceland	63.25	−20.15	100.0	−0.88	0.97	5.02	1.80	−1.71	−0.22	4.84	1.08
IZO	Izana, Canary Islands, Spain	28.30	−16.48	2360.0	−2.66	−1.45	4.74	2.17	−2.92	−2.66	3.84	1.28
MHD	Mace Head, Ireland	53.33	−9.90	25.0	3.98	2.98	1.60	0.87	4.64	4.02	1.55	0.73
MID	Sand Island, Midway, USA	28.21	−177.38	7.7	−14.07	−0.63	10.26	3.88	−13.81	−0.26	9.74	1.49
MLO	Mauna Loa, Hawaii, USA	19.53	−155.58	3397.0	−3.51	−1.87	3.53	2.47	−0.45	−0.78	2.18	1.28
NWR	Niwot Ridge, Colorado, USA	40.05	−105.58	3526.0	−4.05	2.13	3.13	2.50	−0.88	2.72	2.58	1.22
PAL	Pallas, Finland	67.97	24.12	560.0	−1.88	−3.22	4.08	1.63	−0.19	1.51	3.80	0.81
PSA	Palmer Station, Antarctica, USA	−64.92	−64.00	10.0	6.62	−0.20	3.74	0.63	6.52	0.04	3.74	0.61
RPB	Ragged Point, Barbados	13.17	−59.43	45.0	7.13	0.55	3.85	2.08	7.36	−0.12	3.50	1.13
SEY	Mahe Island, Seychelles	−4.67	55.17	7.0	3.84	0.85	3.41	1.75	5.60	0.75	3.08	0.99
SHM	Shemya Island, Alaska, USA	52.72	174.10	40.0	−7.16	−0.29	9.16	3.24	−2.21	0.77	7.96	1.05
SMO	Cape Matatula, Tutuila, American Samoa	−14.24	−170.57	42.0	4.67	0.28	2.48	1.23	5.06	−0.02	2.36	1.04
SPO	South Pole, Antarctica, USA	−89.98	−24.80	2810.0	6.82	0.50	4.50	1.08	6.60	0.35	4.36	1.01
STM	Ocean station M, Norway	66.00	2.00	5.0	0.36	−0.06	6.67	1.98	1.76	0.23	6.39	1.08
SYO	Syowa Station, Antarctica, Japan	−69.00	39.58	14.0	6.52	0.25	3.81	0.57	6.52	0.17	3.81	0.51
TDF	Tierra del Fuego, La Redonda Isla, Argentina	−54.87	−68.48	20.0	5.89	−0.75	3.73	0.66	5.89	−0.53	3.73	0.60
WLG	Mt. Waliguan, Peoples Republic of China	36.29	100.90	3810.0	−33.31	0.18	19.22	4.27	−21.26	−0.32	13.77	1.03
ZEP	Ny−Alesund, Svalbard, Spitsbergen	78.90	11.88	475.0	1.57	1.76	9.94	3.31	−3.10	0.29	7.69	1.11
ALL					−0.58	0.46	5.54	2.17	1.53	0.21	4.55	1.00

For station Sand Island, Midway (Fig. 3.2b), representing the NH midlatitudes, the prior simulation

underestimates observations during the entire period. This is attributed to an underestimation of anthropogenic emissions in the EDGAR inventory, which was compiled for the year 1995. Rapid economic development, particularly in China and India over the last decade led to increased anthropogenic emissions. The posterior simulation shows that increased anthropogenic emissions over China and India (the inversion roughly doubles Asian anthropogenic emissions, see Table 3.2) results in 15–25 ppb higher CO mixing ratios on stations downwind of South East Asia. Individual observations due to pollution plumes that were not reproduced in the prior simulation are captured better by the model in the posterior simulation. This is due to the fact that the 4D-Var system computes emission increments on the grid-scale of the underlying chemistry-transport model and hence, better exploits the spatial information present in the measurements. It is acknowledged, however, that a higher spatial model resolution is required to reduce the artificial smearing of concentration gradients.

The tropics are represented here by station Ascension Island (Fig. 3.2c), and although the improvement from prior to posterior simulation is not clearly visible, Table 3.1 shows that the posterior bias is nearly zero for both cycles, and the posterior χ^2/n diagnostic is reduced from 3.03 in cycle 1 to 1.22 in cycle 2. For the remote SH, represented here by South Pole station (Fig. 3.2d), the prior simulation overestimates the observations by 5–10 ppb all year long. The inversion attributes this to too high production of CO from NMVOCs since the station is far away from major sources, but neglecting the N-S gradient in tropospheric methane in the model, as discussed before, may also play a role. Again, the posterior bias is nearly zero in both inversion cycles and the χ^2/n diagnostic equals to 1.01 (1.08 in cycle 1).

Overall, Table 3.1 shows that the inversion reduces prior biases for most of the stations. Although for some stations the posterior bias is slightly larger in cycle 2 compared to cycle 1 (e.g., ASC, AZR, BMW (acronyms are defined in Table 3.1)), much larger reductions in the bias are observed for other stations (BRW, EIC, GMI). Furthermore, the χ^2/n diagnostic for all stations together is decreased to approximately 1 in cycle 2 (2.17 in cycle 1). However, for remote stations in the SH, χ^2/n is far smaller than 1 indicating that the measurement error of 1.5 ppb might be too conservative or indicating the need to take correlations in the observation errors into account. The observation error is further discussed in Sect. 3.4.2.

3.3.2 Posterior emission estimates

We present the posterior emission estimates and their uncertainties aggregated over continental scale regions as yearly totals, because the monthly emission estimates on grid-scale level are highly variable as a consequence of the loose prior error settings and the small amount of observations. Also, as shown by Meirink et al. (2008b), the posterior errors converge only rapidly for larger spatial and temporal scales (Fig. 3.3).

Table 3.2 and Fig. 3.3 (black, solid line) show that on a global scale, a substantial uncertainty reduction of 60 % for the anthropogenic emissions is achieved. In particular Asian anthropogenic emissions are well-constrained by the observations (258 ± 195 Tg CO a priori compared to 497 ± 107 Tg CO in 2003 and 526 ± 97 Tg CO in 2004 a posteriori, see also Fig. 3.3, dotted black line). In contrast, African and South American anthropogenic emissions show a negligible uncertainty reduction (Fig. 3.3, dash-dotted and dashed line respectively). This was expected though, since atmospheric observations mainly constrain the total emissions and the error reduction in those regions is largest for the dominant biomass burning source term. It is acknowledged here, that the presented posterior error reductions are much smaller compared to the study by Kasibhatla et al. (2002). However, the differences are mainly explained by the inversion approach used. Kasibhatla et al. (2002) used a synthesis inversion approach to optimize anthropogenic and biomass burning emissions for a set of big regions. In such a framework, the posterior emission estimates and their errors can

Table 3.2: *Emissions for 2003 and 2004 per continent for three surface source categories (Anthropogenic, Biomass burning and Natural) and two global chemical production terms (methane and NMVOCs). Per source category, the second and third columns specify the prior emission estimates used, the three right-most columns give the posterior emission estimates for the year 2003 (cycle 2) and 2004 (cycle 1 and cycle 2, respectively). The emissions are given in Tg CO yr^{-1}. Note that the sources of CO production from methane and NMVOC oxidation are given as global totals only, since only a global scaling factor is adjusted. Also, only the biomass burning emission inventory (GFED2) gives year-to-year emissions, the other sources are for the years specified in the footnotes.*

Source/Region	Prior		Posterior		
Anthropogenic[a]	2003/2004		2003	2004 cy 1	2004 cy 2
Nam	105 ± 30		85 ± 27	122 ± 27	105 ± 26
Sam	22 ± 16		-9 ± 16	5 ± 16	0 ± 16
Europe	62 ± 30		67 ± 16	94 ± 16	85 ± 18
Africa	80 ± 52		124 ± 48	159 ± 47	149 ± 45
Asia	258 ± 195		497 ± 107	608 ± 97	526 ± 97
Oceania	5 ± 1		5 ± 1	4 ± 1	4 ± 1
Globe	531 ± 183		770 ± 71	993 ± 68	871 ± 77
Biomass burning	2003	2004	2003	2004 cy 1	2004 cy 2
Nam	32 ± 32	23 ± 19	61 ± 30	47 ± 10	47 ± 10
Sam	60 ± 48	98 ± 105	75 ± 37	115 ± 38	136 ± 39
Europe	3 ± 2	2 ± 1	6 ± 2	4 ± 1	3 ± 1
Africa	162 ± 91	165 ± 94	85 ± 72	224 ± 55	165 ± 63
Asia	114 ± 103	98 ± 79	158 ± 54	59 ± 48	42 ± 52
Oceania	24 ± 28	18 ± 14	13 ± 11	34 ± 14	16 ± 14
Globe	397 ± 138	404 ± 157	400 ± 88	482 ± 68	409 ± 76
Natural[b]	2003/2004		2003	2004 cy 1	2004 cy 2
Nam	15 ± 8		12 ± 8	11 ± 8	14 ± 8
Sam	18 ± 13		8 ± 12	28 ± 12	19 ± 12
Europe	4 ± 4		6 ± 4	4 ± 4	5 ± 4
Africa	21 ± 12		29 ± 12	26 ± 12	25 ± 12
Asia	30 ± 12		30 ± 12	33 ± 16	29 ± 11
Oceania	8 ± 6		5 ± 6	6 ± 6	6 ± 6
Globe	115 ± 24		101 ± 24	123 ± 24	111 ± 24
CH4-CO[c]	2003/2004		2003	2004 cy 1	2004 cy 2
Globe	885 ± 10		883 ± 10	893 ± 10	887 ± 10
NMVOC-CO[d]	2003/2004		2003	2004 cy 1	2004 cy 2
Globe	812 ± 40		574 ± 38	301 ± 37	410 ± 38

[a] EDGARv3.2, compiled for the year 1995.
[b] Houweling et al. (1998).
[c] Constant 1800 ppb CH_4.
[d] From a full-chemistry run with TM4 for 2005 Myriokefalitakis et al. (2008). Most important biogenic VOC emissions in this model, isoprene (501 Tg C/yr) and monoterpenes (127 Tg C/yr), are taken from the POET database.

be computed by a direct matrix inversion and hence the posterior errors are exact. In the 4D-Var framework presented here, the cost function is minimized iteratively and considered converged when the norm of the gradient is reduced by a factor 100 (or 99 %). As a special case we continued the iterative proces up to a gradient norm reduction factor of 10^{10}. For this case the approximation of

the Hessian of the cost function converged to the true Hessian. The resulting posterior errors are indeed very close to the numbers in Kasibhatla et al. (2002) (not shown). However, a gradient norm reduction factor of 10^{10} is not very practical as the computational burden increases up to a factor 5.

For biomass burning emissions, uncertainty reduction is achieved in South America (98 ± 105 Tg CO a priori compared to 136 ± 39 Tg CO a posteriori in 2004, Fig. 3.3 grey dashed line), Asia (114 ± 103 Tg CO a priori compared to 158 ± 54 Tg CO in 2003) and North America (23 ± 19 Tg CO a priori and 47 ± 10 Tg CO a posteriori in 2004 only). Large changes in biomass burning emissions from 2003 to 2004 are observed for South America and Africa. For South America (with posterior emissions of 75 ± 37 Tg CO in 2003 and 136 ± 39 Tg CO in 2004) this increment was partly present in the GFED2 prior. Higher emissions in 2004 were also confirmed by observations from the SCIAMACHY (Scanning Imaging Absorption Spectrometer for Atmospheric Cartography) instrument (Gloudemans et al., 2009), showing the large interannual variability in South American biomass burning emissions. In contrast, the posterior biomass burning emission estimates for Africa in 2003 and 2004 seem to compensate for the difference in NMVOC-CO. This is confirmed by the relatively small error reduction and by the study of Chevallier et al. (2009), who optimized African emissions using MOPITT observations for 2000 to 2006 and did not show large inter annual variability from 2003 to 2004. Table 3.2 confirms that natural emissions are hardly constrained by the data.

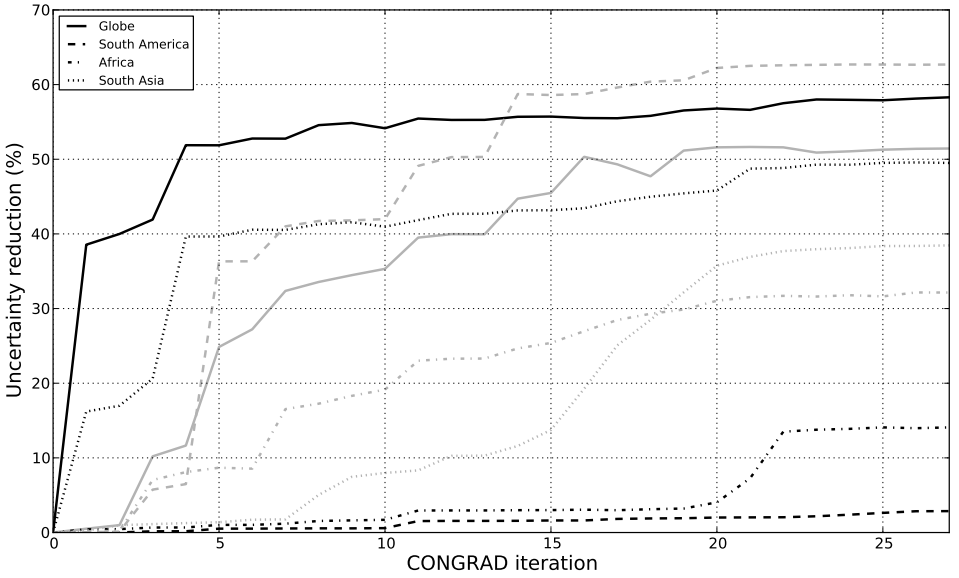

Figure 3.3: *Uncertainty reduction for 2004, defined as* $1-\frac{\sigma_a}{\sigma_b}$*, where* $\sigma_a(\sigma_b)$ *is the aggregated posterior (prior) uncertainty for the anthropogenic emissions (black) and biomass burning emissions (grey) for four large regions as a function of the iteration number in CONGRAD. A convergence criterium of 99 % gradient norm reduction is used here. The regions are defined as rectangular boxes. For the continental-scale regions we give the coordinates of the lower left and the upper right corner. South America: (−85° E,−60° N), (−30° E,13° N). Africa: (−19° E,−36° N), (51° E,36° N). South Asia: (51° E,−10° N), (180° E,36° N).*

Finally, the uncertainty of the global scaling parameters for the production of CO from methane and

NMVOC oxidation is only slightly reduced from the prior to the posterior estimate. This indicates that the current observational dataset does not constrain these individual parameters substantially. However, the value of the scaling factor for the NMVOC-CO source is adjusted significantly from a prior global total of $812 \pm 40\,\mathrm{Tg\,CO}$ to a posterior global total of $574 \pm 38\,\mathrm{Tg\,CO}$ in 2003 and $410 \pm 38\,\mathrm{Tg\,CO}$ in 2004. Despite the small prior error, the NMVOC-CO emissions are considerably reduced, far outside the 2σ (95 %) interval, which is mainly due to the overall very small weight of the single monthly NMVOC-CO scaling parameters in the cost function. Small error settings appeared to be necessary, because the a priori error settings of this global parameter have a strong influence on the solution of the inversion. The optimization approach of NMVOC-CO will be improved in future studies.

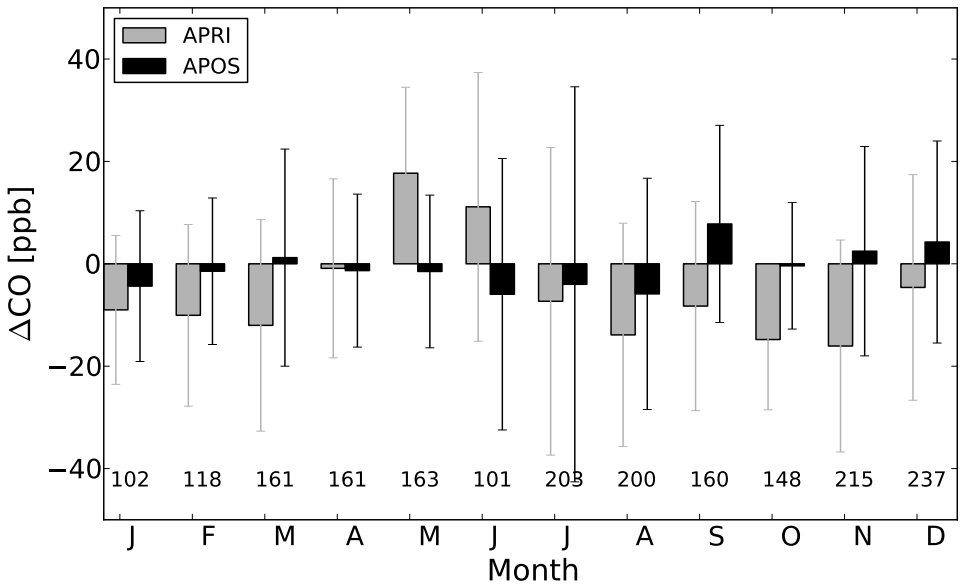

Figure 3.4: *Monthly mean difference between the TM5 model and NOAA aircraft observations for the prior (grey) and posterior (black) simulation. The number of observations per month is also given.*

3.3.3 Validation with independent NOAA aircraft observations and MOPITT total columns

We validate our inferred emissions with independent (non-assimilated) aircraft observations from the NOAA aircraft program for 2004. The comparison with aircraft data provides a valuable test for the vertical transport in the model. The NOAA profiles are taken mainly over North America. Figure 3.4 shows monthly mean deviations (model-observations) for the prior and posterior simulation for aircraft samples at altitudes above 2000 m, thus representing the free troposphere. The prior simulation underestimates the observations throughout the year (except for May and June) probably due to too low anthropogenic emissions in East Asia. The significant overestimation of the prior simulation in May and June is attributed to a too large a priori source of CO from NMVOCs. The posterior

simulation matches the observations much better, since the inversion increased Asian anthropogenic emissions and reduced the NMVOC-CO source (Table 3.2), in particular in May and June (not shown). The uncertainty, given here as a 1σ deviation from the mean, is not reduced significantly from prior to posterior simulation because these observations are not assimilated. Overall, the mean monthly difference is reduced by 50–90 % except for April when deviations were small anyway. The annual mean and standard deviation of the residuals is -6.4 ± 23 ppb a priori and -0.5 ± 22 ppb a posteriori, showing that the inversion is capable to improve the comparison with independent observations in the free troposphere over North America.

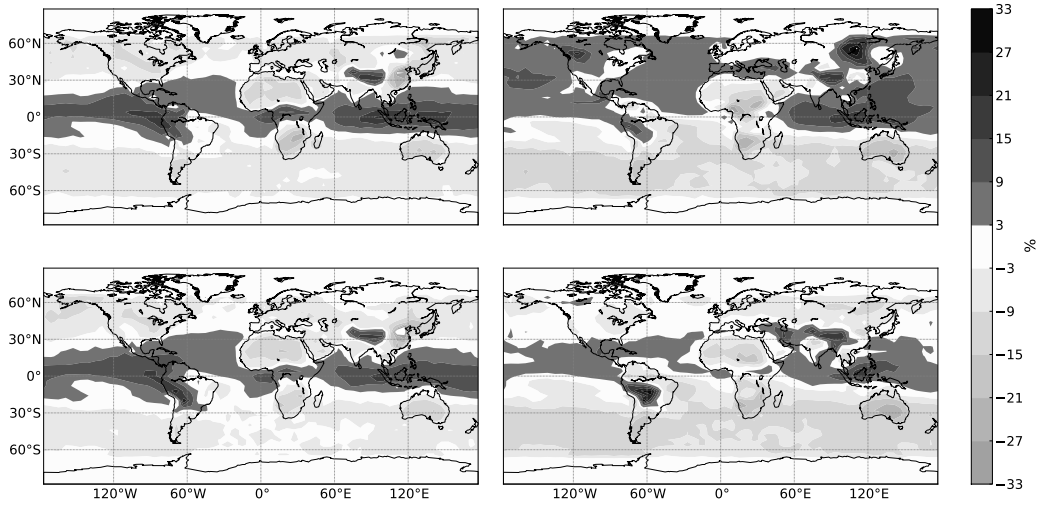

Figure 3.5: *Annual difference in CO total column, TM5-MOPITT relative to TM5 (%) for the years 2003 (top) and 2004 (bottom). Modeled CO total columns are derived using the prior (left) and posterior (right) emissions. Dark grey colors indicate higher TM5 CO total columns compared with MOPITT and light grey colors indicate a lower modeled CO total column compared to MOPITT.*

We further validate our posterior emissions with CO total column retrievals from MOPITT V4 (level 3, gridded daily profiles, Deeter et al., 2003, 2007, 2010). The MOPITT instrument is mainly sensitive to free tropospheric CO (4–7 km altitude) and CO at this altitude originates from oxidation of methane or convective transport of surface CO. Figure 3.5 shows a comparison of observed and modeled CO total columns, where the MOPITT averaging kernels are used to compare properly. Over the well-constrained NH midlatitudes (30° to 60° N), the agreement improves for 2004 from a slight prior underestimate of 5 % to a posterior underestimate of only 1 %. For 2003, the prior underestimate of 5 % turns to a posterior overestimate of 5 %. In the tropics (30° S to 30° N), the comparison improves greatly over the oceans from an a priori model overestimate of 3–5 % to less than 1 % a posteriori in 2004. For 2003 the improvement is smaller. In contrast, over the African continent, the comparison deteriorates from a 3 % underestimate a priori to 6 % a posteriori, probably due to difficulties with the MOPITT retrievals over deserts as observed previously by de Laat et al. (2010). In the remote SH (30° to 60° S), the comparison with MOPITT deteriorates from a slight model underestimate of 4–6 % a priori to an underestimate of 10 % a posteriori in both years. We already showed that the prior simulation overestimates surface observations of CO at the remote SH stations (see Fig. 3.2d). These SH surface observations thus cause a decrease in CO sources (mainly NMVOC-CO) which results in even less CO compared to MOPITT. The model underestimate with

respect to MOPITT may be caused by the treatment of vertical transport in the model. For instance, if vertical transport in the model is too slow, CO emissions will remain at low altitudes where the MOPITT instrument is not very sensitive. The comparison with NOAA aircraft profiles suggested however that the vertical transport in TM5 is reasonable, at least over North America. Hence, a possible bias in the MOPITT V4 product as was the case for the previous product MOPITT V3 (Emmons et al., 2009; de Laat et al., 2010) may also play a role. The apparent inconsistency between surface observations and MOPITT CO total columns over the remote SH was (amongst others) also observed by Kopacz et al. (2010). They inverted CO emissions using satellite data only and SH stations used as validation showed a poorer agreement in the posterior simulation compared to the prior.

In conclusion, validating our inversion results with independent aircraft data shows an improved agreement with respect to the prior simulation in the free troposphere even though only surface observations are assimilated. For satellite data, the agreement with MOPITT total column CO improves over the well-constrained NH, but deteriorates in the SH below 30° S.

Table 3.3: *Comparison of prior (left columns) and posterior (right columns) continental emission estimates for 2004 of this study with four recent studies for the same year. Numbers are the sum of anthropogenic, biomass burning and natural emissions given in Tg CO yr^{-1}. Prior inventories and assimilated datasets are given with footnotes.*

Region	This study		Pison et al. (2009)[a]		Kopacz et al. (2010)[b]		Jones et al. (2009)[c]		Chevallier et al. (2009)[d]	
	prior	posterior	prior	posterior	prior	posterior	prior	posterior	prior	posterior
Nam	142±37	167±25	137	188	57	71	135	165	–	–
Sam	138±107	156±39	146	131	119	183	113	157	–	–
Europe	67±30	92±17	103	128	78	95	110	111	–	–
Africa	266±108	338±74	264	317	214	343	234	359	286	255
Asia	385±212	597±98	296	539	389	660	367	483	–	–
Oceania	31±15	26±15	96	88	23	41	69	165	–	–
Total	1050 ± 242	1390 ± 89	1042	1391	880	1393	1028	1440	–	–

[a] EDGARv3 (1995) + GFED2 combined with flask and continuous surface measurements (56 stations).
[b] EDGAR 3.2FT2000-overwritten with EPA-NEI99 (US), BRAVO (Mexico), EMEP (Europe) and Streets et al. (2006) (Asia/China) + GFED2 combined with MOPITT + AIRS + SCIAMACHY retrievals.
[c] Prior emissions from Duncan et al. (2007) combined with MOPITT + TES retrievals.
[d] EDGARv3 + GFED2 combined with MOPITT retrievals.

3.3.4 Comparison with recent inverse modeling results

The posterior emissions match other recent inverse modeling results for the year 2004 quite well as shown in Table 3.3. Pison et al. (2009) inverted emissions of CO, methane and H_2 simultaneously, using observations from NOAA and updated the OH field within the optimization by assimilating methyl chloroform observations. Results are comparable to our results, but slightly higher for Europe and lower for South America. However, the Australian source of Pison et al. (2009) included CO emissions from Indonesia and is thus significantly higher than in the current study. Kopacz et al. (2010) used satellite data (from MOPITT, the Atmospheric Infrared Sounder (AIRS) instrument and SCIAMACHY) to optimize CO emissions for the period May 2004 to April 2005 and their results showed slightly higher emissions over South America and Asia, but significantly lower emissions over North America. This might be due to their very low prior value for fossil fuel emissions over the United States (35 Tg CO yr^{-1}) based on the US Environmental Protection Agency National Emission Inventory for 1999 (EPA_NEI99). This value was further decreased by 60 % following Hudman et al. (2008). In this study we use 105 Tg CO yr^{-1} as prior anthropogenic emission over North America.

Jones et al. (2009) optimized emissions for November 2004 only, using observations from the MOPITT and TES instruments, and they presented their results as yearly totals. These results are also comparable to the current study except for the Australian source. This is explained by their inclusion of Indonesia into this region. Chevallier et al. (2009) have performed a detailed analysis of African CO emissions for the period 2000–2006. The total emission estimates are by 25 % lower than in this study but stay well within the error bounds. The difference with our results is probably explained by the lack of surface data in the tropics. Chevallier et al. (2009) used MOPITT data to constrain the CO emissions and anthropogenic emissions in particular were more constrained than in the current study. Finally, the large increment in Asian anthropogenic emissions shown in Table 3.2 also confirms the previous findings of e.g., Kasibhatla et al. (2002) and Arellano et al. (2004) that anthropogenic emissions over Asia are too low in EDGARv3.2. All inversions roughly doubled the Asian emission estimate.

3.4 Discussion

In our inversions we have used a limited amount of observations from the NOAA surface network. A consequence of solving a data sparse system is a large solution space, because not all degrees of freedom ($\approx$25 000) are constrained by the observations ($\approx$ 1400 per year). Thus, the obtained solution will depend on the prior emissions and their error settings. Another consequence might be that model errors are compensated for by emission increments. To investigate these issues, a series of sensitivity studies is presented in Sect. 3.5. In the following paragraphs we discuss the capability of the system to separate the emission categories and the observation error.

3.4.1 Separating CO emission categories

In the 4D-Var setup a mismatch between modeled and observed CO mixing ratios is translated to an adjustment of the prior emissions. However, the observations only constrain total CO emissions of all source categories. The posterior total global source estimates in 2003 and 2004 (1744 ± 76 and $1690 \pm 75\,\mathrm{Tg\,CO\,yr^{-1}}$, respectively) are rather similar. For individual source categories, large differences are observed from 2003 to 2004. For example, the anthropogenic source increased from 770 ± 71 in 2003 to $871 \pm 77\,\mathrm{Tg\,CO\,yr^{-1}}$ in 2004, whereas the NMVOC-CO source decreased from 574 ± 38 to $410\pm36\,\mathrm{Tg\,CO\,yr^{-1}}$. Although year-to-year variations in the emission estimates is expected, a drop of $150\,\mathrm{Tg\,CO\,yr^{-1}}$ in the NMVOC-CO source is not physically realistic, but rather an artefact due to the data sparse nature of the current setup.

The prior emission estimates and prior error covariance matrix prescribe the location and timing of the emissions from all source categories. Emissions of sources with a specific timing or spatial pattern prescribed by the prior can be separated. For example, during the dry season (August–November) in the SH, biomass burning is the dominant source of CO, and the system separates the biomass burning source successfully from other CO sources due to its specific timing. In contrast, CO emissions from anthropogenic and NMVOC-CO sources take place throughout the year in the same regions and are therefore difficult to separate. As a consequence, increases of the anthropogenic source are, at least partly, compensated by decreases in the NMVOC-CO source. This may explain the sharp (unphysical) decrease of the NMVOC-CO source from 2003 to 2004, and the increase of the anthropogenic emissions for these years. The inter-dependence of the anthropogenic and NMVOC-CO source is further illustrated in Fig. 3.6. The ellipse shows the range of emission estimates for these two sources with 95 % confidence and the tilted axes indicate the negative correlation between them.

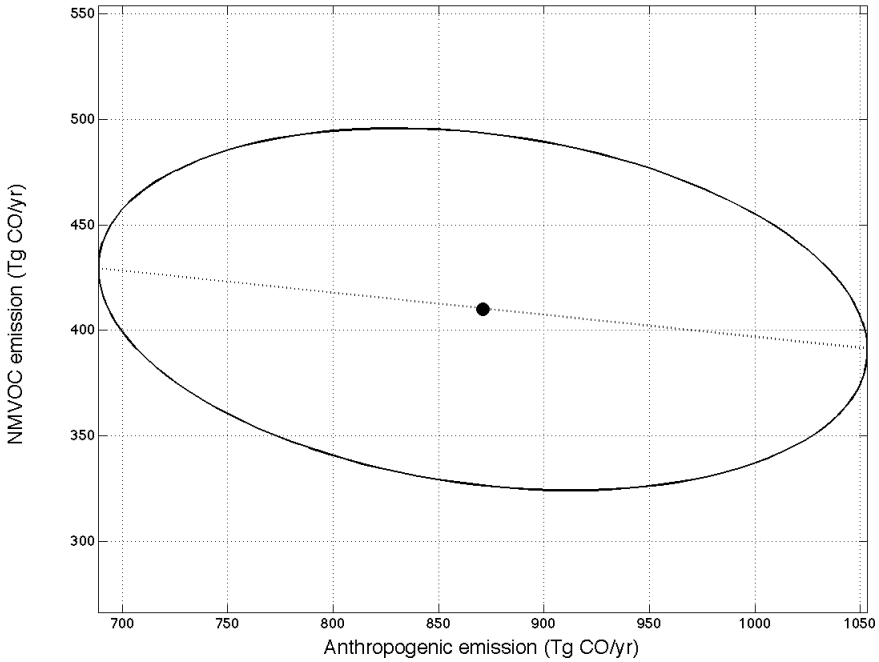

Figure 3.6: *95 % confidence ellipse for the global total annual emissions for the anthropogenic and NMVOC-CO source for 2004. The center of the ellipse (black dot) is the posterior emission estimate for the anthropogenic and NMVOC-CO source (871 and 410 Tg CO yr^{-1}, respectively). The emission estimates fall within the ellipse with 95 % confidence. The slightly tilted principle axis of the ellipse is shown as a straight dashed line through the center.*

Optimizing the NMVOC-CO source by one monthly varying scaling parameter partly caused the compensation between this source and the anthropogenic source. For example, in the remote SH the NMVOC-CO source is the only important source of CO. The prior simulation overestimated the observations in this region, resulting in a decrease of the NMVOC-CO scaling parameter and thus a reduced NMVOC-CO source globally. As a consequence, other sources had to be adjusted to compensate for this reduction. However, even with a more advanced optimization approach for the NMVOC-CO source, compensations are expected as the observations only constrain total CO emissions and hence, negative correlations in the posterior emission estimates remain apparent.

3.4.2 Observation error settings

The inversions in this study are performed in two cycles: after the first cycle, observations that are outside a 3σ interval from the simulated CO mixing ratio, are left out in cycle 2 (Fig. 3.7). This selection criterion is applied to prevent single outliers to bias the inferred emissions. The number of observations that is left out from cycle 1 to cycle 2 varies largely from station to station: in the SH, on average 6 % of the observations are left out. In the NH, on average 25 % of the observations is left out in cycle 2.

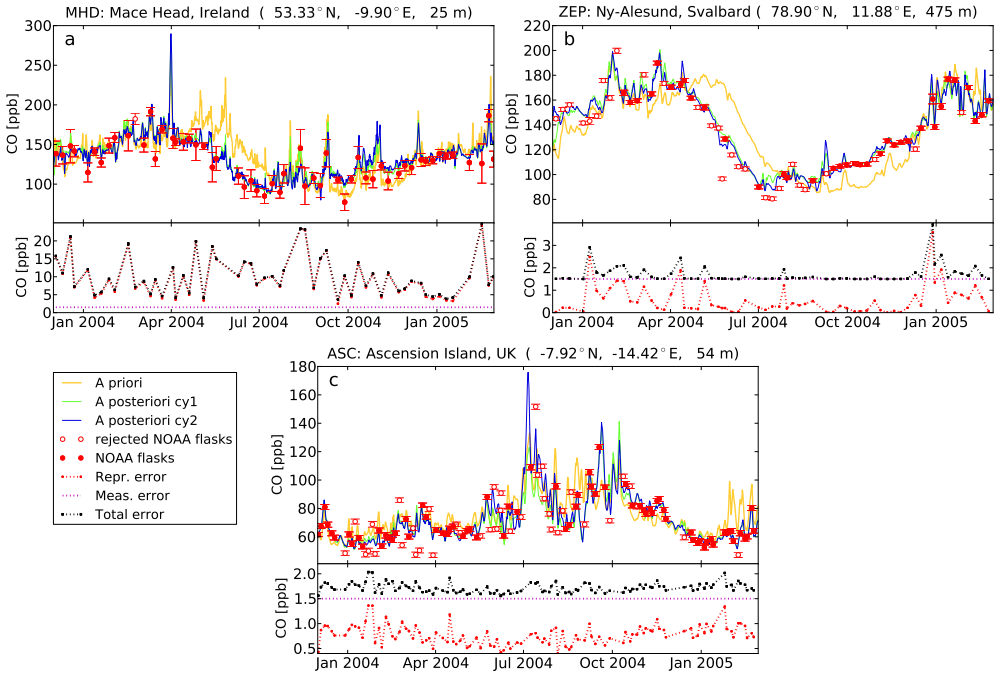

Figure 3.7: *Top: prior (yellow) and posterior (cycle 1 (green) and cycle 2 (blue)) simulations for* **(a)** *Mace Head, Ireland,* **(b)** *Ny-Alesund, Svalbard and* **(c)** *Ascension Island. The NOAA flasks are shown in red with rejected observations from cycle 1 to cycle 2 represented by open symbols. Bottom: the observation error is divided in its fixed part (purple) and the model error (red). The total error is shown in black.*

The observation error consists of a measurement error given by Novelli et al. (1998) as 1.5 ppb and a representativeness error as mentioned in Sect. 3.2.4. This latter contribution varies between 0–20 ppb for most stations. This advanced representation of the observation error has been successfully applied in inversions for methane (Meirink et al., 2008b; Bergamaschi et al., 2010). For the shorter-lived CO, this observation error setting works reasonably for all stations in the remote SH, but only for a few NH stations (e.g., Mace Head, Ireland (MHD), Fig. 3.7a).

Surprisingly, for the other NH stations (and Ascension Island station located on the SH) the observation error appears rather conservative, and approximately 25 % of the observations are rejected from cycle 1 to cycle 2. This can be attributed either to an underestimation of the measurement error (e.g., station Ny-Alesund, Svalbard (ZEP), Fig. 3.7b) or to an underestimation of the representativeness error (e.g., station Ascension Island (ASC), Fig. 3.7c). Indeed, for station Ny-Alesund located on Svalbard, the measurement error of 1.5 ppb is the dominant error term which is clearly too small regarding the number of rejected observations in Fig. 3.7b. For Ascension Island station the model error (given in red in the bottom panel of Fig. 3.7c) never exceeds the measurement error even in periods of high CO levels due to pollution peaks transported from continental source regions in either Africa or South America.

The effect of the data rejection strategy on the inferred emissions can be very large both on regional and global scales (Table 3.2). For example, Asian anthropogenic emissions decrease by 82 Tg CO yr^{-1} from cycle 1 to cycle 2, largely driving the 122 Tg CO yr^{-1} difference on the global scale. In addition, biomass burning emissions reduce significantly in Africa and Oceania but increase for South America. This behavior shows that measurements with both very low and very high CO mixing ratios are rejected. The global biomass burning source decreases by 73 Tg CO yr^{-1} from cycle 1 to cycle 2. In contrast the global NMVOC-CO source increases by 109 Tg CO yr^{-1}. Given the discussion in the previous paragraph a part of this increase likely compensates for the drop in anthropogenic emissions. However, the increase in NMVOC-CO alone is not enough to balance the 195 Tg CO yr^{-1} decrease from cycle 1 to cycle 2 for anthropogenic and biomass burning emissions together. Hence, the rejection of observations leads to significant changes in the emissions, even though for most regions the emission estimates remain within 1σ error bounds.

Finally, a sensitivity study with doubled observational errors reduced the number of rejected data points to 7 %. The emission estimates for this simulation also fall within 1σ error bounds of the base run, indicating that the inferred emission estimates are robust given the posterior uncertainties.

We conclude that it is difficult to design an estimation procedure for the model error that gives correct results for all stations, hence estimates of the model representation error will remain a challenging topic for future research.

3.5 Sensitivity analysis

In this section we discuss 3 sensitivity studies with respect to prior settings and model errors. Sensitivity study GFED3 uses the new version of the GFED product (van der Werf et al., 2010). For the year 2004, this biomass burning inventory prescribes lower emissions by a factor 2 to 3 from January to March compared to GFED2. Peak emissions in September in GFED2 of 69 Tg CO $month^{-1}$ globally are reduced to 55 Tg CO $month^{-1}$ in GFED3.

Since the distribution of OH and its north-south gradient remains uncertain, we also investigate the influence of the tropospheric OH distribution on the inferred emissions by using an OH field computed from a full-chemistry simulation with TM5 (Huijnen et al., 2010) and scaled by a factor 1.02 to obtain comparable CO and methyl chloroform lifetimes as for the OH field used in the base inversion. Compared to the OH field of the base inversion, the north-south gradient (computed as an airmass-weighted average, Lawrence et al., 2001) in the TM5-OH field is more pronounced (NH/SH ratio of 1.15) compared to the OH field used in the base inversion (NH/SH ratio of 1.0).

The next sensitivity study focuses on model uncertainty in the vertical distribution of biomass burning emissions. The base inversion uses an injection height for biomass burning emissions up to 2000 m (distributed as 20 % in layers 0–100 m, 100–500 m and 500–1000 m and 40 % in 1000–2000 m layer). However, some recent studies (Val Martin et al., 2009; Gonzi and Palmer, 2010) found evidence that biomass burning emissions are partly injected higher up in the atmosphere. In this sensitivity study (FVERT) we apply a vertical distribution of biomass burning emissions following the results of Gonzi and Palmer (2010). The vertical biomass burning emission distribution is defined as

- Boreal region ($> 30°$ N): 82 % below 2 km, 10 % in 2–5 km, 2.5 % in each of the layers 5–8 km and 8–11 km. The remaining 3 % is injected above 11 km.
- Tropical region: 85 % below 2 km, 10 % in 2–5 km, 2.5 % in both layers 5–8 km and 8–11 km.

The inversion results for these sensitivity tests are summarized in Table 3.4, where we omit the natural emissions and CH4-CO since these sources do not change significantly from the prior to the posterior emission estimates in the base inversion.

Table 3.4: *Prior and posterior global emission estimates (in Tg CO yr^{-1}) for 2004 and their uncertainty for the sensitivity studies. The first column shows the sources/regions. Columns 2 and 3 show the prior (only different for biomass burning in GFED3 study). The last 4 columns show the posterior emission estimates for the sensitivity studies. The results for the Base inversion (cycle 2) are included for completeness.*

Source/Region	Prior		Posterior			
Anthropogenic	EDGARv3.2		Base	GFED3	OH	FVERT
Nam	105 ± 30		105 ± 26	104 ± 27	114 ± 27	82 ± 26
Sam	22 ± 16		0 ± 16	0 ± 16	1 ± 16	0 ± 16
Europe	62 ± 30		85 ± 18	94 ± 18	76 ± 19	73 ± 18
Africa	80 ± 52		149 ± 45	181 ± 50	140 ± 46	178 ± 44
Asia	258 ± 195		526 ± 97	548 ± 99	630 ± 93	512 ± 86
Oceania	5 ± 1		4 ± 1	5 ± 1	4 ± 1	4 ± 1
Globe	531 ± 183		871 ± 77	932 ± 75	967 ± 74	850 ± 69
Biomass burning	GFED2	GFED3	Base	GFED3	OH	FVERT
Nam	23 ± 19	33 ± 39	47 ± 10	38 ± 7	35 ± 9	58 ± 10
Sam	98 ± 105	64 ± 56	136 ± 39	109 ± 40	106 ± 28	108 ± 31
Europe	2 ± 1	1 ± 1	3 ± 1	1 ± 1	2 ± 1	2 ± 1
Africa	165 ± 94	146 ± 82	165 ± 63	144 ± 44	114 ± 64	214 ± 67
Asia	98 ± 79	69 ± 53	42 ± 52	52 ± 50	42 ± 63	86 ± 50
Oceania	18 ± 14	21 ± 19	16 ± 14	22 ± 18	20 ± 14	16 ± 14
Globe	404 ± 157	334 ± 119	409 ± 76	365 ± 71	321 ± 73	484 ± 76
NMVOC-CO	2004		Base	GFED3	OH	FVERT
Globe	812 ± 40		410 ± 38	433 ± 38	369 ± 38	403 ± 38

3.5.1 Sensitivity study GFED3

The results for sensitivity study GFED3 (Table 3.4) show an increase in biomass burning of 30 Tg CO yr^{-1} globally with respect to the prior estimate of 334 Tg CO yr^{-1}. Biomass burning emissions increase mainly in South America (+45 Tg CO yr^{-1}). However, Asian biomass burning emissions decrease by 17 Tg CO yr^{-1}. To compensate for the lower biomass burning emissions with respect to the base inversion, anthropogenic emissions (932 ± 73 Tg CO) and the NMVOC-CO source (433 Tg CO) are increased. Similar adjustments in biomass burning emissions were also observed for the base inversion. For example, for the base inversion the increase in South America was 38 Tg CO, whereas Asian biomass burning emissions decreased by 56 Tg CO. This sensitivity study does not support the decrease in global emissions in GFED3 compared to GFED2, as emission estimates increase for all regions (except Asia). This could be partly due to the underestimation of agricultural waste burning and deforestation fires in GFED3 (van der Werf et al., 2010).

3.5.2 Sensitivity study OH

The OH field from the TM5 full-chemistry simulation shows lower OH over tropical land masses compared to the OH field from Spivakovsky et al. (2000) (Fig. 3.8, top), in particular over South America. This OH gap is present since large amounts of emitted isoprene are oxidized by OH and hence reduce OH concentrations in the model. However, as shown by Lelieveld et al. (2008), this OH gap is not

confirmed by field campaigns that show high OH over the tropical forests. An OH recycling mechanism was proposed by Lelieveld et al. (2008), but was not yet incorporated in the TM5 simulation (Huijnen et al., 2010). Lower OH concentrations over tropical land masses (Fig. 3.8, top) result in a reduction of biomass burning emissions of $88\,\mathrm{Tg\,CO\,yr^{-1}}$ globally in 2004 compared to the base inversion (Table 3.4, Fig. 3.8 bottom). Africa ($-51\,\mathrm{Tg\,CO\,yr^{-1}}$) and South America ($-30\,\mathrm{Tg\,CO\,yr^{-1}}$) contribute substantially to this decrease. The NMVOC-CO source is reduced to $369\,\mathrm{Tg\,CO\,yr^{-1}}$, which is $41\,\mathrm{Tg\,CO\,yr^{-1}}$ lower than in the base inversion. This reduction is also attributed to the lower OH concentrations in the SH. In contrast, the NH OH concentration is higher compared to the OH field from Spivakovsky et al. (2000). Therefore, higher global anthropogenic emissions are observed for this study ($967\,\mathrm{Tg\,CO\,yr^{-1}}$) compared to the base inversion (871 Tg $\mathrm{CO\,yr^{-1}}$). This difference is clearly observed over India in Fig. 3.8. The comparison with MOPITT is not improved with respect to the base inversion (not shown): the remote SH still underestimates MOPITT total columns.

3.5.3 Sensitivity study FVERT

When biomass burning CO emissions are released higher up in the atmosphere, inferred biomass burning emissions are expected to increase, since the surface concentrations of biomass burning CO decrease and thus higher CO surface emissions are required to match the observations. Indeed, it is observed that the global biomass burning emissions increase by $75\,\mathrm{Tg\,CO\,yr^{-1}}$ with respect to the base inversion (Table 3.4). Moreover, this increase is only partly compensated by decreased anthropogenic emissions (-21 Tg $\mathrm{CO\,yr^{-1}}$) and a decrease in the NMVOC-CO source ($-7\,\mathrm{Tg\,CO\,yr^{-1}}$), indicating that a part of the biomass burning CO emissions released higher in the atmosphere, is not detected by the surface network. Higher biomass burning CO emissions with respect to the base inversion cause the comparison with MOPITT CO total columns to change: over the main biomass burning regions in Africa, South America and South East Asia, the comparison deteriorates, because the base inversion already overestimates MOPITT CO total columns over these regions (Fig. 3.5, bottom-right panel). On the remote SH, the comparison does not change significantly since the NMVOC-CO source shows only minor changes with respect to the base inversion. We conclude that the biomass burning injection height is a potentially important parameter to take into account in inversions. However, the agreement with MOPITT CO on the SH total columns does not improve. As stated before, it seems that the surface observations and MOPITT CO total columns over the remote SH are not consistently modeled.

3.6 Conclusions

We have presented a 4D-Var data assimilation system for CO using simplified chemistry and a fixed OH field, meant to assimilate large satellite datasets, but tested here using surface network observations from NOAA. The posterior simulation reproduces background CO mixing ratios including events with enhanced CO mixing ratios. The mean bias between modeled CO mixing ratios and observations from the NOAA surface network reduces for nearly all stations and the χ^2/n characteristic is reduced to values around 1, indicating that the chosen prior errors result in a well-balanced system. Approximately 15–20 % of the observations is rejected from inversion cycle 1 to cycle 2. This indicates that the model representativeness error requires further improvement. The effect on the inferred emission estimates varies per region. However, for most regions the emission estimates in cycle 1 and cycle 2 are within a 1σ error bound. Uncertainty reductions in the posterior emissions (compared to the prior) up to 60 % on the global scale were observed. For smaller (and less constrained) regions uncertainty reductions varied between 10 and 50 %.

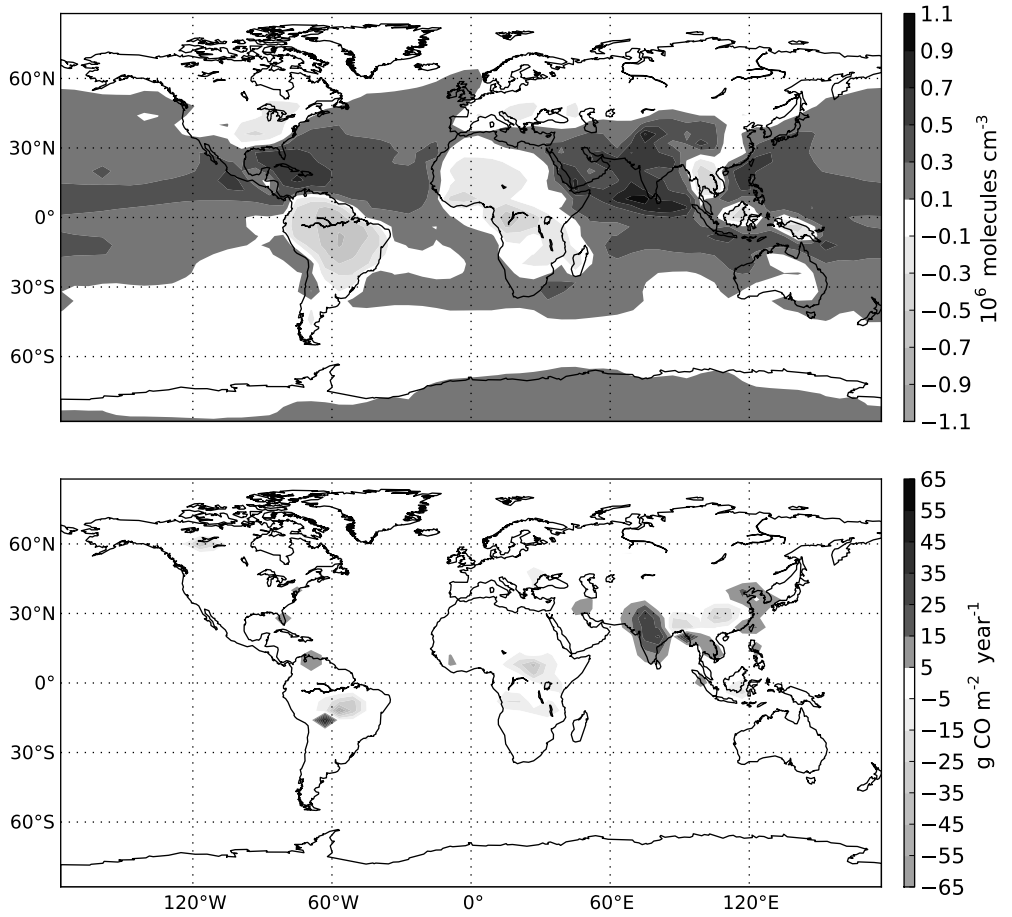

Figure 3.8: *Top: vertically integrated mass- and rate constant weighted OH difference field (TM5 – Spivakovsky et al., 2000). Bottom: emission increments difference for 2004, OH – Base. Dark grey colors indicate higher OH levels in the TM5 OH field compared to the OH field from Spivakovsky et al. (2000) (top) and increased emissions with respect to the base inversion (bottom). Light grey colors indicate lower OH levels (top) and decreasing emissions (bottom).*

Our annual continental emissions compare well with recent inverse modeling studies, indicating that the global budget of CO is well constrained in our inversion. The posterior emissions have been evaluated against non-assimilated aircraft data from NOAA and vertical column data from MOPITT V4. The forward simulation with the inferred emissions showed much more resemblance with NOAA aircraft observations in the free troposphere compared to the prior simulation, showing that the inversion is capable to improve the free tropospheric CO distribution even though only surface observations are assimilated. The comparison with MOPITT total column CO improves over the well-constrained NH and in the tropics (except over Africa) from the prior to the posterior simulation. However, in the remote SH (30°–60° S), the comparison with MOPITT deteriorates from a 4 % negative bias in

the a priori to a 10 % negative bias in the a posteriori solution, due to an emission decrease suggested by SH surface observations.

In general, atmospheric observations only constrain total CO emissions. Since in particular anthropogenic and NMVOC-CO sources are emitted in the same regions and throughout the year, it is difficult to separate these sources. Hence, emission increments in one source, to compensate for emission changes in another, are observed. However, regions where the timing of the biomass burning emissions is very important (e.g. South America) illustrate the capability to distinguish between anthropogenic and biomass burning emissions. In addition, due to the low spatio-temporal resolution of surface flask observations, the inferred emission estimates are influenced by the emission inventories and model errors. This was investigated by employing a different OH field and a different biomass burning emission height. An OH distribution from a full-chemistry simulation with TM5 with a higher N-S ratio in OH largely influenced the inversion results: biomass burning emissions and NMVOC-CO reduced whereas the anthropogenic emissions increased compared to the base inversion, indicating that the OH distribution over the NH and SH is critical for CO inversions. For this OH field the comparison with MOPITT total column CO in the SH did not improve and even less CO emissions were inferred on the SH. The sensitivity study using different fire injection heights showed that the vertical distribution of biomass burning also largely influences the inversion results. Biomass burning emissions increased by 75 $\mathrm{Tg\,CO\,yr^{-1}}$ with respect to the base inversion. Again, the comparison with MOPITT total columns did not improve. Increased biomass burning emissions over emission hotspots in South America, Central Africa and Indonesia result in an even larger discrepancy with MOPITT total columns. On the remote SH the comparison with MOPITT was similarly poor as in the base inversion.

The use of satellite data in combination with the network of surface observations is an obvious next step. Assimilation of MOPITT total column CO is expected to lead to more NMVOC-CO on the remote SH, which in turn might reduce biomass burning emissions over the fire hotspots in the SH. Lower biomass burning emissions will be more in line with the new GFED3 product. However, surface and satellite observations over the remote SH may bring conflicting information. Therefore, like in the assimilation of SCIAMACHY methane observations (Bergamaschi et al., 2009) a bias correction scheme for satellite data is currently being developed.

CHAPTER 4

Comparing optimized CO emission estimates using MOPITT or NOAA surface network observations

This paper compares two global inversions to estimate carbon monoxide (CO) emissions for 2004. Either surface flask observations from the National Oceanic and Atmospheric Administration Earth System Research Laboratory (NOAA/ESRL) Global Monitoring Division (GMD) or CO total columns from the Measurement of Pollution in the Troposphere (MOPITT) instrument are assimilated in a 4D-Var framework. Inferred emission estimates from the two inversions are consistent over the Northern Hemisphere (NH). For example, both inversions increase anthropogenic CO emissions over Europe (from 46 to 94 Tg CO/yr) and Asia (from 222 to 420 Tg CO/yr). In the Southern Hemisphere (SH) three important findings are reported. First, due to their different vertical sensitivity, the stations-only inversion increases SH biomass burning emissions by 108 Tg CO/yr more than the MOPITT-only inversion. Conversely, the MOPITT-only inversion results in SH natural emissions (mainly CO from oxidation of NMVOCs) that are 185 Tg CO/yr higher compared to the stations-only inversion. Second, MOPITT-only derived biomass burning emissions are reduced with respect to the prior which is in contrast to previous (inverse) modeling studies. Finally, MOPITT derived total emissions are significantly higher for South America and Africa compared to the stations-only inversion. This is likely due to a positive bias in the MOPITT V4 product. This bias is also apparent from validation with surface stations and ground-truth FTIR columns. Our results show that a combined inversion is promising in the NH. However, implementation of a satellite bias correction scheme is essential to combine both observational datasets in the SH.[1]

[1]This chapter has been accepted for publication in the Journal of Geophysical Research.

4.1 Introduction

Carbon monoxide (CO) is emitted to the atmosphere by the process of incomplete combustion of fossil and biofuels and biomass burning. CO is also produced in the atmosphere by oxidation of methane and non-methane volatile organic compounds (NMVOCs). Through its main removal process, reaction with the radical OH, CO perturbs the oxidation capacity of the atmosphere (Logan et al., 1981) and in particular the methane lifetime. It is also a precursor of tropospheric ozone in high NO_x conditions, thus contributing to photochemical smog.

The magnitude of CO sources reported in literature shows a large range (e.g., Duncan et al. (2007)). The large uncertainties are caused by several factors, for example increasing emissions from fossil and biofuel combustion in East-Asia for the Northern Hemisphere (NH) as well as interannual variability of CO emissions in the Tropics and boreal NH due to biomass burning (van der Werf et al., 2010). Also, the amount of CO produced by the oxidation of NMVOCs (mainly isoprene and monoterpenes) is uncertain.

Inverse modeling can be used to optimize CO source estimates. So far, inversion studies used either flask observations from surface stations (e.g., Bergamaschi et al. (2000); Kasibhatla et al. (2002); Pétron et al. (2002); Pison et al. (2009); Hooghiemstra et al. (2011)), aircraft observations (Palmer et al., 2003; Heald et al., 2004) or satellite observations (e.g., Arellano et al. (2004); Pétron et al. (2004); Arellano et al. (2006); Stavrakou and Müller (2006); Chevallier et al. (2009); Jones et al. (2009); Kopacz et al. (2009, 2010); Fortems-Cheiney et al. (2011)). Due to the different spatiotemporal resolution, analytical precision and altitude sensitivity, these different types of measurements potentially yield complementary information about CO in the atmosphere.

Although Müller and Stavrakou (2005) used both surface data and observations from Fourier-Transform Infrared Spectrometers (FTIR), to our knowledge, at present no study assimilated both surface and satellite observations jointly in a four-dimensional variational (4D-Var) data assimilation system for CO. For methane, Bergamaschi et al. (2007, 2009) and Meirink et al. (2008a) performed inversions using both flask measurements from the National Oceanic and Atmospheric Administration Earth System Research Laboratory (NOAA/ESRL) Global Monitoring Division (GMD) and total columns from the Scanning Imaging Absorption Spectrometer for Atmospheric Chartography (SCIAMACHY) instrument. They found that a bias correction scheme was necessary to obtain good agreement of model simulations with both datasets. Hence, before we can actually perform inversions combining surface and satellite observations for CO, it is important to analyse the consistency and possible differences between inversions using either dataset.

Therefore, we present in this study two inversions for the year 2004: The first inversion assimilates flask observations from the NOAA surface network. The second inversion uses CO total columns from the Measurement of Pollution in the Troposphere (MOPITT) instrument, version 4 (V4) to constrain the emissions. Since the MOPITT V4 product (Deeter et al., 2010) is modeled using log-normal probability distributions, we will describe in detail how we assimilated these observations in our 4D-Var system. According to Deeter et al. (2010), the MOPITT V4 product is improved on retrieval performance, i.e., more retrievals converge leading to more observations, in particular in very clean and highly polluted regions. This was confirmed by Fortems-Cheiney et al. (2011), who compared a prior model simulation to MOPITT V3 and MOPITT V4 columns and reported a mean model data bias reduction of 80% for V4 compared to V3. However, the long-term bias drift present in V3 has not been solved and is still present in the V4 product (Deeter et al. (2010)). Fortems-Cheiney et al. (2011) reported the first CO inversion results in a variational data assimilation using MOPITT V4 data and the posterior simulation was shown to improve the agreement with independent NOAA surface flasks in the NH and the Tropics. However, the agreement deteriorated significantly in the SH, where posterior modeled CO mixing ratios are much higher compared to the NOAA stations

in the remote SH. In the current framework we will explicitly test the consistency in optimized emissions using either NOAA surface flask observations or MOPITT total columns. This is another step in evaluating the effect of the assimilated observations on the inferred emission estimates. To test the validity of our inferred emission estimates, we will validate our results with independent (non-assimilated) observations.

With respect to our previous study (Hooghiemstra et al., 2011), we have optimized CO from NMVOC oxidation on the resolution of the underlying model. This approach was first used by Stavrakou and Müller (2006) and more recently in the studies of Pison et al. (2009) and Fortems-Cheiney et al. (2011). Jiang et al. (2011) recently showed that aggregating the NMVOC-CO source to a global source has large effects on the inferred emission estimates. Therefore, it is interesting to compare our results to previous (inverse) model studies, because some recent inversion studies (Jones et al., 2009; Kopacz et al., 2010) did not optimize the NMVOC-CO source explicitly on the resolution of the model, bearing the risk that deficiencies in the NMVOC-CO priors used might be projected on either the biomass burning or anthropogenic emissions. For example, Kopacz et al. (2010) and Liu et al. (2010) found that (apart from underestimated fossil and biofuel combustion emissions in East Asia) in particular biomass burning CO emissions seem to be underestimated in the Global Fire Emissions Database (GFED) version 2.

This paper is organized as follows: The 4D-Var system is described in Sect 4.2, where we introduce the chemistry transport model TM5 and the prior information used. Furthermore, we describe the observational datasets that are assimilated and those used for validation. In addition, technical details concerning the convergence of the method and data rejection criteria are given. In Sect. 4.3 the inferred emissions of the two inversions are discussed and compared in detail. Furthermore, our results are compared to recent literature studies and validated with independent data. A series of sensitivity studies is presented in Sect. 4.4. Conclusions are presented in Sect. 4.5.

4.2 Method

The 4D-Var system used in this study is based on the system described in Hooghiemstra et al. (2011) (Chapter 3). In short, 4D-Var inverse modeling optimizes a state vector $\mathbf{x}$ (containing e.g. emissions) such that modeled CO mixing ratios $H(\mathbf{x})$ are close to a set of observations $\mathbf{y}$ weighted with the observational error covariance matrix $\mathbf{R}$, while staying close to the prior state $\mathbf{x}_b$ weighted with the prior error covariance matrix $\mathbf{B}$. Mathematically this means that

$$\begin{aligned} \hat{\mathbf{x}} &= \min \arg \mathcal{J}, \\ \mathcal{J}(\mathbf{x}) &= \frac{1}{2}(\mathbf{x}-\mathbf{x}_b)^\top \mathbf{B}^{-1}(\mathbf{x}-\mathbf{x}_b) + \frac{1}{2}\sum_{i=1}^{M}(H(\mathbf{x})_i - \mathbf{y}_i)^\top \mathbf{R}_i^{-1}(H(\mathbf{x})_i - \mathbf{y}_i), \end{aligned} \tag{4.1}$$

where $\hat{\mathbf{x}}$ is the optimized state vector, i refers to the time step, M is the number of time steps with observations and T is the transpose operator. We use the iterative minimizer CONGRAD (Fisher and Courtier, 1995) which is based on the conjugate gradient method, (Hestenes and Stiefel, 1952) and the Lanczos algorithm (Lanczos, 1950). After N iterations CONGRAD returns both $\hat{\mathbf{x}}$ and the N leading eigenpairs (λ_j, ν_j), $j = 1, ..., N$ of the Hessian of the cost function. These eigenpairs are used to construct an approximation of the posterior error covariance matrix corresponding to $\hat{\mathbf{x}}$. We applied a stricter stopping criterion for the iterative minimization method with respect to our previous work. We now require a gradient norm reduction (preduc) of 10^6 for convergence (100 in Hooghiemstra et al. (2011)), since calculations showed that for preduc values of 50, 200 and 1000, the annual posterior emission estimates may still vary regionally. The sensitivity of the inferred emissions

with respect to the chosen preduc value will be further discussed in Sect. 4.4. Generally, a preduc value of at least 1000 is required for convergence of the emissions in our system. As outlined by Meirink et al. (2008b), the system first optimizes large scale patterns to obtain a large cost function reduction. In later iterations fine scale patterns are optimized, which is accompanied by a convergence of the posterior errors. Therefore we use a preduc factor of 10^6 for our base inversions to obtain the best estimate of the posterior error covariance matrix.

4.2.1 Chemistry Transport Model TM5

The chemistry transport model TM5 is used to simulate CO mixing ratios. TM5 (Krol et al., 2005) uses meteorological fields from the European Centre for Medium-Range Weather Forecasts (ECMWF). These fields drive model transport on a 3-hourly basis (6-hourly for 3-D fields). As in our previous study, we use the TM5-CO only version (Hooghiemstra et al., 2011). Hence, climatological OH (Spivakovsky et al., 2000), scaled with a factor 0.92 (based on methylchloroform simulations for the years 2000-2006, Huijnen et al. (2010)), is used to keep the model linear. All simulations are performed on a 6°x4° grid resolution with 25 vertical levels.

4.2.2 Prior Information and Error Structure ($\mathbf{x}_b$, $\mathbf{B}$)

The prior state vector $\mathbf{x}_b$ consists of monthly mean CO emissions for three categories. Anthropogenic (combustion of fossil and biofuels) emissions are taken from the Emissions Database for Global Atmospheric Research (EDGARv4.1, compiled for the year 2004, European Commission and Netherlands Environmental Assessment Agency (2010)) and total to 462 Tg CO in 2004. Biomass burning (vegetation fires) emissions from the Global Fire Emissions Database (GFED3, van der Werf et al. (2010)) are used with a total of 334 Tg CO in 2004. The natural source consists of direct emissions from plants and the oceans amounting to 115 Tg CO/yr (Houweling et al., 1998) and the contribution of NMVOC-CO. We add NMVOC-CO to the natural source since the bulk of this source consists of biogenic (isoprene and monoterpenes) emissions. The NMVOC-CO source is based on monthly 3-D CO production fields (the same as used in Hooghiemstra et al. (2011), but following their posterior emission estimates, scaled to an annual total of 400 Tg CO/yr) from a full-chemistry run with the TM4 model (Myriokefalitakis et al., 2008). These fields are summed over the vertical coordinate and combined with the direct emissions from plants and the oceans to obtain a monthly 2-D emission field, while archiving the corresponding vertical distribution. The resulting 2-D field is added to the state vector and totals to 515 Tg CO/yr. In this way we effectively optimize a volume CO source. A similar approach has been adopted in the studies of Pison et al. (2009) and Fortems-Cheiney et al. (2011). However, in their model a separate formaldehyde tracer was added whereas here we emit directly CO. Moreover, Fortems-Cheiney et al. (2011) optimized the full 3-D chemical production field of formaldehyde. Here we have chosen to assume the vertical distribution to be known a priori and only optimize 2-D emission fields to reduce the length of the state vector. In contrast to Hooghiemstra et al. (2011) we do not optimize CO production from methane oxidation. Instead we use optimized methane mixing ratio fields from a 4D-Var inversion for methane (Bergamaschi et al. (2009), Houweling et al. [2011], in prep.) that are consistent with the NOAA surface network. The production of CO from methane (assuming a CO yield of 1.0) accounts for 865 Tg CO/yr. Hooghiemstra et al. (2011) used a constant tropospheric methane mixing ratio of 1800 ppb resulting in 885 Tg CO/yr from methane oxidation. The total prior emissions (including CO from methane oxidation) amount to 2176 Tg CO in 2004. Although the emissions presented here are optimized as 2-D fields, biomass burning and natural emissions are distributed vertically as shown in Fig. 4.1 (a and d, respectively). As shown also by Val Martin et al. (2009), biomass burning CO is mostly released within

the boundary layer, except when pyrogenic clouds are triggered. In contrast, CO production from the oxidation of methane and NMVOCs occurs at higher altitudes.

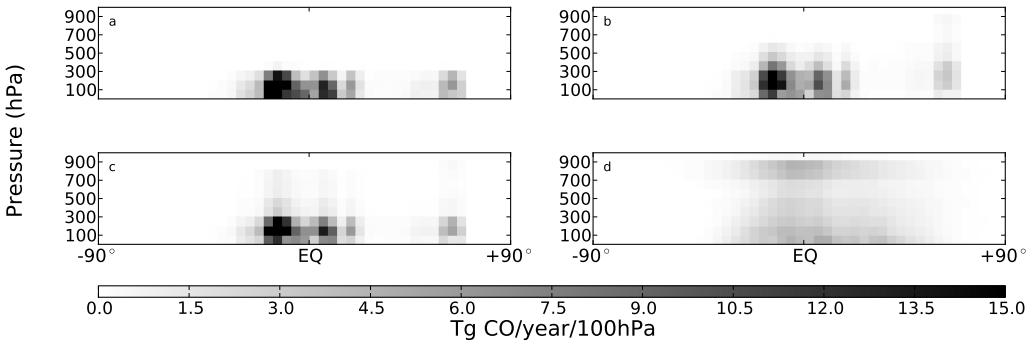

Figure 4.1: *Zonally and yearly averaged biomass burning emissions (panels a, b and c) and NMVOC-CO emissions (panel d). The biomass burning vertical distributions correspond to the base simulation (a, all emissions released below 2 km), the FVERT used in this study (b) and the FVERT sensitivity simulation in Hooghiemstra et al. (2011) (c). NMVOC-CO (d) is emitted higher up in the troposphere.*

The prior error structure used in our inversions is kept the same as in Hooghiemstra et al. (2011): Grid-scale monthly errors of 250% of the corresponding grid-scale emissions are chosen for the natural source and the biomass burning source. For the anthropogenic source the grid-scale error is set to 50% for the Western developed world (North America, Europe and Australia) and to 250% for the rest of the world. Note that these large prior errors implicitly allow for the possibility of negative emissions. This could be avoided by employing a 'semi-exponential' description of the emission distribution as is done recently for methane inversions (Bergamaschi et al., 2009, 2010). However, this would lead to a non-quadratic cost function for which the conjugate gradient method is not suited anymore. This will be discussed in more detail in Sect. 4.2.3.2. We assign spatial and temporal error correlations to reduce the effective number of variables to be optimized by the inversion. A Gaussian spatial correlation length of 1000 km is used for all emission categories. This is in particular important for the stations-only inversion in which the number of observations is much smaller compared to the number of state vector elements. For a fair comparison, this correlation length was kept 1000 km in the MOPITT-only inversion. An e-folding temporal correlation length of 9.5 months (0.9 month-to-month correlation coefficient) is set for the anthropogenic and natural emissions. For biomass burning emissions an e-folding temporal correlation length of 0.62 months (0.2 month-to-month correlation coefficient) is used.

4.2.3 Observations Assimilated in 4D-Var $(\mathbf{y}, \mathbf{R})$

In this section we describe the observations that are assimilated in the 4D-Var system. For both NOAA surface flask observations and MOPITT total columns, the observations used are described as well as the assigned uncertainty and the contribution of an observation to the cost function (Eq. 4.1).

4.2.3.1 NOAA Surface Flask Observations

Currently the NOAA ESRL surface network consists of over 50 surface stations worldwide at which CO mixing ratios are measured weekly with very high analytical precision by using flask samples (Novelli et al., 2003). However, model simulations on a coarse grid are difficult to compare one-to-one with these flask observations, specifically due to model representativeness errors. For example, in the model the emissions are given per grid box and time step and are instantaneously mixed over the grid volume. In reality, the subgrid-scale variability of the emissions leads to a heterogeneous distribution of CO mixing ratios in that box. Hence, a station located downwind of an emission, would observe higher CO mixing ratios compared to the model. Furthermore, strong gradients in CO mixing ratios due to passing pollution plumes are much sharper in reality than the model can represent.

For these reasons, inverse modeling studies deweight or reject some stations before assimilation to prevent biased results. For example, in CarbonTracker Europe (optimization of CO_2 fluxes using Kalman filtering, Peters et al. (2010)) 2 stations are explicitly not assimilated and stations in strong emissions regions are assigned large fixed errors (of 7.5 ppm CO_2). In Bergamaschi et al. (2010) (4D-Var optimization of methane fluxes) an advanced description of the model representativeness error in TM5 is given. The total observational error σ_{obs} is the sum of a measurement error and the model representativeness error, consisting of errors due to local emissions, modeled 3-D gradients and variations in time. It was shown that the observational errors calculated in this way vary largely from station to station and can vary in time for a certain station throughout the year.

In this study we first apply a quantitative criterion to select the stations that we assimilate in the system and then apply the scheme to estimate the overall observational error of (Bergamaschi et al., 2010). The criterion is based on a model simulation with prior sources for the year 2004. The idea is that stations with a large diurnal cycle, most likely due to nearby sources in the model, are excluded whereas background stations and stations influenced by seasonal emissions from for example biomass burning, are maintained. With a model time step of 45 minutes, the model samples each station 32 times per day. From these modeled CO mixing ratio series we compute a daily standard deviation and use the mean daily standard deviation over the whole year as a measure of the diurnal variation. If this measure exceeds a certain threshold (set to 3.5 ppb in this study), the station is not assimilated in the 4D-Var system. As an illustration, the modeled simulation and the mean daily standard deviation for three stations are presented in Fig. 4.2. For comparison also the standard deviation of the complete model time series (annual standard deviation) is given. For station Sede Boker (top panel in Fig. 4.2), the mean daily standard deviation amounts to 8.7 ppb and the station is not assimilated. In contrast, although station Barrow, Alaska (middle panel) has an annual standard deviation of 23.5 ppb, the mean daily standard deviation is only 2 ppb. This station is maintained in the assimilation because the model is expected to reproduce the seasonal cycle more accurately than the diurnal cycle. For comparison, station South Pole, Antarctica shows only a very small spread throughout the year (6.9 ppb) and no daily spread as there are no sources of CO nearby. We acknowledge that since the criterion is based on a model simulation, the choice of stations to be assimilated depends strongly on the emissions used in this simulation. Here we used the prior emissions as described in Sect 4.2.2 and we believe that we assimilate mainly stations for which the coarse model can reproduce the observations. The location of the 34 stations maintained in the assimilation are shown in Fig. 4.3.

With respect to our previous study, the measurement error has been increased to 3 ppb, because Hooghiemstra et al. (2011) found that a measurement error of 1.5 ppb was too conservative in particular on the remote SH. This was likely due to an underestimate of the model error in this region as potential chemistry and transport errors were not included in this error. As a consequence, a large fraction of the observations was not assimilated in the second cycle (see below). With the enhanced observational errors, the total observational error ranges typically from 3 - 20 ppb. Close to emission regions, the error can even become as large as 100 ppb. In the clean remote SH, the observation error

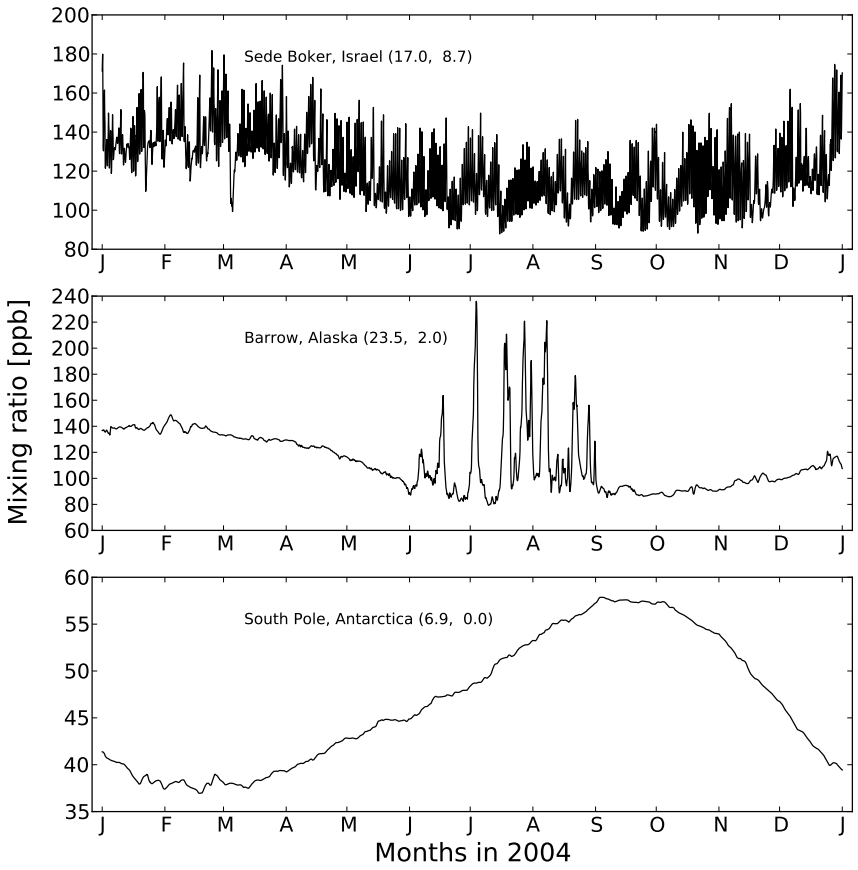

Figure 4.2: *Modeled CO mixing ratio at three NOAA stations for 2004. Numbers between brackets represent the annual standard deviation (ppb) and the mean daily standard deviation (ppb), respectively. The daily standard deviation is computed as the standard deviation of the model CO mixing ratios sampled in each time step during one day. The mean daily standard deviation is the average of these daily standard deviations over the whole year. The annual standard deviation is computed as the standard deviation of the model CO mixing ratios sampled per time step during the year. Our station selection criterion rejects stations with a mean daily standard deviation* > 3.5 *ppb.*

is dominated by the measurement component of 3 ppb. In contrast, in the polluted NH, where most surface CO is released, the model representativeness error is the dominant error term (e.g., see the black bars representing the total observational error in Fig. 4.7).

Each flask observation contributes to the observational part of the cost function. The costs for a mismatch are defined as $\frac{1}{2}\left(\frac{y_m - y}{\sigma_{obs}}\right)^2$, where y_m is the mean modeled CO mixing ratio during a 3 hour period, y is the observed CO mixing ratio and σ_{obs} is the observation error. We assume the errors to be uncorrelated leading to a diagonal observational error covariance matrix $\mathbf{R}$.

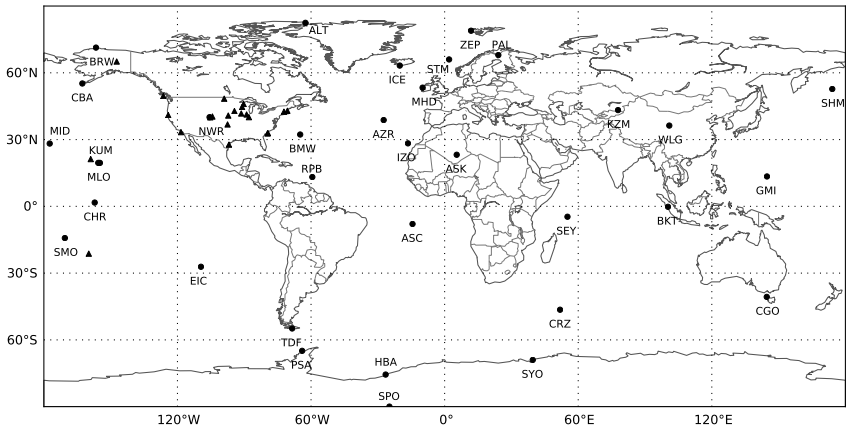

Figure 4.3: *Positions of the 34 stations assimilated in the stations-only inversion (dots) and the NOAA aircraft sites used for validation (triangles).*

We perform the inversion using surface flask observations in 2 cycles following the approach of Bergamaschi et al. (2005). After the first inversion cycle, all observations outside a 3σ interval are not used in the second cycle to avoid single outliers to bias the emission estimates. In our previous work, the amount of rejected data points was $15 - 20\%$ influencing the inferred emissions regionally from cycle 1 to cycle 2. With the larger observation errors used in this study, the number of rejected data points is reduced to around 8% based on a preduc factor of 100 as used by Hooghiemstra et al. (2011). Moreover, for a preduc factor of 10^6, this number further reduces to 4% since the model fits the observations more accurately. As a result, the difference in inferred emissions from cycle 1 to cycle 2 becomes much smaller. We acknowledge that a rejection of 4% is still a large number given the Gaussian range of 3σ that statistically should lead to a rejection of less than 1% of the data. However, this 4% is mainly caused by a few stations that are still difficult to fit, most likely due to transitions from polluted to very clean air masses that the coarse model can not resolve and is difficult to model as a representativeness error.

4.2.3.2 MOPITT V4 CO Total Columns

The MOPITT instrument was launched in December 1999 on board NASA's Terra satellite. Although a cooler failure occurred at one side in May 2001, the instrument is already supplying valuable CO observations for 11 years. The MOPITT instrument measures upwelling radiances in a thermal-infrared (TIR) spectral band near 4.7μm and in a short-wave infrared (SWIR) spectral band near 2.3μm. An optimal estimation technique is used to derive CO profiles (Deeter et al., 2003). A priori information is supplied since the optimization problem is ill-conditioned. In this paper we use MOPITT Version 4, Level 3 data (Deeter et al., 2010), which are based exclusively on TIR observations. This data comes as a daily product, gridded at a 1°x1° resolution and the a priori profile, retrieved profile and the corresponding averaging kernel matrix are supplied. As for the extensively validated MOPITT V3 (e.g., Emmons et al. (2009)), we use daytime observations between 65°S and 65°N only. Except in regions of strong thermal contrast, the MOPITT TIR-based V4 product is mainly sensitive to free tropospheric CO at altitudes from 4–7 km and per profile on average less than 2 independent pieces of information are inferred. Since the total column is generally retrieved

more accurately than a single level (Deeter et al., 2003), we only use the CO tropospheric mean mixing ratio expressed in ppb. Figure 4.4 shows the differences in the CO tropospheric mean mixing ratio between MOPITT V3 and V4 for the months of March and September 2004. In general, MOPITT V4 is significantly lower compared to MOPITT V3. On the NH, differences up to 30 ppb are observed. In the SH, differences are smaller (up to 20 ppb in September) but the relative differences are as large as on the NH due to the North-South gradient in CO mixing ratios.

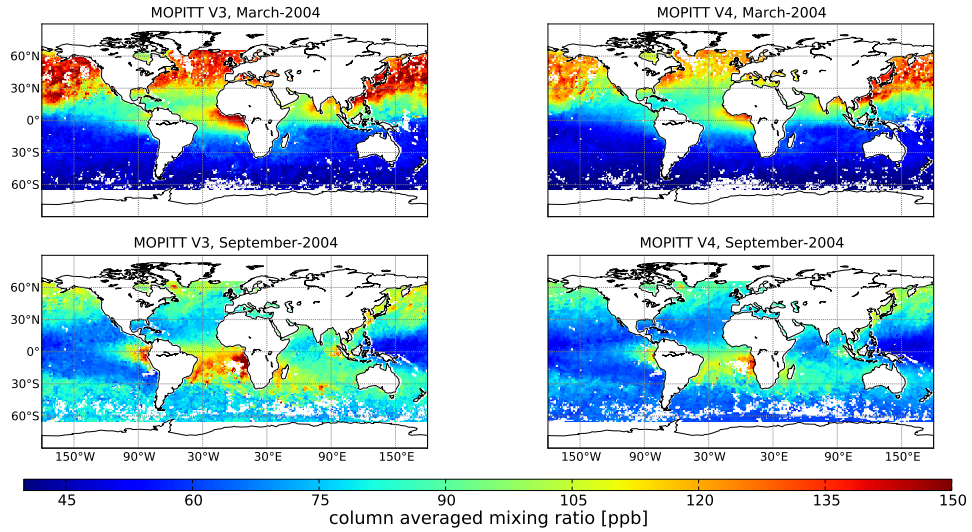

Figure 4.4: *Column-averaged CO mixing ratios from MOPITT products V3 (left) and V4 (right) for the months March (top) en September (bottom) 2004.*

So far, inversion studies assimilating MOPITT columns always used all MOPITT pixels over both ocean and land surfaces. However, de Laat et al. (2010) and Hooghiemstra et al. (2011) showed that MOPITT columns over deserts are biased high. de Laat et al. (2010) compared observed MOPITT V3 total columns in a latitude band over the Sahara desert to model columns and SCIAMACHY observed columns (taking into account the averaging kernels for MOPITT and assuming the SCIAMACHY averaging kernels to be unity (de Laat et al., 2010)). They found that while all three were in good agreement over the Atlantic ocean, a sharp increase in MOPITT observed CO total columns at the land-ocean boundary was found, whereas the model and SCIAMACHY data did not show such an increase. Over the Sahara desert MOPITT total columns were on average 25% higher than model and SCIAMACHY columns. Moreover, Deeter et al. (2010) also showed that MOPITT V4 at 700 hPa was 10 - 30 ppb higher compared to the NOAA station Assekrem, Algeria. Hooghiemstra et al. (2011) conducted a global inversion for the year 2004 using NOAA surface flasks and compared both the prior and the posterior simulation with MOPITT V4 columns. They found differences over the Sahara desert of 15% between MOPITT and the model simulation for both the prior and the posterior simulations. Figure 4.5 shows the mean modeled and observed total columns between 15-26°N for all longitudes and the differences (in black on the right axis) with the columns simulated using the prior emissions. MOPITT columns are up to 20% (and 20 ppb) higher over the Sahara desert and the Arabian Peninsula, located between longitudes -15° and 55°E. This discrepancy can not be explained by emissions or by transport. Therefore, we decided not to assimilate MOPITT land pixels in our 4D-

Var system in this study. One might expect an unbalanced or even biased system due to this approach as the SH contains more ocean surface compared to the NH and is thus heavier constrained by the observations. However, a sensitivity study using all MOPITT observations (including land pixels) showed only large differences in inferred emission estimates for Africa (see Fig. 4.13). Moreover, this inversion was not able to reduce the prior mismatch over the Sahara desert completely due to the lack of emissions in this region in the prior emission inventory. Sensitivity studies will be discussed in detail in Sect. 4.4.

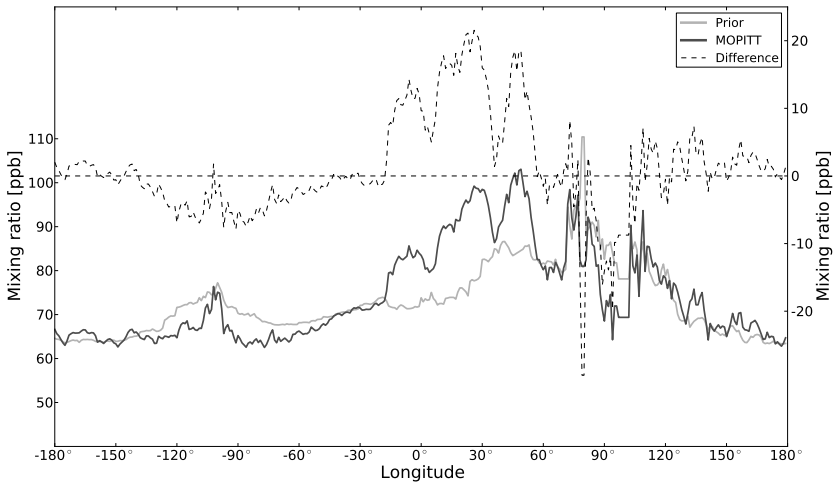

Figure 4.5: *MOPITT observed (solid black line) and prior modeled (solid grey line) CO total columns for a latitude band from 15-26° N as a function of longitude. The dashed line illustrates the differences (MOPITT-model) given on the right axis.*

The contribution to the observational part of the cost function for a MOPITT observation is in principal calculated in the same way as for the surface stations described above. Thus, the costs are defined as $\frac{1}{2}\left(\frac{y_m - y}{\sigma_{obs}}\right)^2$. y_m and σ_{obs} are detailed below. In contrast to the MOPITT V3 retrievals resulting in CO profiles in volume mixing ratios (VMR), the MOPITT V4 retrieved profiles are modeled as log(VMR) values. The V4 averaging kernels describe the sensitivity of retrieved log(VMR) to true atmospheric log(VMR) values. According to the MOPITT V4 user guide (Deeter, 2009), an in-situ or model profile should be transformed using the averaging kernel and a priori profile, resulting in a pseudo profile:

$$\ln(\mathbf{x}_{ps}) = \ln(\mathbf{x}_a) + \mathbf{A}(\ln(\mathbf{x}_m) - \ln(\mathbf{x}_a)), \tag{4.2}$$

where $\mathbf{x}_{ps}$ is the resulting pseudo profile, $\mathbf{x}_a$ is the MOPITT V4 a priori profile, $\mathbf{A}$ is the MOPITT V4 averaging kernel and $\mathbf{x}_m$ is the modeled CO profile, interpolated to the MOPITT pressure grid. The logarithms in Eq. (4.2) however, require the arguments to be positive. Due to the large Gaussian prior errors assigned to the emissions, negative emissions may arise during the iterative 4D-Var process. These negative emissions may occasionally lead to negative model profiles ($\mathbf{x}_m$) and invalid logarithms in Eq. (4.2). Another disadvantage of the formulation in Eq. (4.2) is that it leads to a non-linear

observation operator in the 4D-Var framework and prevents us from using the conjugate gradient method. This method has the important advantage that posterior emission uncertainties can be easily computed (Meirink et al., 2008b). Therefore, we have chosen to approximate the averaging kernel to first order (derivation in the appendix), resulting in an averaging kernel $\tilde{\mathbf{A}}$ that can be used in the following way to construct the pseudo profile:

$$\mathbf{x}_{ps} = \mathbf{x}_a + \tilde{\mathbf{A}}(\mathbf{x}_m - \mathbf{x}_a). \tag{4.3}$$

From the pseudo profile $\mathbf{x}_{ps}$, the scalar tropospheric-mean mixing ratio y_m is computed by

$$y_m = \frac{1}{p_{\text{surf}}} \sum_{i=1}^{N_{lev}} (x_{ps})_i (\Delta p)_i, \tag{4.4}$$

where p_{surf} is the surface pressure, N_{lev} is the number of levels for the MOPITT profile (10 or less depending on orography) and Δp is the vector of layer thicknesses in pressure units. We analyzed the differences in modeled CO columns using Eq. (4.3) compared to Eq. (4.2). The global monthly mean differences are typically within 2% (1 ppb). However, larger regional differences up to 10% (15 ppb) may occur as shown in Fig. 4.6. These differences also vary over the year as the linearized approach leads to higher model columns on the SH and the NH Tropics, but slightly lower columns on the NH mid-latitudes in March 2004 (top panel). For September 2004, slightly higher model columns are found over much of the NH. In the SH both larger and smaller model columns are present when using the linearized averaging kernel compared to the formulation of Eq. (4.2). Hence, we note that this approach may introduce a small bias and thus slightly biased emission estimates. However, a sensitivity study in which we explicitly corrected for the difference between application of Eq. (4.3) and Eq. (4.2) by subtracting the difference from the model columns in the prior simulation, led to optimized emissions well within the error bounds of the base inversion for each emission category (see Table 4.5).

For multiple 1°x1° MOPITT profiles in the same 6°x4° model grid box (up to 24), we use the same model profile $\mathbf{x}_m$ to compute $\mathbf{x}_{ps}$ in Eq. (4.3) and y_m in Eq. (4.4). However, since every MOPITT retrieval has its own prior and averaging kernel, the values of y_m in the same model grid box will differ. Due to the varying orography in a grid box, the surface pressure defined on the 6°x4° grid may differ from the retrieved surface pressure for the MOPITT observation that is given on 1°x1°. To solve this, a surface pressure filter adopted from Bergamaschi et al. (2009) is used in which only observations are used with a surface pressure that is within 25 hPa of the model surface pressure.

For the MOPITT observations we specify an observation error (σ_{obs}) for each (1°x1°) observation. This error consists of a model error σ_{mod} and two types of measurement error (σ_{unc} and σ_{var}) such that

$$\sigma_{obs} = \sqrt{\sigma_{mod}^2 + \sigma_{unc}^2 + \sigma_{var}^2}. \tag{4.5}$$

σ_{var} is given in the MOPITT product and represents the variability of all MOPITT profiles falling in the 1°x1° box. The model error σ_{mod} is non-zero only if multiple MOPITT observations fall in the same 6°x4° model grid box and is defined as the standard deviation of the modeled CO total columns y_m within that grid box. The dominant part of the observation error is σ_{unc} which represents the uncertainty in the MOPITT observation. The resulting σ_{obs} is approximately 10% per observation. As for the surface flask observations, we do not include correlations between observations in the observation error covariance matrix. However, correlations are present in both the observations (as roughly the same airmass might be sampled more than once) and in the modeled columns. So

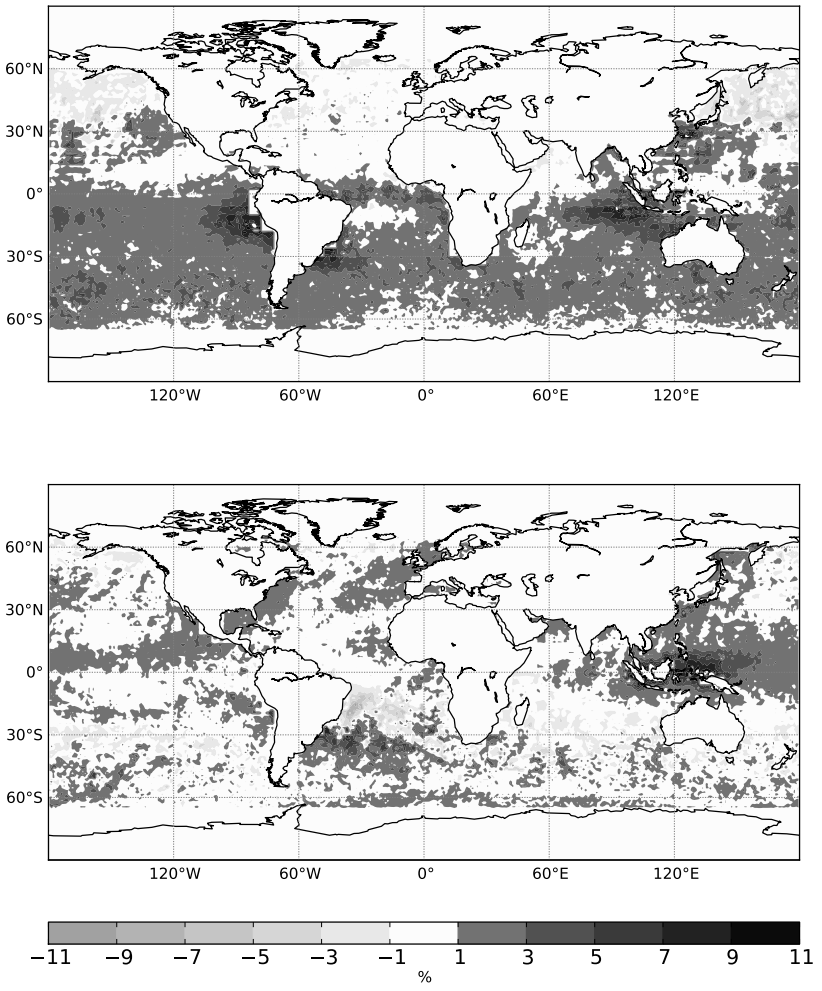

Figure 4.6: *Relative model column differences using the linearized averaging kernel Eq. (4.3) minus model columns using the log-normal averaging kernels Eq. (4.2) for March (top) and September (bottom) 2004.*

far, similar studies have ignored correlations between observations by rebinning the observations on larger spatial scales, e.g., the model resolution. Chevallier (2007) performed an Observing System Simulation Experiment (OSSE) for CO_2 using simulated OCO measurements binned to the 3°x2° model resolution. This study investigated the effect of different treatments for the observations on the inferred emissions. It turned out that the best results are obtained by inflation of the observation errors as an approximation to taking all correlations between observations into account. More recently,

Mukherjee et al. (2011) introduced the statistical CAR model to take care of observation correlations. The statistical model is described by a few parameters that are jointly optimized with the emissions in the inversion. In addition, this approach was capable to fill in missing observations. Although they showed this approach to be appealing, it was only applied in a so-called big-region approach (Stavrakou and Müller (2006)) in which the length of the state vector remains small. However, Mukherjee et al. (2011) state that this approach is scalable to larger state vectors typically used in 4D-Var systems.

Chevallier (2007) used an arbitrary error inflation factor of 2 in combination with observations that were binned to a 3°x2° model resolution. Would Chevallier (2007) have assimilated the observations on a 1°x1° resolution, the number of observations would have roughly scaled with a factor 6 and hence it is expected that the observational part of the cost function also increases by a factor 6. Therefore, since we assimilate the MOPITT columns on a 1°x1° resolution, we should reduce the cost function by inflation of the error by an additional factor of $\sqrt{6}$. Therefore, we initially used an inflation factor of $\sqrt{24}$, but this led to unrealistic emission estimates as the observations were overfitted (possibly due to the grid-scale emission error of 250%). We ultimately chose a rather large inflation factor of $\sqrt{50}$. With this choice we obtained an observational cost function value for the MOPITT dataset that was roughly twice the size of the corresponding cost function for the stations-only inversion. The rather large factor of $\sqrt{50}$ is justified by the fact that there are unknown correlations between the MOPITT observations. Moreover, in a future joint assimilation one needs to balance the observational costs of the individual datasets, otherwise the system may fit mainly the satellite observations and the fit with the stations might deteriorate significantly in the SH as reported in previous studies (e.g., Arellano et al. (2006); Kopacz et al. (2010); Fortems-Cheiney et al. (2011)).

4.2.4 Observations Used for Validation

The assimilation of CO observations leads to emission changes with respect to the prior emissions. Model simulations using the optimized emission estimates are compared to independent observations for validation. If the inversion yields a more realistic model state, the agreement with non-assimilated observations should improve from the prior to the posterior simulation. Below we describe the observations used for validation in this study.

4.2.4.1 Aircraft Observations

In addition to surface flasks, NOAA also samples flask data using aircraft. These observations are mainly over North America and below 8 km altitude. In this work we compare modeled CO mixing ratios to flask measurements at altitudes $>$ 2 km above the sites shown in Fig. 4.3 as red triangles.

The MOZAIC (Measurement of OZone, water vapour, carbon monoxide and nitrogen oxides by Airbus In-service airCraft) program produces in-situ measurements of CO during commercial flights (Nedelec et al., 2003). These flights are mainly over the NH from Europe to the US, Asia and the Middle East. The SH is poorly covered by these flights. We compare model CO with in-situ measurements at altitudes $>$ 2 km to validate our results above the polluted boundary layer. A large fraction of these data is sampled at aircraft cruise altitude (10-12 km). Hence, in the mid and high latitudes of the NH, these flights cross the stratosphere in which the model chemistry and also the vertical transport are less accurate. These measurements are therefore omitted from the comparison.

4.2.4.2 FTIR Total Column Observations

Several Fourier-Transform Infrared Spectrometer (FTIR) stations worldwide measure CO total columns from the ground. The data used in this paper is publicly available from the website of the Network for the Detection of Atmospheric Composition Change (NDACC: http://www.ndsc.ncep.noaa.gov/). We compare our modeled CO on the coarse model resolution (6°x4°) to column data taking into account the averaging kernels if available. Due to the small footprint of the FTIR measurements, the model will likely overestimate the observations in mountain regions as the model surface pressure will be larger and hence, the model column will be deeper compared to the FTIR column. For a fair comparison, the partial model column below the FTIR surface pressure is ignored.

4.3 Results and Discussion

4.3.1 Emission Increments and the Fit to the Observations

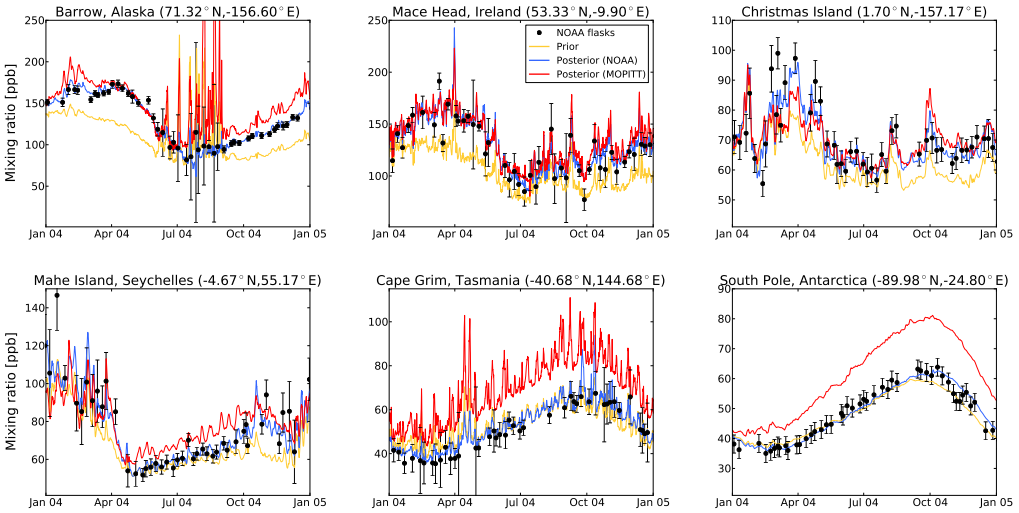

Figure 4.7: *Prior (yellow) and posterior (blue) simulation for 2004 sampled at 6 NOAA stations that were assimilated in the 4D-Var inversion stations-only. The red line represents the simulation using optimized emissions from the MOPITT-only inversion. Black dots represent the NOAA flask observations. Error bars denote the total observation error (including the model representativeness error). The comparison with additional stations is presented in the supplementary material, which is available in the online paper.*

We start this section with a comparison between simulated and observed CO mixing ratios for those observations that have been assimilated in the 4D-Var system. For NOAA surface network observations, Fig. 4.7 shows the prior (yellow line) and posterior simulation for the stations-only inversion (blue line) at 6 stations as well as the flask observations (black dots with computed 1σ observation errors). The red line shows the posterior simulation using MOPITT derived emissions and will be discussed in Sect. 4.3.3. For the NH stations (top row), the prior simulation underestimates the

observations whereas for the SH (bottom row), the prior simulation compares well with the NOAA surface observations. For the MOPITT inversion, the comparison with MOPITT total columns is shown in Fig. 4.8. Three-monthly composites of the difference between the model simulation and the observations are shown for the prior simulation (left column) and the posterior simulation (middle column). Dark grey colors indicate a model underestimate and light grey colors indicate a model overestimate compared to the MOPITT observations. The right most column shows the comparison for the posterior simulation using emissions derived from the stations-only inversion and will be discussed in Sect. 4.3.3. As for the NOAA stations, the prior simulation (Fig. 4.8, left column) underestimates the MOPITT observations in the NH. In contrast to the NOAA stations, however, in the SH the prior simulation also underestimates MOPITT total columns. This inconsistency in the SH for the prior simulation compared to the observations will result in different optimized emissions. Below the inferred emission estimates from the two inversions are discussed.

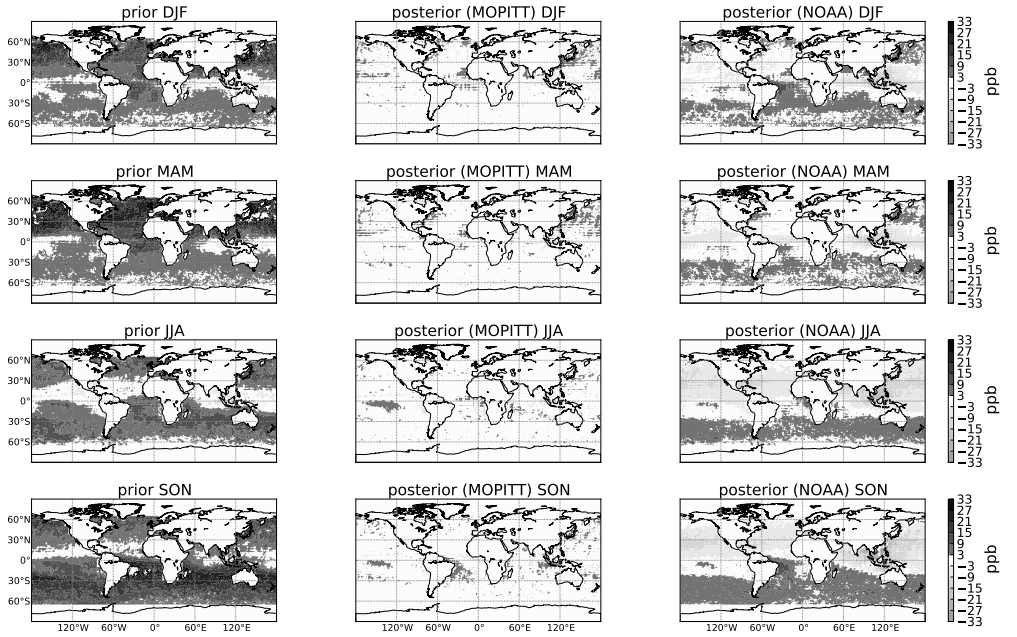

Figure 4.8: *Column-averaged CO mixing ratio differences MOPITT-TM5 with prior (left) and posterior (middle) emissions. We show 3 month composites per season. For the winter season (December - February) we used January, February and December 2004. Right panels: MOPITT-TM5 for the posterior simulation with emissions inferred from the stations-only inversion.*

Figure 4.9 shows the prior (dark grey) and posterior (light grey (NOAA) and black (MOPITT)) emissions for the three emission categories for the continents and the globe. The large global increment in anthropogenic emissions is mainly attributed to Asia and to a lesser extent to Europe and Africa. Both inversions yield significantly higher emissions for Asia than the new EDGARv4.1 inventory. Table 4.1 reports the emissions including the uncertainties as calculated from the posterior error covariance matrix. The anthropogenic source in Asia is increased by 191 Tg CO/yr and 210 Tg CO/yr, respectively for the stations-only and the MOPITT-only inversion. In addition, the uncertainty reduction for both inversions is large (65% and 70%) as the observations constrain the emissions in the

region well and because the uncertainty assigned to the prior emissions was large. However, the spatial correlation lengths of 1000 km may lead to some aggregation error and hence a slightly overestimated uncertainty reduction (Meirink et al., 2008b). The emission increment leads to an improved fit with the MOPITT observations (Fig. 4.8 second column). For Europe, optimized anthropogenic emissions are nearly a factor 2 higher than the prior estimates, indicating that EDGARv4.1 is also too low for Europe. The 50% uncertainty reduction for the stations-only inversion is larger than for the MOPITT-only inversion (20%), likely due to the three high-latitude European stations (Ocean Station M (STM), Pallas, Finland (PAL) and Ny-Alesund, Spitsbergen (ZEP)) that constrain the emissions well. This is further illustrated in Fig. 4.10 showing the grid-scale annual uncertainty reduction. Note that we only use MOPITT CO columns over the oceans between 65°S and 65°N, which typically lead to less uncertainty reduction for the NH continents. North American emissions remain close to the prior estimates, indicating that the inferred emissions are consistent with EDGARv4.1. In general, the NOAA surface observations and MOPITT total column observations result in comparable emission estimates in the NH.

Table 4.1: *Prior and posterior emission estimates per emission category, aggregated to continental-scale regions for the stations-only and the MOPITT-only inversions in Tg CO/yr.*

Source/Region	Prior	Posterior	
Anthropogenic		stations-only	MOPITT-only
Nam	80 ± 23	73 ± 19	90 ± 20
Europe	46 ± 30	93 ± 15	95 ± 24
Asia	222 ± 165	413 ± 58	432 ± 49
Sam	28 ± 25	12 ± 23	57 ± 21
Africa	56 ± 37	92 ± 35	144 ± 34
Oceania	27 ± 26	36 ± 19	-11 ± 17
NH	401 ± 175	681 ± 66	714 ± 61
SH	62 ± 37	43 ± 32	92 ± 29
Globe	**463 ± 180**	**724 ± 75**	**806 ± 69**
Natural + NMVOC			
Nam	69 ± 37	100 ± 24	70 ± 19
Europe	16 ± 15	28 ± 13	29 ± 14
Asia	101 ± 49	149 ± 45	81 ± 41
Sam	102 ± 76	116 ± 49	176 ± 24
Africa	102 ± 64	157 ± 46	178 ± 33
Oceania	62 ± 37	74 ± 19	108 ± 20
NH	303 ± 87	448 ± 62	299 ± 53
SH	212 ± 82	256 ± 51	434 ± 29
Globe	**515 ± 128**	**704 ± 78**	**733 ± 60**
Biomass burning			
Nam	33 ± 39	35 ± 9	42 ± 9
Europe	1 ± 1	1 ± 1	2 ± 1
Asia	38 ± 39	26 ± 20	36 ± 14
Sam	64 ± 56	105 ± 33	60 ± 15
Africa	145 ± 82	151 ± 52	128 ± 16
Oceania	51 ± 36	74 ± 19	32 ± 9
NH	144 ± 71	126 ± 42	148 ± 21
SH	191 ± 96	268 ± 43	157 ± 26
Globe	**334 ± 119**	**394 ± 60**	**304 ± 28**

When we compare the posterior emissions for the SH continents, a first difference between the inversions in the total emission increment is observed: The large prior model underestimate compared to MOPITT total columns in the SH (Fig. 4.8) results in higher posterior emissions compared to the stations-only inversion for South America (+60 Tg CO/yr) and Africa (+50 Tg CO/yr). However, the opposite is true for Oceania, where lower emissions are inferred (-55 Tg CO/yr) when assimilating

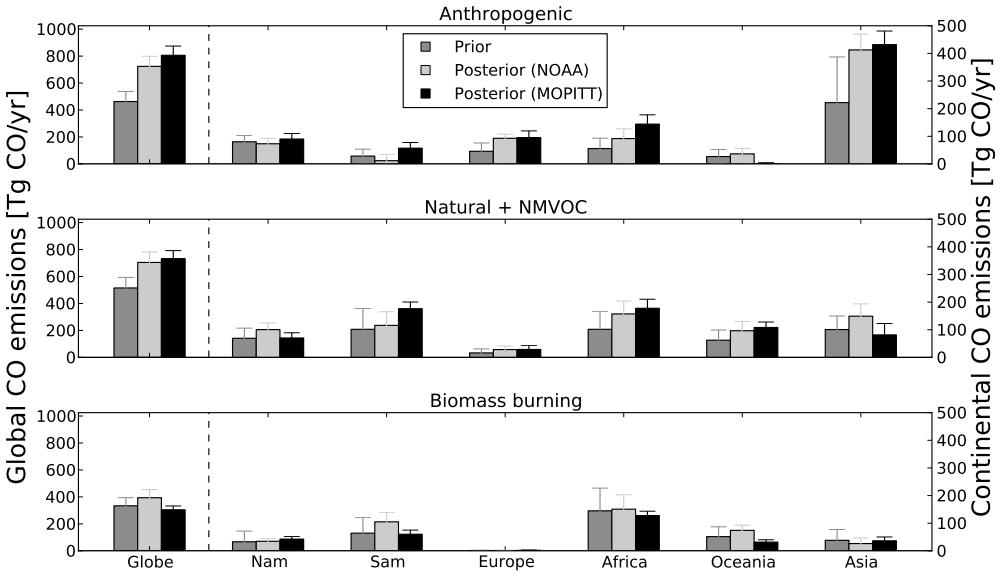

Figure 4.9: *Prior and posterior emission estimates for the three categories: anthropogenic (top), natural + NMVOC (middle) and biomass burning (bottom). Prior emissions are in dark grey, posterior emissions assimilating NOAA surface network observations are in light gray and posterior emissions assimilating MOPITT total column observations are in black. Note that the emissions on the global scale correspond to the axis on the left whereas the continental emissions correspond to the axis on the right. Error bars show the 1-σ uncertainty in the aggregated emissions, based on the approximated inverse Hessian. See text for details.*

MOPITT compared to the assimilation with NOAA stations. For the entire SH, the stations-only and MOPITT-only inversion yield 568 and 683 Tg CO/yr, respectively. Due to the 3-day global coverage of MOPITT, the uncertainty reduction for the SH continental regions is much larger compared to the stations-only inversion (Fig. 4.10). For example, African and South American biomass burning emissions show an uncertainty reduction of 80 and 73% respectively for the MOPITT-only inversion. The stations-only inversion results in an uncertainty reduction of 37 and 41% for those two regions, but this is likely due to the large prior errors we assigned to the emissions. In general, the MOPITT-only inversion constrains in particular the emissions in the Tropics, whereas the surface stations constrain the NH.

Furthermore, a remarkable shift from the biomass burning source to the natural source is observed (Table 4.1 and Fig. 4.9). For example, the stations-only inversion increases GFED3 biomass burning emissions for South America (+41 Tg CO/yr), Africa (+6 Tg CO/yr) and Oceania (+23 Tg CO/yr), whereas the MOPITT-only inversion decreases biomass burning emissions for these regions (-4 Tg CO/yr, -17 Tg CO/yr and -19 Tg CO/yr for South America, Africa and Oceania, respectively). However, the MOPITT-only inversion increases the natural source (mainly CO from NMVOC oxidation) significantly. For example, natural emissions are roughly doubled over South America, Africa and Oceania with respect to the prior, whereas the stations-only inversion shows much smaller increments

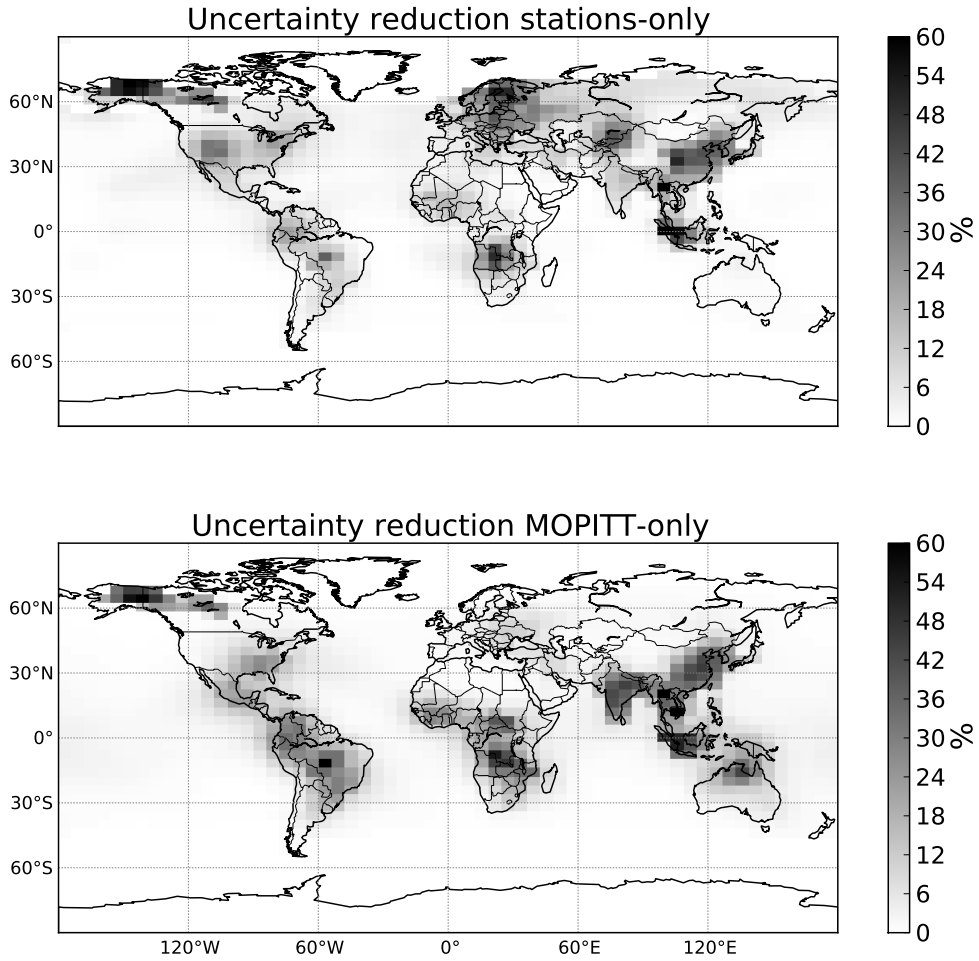

Figure 4.10: *Uncertainty reduction for the stations-only (top) and MOPITT-only (bottom) inversions. Uncertainty reduction is defined as* $100\% \left(1 - \frac{\sigma_a}{\sigma_b}\right)$*, where* σ_a *is the standard deviation of the posterior emission (aggregated over some time window and or spatial region) and* σ_b *is the standard deviation corresponding to the prior emissions. Here we show the uncertainty reduction for the total emissions (anthropogenic + natural + biomass burning) on the grid-scale, aggregated over the whole year 2004.*

for this source in these regions. The shift in emission increments from the biomass burning source to the natural source can be explained as follows: Due to the observations (from MOPITT or the NOAA surface network), the emissions over SH continents are required to increase. However, this

increment can be added to either of the three sources in a certain region. For the stations-only inversion, since there are almost no surface stations close to the source regions in the SH, it is cheapest in terms of costs in the cost function to increase the biomass burning emissions that stay much closer to the surface compared to the natural emissions and only take place in a specific part of the year (the dry season) and over relative small areas (compared to the natural emissions). These increased biomass burning emissions will be partly diluted and partly chemically removed in the atmosphere and thus only slightly enhance CO concentrations at the stations. The MOPITT instrument is more sensitive to the natural source than the biomass burning source, as the NMVOC-CO in the natural source is released higher up in the troposphere (see Fig. 4.1 a and d for the vertical distributions of biomass burning and the natural source, respectively). Also, since the natural emissions are specified in the prior throughout the year and over larger geographical areas compared to the biomass burning emissions, increasing this source results in a reduction of the prior mismatch between model and observations with minimal costs in the background part of the cost function. Moreover, increasing biomass burning as in the stations-only inversion does not improve the agreement with MOPITT columns (Fig 4.8, right column) as the model overestimates CO in the Tropics (in particular in Indonesia). We acknowledge that deficiencies in the vertical distribution of the natural emissions, i.e., a too high injection height may cause model data mismatches to be projected on the natural emissions, specifically for the MOPITT-only inversion.

In conclusion, the difference in vertical sensitivity of the two observational datasets (NOAA stations are mainly sensitive to boundary layer CO, whereas MOPITT is mainly sensitive to lofted CO), and the higher spatiotemporal resolution of the MOPITT observations and thus better global coverage leads to a shift in the partitioning of the emissions into different source categories. Furthermore, inconsistencies in the prior mismatch between model and observations lead to different emission increments for the MOPITT-only inversion compared to the stations-only inversion.

It should be noted here that the inverse modeling system can only optimize total CO emissions given a certain mismatch between model and observations. Hence, separation of different sources is only possible if realistic spatial and temporal information from prior inventories is supplied to the inversion system. In the current inversions the system has difficulties to separate the anthropogenic from the natural CO source. Aggregated to continental scales and an annual time scale, the derived posterior correlation coefficient ranges from -0.62 for South America to -0.88 for North America. The system is better capable to separate the biomass burning source from the anthropogenic source due to differences in the spatial patterns of the prior emissions. The posterior correlations are less than -0.2. Although in particular in the Tropics the spatial patterns of the biomass burning and natural CO emissions overlap, the specific timing of biomass burning in the dry season leads to posterior error correlations on yearly time scales of around -0.3.

4.3.2 Comparison with Recent Studies

Our emission estimates are compared with four recent global inversions, all for the year 2004 (or parts of that year). Jones et al. (2009) assimilated MOPITT V3 and TES (Tropospheric Emission Spectrometer) observations separately for November 2004 and we compare our results with their MOPITT-based emissions. Kopacz et al. (2010) assimilated observations from three satellite instruments (AIRS, MOPITT V3 and SCIAMACHY). However, the number of AIRS measurements used was three times higher compared to the number of MOPITT observations and even 36 times larger than the number of SCIAMACHY observations. Fortems-Cheiney et al. (2011) used MOPITT V4 (as in the current study) and Hooghiemstra et al. (2011) assimilated NOAA surface flasks. All satellite derived emissions in the literature studies used observations over land and ocean. The comparison is difficult due to differences in the inversion setup (e.g., definition of the state vector and error settings), the definition of the aggregation regions, the observations that have been assimilated, and

the atmospheric chemistry models used. In Table 4.2 we report the sum of the anthropogenic and biomass burning emissions. In addition, we give the global source of CO due to oxidation of NMVOCs and methane. Our North American (108 and 132 Tg CO/yr) and European (94 and 97 Tg CO/yr) emission estimates (for the stations-only and the MOPITT-only inversions, respectively) are in the low end of the range reported in the studies in Table 4.2. For Asia, our emission estimates are slightly lower compared to the other studies. Also in the SH, our emission estimates are somewhat lower compared to the other studies. For example, our South American emission estimates are 117 Tg CO/yr compared to previous emission estimates ranging from 141 to 184 Tg CO/yr. Similarly, for Africa, where our emission estimates of 243 and 272 Tg CO/yr are in particular lower compared to Kopacz et al. (2010) emission estimate of 343 Tg CO/yr.

Table 4.2: *Comparison of our derived total emissions (sum of anthropogenic and biomass burning emissions) using either NOAA stations or MOPITT observations with recent values from literature. All studies shown here performed an inversion for the year 2004 (or parts of that year). The global estimate of CO from oxidation of NMVOCs and methane and the total CO production for 2004 are also given. For studies that only reported an oxidation source of CO (from methane and NMVOCs), we report that number.*

Region	This study		Jones et al. (2009)	Kopacz et al. (2010)	Fortems-Cheiney et al. (2011)	Hooghiemstra et al. (2011)
	stations	MOPITT				
Nam	108 ± 21	132 ± 22	146	71	199	166
Europe	94 ± 15	97 ± 24	111	95	137	92
Asia	439 ± 56	468 ± 48	531	660	506	597
Sam	117 ± 37	117 ± 24	141	183	184	156
Africa	243 ± 62	272 ± 38	304	343	283	338
Oceania	110 ± 26	21 ± 19	185	-	117	-
Subtotal	**1118 ± 88**	**1110 ± 71**	**1417**	**1350**	**1441**	**1390**
NMVOC-CO	704 ± 78	733± 60	1344	1290	1176	410
CH_4-CO	865	865				887
Total	**2687**	**2708**	**2762**	**2642**	**2602**	**2646**

The main reason for these differences is likely our approach to 1) optimize the NMVOC-CO source on the model resolution and 2) use a vertical distribution which releases significant amounts of CO in the free troposphere. Some recent studies (Jones et al., 2009; Kopacz et al., 2010) optimized the CO production from oxidation of NMVOCs by a single parameter. But for these studies, posterior production terms for oxidation of methane and NMVOCs remained close to the prior terms, possibly due to too tight error settings on these sources. As a consequence of this approach, any prior mismatch between the model and observations will be projected on either the biomass burning emissions or the anthropogenic emissions. In our previous study (Hooghiemstra et al., 2011) we also used monthly global scaling parameter for NMVOC-CO and CH_4-CO sources. The relatively large differences in emissions estimates in the current study compared to the results in Hooghiemstra et al. (2011) is explained by 1) the aggregation of the NMVOC-CO source in a single parameter and 2) the compensation mechanism which is extensively described in (Hooghiemstra et al., 2011). In short, since the observations mainly constrain total emissions, an increase in one emission category may be compensated for by a decrease in another emission category. In the current setup, the natural emissions (see Table 4.1) increase in both inversions for all regions. This results in global natural emissions of 704 or 733 Tg CO/yr (for the stations-only and the MOPITT-only inversion, respectively). When we add the CH_4-CO-source, our total oxidation source of CO amounts to 1569 and 1598 Tg CO/yr (for the stations-only and the MOPITT-only inversions, respectively). This is in contrast with the study of Fortems-Cheiney et al. (2011), in which the posterior CO production through oxidation of formaldehyde was reduced compared to the prior (Fortems-Cheiney, personal

communication, 2011) and resulted in a total oxidation source of CO of 1176 Tg CO/yr. The main reason for this difference is likely our large prior grid-scale error of 250%. However, this error choice is justified because also the NMVOC-CO source strength is uncertain and more constraints on this emission category seem needed. Joint assimilation of formaldehyde and CO columns may lead to more accurate emission estimates particularly in the Tropics. Stavrakou et al. (2009a) for example, used space-based formaldehyde columns to infer isoprene emissions. Although their inversion results were close to the prior emission estimates on a global scale, large emission increments (up to 55%) were found regionally.

If we compare biomass burning emissions only, our optimized biomass burning emissions from the MOPITT-only inversion are not in agreement with recent studies. For example, Kopacz et al. (2010) and Liu et al. (2010) found that the GFED2 biomass burning inventory was too low by up to a factor 2. Here we started from the more recent GFED3 (van der Werf et al. (2010)) inventory that is even lower than GFED2 by about 70 Tg CO/yr globally and posterior biomass burning emission estimates are another 20 Tg CO/yr reduced (Table 4.1). Kopacz et al. (2010) inverted CO emissions using 3 satellite instruments, including MOPITT. They optimized the total CO surface emissions and attributed large corrections to the total prior emissions in the biomass burning season to deficiencies in the GFED2 product. However, Arellano et al. (2006) showed that both the anthropogenic source and the biomass burning source increased from the prior to the posterior estimate even during the biomass burning season. This indicates that not all increments in this period should be attributed to biomass burning emissions only. Moreover, the posterior simulation corresponding to the optimized emissions from the joint inversion were not in agreement with MOPITT V3 columns. This was shown to be caused by a not-corrected positive bias in the AIRS observations on the SH ($> 10\%$) in combination with the large weight of these observations. Liu et al. (2010) performed forward model simulations with two sets of meteorological data (GEOS-4 and GEOS-5) and compared the simulations with TES and MLS data. They showed that simulations with either bottom-up emission estimates or bottom-up emissions scaled using parameters derived by Kopacz et al. (2010) were not fully consistent with the observations in the Tropics. They concluded that apart from deficiencies in the emissions, meteorological fields and model transport may dominate model-data mismatches.

4.3.3 Validation of Posterior Emission Estimates with Independent Observations

As a first validation step, we used so-called cross validation of the inferred emissions to validate the two inversions. In this context, cross validation means that the posterior simulation using optimized emissions from either inversion are compared to the other observational dataset.

Cross validation of the MOPITT-only inversion with the NOAA stations is shown in Fig. 4.7 (red line). Generally good agreement on NH stations is found and the fit with the stations improves even though these observations are not assimilated. In particular for Europe (represented here by station Mace Head) the red line is really close to the posterior simulation corresponding to the stations-only inversion (blue line). For the high latitude NH (represented by station Barrow, Alaska) the agreement with the observations is in particular good in the first part of the year. Biomass burning emissions from the MOPITT-only inversion are significantly higher for this region (compared to the stations-only inversion: 42 Tg CO/yr versus 35 Tg CO/yr) and modeled CO mixing ratios are therefore higher than the observations in summer. However, for the SH, the MOPITT-only simulation largely overestimates the observed CO mixing ratios on the SH stations (Mahe Island, Seychelles (+10 ppb), Cape Grim, Tasmania (+20 ppb) and South Pole station (+20 ppb), see Fig. 4.7 (bottom row)), indicating an overestimation of SH emissions, probably due to some bias in the MOPITT observations.

Figure 4.8 (third column) shows the cross validation the other way around. A clear improvement from

prior to posterior simulation (for the stations-only inversion) in all seasons is observed on the NH, mainly due to increased anthropogenic emissions over Asia and Europe. For the SH, the stations-only simulation underestimates the MOPITT total columns south of 30°S in all seasons by about 5-8 ppb and overestimates CO columns in particular in Indonesia (Fig. 4.8, third column). From this validation it seems likely that MOPITT CO total columns have some positive bias in the SH south of 30°S.

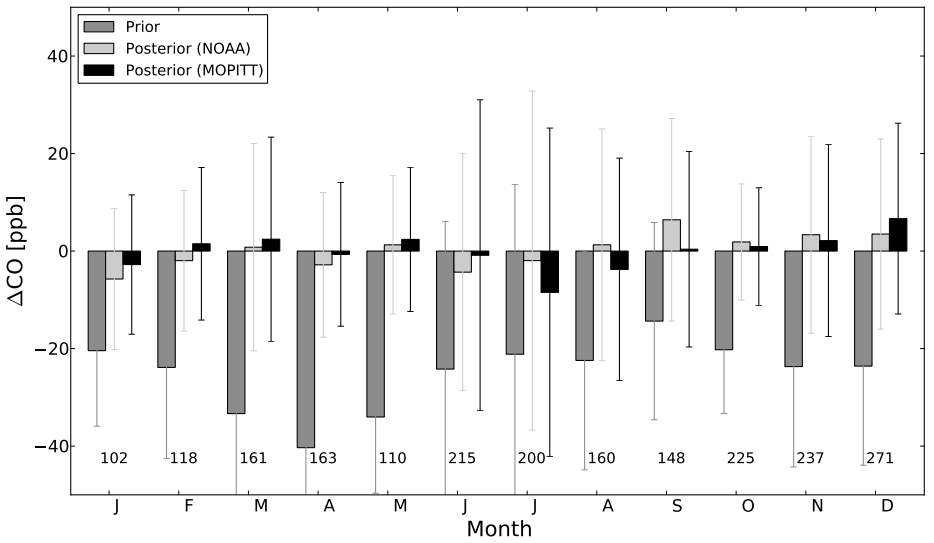

Figure 4.11: *Comparison of model with independent aircraft observations > 2 km from NOAA, mainly over North America. Per month, the mean difference (model - observation) is given for the prior simulation (dark grey), the posterior simulation using optimized emissions from an inversion assimilating NOAA surface network observations (light gray) and the posterior simulation using optimized emissions from an inversion assimilating MOPITT total column observations (black). Numbers represent the amount of observations we compared with per month. The error bars are defined as the standard deviation of the differences per month.*

A second validation is performed using aircraft data. Figure 4.11 shows monthly mean differences (modeled minus observed CO mixing ratio) for all NOAA aircraft flasks above 2 km altitude. The posterior simulation improves the comparison with NOAA aircraft observations compared to the prior simulation for both inversions in very similar ways: The prior underestimate ranging from 10-40 ppb per month is reduced to less than 10 ppb for all months in both inversions. This indicates that the model reproduces CO mixing ratios over North America very well up to 8 km. This agreement was also found by Deeter et al. (2010) who found no significant bias when comparing MOPITT V4 data with the NOAA aircraft data. This is in sharp contrast, however, with the validations of MOPITT V3 performed by Emmons et al. (2007, 2009). They reported a positive bias of 7±9% with respect to the NOAA aircraft data in 2004, but on the SH, a bias of +20% was reported. Figure. 4.12 shows the comparison for modeled and observed CO mixing ratios from the MOZAIC program. Above 10 km altitude, only measurements south of 40°N have been used to avoid stratospheric influence. Since there are almost no flights in the SH, such a cut-off was not necessary there. The majority

of the MOZAIC measurements is from flights between Europe and the US or between Europe and East Asia and the middle East. The measurements were averaged into 1 km bins from 2 to 12 km altitude and are shown as grey boxes in Fig. 4.12, the error bars denote the corresponding standard deviation of the observations. The co-sampled model prior simulation (circles) and the posterior model simulations corresponding to the the stations-only (stars) and MOPITT-only (diamonds) inversions are also shown. Throughout the troposphere, the prior model simulation underestimates observed CO by 10 to 30 ppb. The largest differences are found near the surface reflecting the too low prior emissions on the NH. The posterior simulations show an improved agreement and are typically within a few ppb in the lower troposphere (3-7 km). At higher altitudes ($>$ 7 km) the agreement between observations and the MOPITT-only inversion is much better than the agreement with the stations-only inversion due to the higher sensitivity of MOPITT at this altitude. At aircraft cruise altitudes (10-12 km) this tendency continues. The model prior and MOPITT posterior simulation remain quite close to the observations at these altitudes, but the stations-only simulation largely overestimates the observations. This is attributed to the natural emissions that are approximately 140 Tg CO/yr higher on the NH in the stations-only inversion compared to the MOPITT-only inversion (see Table 4.1) and are injected higher up in the troposphere. Clearly this is not in agreement with both MOPITT and aircraft observations. Unfortunately, no aircraft profiles are available south of 30°S, where the MOPITT bias appears to be most prominent.

Further validation with FTIR total column observations showed overall good agreement on the NH (Table 4.3): the prior underestimate of 16-20% (13-22 ppb) is significantly reduced for all FTIR stations due to increased emissions over the NH. Although both inversions slightly underestimate the FTIR total columns at Reunion Island, this is different for the other two FTIR sites in the SH (Table 4.3). For Lauder, New Zealand and Arrival Heights, Antarctica, the MOPITT-only inversion results in too high CO columns for both Lauder (+7% or 3.5 ppb) and Arrival Heights (+9% or 4.6 ppb). For the FTIR measurements made in Lauder, this was already shown by Yurganov et al. (2010) who performed a direct comparison between MOPITT and the FTIR observations. For these FTIR sites, the stations-only inversion tends to underestimate the FTIR CO columns by 9% (4.8 ppb) and 10% (4.9 ppb) for Lauder and Arrival Heights, respectively.

Table 4.3: *Comparison with independent FTIR observations for seven sites around the globe. Reported values are averaged annual modeled and observed column-averaged CO mixing ratios in ppb. Values between parentheses represent modeled columns when the averaging kernel was not taken into account. Note that for stations Lauder, New Zealand and Arrival Heights, Antarctica, no averaging kernels were available.*

Station	lat [°]	lon [°]	alt [m.a.s.l.]	Observed	Prior	Posterior (NOAA)	Posterior (MOPITT)
Kiruna, Sweden	67.84	20.41	419	104.8	82.6 (84.1)	107.1 (108.7)	108.0 (109.5)
Zugspitze, Germany	47.42	10.98	2964	82.4	69.0 (69.2)	88.4 (89.1)	84.0 (84.2)
Jungfraujoch, Switzerland	46.55	7.98	3580	86.7	73.6 (70.3)	92.3 (89.1)	88.7 (85.4)
Izaña, Tenerife, Spain	28.30	-16.48	2367	81.7	68.7 (69.1)	85.5 (86.0)	77.8 (78.1)
Reunion Island, France	-20.90	55.50	10	94.5	67.8 (64.4)	83.0 (79.7)	88.3 (84.9)
Lauder, New Zealand	-45.04	169.68	370	52.9	46.0	48.1	56.4
Arrival Heights, Antarctica	-77.82	166.65	250	51.5	43.1	46.4	56.1

4.4 Sensitivity Studies

Although it seems that the MOPITT-only inversion results in too high CO in the SH compared to other observations due to a positive bias in the MOPITT V4 product in the SH, model uncertainties

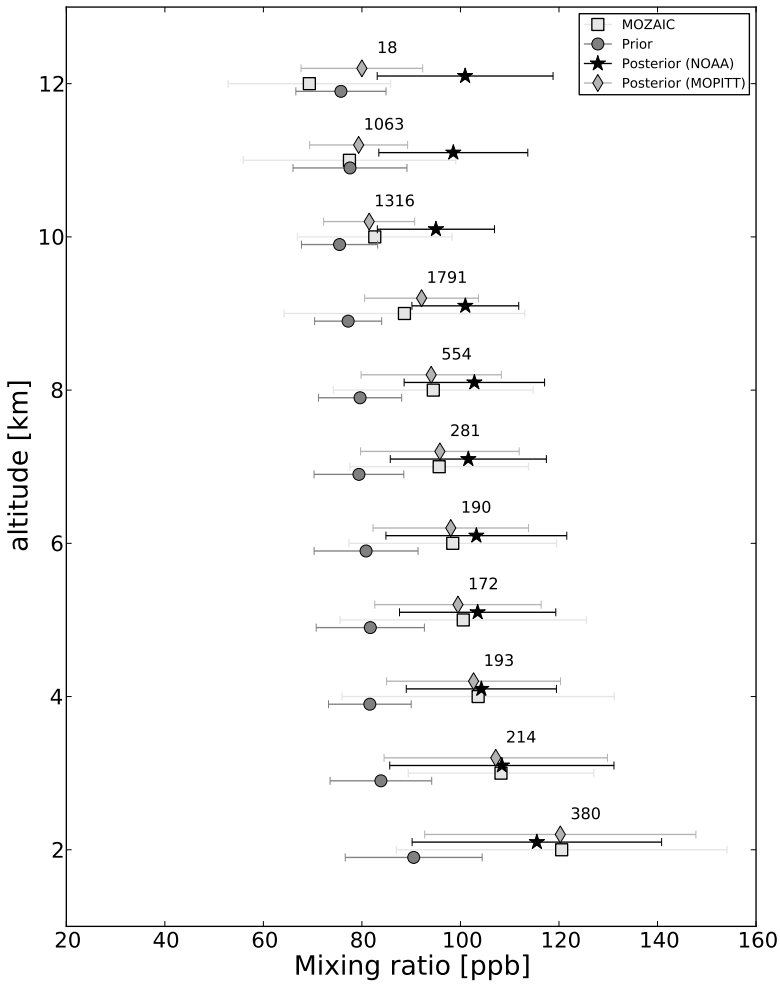

Figure 4.12: *Comparison of the model with MOZAIC in-situ aircraft data averaged per altitude level. Rectangular symbols represent the mean of all MOZAIC observations in the layer (of width 1 km) above the corresponding altitude. Model simulations are represented by circles (prior), stars (posterior NOAA) and diamond (posterior MOPITT) markers. The error bars indicate the standard deviations corresponding to the means. Numbers indicate the amount of observations used in this validation per layer. For altitudes above 10 km, only observations south of 40° N are used to minimize stratospheric sampling.*

may also play a role. For example, the climatological OH field used and the vertical distribution of biomass burning emissions can have large impacts on the inferred emissions as shown in Hooghiemstra et al. (2011). But also deficiencies in model transport and the effect of linearizing the MOPITT averaging kernels may influence the inferred emission estimates. Therefore, we present a series of sensitivity inversions to address these issues. For the stations-only inversion we performed three sensitivity simulations using (S1) a preduc factor of 50 and (S2) a preduc factor of 200 (instead of a preduc factor of 10^6) (S3) a different OH field from a full-chemistry simulation with TM5 (Huijnen et al. (2010)) and (S4) a different vertical distribution for biomass burning emissions (FVERT). The vertical distribution for this sensitivity inversion is shown in Fig. 4.1 b as a function of latitude and model level. This distribution is slightly different compared to the one we used in Hooghiemstra et al. (2011) (Fig. 4.1 c). The current choice combines the findings in reported literature that boreal forest fires inject CO at higher altitudes (Val Martin et al., 2009), whereas in the Tropics, biomass burning emissions from savannah fires remain largely below 3 km, but tropical forest fires in South East Asia and Indonesia also inject biomass burning CO in the free troposphere. In contrast, the vertical distribution in a sensitivity experiment in Hooghiemstra et al. (2011) followed the injection height derived by Gonzi and Palmer (2010) that also emitted biomass burning CO in the free troposphere in the Tropics.

For the MOPITT-only inversion we performed sensitivity studies (S5) and (S6) similar to studies S3 and S4 described above and in addition we assimilated (S7) all MOPITT observations (S8) all MOPITT observations with a different vertical distribution of biomass burning emissions (Fig. 4.1 b) and (S9) corrected for the linearization of the averaging kernel (CORRECTION). The correction is applied as follows: For the prior simulation we compute the tropospheric-mean mixing ratio using either Eq. (4.2) or Eq. (4.3) and archive the differences. In subsequent iterations, these differences are subtracted from the calculated modeled tropospheric-mean mixing ratios. To reduce the computational burden we used a preduc factor of 1000 for the sensitivity studies (except for S1 and S2). The sensitivity studies are detailed in Table 4.4. The results are summarized below and visualized in Fig. 4.13 and Table 4.5.

Table 4.4: *Details of the sensitivity studies described in Sect. 4.4. See text for details.*

Study	Data assimilated	OH field	preduc	FVERT	CORRECTION
S1	stations	Spivakovsky et al. (2000)	50	< 2 km	–
S2	stations	Spivakovsky et al. (2000)	200	< 2 km	–
S3	stations	Huijnen et al. (2010)	1000	< 2 km	–
S4	stations	Spivakovsky et al. (2000)	1000	$35\% > 2$ km	–
S5	MOPITT	Huijnen et al. (2010)	1000	< 2 km	No
S6	MOPITT	Spivakovsky et al. (2000)	1000	$35\% > 2$ km	No
S7	MOPITT	Spivakovsky et al. (2000)	1000	< 2 km	No
S8	MOPITT	Spivakovsky et al. (2000)	1000	< 2 km	No
S9	MOPITT	Spivakovsky et al. (2000)	1000	< 2 km	Yes

1. A preduc factor of 50 or 200 (S1 and S2) does influence the posterior emission estimates compared to a fully converged optimization with a preduc factor of 10^6. Although on the global scale the effects are rather small, on a continental scale difference range from 10-40%. However, these differences in optimized emissions are in a similar range as the effect of a different OH field and to a lesser extend, the correction for the linearization of the averaging kernel (see below). Moreover, the comparison with independent observations does not improve from preduc 50 to preduc 10^6. Still, we find a preduc factor of 10^6 useful since for smaller preduc values, derived posterior emission uncertainties haven not yet converged and remain larger compared to a fully converged inversion (Meirink et al., 2008b). In addition, since the small scale emissions are

optimized only in these later iterations, a large preduc value is typically necessary to infer CO emissions on a higher spatial resolution (in combination with a spatial correlation length < 1000 km).

2. A different OH field (S3 and S5) has a large effect. As outlined in Hooghiemstra et al. (2011), the TM5-based OH field has a larger North-South ratio (1.15) compared to the OH field from Spivakovsky et al. (2000) used in the base inversion (North-South ratio of 1.0) and thus results in higher inferred emissions on the NH and lower emissions on the SH. Magnitudes are similar to what was reported in Hooghiemstra et al. (2011).
3. With a different distribution of biomass burning emissions, one would expect more emissions in the stations-only inversion (S4), as these emissions are lofted and not picked up by the stations, and lower emissions for the MOPITT-only inversion (S6), as the emissions are more easily observed by the instrument. However, the sensitivity to this distribution appears to be only small. This is in contrast with our previous study (Hooghiemstra et al. (2011)), where the difference was as large as 70 Tg CO/yr. This is likely due to the new implementation of the NMVOC-CO source, but the lower injection height in the Tropics compared to Hooghiemstra et al. (2011) might also play a role. For the MOPITT-only inversion the sensitivity to a different biomass burning injection height is negligible. This is explained by comparing the vertical distribution to the distribution for the NMVOC-CO source (Fig. 4.1 b and d). Since the NMVOC-CO emissions are injected much higher, the MOPITT-only inversion is mainly sensitive to this source and less sensitive to biomass burning injection heights.
4. Including MOPITT land observations (S7 and S8) makes a minor difference except for Africa and Asia. Due to the absence of CO sources in the prior over the Sahara desert where the large mismatch is found, natural emissions increase heavily in Africa. As a compensating result, this source decreases for Asia. Since the emissions from the inversion including MOPITT land observations deviate more from the stations-only inferred emissions, this points to a positive bias of MOPITT over desert areas.
5. Correcting for the linearization of the averaging kernel (S9) results in higher anthropogenic emissions (in Asia and Africa) and somewhat lower natural emissions (including NMVOC-CO). In addition, the biomass burning emissions slightly increase from 311 Tg CO/yr in the base inversion to 335 Tg CO/yr. On both global and continental scales, however, the differences are generally within the error bounds of the base MOPITT inversion.

Table 4.5: *Global emission estimates per emission category for 2004 for 9 sensitivities studies. The results of the base inversions are also included.*

Stations-only			S1	S2	S3	S4	
	Prior	Posterior (base)	preduc (50)	preduc (200)	OH	FVERT	
ANT	463± 180	724± 75	778± 107	747± 92	796± 89	756± 87	
NAT	515± 128	704± 78	667± 108	689± 105	630± 90	688± 91	
BB	334± 119	394± 60	416± 100	391± 95	353± 67	386± 69	
Total	1312± 251	1822± 45	1860± 115	1827± 73	1779± 57	1831± 64	
MOPITT-only			S5	S6	S7	S8	S9
	Prior	Posterior (base)	OH	FVERT	ALL	ALL-FVERT	CORRECTION
ANT	463± 180	806± 69	702± 73	742± 75	761± 75	758± 73	805± 74
NAT	515± 128	733± 60	791± 67	784± 70	829± 66	804± 66	734± 67
BB	334± 119	304± 28	265± 39	307± 42	282± 40	304± 35	335± 38
Total	1312± 251	1843± 12	1758± 14	1834± 16	1873± 11	1868± 10	1874± 16

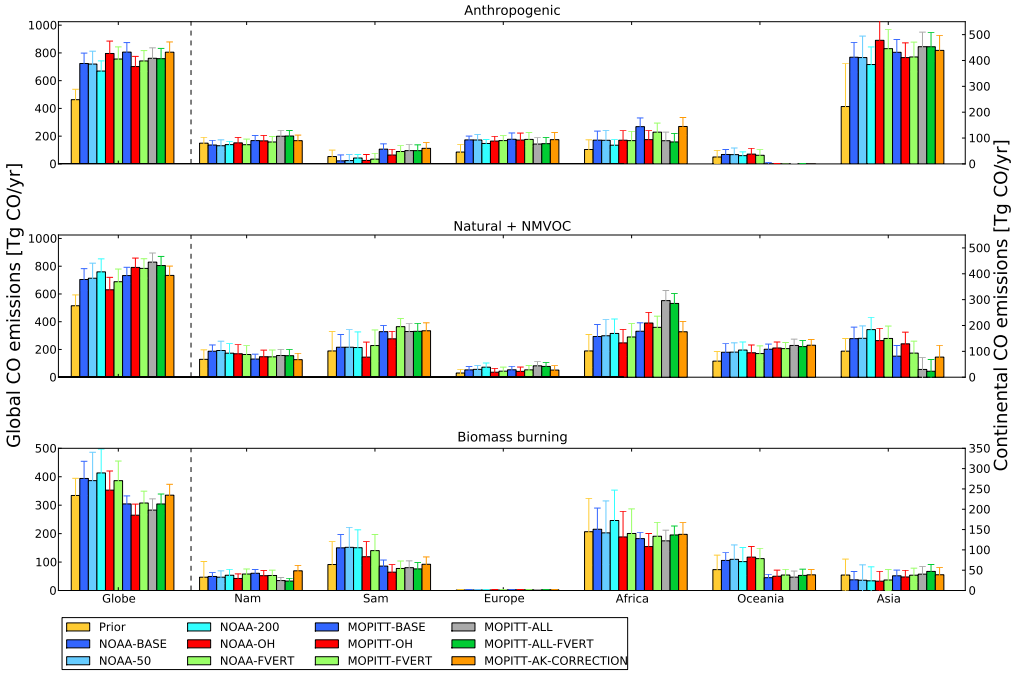

Figure 4.13: *Idem to Fig. 4.9 but for a series of sensitivity experiments. The bars corresponding to the base inversions (stations-only and MOPITT-only) are also given (in dark blue). Note that the global annual emission estimates are specified on the left axis. Error bars show the 1-σ uncertainty in the aggregated emissions, based on the approximated inverse Hessian. See text for details.*

Despite regional differences, the results of the sensitivity inversions are largely within error bounds of the base inversions on continental and regional scales for the individual emission categories. However, since the system has difficulties separating the different source categories, the inversion finds negative posterior correlations between the categories which lead to much smaller posterior uncertainties for the total CO source compared to the individual categories (Hooghiemstra et al., 2011). Our reported total CO emissions for the sensitivity studies (Table 4.5) vary typically more than the calculated posterior error for the base inversion. This posterior error (12 Tg CO/yr for the MOPITT-only base inversion) becomes small because it is the result of a total global source that has to compensate the global total sink (OH and surface deposition) such that a set of observations is optimally fitted. The sensitivity studies show that the global total emissions are typically estimated within 10%. Hence, the true error is probably larger than the approximation we calculate and depends on the OH sink, the vertical distribution of the emissions and on the set of measurements used in the inversion. Additional model errors may also play a role (e.g., transport). A first attempt to quantify systematic model errors was made by Jiang et al. (2011). They also found that model transport, the OH field and the treatment of the NMVOC-CO source yield differences in inferred emission estimates up to 20%. Nonetheless, we think that the approximation of the posterior uncertainties as presented here are valuable in assessing the information content of the assimilated observations.

4.5 Summary and Conclusions

CO emission estimates have been derived using a 4D-Var framework and utilizing two different observational datasets: surface observations from the NOAA network and total columns from the MOPITT instrument on board NASA's Terra satellite. We have discussed and validated the optimized emission estimates and compared them to values reported in the recent literature. The main conclusions are:

1. Optimized emissions using either dataset show a global increase of CO emissions from the prior to the posterior estimate of 500 Tg CO/yr. Our estimates for total annual CO emissions from the anthropogenic, biomass burning and natural sources (excluding the oxidation of methane) amount to 1822 ± 45 and 1843 ± 12 Tg CO in 2004 for the stations-only and the MOPITT-only inversions, respectively. The regions to which this increment is attributed are East Asia, South America, Europe and Africa. Our results suggest that the EDGARv4.1 bottom up inventories for East Asia and Europe could be too low by up to a factor 2. In South America and Africa, in particular CO production from oxidation of NMVOC-CO is increased when only MOPITT total columns are assimilated, whereas biomass burning emissions are increased when assimilating only NOAA surface observations.
2. Applying the 4D-Var analysis to CO emission estimates reduces the prior uncertainty for the different source categories significantly. With MOPITT's higher spatiotemporal resolution and better coverage in the Tropics and in the SH compared to the NOAA surface stations, the MOPITT derived emissions show larger uncertainty reductions over the tropical regions. However, due to the high density of NOAA stations on the NH, the high precision of these measurements and the fact that we do not assimilate MOPITT land pixels, uncertainty reduction in the NH midlatitudes is typically largest for the stations-only inversion.
3. A detailed comparison of the stations-only and the MOPITT-only inversions shows that in particular the partitioning of the SH sources is different. The difference in optimized biomass burning (or natural) emissions between the stations-only and the MOPITT-only inversions is attributed to the different vertical sensitivity of these observational datasets. Due to the faster vertical mixing in the Tropics, Tropical NOAA stations are quite insensitive to CO emissions and hardly constrain emissions that are released higher up in the atmosphere. In contrast, MOPITT columns are sensitive to free tropospheric CO and attributes model data mismatches mostly to the natural source. However, also the much higher spatiotemporal resolution of the MOPITT observations, and thus the better global coverage compared to the NOAA observations, plays a role.
4. We showed that by optimizing the NMVOC CO source on the model resolution, the biomass burning source in the MOPITT-only inversion was no longer increased, as opposed to some recent studies that found that the GFED2 inventory underestimated biomass burning emissions. Our approach reduces the risk that all mismatches between the prior model simulation and the observations is projected onto the biomass burning source in the Tropics.
5. The posterior emission estimates have been validated with aircraft observations from NOAA (observations up to 8 km) and showed large improvement with respect to the prior comparison for both inversions. The comparison with MOZAIC aircraft observations also improved in the lower troposphere. However, higher up in the troposphere (above 8 km), in particular the stations-only posterior simulation diverged from the observations, whereas the MOPITT-only posterior simulation remained close to the observations. Additional comparisons with FTIR total column measurements improved particularly for the NH sites.
6. Validation in the SH is limited by the amount of independent data available. A cross validation showed that MOPITT-only derived emissions yield too high CO mixing ratios on the SH stations Cape Grim (+20 ppb) and South Pole (+20 ppb). Validation with FTIR total columns at

Lauder, New Zealand and Arrival Heights, Antarctica also hint towards a small but significant positive bias in MOPITT. It should be kept in mind however, that model uncertainties such as model transport and the OH climatology used as well as the linearized MOPITT averaging kernels may introduce biases in the optimized emission estimates. However, the inferred emission estimates of sensitivity studies aggregated to continental and global scales are within the error bounds from the base inversions.

With the results presented in this paper it seems an obvious next step to combine surface observations with satellite retrievals to estimate surface sources of CO. In the NH, both datasets seem to be broadly consistent. However, on the high latitude SH and Indonesia, large differences in inferred emission estimates using the two datasets are apparent. Similar to the station - SCIAMACHY inversion performed for methane (Meirink et al., 2008a; Bergamaschi et al., 2009, 2010), a bias correction scheme seems to be necessary to obtain accurate and realistic emission estimates that are in agreement with both datasets and independent observations. Furthermore, extra constraints in the form of formaldehyde columns could serve to better constrain the NMVOC-CO source. Also, higher spatial model resolution should lead to smaller model representativeness errors.

4.6 Appendix A: Derivation of $\tilde{\mathbf{A}}$

To properly compare a model profile to a MOPITT retrieved profile, one has to use the averaging kernel as described in Deeter (2009). This averaging kernel is modeled in terms of a log-normal distribution and hence one typically computes:

$$\ln(\mathbf{x}_i^{ps}) = \ln(\mathbf{x}_i^a) + \sum_{j=1}^{n} \mathbf{A}_{ij}(\ln(\mathbf{x}_j^m) - \ln(\mathbf{x}_j^a)), \tag{4.6}$$

where $\mathbf{x}^{ps}$ is the model profile smoothed with the MOPITT averaging kernel $\mathbf{A}$ and a priori profile $\mathbf{x}^a$ and $\mathbf{x}^m$ is the original profile interpolated to the MOPITT pressure grid and n is the number of pressure levels. Rewriting this to avoid the logarithms yields:

$$\mathbf{x}_i^{ps} = \mathbf{x}_i^a \cdot \prod_{j=1}^{n} \left(\frac{\mathbf{x}_j^m}{\mathbf{x}_j^a} \right)^{\mathbf{A}_{ij}}. \tag{4.7}$$

For a Gaussian distributed averaging kernel ($\mathbf{K}$) Eq (4.6) would read

$$\mathbf{x}_i^{ps} = \mathbf{x}_i^a + \sum_{j=1}^{n} \mathbf{K}_{ij}(\mathbf{x}_j^m - \mathbf{x}_j^a), \tag{4.8}$$

from which it follows that

$$\mathbf{K}_{ij} = \frac{d\mathbf{x}_i^{ps}}{d\mathbf{x}_j^m} \tag{4.9}$$

Now, taking the derivative of Eq (4.7) to $\mathbf{x}_j^m$ yields

$$\frac{d\mathbf{x}_i^{ps}}{d\mathbf{x}_j^m} = \frac{\mathbf{A}_{ij}}{\mathbf{x}_j^m}\mathbf{x}_i^{ps}, \tag{4.10}$$

hence, if we define

$$\tilde{\mathbf{A}}_{ij} = \frac{\mathbf{A}_{ij}}{\mathbf{x}_j^m}\mathbf{x}_i^{ps} \tag{4.11}$$

it is consistent with $\mathbf{K}_{ij}$ to first order. However, since both $\mathbf{x}_j^m$ and $\mathbf{x}_i^{ps}$ depend on the model simulation, they change every iteration when the emissions are perturbed during the iterative optimization. To avoid this and to obtain a formula for the averaging kernel that is constant during the iterative process, we approximate those terms by values given by MOPITT. Naturally, $\mathbf{x}_j^m$ is approximated by the MOPITT prior $\mathbf{x}_j^a$ and $\mathbf{x}_i^{ps}$ is approximated by the MOPITT retrieval $\mathbf{x}_i^{\text{retr}}$:

$$\tilde{\mathbf{A}}_{ij} = \frac{\mathbf{A}_{ij}}{\mathbf{x}_j^a}\mathbf{x}_i^{retr}. \tag{4.12}$$

It has been tested that this approximation yields mean model total column CO values that are on average within 2% of the columns using the non-linear formulation. Regionally, larger differences up to 10% are observed.

CHAPTER 5

Interannual variability of carbon monoxide emission estimates over South America from 2006 to 2010

We present the first inverse modeling study to estimate CO emissions constrained by both surface and satellite observations. Our 4D-Var system assimilates National Oceanic and Atmospheric Administration Earth System Research Laboratory (NOAA/ESRL) Global Monitoring Division (GMD) surface and Measurements Of Pollution In The Troposphere (MOPITT) satellite observations jointly by fitting a bias correction scheme. This approach leads to the identification of a positive bias of maximum 5 ppb in MOPITT column-averaged CO mixing ratios in the remote Southern Hemisphere (SH). The 4D-Var system is used to estimate CO emissions over South America in the period 2006-2010 and to analyze the interannual variability (IAV) of these emissions.

We infer robust, high spatial resolution CO emission estimates that show slightly smaller IAV due to fires compared to the Global Fire Emissions Database (GFED3) prior emissions. Inferred dry season (August and September) biomass burning emission estimates amount to 60, 92, 42, 16 and 88 Tg CO/yr for 2006 to 2010, respectively. Moreover, CO emissions probably associated with pre-harvest burning of sugar cane plantations are underestimated in current inventories by 50-100%.

We conclude that climatic conditions (such as the widespread drought in 2010) seem the most likely cause for the IAV in biomass burning CO emissions. However, socio-economic factors (such as the growing global demand for soy, beef and sugar cane ethanol) and associated deforestation fires, are also likely as drivers for the IAV of CO emissions, but are difficult to link directly to CO emissions[1].

[1]This chapter is in preparation for submission to the Journal of Geophysical Research.

5.1 Introduction

The Amazon is the largest tropical rainforest region in the world and hosts a large diversity of flora and fauna (Sala et al., 2000). Intact forests are suggested to be a net carbon sink (Malhi et al., 2008) and appear much more resilient to drought conditions than damaged forests. The Amazon region is also important for the local hydrological cycle, since 25 to 50% of rainfall water is recycled by the forest (Eltahir and Bras, 1994). However, large parts of the forest are currently at risk due to climate change and land-use changes. Tropical forest clearing is often associated with biomass burning leading to higher greenhouse gas emissions (Hoffmann et al., 2002; Malhi et al., 2008). Furthermore, it may have important consequences for 1) the regulation of regional (Nobre et al., 1991) and global climate (Shukla et al., 2000; Bala et al., 2007), 2) biogeochemical cycles (Houghton, 2006) and 3) maintenance of soil fertility (Davidson et al., 2007).

Before the 1960's, access to the Amazon forest was restricted (Kirby et al., 2006). However, with the pavement of the first highways through the forest to connect the northwestern states to the rest of Brazil, colonization of the region began (Fearnside, 2005). Large-scale deforestation began in the early 1970's. Currently deforestation mainly takes place in the arc-of-deforestation along the southern and eastern borders of the Amazon (Morton et al., 2006). Intact forest is cleared and converted to agricultural lands for cattle grazing or crop production.

Deforestation and climate change are interlinked: For example, removal of 30 to 40% of the forest may lead to a significantly drier climate, in which parts of the eastern Amazon forest are turned into savannas and a dry desert emerges in the dry Northeast of Brazil (Oyama and Nobre, 2003). A drier climate would be disastrous for the densely populated state of São Paulo, in which water deficits could have large effects on agriculture, forestry and hydroelectric production (Dufek and Ambrizzi, 2007).

Historically, the main post-deforestation land-use is cattle ranching (70%) (Fearnside, 2005). In the last decades, land-use changes from forest to pastures or croplands, or from pastures to croplands increased heavily due to enhanced agricultural practices (Morton et al., 2006). Currently, 55% of Brazil is still covered by forest, 35% is used as pasture lands for ranching and only 7% for agriculture (soy and corn using half of this) (Rovere et al., 2011).

Another potential thread to the Amazon is the expansion of sugar cane plantations. With the launch of the Brazilian Alcohol Program in 1975 to produce biofuels from sugar cane to decrease the Brazilian dependence on fossil fuels, large sugar cane plantations have emerged, concentrated in São Paulo state. Since then, the yield of ethanol production from sugar cane has increased and becomes cost effective when the oil price exceeds US$ 30 per barrel (a level that was reached in the year 2000) (Rovere et al., 2011). Nowadays, sugar cane ethanol is used as a fuel (in combination with gasoline in so-called flex-fuel cars) in Brazil and this country is also the largest exporter of sugar cane ethanol in the world. Global demands for sugar cane ethanol are expected to rise enormously in the coming decades to meet lower carbon dioxide (CO_2) emissions (Rovere et al., 2011; Walter et al., 2011; Cardoso et al., 2012). However, this higher demand calls for more agricultural land and hence, expansion of sugar cane plantations might lead to additional deforestation.

Fire is the main clearing tool in the deforestation process: in the states of Mato Grosso and Pará in Brazil, highly mechanized land clearing is done by large landholders (van der Werf et al., 2009). The remaining biomass is piled up and ignited multiple times until the biomass is completely burned and large plantations can be started up.

The biomass burning fires emit large amounts of carbon in the form of CO_2, carbon monoxide (CO) and other gases and aerosols into the atmosphere. Enhanced trace gas concentrations can be observed by space-borne satellite instruments. Large interannual variability (IAV) in aerosol loading

has been identified by Torres et al. (2010) for the last decade. Torres et al. (2010) found that the high aerosol loads correlated well with fire counts and were inversely related to precipitation. The link between fire activity and precipitation was also found by Aragão et al. (2008), who also reported the peak deforestation month to be 3 months before the peak fire month. Interannual variability in SCIAMACHY (SCanning Imaging Absorption spectroMeter for Atmospheric CartograpHY) CO was reported by Gloudemans et al. (2009) for the period 2003-2007. The years 2004, 2005 and 2007 showed the largest CO columns, likely associated with enhanced biomass burning emissions compared to the years 2003 and 2006.

The IAV in carbon emissions from biomass burning have been estimated by van der Werf et al. (2010) for the period 1997 to 2009. Estimates of emission factors were used to convert carbon emissions to trace gas emissions for CO, CO_2 and other gases. This database was released as the Global Fire Emission Database (GFED) version 3 inventory. Some recent studies reported that the previous GFED2 product was too low over South America. For example, Kopacz et al. (2010) used an inverse modeling approach and found that GFED2 was too low over South America by 50-100% for 2004. In contrast, (Hooghiemstra et al. (2012), accepted by JGR), found that GFED3 (already lower than GFED2) was slightly too high to fit MOPITT observations in 2004 over this region. Hence, the uncertainty in the bottom-up biomass burning inventory remains large and a reliable top-down method to quantify the emissions is needed. CO is a perfect tracer of these pyrogenic emissions due to its relatively long lifetime in comparison with volatile organic compounds and aerosols emitted during fires and its short lifetime relative to CO_2 and methane. With a lifetime of approximately two months, CO can be traced as it travels between continents (Gloudemans et al., 2006; Edwards et al., 2006a).

Earlier inverse modeling studies focussing on CO used only surface observations (mainly from the NOAA network) to constrain the emissions (Bergamaschi et al., 2000; Kasibhatla et al., 2002; Pétron et al., 2002; Pison et al., 2009; Hooghiemstra et al., 2011). These measurements are performed with high accuracy and precision and the measurement time series goes back to the early 1990's (Novelli et al., 1998, 2003). However, the location of the surface stations is biased towards the Northern Hemisphere (NH). There are a few stations in the remote Southern Hemisphere (SH), and particularly the Tropics are poorly constrained by these observations. Moreover, the temporal resolution of the NOAA flask observations is typically weekly and hence these observations might miss short term pollution events. Most recent inverse modeling studies therefore use satellite derived CO columns (e.g., Arellano et al. (2004); Pétron et al. (2004); Arellano et al. (2006); Stavrakou and Müller (2006); Chevallier et al. (2009); Jones et al. (2009); Kopacz et al. (2009, 2010); Fortems-Cheiney et al. (2011)). Satellite observations have the great benefit that they provide global coverage, typically within a couple of days. Hence the much greater spatial and temporal resolution of these observations over the Tropics and the SH can be used to constrain emissions better in these regions. However, thermal infrared (TIR) sounders such as MOPITT, the Atmospheric Infrared Sounder (AIRS), the Tropospheric Emission Spectrometer (TES) and the Infrared Atmospheric Sounding Interferometer (IASI), are mainly sensitive to free tropospheric CO and have poor sensitivity towards the surface where the emissions are released. Moreover, satellite derived CO column measurements come with substantial uncertainties and biases. As a result, a biased (satellite) observation may result in artificial emission increments in an inverse modeling exercise. For example, CO emissions as derived in current satellite-driven inverse modeling studies, show large discrepancies in the remote SH compared to NOAA surface flask observations (Arellano et al., 2006; Kopacz et al., 2010; Fortems-Cheiney et al., 2011; Hooghiemstra et al., 2012). Ideally, one would like to use the surface observations to anchor the inversion and the satellite observations to constrain CO emissions on high resolution.

The goal of this study is to infer robust monthly total CO emission estimates for South America at a high spatial resolution of 1°x1° for the period 2006-2010. These years are in particular interesting because the Amazonian drought of 2010 (Lewis et al., 2011) is included in this time window and

because deforestation rates have decreased. Moreover, we present the first study in which surface and satellite observations of CO are jointly assimilated in a four-dimensional variational (4D-Var) data assimilation system to optimally constrain the CO emissions. To accomplish this, a bias correction scheme had to be implemented.

The outline of this study is as follows: Sect. 5.2 describes the inversion methodology, the atmospheric chemistry and transport model TM5, the observations and the bias correction scheme. In Sect. 5.3 we describe our main results for the 2006-2010 optimized emissions over South America, which are further discussed in Sect 5.4. We conclude our findings in Sect. 5.5.

5.2 Inverse Modeling

The 4D-Var approach starts with the definition of the cost function $\mathcal{J}(\mathbf{x})$ (Eq. 5.1) to be minimized.

$$\begin{aligned} \hat{\mathbf{x}} &= \min \arg \mathcal{J}, \\ \mathcal{J}(\mathbf{x}) &= \frac{1}{2}(\mathbf{x}-\mathbf{x}_b)^\top \mathbf{B}^{-1}(\mathbf{x}-\mathbf{x}_b) + \frac{1}{2}\sum_{i=1}^{M}(H(\mathbf{x})_i - \mathbf{y}_i)^\top \mathbf{R}_i^{-1}(H(\mathbf{x})_i - \mathbf{y}_i), \end{aligned} \tag{5.1}$$

where $\hat{\mathbf{x}}$ is the optimal state vector that, when simulated by the model H, fits the measurements $\mathbf{y}_i$ (with observation error covariance matrix $\mathbf{R}_i$) while staying close to the prior state $\mathbf{x}_b$ (with prior error covariance matrix $\mathbf{B}$). M is the number of measurements and $\top$ the transpose operator. The cost function is minimized iteratively using the CONGRAD method (Fisher and Courtier, 1995), which is based on the conjugate gradient method (Hestenes and Stiefel, 1952) and the Lanczos algorithm (Lanczos, 1950). This algorithm is capable to produce the optimal posterior state as well as an estimate of the posterior error covariance matrix. As in our previous study, we use the TM5-4D-Var system for CO (Hooghiemstra et al., 2012). The main changes applied to the system for this study are described below.

5.2.1 TM5 model

The atmospheric chemistry and transport model TM5 (Krol et al., 2005) and its adjoint (Meirink et al., 2008b) are used to simulate CO mixing ratios given a set of emissions and calculating the sensitivity of the emissions to a set of model-data mismatches, respectively. In this study, the parallelized version of TM5 has been used which heavily reduced the runtime of the model (by a factor 4 with respect to our previous work). Model transport is driven by 3-hourly meteorological fields (6-hourly for 3-D fields) from the European Centre for Medium-Range Weather Forecasts (ECMWF). Here, the ERA-Interim meteorological fields have been used, on a subset of 25 of the originally 60 hybrid ECMWF layers. The TM5-4D-Var system uses a climatological OH field (Spivakovsky et al., 2000) which is scaled by a factor 0.92. This factor is based on methylchloroform simulations for the period 2000-2006 (Huijnen et al., 2010). Although a coarse global model resolution (6°x4°) is used, the nested zoom capability of TM5 is exploited over South America. Via an intermediate zoom region with a resolution of 3°x2°, the model resolution is refined to 1°x1° over a part of South America. The zoom region covers the Amazon forest and is bounded by the coordinates (30°S, 78°W) in the lower left corner and by (10°N, 36°W) in the upper right corner (see Fig. 5.1).

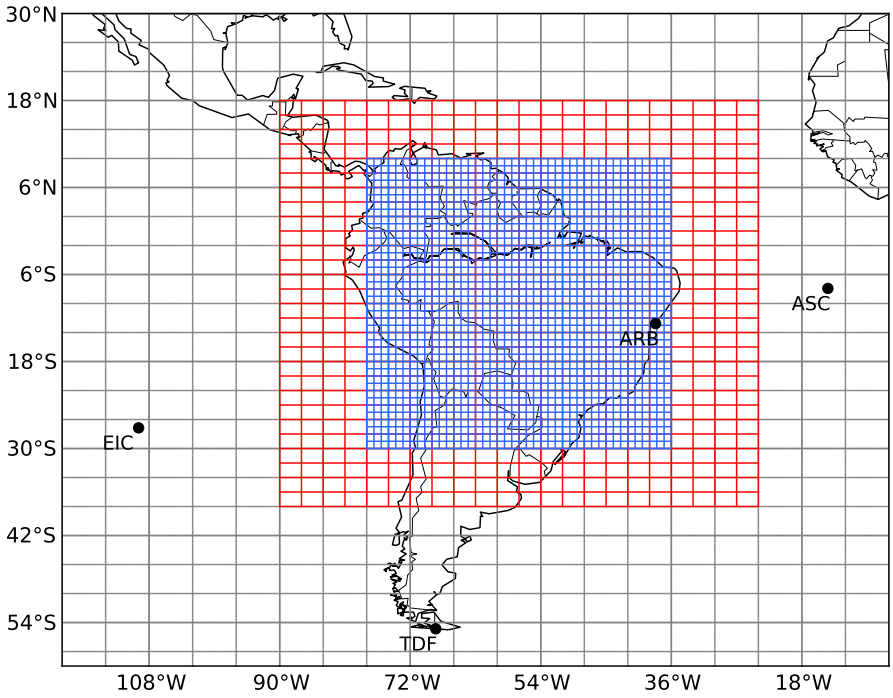

Figure 5.1: *The nested grid of TM5. The gray lines represent the coarse 6°x 4° resolution, the red lines are the intermediate 3°x 2° zoom region and the blue lines correspond to the finest zoom region with a resolution of 1°x 1°. The locations of the NOAA stations Ascension Island (ASC), Easter Island (EIC) and Tierra del Fuego (TDF) are also given as well as the validation station Arembepe, Bahia, Brazil (ARB).*

5.2.2 Prior state and uncertainties

The 5 year inversion period (2006-2010) is split in five inversion periods. Since we are specifically interested in the South American biomass burning season (July-October), each inversion starts on April 1 and ends on December 31. The first 3 months (April, May and June) are used as spin-up, the last two months (November and December) are used to constrain in particular the emissions in October. Hence, although we report the emissions for the spin-up and spin-down periods, these numbers should be interpreted with care since they may be influenced by for instance the starting CO field. The starting CO mixing ratio field on April 1 is constructed by a forward simulation for three months starting at January 1 with a climatological CO mixing ratio field from a previous multi-year forward simulation.

In contrast with our previous work (Hooghiemstra et al., 2012), we only optimize the total CO

emissions, on a monthly resolution. This is done because the posterior correlations in a three-category inversion are highly negatively correlated on monthly time scales. In particular the biomass burning and natural+NMVOC CO sources can hardly be distinguished by the system (resulting in a posterior correlation coefficient of -0.8 for the monthly emissions). In our previous inversions results were aggregated over a yearly time scale. This allowed for a clearer separation due to the differences in seasonal cycle of the two emission categories. Although we do not optimize biomass burning emissions separately, the biomass burning CO emissions are the dominant CO source in the dry season over South America and we assume that the IAV in total CO emissions can be largely attributed to biomass burning CO emissions.

The prior emissions are the sum of a fossil fuel and biofuel component, a biomass burning component and a biogenic source (direct CO emissions from vegetation and the ocean, plus the production of CO from NMVOC oxidation). We have used the Emissions Database for Global Atmospheric Research (EDGARv4.1, compiled for the year 2004, European Commission and Netherlands Environmental Assessment Agency (2010)) for the fossil fuel and biofuel source (462 Tg CO/yr). For biomass burning the GFED3 (van der Werf et al., 2010) inventory was used (in which biomass burning CO emissions are 34, 86, 21, 7 and 109 Tg CO for both August and September for 2006 to 2010, respectively over the South American 1°x1° zoom region). For the natural source we use the emissions as described in Hooghiemstra et al. (2012) (515 Tg CO/yr). Production of CO from methane oxidation is not optimized in our system. Instead we use optimized methane 3-D mixing ratio fields (Bergamaschi et al. (2009), Houweling et al. [2011], in prep.), which are oxidized in the model using a CO-yield of 1.0 and yielding another 865 Tg CO/yr on the global scale.

The prior grid-scale errors are defined as 50% of the corresponding grid-scale monthly emissions. This relatively tight error setting was chosen because small errors are needed to obtain a balanced cost function in a system that assimilates both surface and satellite observations. Although with a grid-scale error of 50% the background part of the cost function (first term in Eq. (5.1)) is still roughly one order of magnitude smaller compared to the observational part of the cost function (second term in Eq. (5.1)), the weight of the background part of the cost function has increased significantly compared to a grid-scale error of 250% that we used in our previous work. Especially for inversions in which we assimilate both surface and satellite observations combined with a bias correction (see Sect. 5.2.4), small errors appeared necessary to prevent overfitting of the data and aliasing between emissions and the bias correction.

To decrease the effective number of variables to be optimized in the system, spatial and temporal correlations are proposed in the prior error covariance matrix $\mathbf{B}$. We use a Gaussian spatial correlation length of 100 km. This means that the prior emissions in two adjacent grid boxes (in the 1°x1° zoom region) have a correlation coefficient of 0.29. Similarly, we use an e-folding temporal correlation length of 3 months which is equivalent to a month-to-month correlation coefficient of 0.72.

5.2.3 Observations

With the current setup of the 4D-Var system, either surface flask observations from the National Oceanic and Atmospheric Administration Earth System Research Laboratory (NOAA/ESRL) Global Monitoring Division (GMD) can be assimilated or CO columns derived from space borne satellite instruments, or both. Independent observations used to validate the optimized emission estimates are also described here.

5.2.3.1 Assimilated observations

Surface flask observations from 34 NOAA background sites are assimilated in the 4D-Var system. We use exactly the same list of stations as in our previous study (Hooghiemstra et al., 2012), but the data (up to 2010) have been updated (downloaded from ftp://ftp.cmdl.noaa.gov/ccg/co/flask/ in November 2011) and show slight differences with respect to the data we used in our earlier work. The reason for the change of data is a change in the calibration of the gas chromatograph used for measuring CO mixing ratios in the NOAA laboratory in Boulder, Colorado (P. C. Novelli, personal communication, 2011). For most observations, the differences are very small, but for remote sites in the SH, like the South Pole station, the new calibration results in higher CO mixing ratios up to 10% in particular in Austral summer when CO mixing ratios are low.

In contrast with our previous work, modeled CO mixing ratios are no longer temporal averages over 3 hours. Instead, modeled CO mixing ratios are instant model values at the time of the observation. The observation error for the flask measurements consists of a fixed measurement error of 3 ppb (1.5 ppb for remote SH stations to give these measurements more weight in the cost function) and a model representativeness error. The latter is slightly different compared to our previous work and is solely based on modeled 3-D CO mixing ratio gradients.

CO total columns from the Measurement of Pollution in the Troposphere (MOPITT) instrument are assimilated in the system. MOPITT was launched in 1999 onboard of NASA's Terra satellite. In this study we use the MOPITT version 4 (V4) total column product (Deeter et al., 2010) which is based on the MOPITT retrieval of CO in the thermal-infrared (TIR) at a wavelength of 4.7 µm (Deeter et al., 2003). These columns are mainly sensitive to CO in the free troposphere. As described in Deeter et al. (2010), the MOPITT V4 product suffers from a temporal bias drift. The CO total column drifts of by about 1 ppb/yr and may be due to long-term changes in the modulation cells or other instrumental parameters. Although such a temporal bias might influence the results of an inversion, we believe that the effect on posterior emission estimates will be small.

However, there is currently also a MOPITT V5 product based on retrieved CO columns in both the TIR and the shortwave-infrared (SWIR at 2.3 µm), which is also sensitive to CO in the boundary layer. This product is not used in the current study because it typically comes with larger random errors and is not yet fully validated. Here we assimilate MOPITT V4, Level 3, daytime observations which are gridded on a 1°x1° resolution. In contrast to our previous study, in which only MOPITT ocean pixels were assimilated, here we also use MOPITT over South America to obtain better coverage specifically over this region during the biomass burning season and to pick up specific biomass burning events.

We linearize the MOPITT V4 averaging kernel as before (Hooghiemstra et al., 2012) to keep the model linear and the cost function quadratic such that the CONGRAD method is a feasible minimizer for the cost function. No additional corrections for the linearization are used in this study. The linearized MOPITT averaging kernels are applied to model columns but in the current study we interpolate the (coarse) model columns to the location of the satellite observations, which are provided on a 1°x1° grid.

5.2.3.2 Validation observations

Independent observations of CO are used to validate the optimized emissions. Unfortunately, there are almost no regular aircraft data, e.g., from the Measurement of OZone and water vapour by AIrbus in-service airCraft (MOZAIC) or the Civil Aircraft for the Regular Investigation of the atmosphere Based on an Instrument Container (CARIBIC) programs, for our study region. However, CO flask observations are performed by the Instituto de Pesquisa Energéticas e Nucleares (IPEN), Lab. Química

Atmosferíca (CQMA) at station Arembepe, located at the east coast of Brazil (12.77°S, 38.17°W, see Fig. 5.1) from 2006 onwards (no data for 2010 released yet). Since this station is most likely sensitive to biomass burning CO in the period August - October, simulated mixing ratios will be compared to these observations in Sect. 5.3.3.

The Infrared Atmospheric Sounding Interferometer (IASI) onboard the MetOp satellite (launched in October 2006) also measures CO columns at a wavelength of 4.7 µm. IASI has a somewhat smaller footprint and a larger swath width compared to MOPITT. This results in nearly daily global coverage by this instrument. Due to the smaller footprint, IASI observations are less often masked by clouds and hence pick up even more specific biomass burning events over South America. The altitude sensitivity specified by the averaging kernel for IASI is comparable to MOPITT and IASI is thus mainly sensitive to free tropospheric CO. Here we use IASI day time total column observations, retrieved using the FORLI (Fast Optimal Retrievals on Layers for IASI) optimal estimation algorithm (Turquety et al., 2009; George et al., 2009). Data for the August-October period for the years 2007-2010 over the 1°x1° zoom region are used for validation.

5.2.4 Bias correction

Most recent CO inverse modeling studies used satellite observations as constraints for the emissions. However, due to possible biases in both atmospheric transport models and satellite retrieved CO columns, simulations with optimized emissions are significantly overestimating observed surface CO mixing ratios in the remote Southern Hemisphere (Arellano et al., 2006; Kopacz et al., 2010; Fortems-Cheiney et al., 2011; Hooghiemstra et al., 2012). Since not all biases in satellite observations are fully understood at the moment, we attempt to use the surface observations as an anchor point in the inversion. Ideally, one combines the assimilation of surface observations (to obtain a correct background CO distribution) with assimilation of satellite observations to constrain the emissions in the Tropics and other regions where only a few surface observations are available.

Hooghiemstra et al. (2012) found that in particular for the Tropics and the SH, surface flask and satellite based inferred emission estimates are inconsistent, at least in the TM5 transport model. In this study, we assimilate both surface and satellite observations jointly in the 4D-Var system and in addition fit a set of bias parameters to obtain realistic emissions that are in agreement with both observational datasets. For inverse modeling of methane using surface network observations and SCIAMACHY columns, Meirink et al. (2008a) and Bergamaschi et al. (2009) fitted a polynomial bias correction along the latitude direction, based on 4 bias parameters. Here, we propose a bias correction scheme with one parameter for each degree in latitude. Since we assimilate MOPITT CO columns between 65°N and 65°S only, we use a set of 130 bias parameters. In order to obtain a smooth bias correction and to reduce the number of effective bias correction parameters, the parameters are correlated in space using a correlation length of 5° (correlation coefficient of 0.85 for two parameters 2° apart). A rather tight prior error of 0.5 ppb per parameter is chosen in order to prevent aliasing (in which the bias correction is used to compensate for unphysical emission changes). The bias parameters are set to zero a priori. For each MOPITT observation (gridded on 1°x1°) we subtract the value of the bias parameter corresponding to the latitude of the observation, from the MOPITT column-averaged CO column. Hence, a positive (negative) bias parameter decreases (increases) the corresponding MOPITT column.

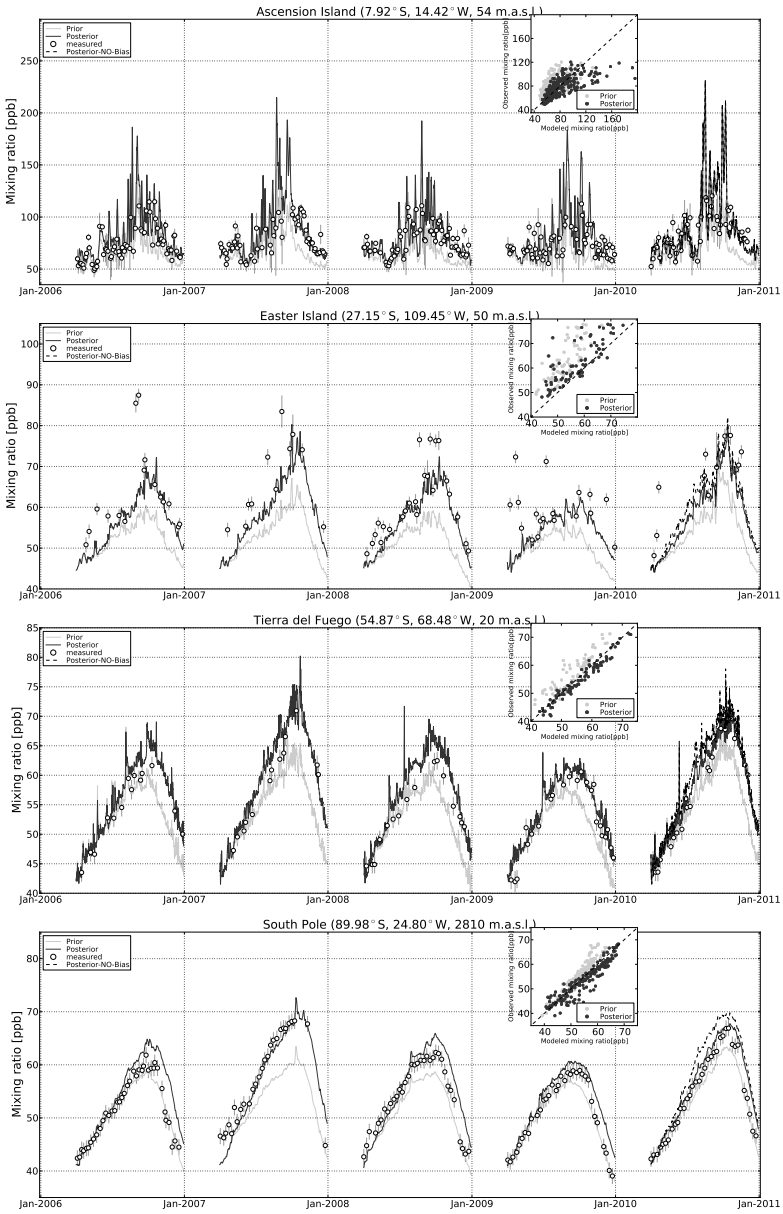

Figure 5.2: *Prior (light grey) and posterior (black solid line) simulated mixing ratio for 4 NOAA stations that have been assimilated. NOAA flask observations (including a 1-σ error) are shown as open symbols. The inset shows the fit with the data as scatterplots for the prior and posterior simulations. The posterior simulation corresponding to a sensitivity inversion for 2010 without bias correction is shown as a dashed black line. For South Pole stations the fit with the observations typically deteriorates near the end of the year since the inversions all finish at December 31.*

5.3 Results

In this section we present the results of the base inversion for the period 2006-2010. The following paragraphs discuss the fit of the prior and posterior modeled CO mixing ratios with the assimilated observations and the resulting bias correction. Next, we analyze the interannual variability of CO mixing ratios and emissions over South America. This section concludes with the validation of the derived emissions with independent observations.

5.3.1 Fit with assimilated observations

5.3.1.1 NOAA surface stations and the bias correction

The prior (light grey) and posterior (black solid line) simulation at 3 NOAA stations in or close to South America are plotted in Fig. 5.2 together with the South Pole results. The NOAA flask observations are shown as open symbols and the error bars denote the 1-σ observation error. A scatterplot of modeled versus observed CO mixing ratios is also shown for each station. Station Ascension Island, located in the Atlantic ocean between Africa and South America, is sensitive to polluted air masses arriving from either continent. The highest CO mixing ratios are observed from August to October mainly due to biomass burning in Africa and South America. The prior simulation tends to underestimate the observations towards the end of the year, and this mismatch is reduced in the posterior simulation. Interannual variability in observed CO mixing ratios is rather small, indicating that enhanced CO over Ascension Island is mainly due to emissions on the African continent, where the IAV in biomass burning CO is less pronounced compared to South America (Torres et al., 2010; van der Werf et al., 2010).

For station Easter Island, to the west of the South American continent, the prior simulation typically underestimates observed CO mixing ratios by 5-10 ppb (up to 20 ppb in the dry season). Due to the assimilation of these and other NOAA and MOPITT measurements, the posterior fit is much better. However, some high mixing ratios in summer are not fitted well. This is likely caused by the coarse resolution of the model outside the zoom region over the ocean (Hooghiemstra et al., 2011).

In the southernmost point of Argentina, station Tierra del Fuego represents the remote SH. The prior simulation underestimates NOAA flask observations in the last part of the year. The posterior simulation increases the modeled mixing ratios by 5-10 ppb, from July onwards. For this station (as for Easter Island station) we do observe IAV, likely due to transport from biomass burning CO emissions. The fit with the measurements remains remarkably good for the posterior simulation even though we assimilated MOPITT columns also in our inversions. Previous inverse modeling studies using MOPITT to constrain the emission estimates reported large differences when comparing their posterior simulations with NOAA observations in the remote SH (Arellano et al., 2006; Kopacz et al., 2010; Fortems-Cheiney et al., 2011; Hooghiemstra et al., 2012). In the inversions presented here, we fitted a bias correction to the MOPITT columns and used the station observations as anchor points for the inversion. Even observed background CO mixing ratios at South Pole station are nicely fitted by the inversion, in sharp contrast with previous inversions that overestimated observed mixing ratios at the South Pole by 20 ppb. A sensitivity run assimilating both datasets without fitting a bias correction is shown as a dashed black line for the year 2010 only. Clearly, the assimilation of the NOAA surface stations already brings the modeled CO mixing ratios close to the observations compared to earlier satellite only inversions, but the added effect of the bias correction (see below) improves the fit even more.

The bias correction obtained for the years 2006-2010 is shown in Fig. 5.3. The positive bias on almost the entire SH may be associated with a retrieval bias in very clean environments. Note that

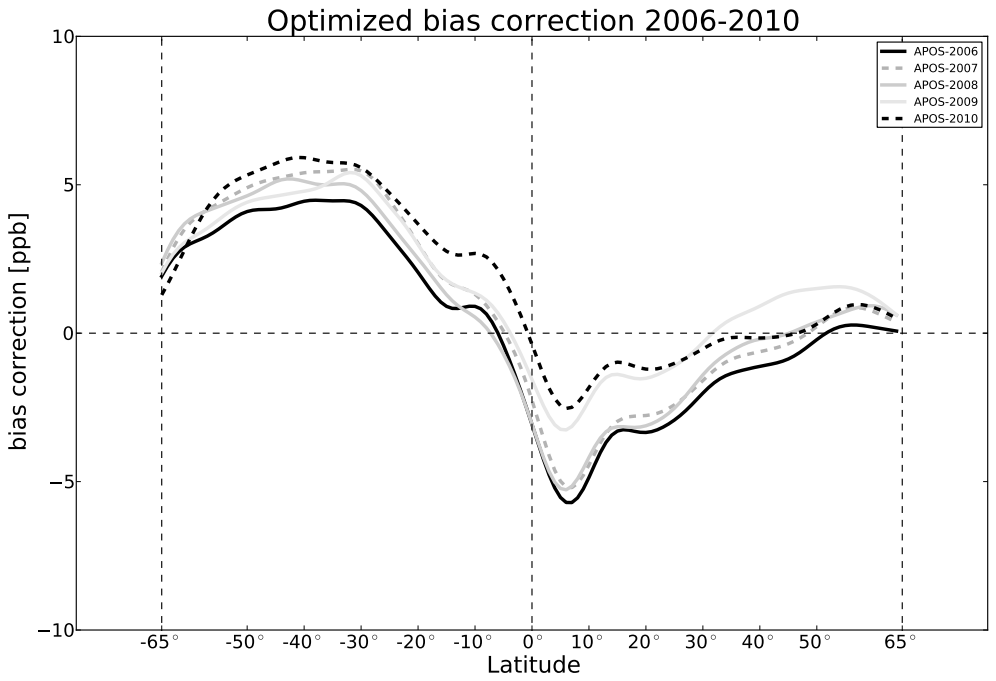

Figure 5.3: *Bias correction for the joint inversions for 2006–2010. Note that the bias (in ppb) is subtracted from the MOPITT column-averaged CO mixing ratio. Therefore, a positive bias (leading to smaller observed columns) typically leads to a reduction in the emissions compared to no bias.*

the value of a bias parameter is subtracted from the MOPITT columns at the corresponding latitude. Hence, with a positive bias on almost the entire SH, MOPITT columns are reduced by the inversion by a maximum of 5 ppb for the latitude range $30° - 50°$S. This implies that optimized CO emissions for the South American continent are somewhat lower using this approach compared to a MOPITT-only inversion. Given that the 5 year period is treated as 5 separate inversions, the derived bias is remarkably robust for the period 2006-2010. Assuming a column-averaged CO mixing ratio between 50 and 100 ppb in the SH, we infer a positive bias in MOPITT V4 of 5 to 10% in the SH. This is significantly lower compared to the bias in MOPITT V3 in the SH (up to 20%), which was deduced from comparison with aircraft profiles (Emmons et al., 2007, 2009). In contrast, the NH Tropics show a small negative bias (meaning that MOPITT is too low according to the inversion) of 3 to 5 ppb. At NH mid and high-latitudes, the inferred bias is close to zero. Note that we used only MOPITT ocean observations (except for the South American continent) and that the bias pertains to MOPITT over the oceans.

5.3.1.2 Fit with MOPITT

Figure 5.4 shows monthly composites of the prior and posterior modeled CO columns and the assimilated MOPITT observations (with the bias correction applied to these observations) for August 2008

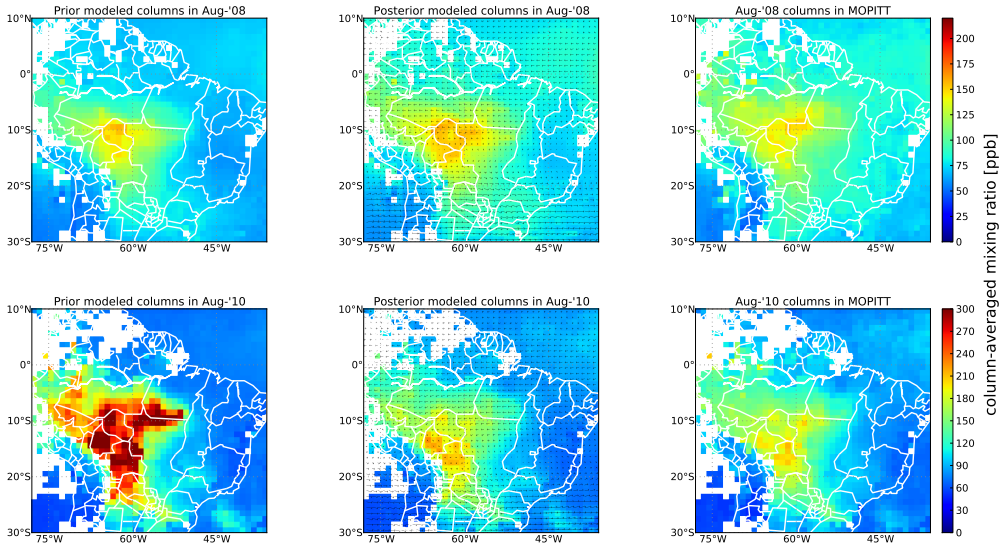

Figure 5.4: *Prior and posterior modeled column-averaged CO mixing ratio and MOPITT observations for August 2008 (top) and 2010 (bottom). Monthly average wind fields at 600 hPa are shown in the middle panels. The observations have been corrected with the posterior bias (Fig. 5.3). Note the different scales between the top and bottom panels.*

(top) and 2010 (bottom). This figure clearly illustrates the power of the 4D-Var approach: although we optimize monthly emissions only, and fire emissions typically change on shorter time scales, the fine scale pollution events (due to fires) are fitted very well. The prior simulation for 2008 is already quite close to the observations and mainly the background columns are increased from the prior to the posterior simulation. For 2010, however, the prior simulation largely overestimates observed columns in Western Brazil, Bolivia and parts of Paraguay. The posterior simulation (with reduced emissions) is indeed much closer to the observed columns.

Although the main biomass burning emission hotspots in the GFED3 inventory are located in the states of Mato Grosso and Pará (in particular for 2010), satellite-observed CO hotspots are mainly visible more westwards in Rondônia and southwards to Bolivia. This feature is due to transport of biomass burning pollution plumes to the west and southwest, where CO accumulates at the foot of the Andes mountain range. The westerlies then transport CO enhanced air southeastwards to the Atlantic ocean. These transport patterns are also shown in Fig. 5.4 (middle panels). A different pathway may also transport CO enriched air further to the west towards the Pacific ocean.

5.3.2 Interannual variability of CO emissions over South America

5.3.2.1 Time series of column-averaged CO mixing ratios

Interannual variability of CO mixing ratios is clearly visible in Fig. 5.5, which shows modeled and observed column-averaged CO mixing ratios for 4 regions in and close to South America. For example,

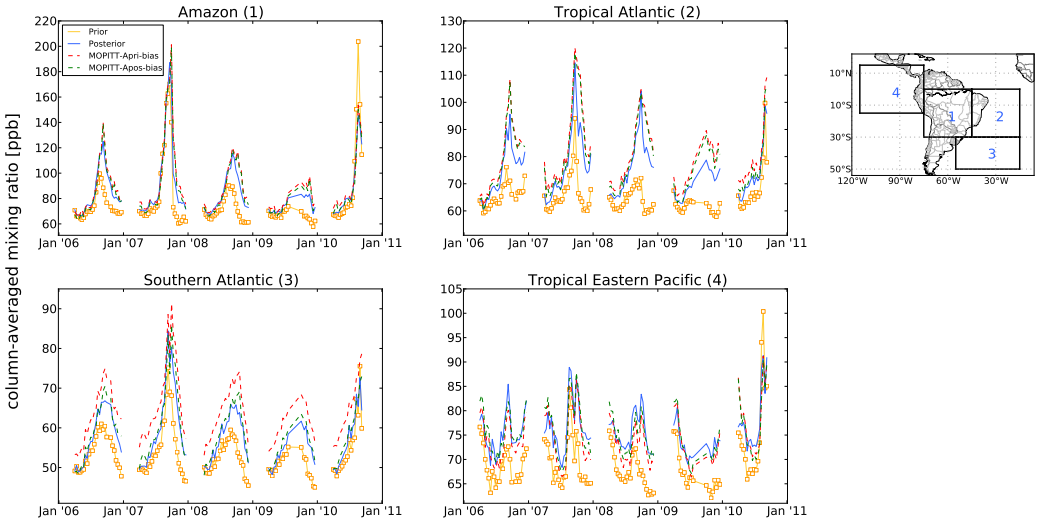

Figure 5.5: *5-year time series for 4 regions in and close to South America. Prior (yellow), posterior (blue) and observed (red dashed and green dashed) column-averaged CO mixing ratios are shown for the period April - Decmber for each year. A bias correction (per latitude, in ppb) is fitted to the observed MOPITT columns. The prior bias is zero for all latitudes, the posterior bias is non-zero (further illustrated in Fig. 5.3) and subtracted from the original MOPITT columns leading to the green dashed line. Modeled and observed columns have been averaged over 10 day periods and the individual data points are indicated in the prior simulation by rectangular markers. Note the data gap in August and September of 2009 and in the last months of 2010.*

the MOPITT observed columns (dashed red lines) show peak values over the Amazon of 200 ppb in 2007, but the maximum in 2009 is below 100 ppb. For the South American outflow regions IAV is also observed, albeit less pronounced compared to the continental region. Similar IAV is modeled using the prior emissions (yellow line) and is caused by the IAV in the biomass burning emissions of GFED3. The prior simulation largely underestimates observed CO columns (except for 2010), in particular for the Atlantic outflow regions. The prior underestimate outside the biomass burning season (April to June and November and December) indicates that the background CO levels due to anthropogenic and natural CO emissions are too low. An underestimation of biomass burning emissions in the GFED3 prior may also play a role. Note that the dashed green lines represent the bias corrected MOPITT columns, which deviate from the uncorrected MOPITT columns only over the Southern Atlantic. The bias correction reduces the MOPITT columns by approximately 5 ppb at these latitudes (see Fig. 5.3).

If we zoom in on smaller regions (illustrated in Fig. 5.6), similar IAV is observed as compared to the large regions. However, for region 1 (in the arc-of-deforestation in the states of Mato Grosso and Pará in Brazil (Morton et al., 2006)), the prior simulation overestimates the observations in 2007 and in particular in 2010, in which the Amazon suffered an extreme drought (Lewis et al., 2011; Xu et al., 2011). Extremely dry years usually trigger larger biomass burning events due to extensive drying of the biomass (Aragão et al., 2008) and hence, peak CO columns > 300 ppb are simulated. The overestimation in these two years may indicate that GFED3 emissions are locally somewhat too high in these years.

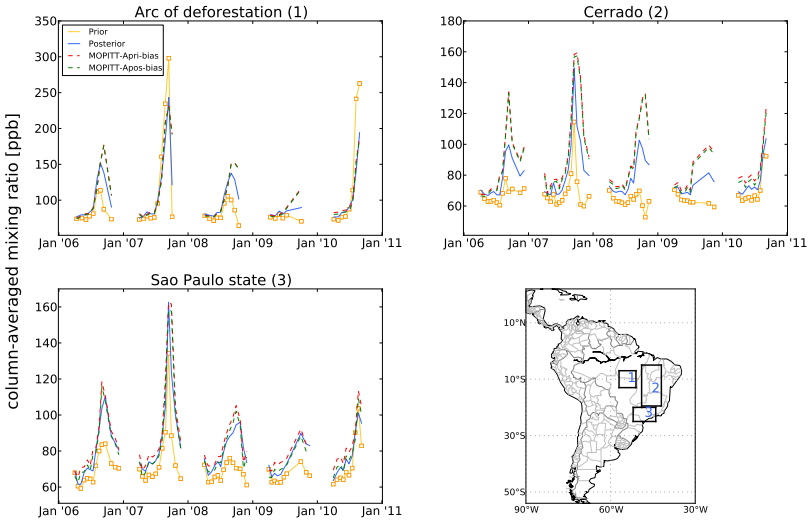

Figure 5.6: *As in Fig. 5.5, but for small regions in South America. Region 1 is in the arc of deforestation (Morton et al., 2006), region 2 is the Brazilian Cerrado (mainly savanna and grasslands) and region 3 is the state of São Paulo.*

The posterior simulation (shown in blue), fits the bias corrected observed columns (dashed green lines) very well, especially when averaged over large regions as shown in Fig. 5.5. For the smaller regions in Fig. 5.6, the fit with the observations is also remarkably good given the constraint that emissions may vary only on monthly time scales. However, for the Brazilian Cerrado (region 2 in Fig. 5.6), the posterior simulation still underestimates the observations by up to 20-40 ppb. This illustrates the compromise in the 4D-Var approach: the posterior simulation tries to fit the available observations as good as possible but deviations from the prior emissions also result in a penalty in the cost function (Eq. (5.1)). In addition, the number of observations available for each region (which are given per month in Table 5.1) plays a role here. The low number of observations in 2009, in particular for the small regions results in emissions that remain close to the prior estimate.

5.3.2.2 Optimized emissions

The total prior and posterior emissions, aggregated per month for the 1°x1° zoom region are shown in Fig. 5.7. As expected, the total emissions are increased for all months (except for August in 2007 and 2010). The emission increments outside the dry season, i.e., from April to June and in November and December may indicate that the emissions from anthropogenic and natural sources are too low in our prior inventories. A sensitivity study in which we used the POET database (Olivier et al., 2003) as prior inventory for the natural source (which gives two times higher natural CO emissions for South America), resulted in a decrease in the emissions outside the dry season indicating that the truth is likely somewhere in between these two estimates for the natural CO emissions. This and other sensitivity studies are presented in Appendix A.

For the dry season, total emissions are increased except for the year 2010. We assume here that the IAV in dry season total CO emissions can be attributed entirely to the IAV in biomass burning

Table 5.1: *Number of gridded (1°x1°) MOPITT observations per month per region. The eight regions that have been used in this paper are the 1°x1° zoom region (see Fig. 5.1), the four large region (Fig. 5.5) and the three small regions (Fig. 5.6). Note that due to a cooler malfunction, the MOPITT instrument was turned off from July 28 to September 28, 2009. For comparison, the number of IASI observations (also binned to 1°x1°) for August 2010 for region 1 equals 32523 and for region 8 IASI reported 942 observations.*

	Region	2006	2007	2008	2009	2010
July	1	8760	7671	8837	6692	7567
	2	5546	4679	5791	4109	4998
	3	6381	5687	6247	5179	5325
	4	2517	2334	2486	2173	2664
	5	4518	4522	3844	3587	3431
	6	263	275	342	271	304
	7	727	758	760	723	758
	8	302	220	327	161	285
August	1	9068	8244	9067	0	8609
	2	5746	5284	5693	0	5770
	3	6316	5874	6130	0	5452
	4	2501	2321	2957	0	2378
	5	4368	3359	3632	0	2674
	6	306	306	317	0	328
	7	831	833	844	0	782
	8	303	326	274	0	308
September	1	7311	7936	7757	292	3938
	2	4000	4762	4344	117	2304
	3	5503	5089	5318	222	2581
	4	2635	2082	1984	149	1121
	5	4537	3517	3381	82	1522
	6	174	239	194	0	143
	7	513	738	633	60	371
	8	209	306	261	8	138
October	1	2804	4838	5888	3897	478
	2	1221	2294	2730	1947	146
	3	2995	5181	5473	3705	509
	4	2165	3551	3105	2516	285
	5	3032	4098	4225	3267	473
	6	17	68	110	62	0
	7	70	388	522	47	6
	8	119	194	118	102	6

CO emissions. Biomass burning CO emissions (for both August and September) are therefore calculated by subtracting a constant background from the total CO emissions summed over August and September for each year in the period 2006-2010. The background term is the sum of anthropogenic

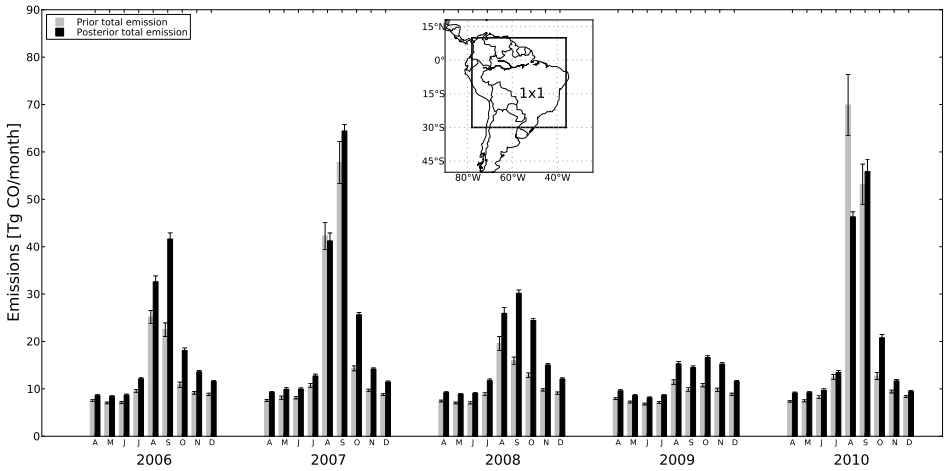

Figure 5.7: *Prior and posterior total monthly CO emission estimates for the South American 1°x1° zoom region from 2006 to 2010. Note that emissions for the period January to March have been omitted since our inversions ran from April to December. Error bars denote the prior and posterior 1-σ uncertainty in the emission estimates. The inset shows the zoom region.*

and natural CO emissions corrected for additional biomass burning emissions outside the dry season (estimated as 1 Tg CO/month). By inspection of the posterior CO emissions outside the dry season (Fig. 5.7), we estimate the background emission term to be 7 Tg CO/month. The resulting IAV of biomass burning CO emissions is detailed in Table 5.2. The dry season of 2007 and 2010 show very high biomass burning emissions of 92 and 88 Tg CO, respectively. In contrast, in 2006 and 2008, 60 and 42 Tg CO is emitted and in 2009 (a very wet year), emission estimates are as low as 16 Tg CO. In comparison with the prior emission inventory from GFED3, the IAV has reduced. This is indicated by the smaller spread in the inferred emission estimates compared to the prior (see bottom row of Table 5.2). Using prior emissions that are constant from year to year (i.e., start with zero IAV, see Appendix A), the IAV in inferred emissions is further reduced, confirming that the prior information in these inversions remains important. Another feature following directly from Table 5.2 is that the biomass burning emissions in the dry season dominate South American annual emissions. Except for 2008 and 2009, August and September emissions account for more than 50% of the annual biomass burning emissions in South America. This percentage increases to roughly 70% for 2007 and 2010. In addition, the inversion shifts the emission maximum to September. Possible reasons for the differences between GFED3 and our inferred emission estimates are further discussed in Sect. 5.4.1.

For 2006 to 2010, the derived spatial patterns of the total CO emissions for August and September are shown in Fig. 5.8. The first and second row panels of this figure present the prior and posterior total CO emissions, respectively. The third row shows the percentual emission increment, relative to the prior emissions. Two-month total CO emissions (in Tg CO) aggregated over the 1°x1° zoom region are given in brackets. Focusing on the arc of deforestation, the region in northern Mato Grosso and southern Pará (region **1** in the top left panel), emissions in this region increase compared to the prior in 2006 and to a lesser extent in 2008 and 2009. In contrast, large reductions in emissions for this region are inferred for 2007 and 2010. Since the biomass burning CO emissions dominate the prior spatial emission pattern (not shown), we attribute these increments to under- (2006, 2008 and

2009) and overestimates (2007 and 2010) of the GFED3 inventory. A second region of interest is the Brazilian Cerrado (from the north- to the southeast, region **2**). Here, the inversions increase emissions for all years and the increments are likely attributed to too low emissions in GFED3 possibly combined with too low background emissions from both the natural (NMVOC) source and the anthropogenic source. A third region of interest is the state of São Paulo (region **3**). CO emissions in this region are associated with pre-harvest burning of sugar cane plantations. Despite the fact that by accident the sugarcane emissions from both the GFED and the EDGAR inventories were included in the prior emission and the prior estimate was therefore too high, the inversion further increased the emissions by 50-100% for all years. Given the growing demand for sugar cane ethanol as a fuel and as an export product (Cardoso et al., 2012), it is likely that both prior inventories underestimate these emissions for the period 2006-2010.

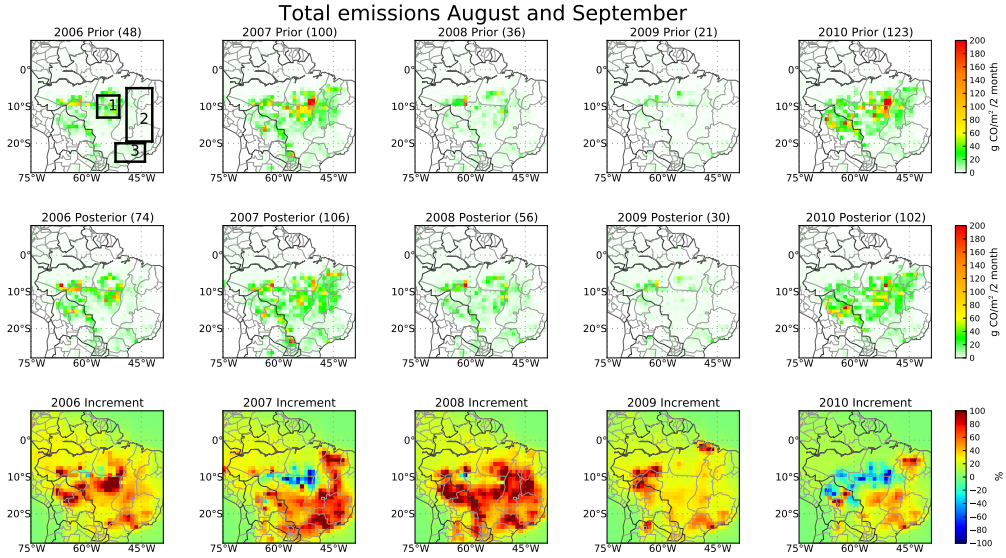

Figure 5.8: *Prior emissions, posterior emissions and increments of the total CO emissions for August and September for the years 2006–2010 in g CO (2 month)$^{-1}$m^{-2}. Numbers in the titles represent the two monthly total emission (Tg CO) for the 1°x1° South American zoom region.*

Table 5.2: *Calculated interannual variability in biomass burning CO emissions for both August and September in Tg CO (columns 2-4). Interannual variability in biomass burning emissions for the complete inversion period of 9 months (columns 5-7). Total CO (from anthropogenic, biomass burning and the natural source, including NMVOC-CO) is shown in columns 8 and 9. Finally, an estimate of yearly emissions of anthropogenic (ANT) and biomass burning (BB) emissions are given for our study (column 10) and the numbers reported by Fortems-Cheiney et al. (2011) (column 11). We have estimated our annual surface emissions by subtracting the NMVOC-CO for the 9-month period (total of 48 Tg CO), adding the prior anthropogenic and biomass burning emissions for 3 months (totaling to 7 Tg CO) and the annual contribution of direct emissions from vegetation (12 Tg CO/yr).*

	Biomass burning CO (corrected)						Total CO		Surface emissions	
	August + September			April - December			April - December		Year	
	Prior	Posterior		Prior	Posterior		Prior	Posterior	Posterior	Fortems-Cheiney et al. (2011)
Year	GFED3.1	Base	GFED-mean[a]	GFED3.1	Base	GFED-mean[a]				
2006	34	60	64	44	92	96	108	155	128	138
2007	86	92	83	106	136	125	167	199	174	198
2008	21	42	52	34	84	87	98	147	120	128
2009	7	16	51	16	45	81	80	108	80	131
2010	109	88	80	125	123	112	189	186	157	-
Mean±STD	51±39	60±29	66±13	65±43	96±32	100±16	128±42	159±32	119±32	149±29

[a] The term GFED-mean refers to the prior biomass burning emissions calculated from GFED3 by taking the 5-year mean emission estimate.
Prior biomass burning emissions for these inversions are set to 51 Tg CO (for August and September) and 63 Tg CO for the April - December period.

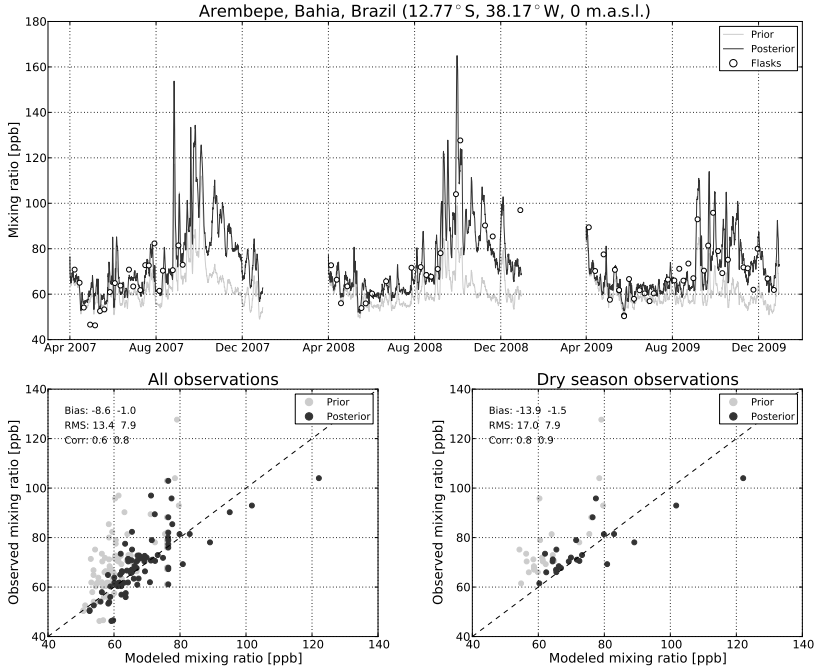

Figure 5.9: *Validation with independent data from station Arembepe, Bahia, Brazil for the period 2007–2009. This station has not been assimilated in the inversion. Top: The prior and posterior simulations are shown in light grey and black, respectively. Flask observations are denoted by the open symbols. Bottom: Scatterplots of modeled versus observed mixing ratios for all observations (left) and observations in the dry season, defined as the months August to October (right). Numbers in the panels present the statistics for the bias, root mean square (RMS) and the correlation coefficient for the prior and posterior simulation, respectively.*

5.3.3 Validation with independent observations

Independent observations, i.e. observations that have not been assimilated in the 4D-Var system, are used to validate the inferred emission estimates. We start with a comparison with CO flasks measured at station Arembepe, Brazil, which are available since the end of 2006. Figure 5.9 shows the comparison with these independent observations: The prior simulation for 2007 to 2009 (in grey) and the posterior simulation (in black) are shown as well as the flask observations. A scatterplot for all observations and for the dry season observations is presented in the bottom panels of Fig. 5.9. The comparison with the flask observations improves in particular in the dry season, for which the prior simulation was too low in 2007-2009. The posterior simulation shows excellent agreement with peak CO observations due to pollution plumes which are well captured by the high resolution model.

Prior and posterior model simulations are also compared to IASI columns. Figure 5.10 shows the prior (left column) and posterior (middle column) modeled CO total column in 10^{18} molecules cm^{-2} (based on our joint MOPITT/NOAA inversion) and the IASI total columns (right column) for August, September and October 2010. The model is sampled with collocated IASI observations and the IASI

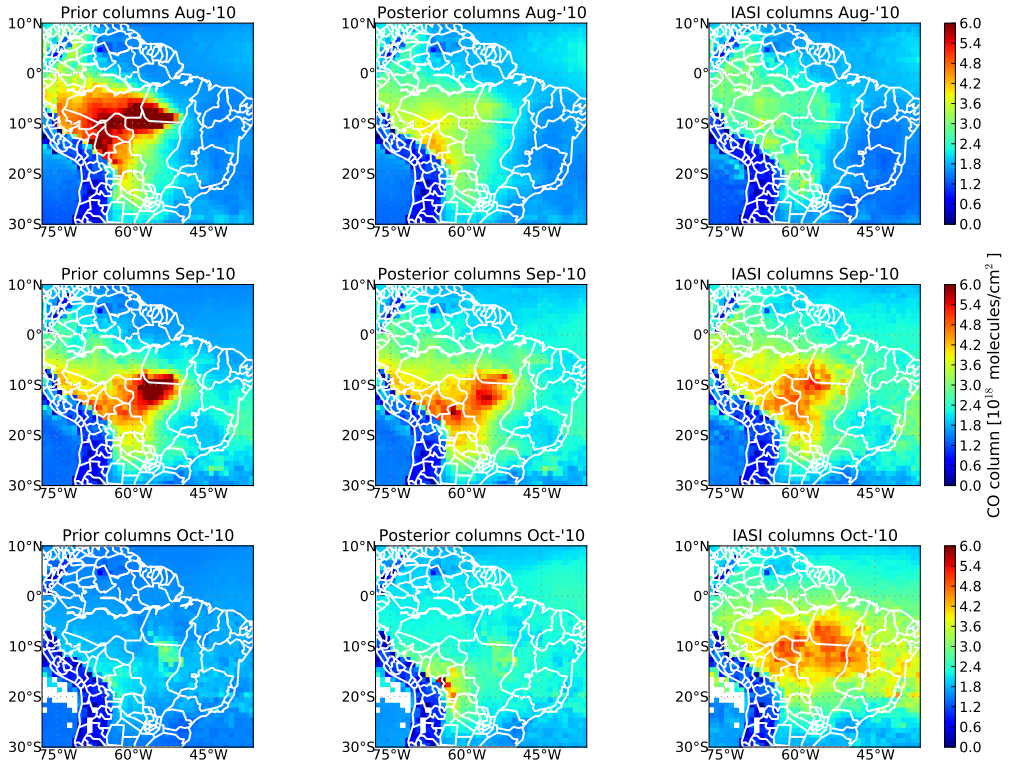

Figure 5.10: *Prior and posterior modeled total column CO (in* 10^{18} *molecules/cm*^{2}*) and IASI observations for August to October 2010. Note that there was hardly any MOPITT data to constrain the emissions in October 2010.*

averaging kernels are used for a proper comparison. The comparison with IASI columns confirms that the prior emissions were too high in August and September 2010. Hence, the system reduces the emissions and the posterior simulation shows very good agreement with IASI columns. For October 2010 however, there is poor agreement with IASI columns. This can be explained by the low amount of data available from MOPITT for this month (see Table 5.1). This was also found for August and September 2009 (not shown). For these months there was no MOPITT data and emissions were only constrained by observations from October onwards.

5.4 Discussion

The resulting emission estimates from application of the high resolution 4D-Var system presented so far show significant differences compared to the GFED3 prior inventory and strong year-to-year variation. Below we discuss potential explanations for differences found between our emission estimates

and the GFED3 prior and we discuss possible drivers of the inferred interannual variability in CO emissions.

5.4.1 GFED3

For the period 2006 to 2010 significant differences between our emission estimates and the GFED3 prior inventory were shown. We acknowledge that since we can not separate the individual CO emission categories in the 4D-Var framework, our derived biomass burning CO emissions (as given in Table 5.2) carry some uncertainties. However, deficiencies in the GFED3 product also play a role. The GFED3 CO emission inventory (van der Werf et al., 2010) for biomass burning is based on four quantities: burned area, fuel loads, combustion completeness and emission factors, all bearing their own uncertainties. We discuss the impact of these uncertainties below:

1. In this study we have used the GFED3 emissions on a monthly resolution. In reality, these fires vary probably on a day-to-day basis. In our current framework, we can only optimize grid-scale emissions on a monthly time-scale and hence, CO emissions due to multiple fire events in a single grid box are averaged over the whole month.
2. GFED3 uses constant emission factors throughout the year per biome. Our inversion indicated that high fire years were overestimated, and low fire years underestimated in GFED3. One potential reason could be that these emission factors vary over time and space, something that is not taken into account in GFED3. During drought years, burning efficiency is higher and the amount of CO released per unit biomass consumed is lower. In the future, building dynamic emission factors into GFED (van Leeuwen and van der Werf, 2011) that would dampen inter-annual variability may thus explain part of the discrepancies found. This reasoning, however, does not explain the shift in peak emissions from August to September.
3. Another source of uncertainty in this region relates to the combustion completeness (CC). In GFED3, CC is modeled as a function of climatological conditions and a fire persistence metric based on active fire observations as a proxy for the amount of repeated burning (Morton et al., 2008).
4. The same fire persistence metric is used to boost burned area estimates (Giglio et al., 2010) in deforestation regions to better mimic reported deforestation rates (van der Werf et al., 2010). Both the CC and burned area formulation in GFED are thus crude, and better comparisons against ground measurements is required to understand the underlying reasons behind the differences between bottom-up and top-down estimates.

5.4.2 IAV in biomass burning emissions

We have inferred significant IAV in biomass burning emission estimates for the period 2006-2010. Year-to-year variability in precipitation combined with IAV in deforested area is likely the main driver of IAV in biomass burning CO emissions. For example, during an anomalous wet year such as 2009 (Torres et al., 2010), biomass burning due to deforestation may be postponed because of high fuel moisture. This would typically lead to a reduction in CO emissions in that year but the emissions associated with that specific biomass debris will be added to the biomass burning CO emissions of the next year. Such a mechanism could for example explain our inferred CO emissions estimates for 2009 and 2010. In contrast, in very dry years such as 2007 and 2010 (Lewis et al., 2011), biomass burning fires may easily run out of control due to the extensively dried vegetation leading to high CO emissions. In addition, smoldering ground fires release large amounts of CO to the atmosphere. Torres et al. (2010) found high correlations between OMI derived aerosol loads, precipitation and fire

counts, concluding that the IAV in aerosols from 2001-2009 was due to biomass burning. The year 2008 showed very low aerosol loads and fire counts but was certainly not an above average wet year. Therefore, Torres et al. (2010) concluded that perhaps economic or regulatory factors were the main drivers of the low fire activity and aerosol load in 2008. The inferred CO emissions from our 5 year inversion show a similar correlation with the rainfall anomalies as the aerosol observations presented by Torres et al. (2010) in which the year 2008 stands out for its low emissions. The IAV in inferred CO emission estimates was further compared to CO emission estimates reported by Fortems-Cheiney et al. (2011). Overall, the IAV in their CO emissions agrees quite well with our findings, although their estimates are somewhat larger. This comparison is further detailed in Appendix B.

IAV in deforested areas may be linked to the global demand for goods such as beef and soy and their associated prices. For example, Laurance (2007) described how a global increase in the price of soy has an impact on deforestation in Amazonia. The higher global demand for soy directly triggers forest conversion to soy plantations in the Amazon region. Either intact forest is cleared or pasture lands from ranchers are purchased and converted for crop production. Cattle ranchers in turn are pushed into the forest frontier clearing new forest for pasture lands. Governmental legislation also influences deforestation. For example, the 'Forest Law' (active since 1965), requires protection of 80% of the forest of private lands in the Amazon. This law is currently about to change, which may lead to more deforestation in the coming years (Sparovek et al., 2010). Moreover, the 'Forest Law' only protects the Amazon region whereas the Brazilian Cerrado is unprotected and converted rapidly to agricultural lands. Deforested area in the Amazon region is closely monitored from space by the Brazilian institute for Space Research (INPE) and shows a steadily decreasing trend in deforested area since 2004 (with only one small increase in 2008). In contrast, although our inferred CO emission estimates decrease from 2007 onwards (Table 5.2), CO emissions returned to high levels in 2010.

Top-down estimates of biomass burning emissions as presented in this paper would be a valuable addition to existing methods to monitor deforestation (INPE, GFED). However, it is difficult to link deforestation one-on-one to CO emissions for the following reasons. First, since not all deforested biomass may be burned in the year of deforestation, piles of biomass debris may be ignited several times in the years after the deforestation took place (van der Werf et al., 2009) and hence, emit much more CO than expected based on the deforested area. Second, besides deforestation fires, also savanna and woodland fires in the Brazilian Cerrado contribute to the total CO emissions from biomass burning. In the future, a closer collaboration between bottom-up approaches to understand and partition fire sources and top-down work as presented here to constrain total emissions may yield better insights into fire processes and the quantitative effect of biomass burning on the composition of the atmosphere.

5.4.3 Expansion of sugar cane plantations

Our inversions strongly increase CO emission estimates over São Paulo state, likely associated to pre-harvest burning of sugar cane plantations. With a growing world wide demand for sugar cane ethanol as a fuel and associated expansion of sugar cane plantations, the question is whether this leads to additional deforestation. Some studies claim that most new sugar cane plantations are started on lands previously used for cattle ranching or crop growing and therefore do not lead to more deforestation (Walter et al., 2011; Rovere et al., 2011). However, other studies expect that the expansion of sugar cane plantations have an indirect effect on deforestation by pushing ranchers into the forest frontier (Lapola et al., 2010). The benefit of avoiding greenhouse gas emissions by using biofuels instead of fossil fuels may be offset by enhanced greenhouse gas emissions associated with deforestation. However, with proper regulation, it is suggested that the growing demand for sugar cane ethanol can be achieved without additional deforestation if strategies for cooperation between ranchers and plantations are formed (Lapola et al., 2010). Although pre-harvest burning of sugar

cane will be phased out by 2021 (in São Paulo state), high resolution satellite CO observations during the coming decade in combination with inverse modeling, may be useful to identify land-use changes, by monitoring pre-harvest fires on sugar cane plantations.

5.5 Summary and conclusions

In this study we have performed a 5-year inversion for CO, specifically focusing on the biomass burning season in South America for 2006 to 2010. The inversions were performed in 9-month periods from April to December using the TM5-4D-Var system. Although the inversions optimized CO emissions on a global scale, we used the nested zooming capability over South America to resolve the emissions in this region on a high spatial model resolution of 1°x1°. To our knowledge, this is the first study that assimilated column-averaged CO mixing ratios from MOPITT over the oceans and the South American continent in combination with NOAA surface flask observations. A bias correction scheme was used to obtain posterior emission estimates that were consistent with both observational datasets. The main conclusions of this study are listed below:

1. Assimilation of MOPITT and NOAA observations in combination with the bias correction leads to a significantly improved fit with the surface observations compared to a MOPITT-only inversion. In contrast with previous inverse modeling studies using MOPITT, the fit with remote SH NOAA stations does not deteriorate. The resulting bias correction indicates a robust positive bias in MOPITT V4 in the SH up to 5 ppb (in column-averaged CO mixing ratio) between latitudes 30°S and 50°S and a slightly negative bias in the NH Tropics in all years of the assimilation.
2. South American total CO emissions show large interannual variability over the period 2006–2010 and this IAV is most likely driven by biomass burning CO emissions. A priori IAV in the GFED3 inventory is somewhat reduced by the inversion. The dry season (August and September) biomass burning CO emissions over the South American zoom region for the 5 year inversion are 60 (34), 92 (86), 42 (21), 16 (7) and 88 (109) Tg CO/yr for 2006 to 2010, respectively (GFED3 prior emission estimates are shown between brackets). These total emissions are found to be robust as a sensitivity inversion with 5 year mean GFED3 emissions resulted in emission estimates within 15% except for 2009.
3. The biomass burning inventory GFED3 seems to estimate too high emissions for 2007 and 2010 in the arc-of-deforestation in Brazil. However, emissions in the savanna regions in eastern Brazil tend to be underestimated. For the other years of this study, the inferred emission estimates are higher than GFED3.
4. For the entire 2006-2010 period, CO emissions are increased in São Paulo state by 50 to 100%. These emissions, probably from pre-harvest burning of sugar cane plantations seem to be underestimated in current inventories.
5. Validation with independent observations from IASI gives a very good comparison for months in which enough MOPITT data is available for assimilation. However, large discrepancies are observed for months which were not constrained by MOPITT data (e.g., October 2010), for which the posterior emission estimate stays very close to the prior.
6. The interannual variability in derived biomass burning CO emissions does not agree with the steady decrease in deforestation in Brazil since 2006 as reported by INPE. Although a decrease in deforestation as monitored from space may lead to less biomass burning CO emissions, climatic influences (in the form of droughts) may have very large effects as can be seen in the large increase in biomass burning CO emissions in 2007 and 2010.

In combination with a state-of-the-art prior emission set, combined assimilation of accurate and high-precision flask measurements and satellite observations with global coverage has been shown to be an effective way to obtain high resolution CO emission estimates for South America.

Our study period of 5 years is likely too short to draw conclusions on long-term trends in CO emissions over South America. In the coming decade it will become clear if the Brazilian government is able to reduce deforestation by 2020 to 20% of the average 1996-2005 levels (Nepstad et al., 2009). With the expected expansion of sugar cane and soy plantations for the large-scale production of biofuels, the question remains how this will influence deforestation and carbon emissions in this region. In this light, top-down estimates as presented in this paper may provide additional and independent information about deforestation and associated biomass burning emissions.

For future inverse modeling studies, we recommend to optimize biomass burning emissions on a sub-monthly temporal resolution, but only if combined with high resolution satellite observations. For example the IASI instrument results in a denser set of observations compared to MOPITT. Assimilation of the MOPITT V5 product, which exploits both the thermal and short-wave infrared channels of the MOPITT instrument may be useful since it provides sensitivity to surface CO, where the emissions occur. The upcoming TROPOMI mission (planned for launch in 2015) will also measure CO in the short-wave infrared with high resolution and is expected to be an additional valuable source of information on CO.

5.6 Appendix A: Sensitivity studies

The base inversion for 2006-2010 shows large interannual variability in biomass burning emissions, with only 16 Tg CO in 2009 and up to 92 Tg CO in 2007 (Table 5.2). The robustness of the derived interannual variability of the total emissions is analyzed by repeating the same 5-year inversions, but using a 5-year GFED3 mean as prior biomass burning emission. Hence, the prior biomass burning emission in a certain box is the average of the GFED3 emissions in this box for the 2006 to 2010 period. The GFED3 prior emission for both August and September in these inversions amounts to 51 Tg CO. The derived biomass burning CO emissions from these sensitivity inversions for August and September are shown in Table 5.2. As in the base inversion, the years 2007 and 2010 show the highest emissions (83 and 80 Tg CO/yr respectively), but approximately 10% lower compared to the base inversion. The other years show higher biomass burning CO emissions, in particular 2009, in which we derive 51 Tg CO due to biomass burning. This is explained by the fact that there are no MOPITT measurements from July 28, 2009 up to September 29, 2009 and hence, the 2009 biomass burning season is poorly constrained by the observations. However, comparison of the posterior base simulation (16 Tg CO biomass burning CO) with IASI (not shown) showed much better agreement compared to this sensitivity inversion, indicating that the derived emission estimate of 51 Tg CO in 2009 is based on the prior emission estimate due to the poor coverage of MOPITT for this period.

Although Fig. 5.4 gives convincing evidence that the 4D-Var system is indeed capable to optimize monthly emissions on a high resolution that fit MOPITT columns well, the question remains how much this fit depends on the prior assumptions we made. For example, how important is the spatial pattern of the biomass burning emissions we use in the prior? And how well are the natural emissions constrained by the observations? To investigate these issues, we performed two additional inversions for 2010 using (1) uniform biomass burning emission instead of GFED3 and (2) natural emissions based on the POET database (Olivier et al., 2003). The uniform prior has the same annual total biomass burning emissions as GFED3, but the emissions per grid box are constant throughout the year. Therefore, the total biomass burning emissions in the dry season are significantly lower than GFED3. The publicly available POET database consists of high resolution (1°x1°) inventories of

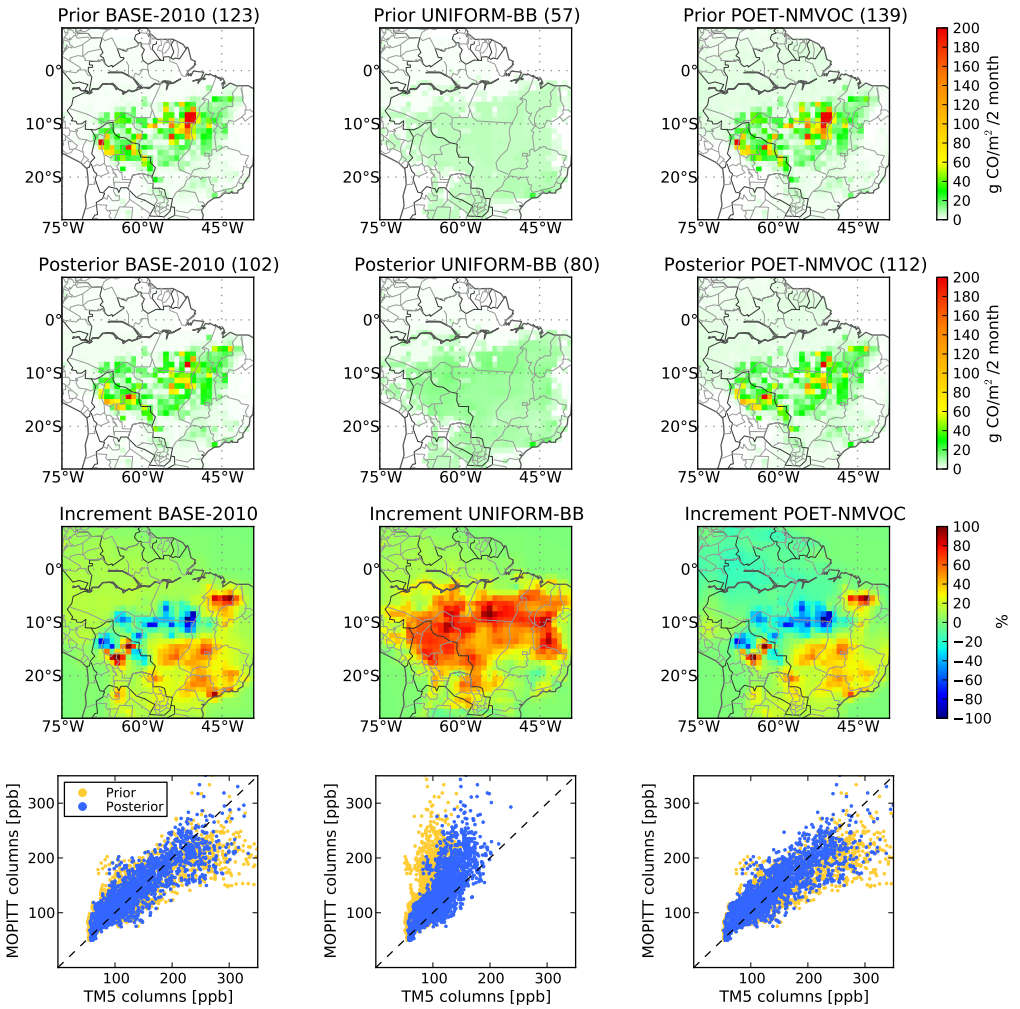

Figure 5.11: *Prior emissions, posterior emissions and increments total CO emissions for August and September for the year 2010 in g CO (2 month)$^{-1}$ m^{-2} for a series of sensitivity inversion. Numbers in the titles represent the two monthly total emission (Tg CO) for the 1°x1° South American zoom region. The bottom row plots show scatterplots of modeled versus observed CO columns for the prior (yellow) and posterior (blue) simulation.*

several precursors of CO (e.g., isoprene, terpenes, methanol and acetone) as well as inventories of CO emissions from plants and the ocean. We constructed a prior natural emission inventory based on POET using the following yields for CO production (Duncan et al., 2007): 0.2 for isoprene and

terpenes, 0.67 for acetone and 1 for methanol. For the sensitivity studies, the prior and posterior emissions for August and September 2010 and the increments are illustrated in Fig. 5.11. The bottom row panels show scatterplots of the the prior and posterior fit with MOPITT columns over the South American zoom region.

For the uniform prior, the 4D-Var system increases the total emissions in the dry season over South America from 57 Tg CO to 80 Tg CO, which is still 20% lower than the base inversion for 2010 (resulting in 102 Tg CO). Moreover, the spatial patterns for this inversion are completely different as there are no emission hotspots in the posterior emission estimate. The reason for the derived uniform emissions is 1) the lack of emission hotspots in the prior and 2) our methodology for setting the prior errors as a percentage of the corresponding emissions. Hence, for a spatially heterogeneous prior such as GFED3, the system adjusts regions with high emissions rather than regions with low emissions to fit the observations. For a spatially homogeneous prior this is not the case and the whole emission field is scaled to fit the observations. The fit with MOPITT columns is compared in the scatterplots (bottom panels in Fig. 5.11). In particular the high CO columns observed by MOPITT (due to pollution events) are significantly underestimated. This sensitivity study thus clearly illustrates the need of a realistic prior emission inventory like GFED.

The sensitivity inversion starting from the POET based natural CO emissions results in somewhat larger total CO emissions in both the prior (139 Tg CO versus 123 Tg CO in the base) and the posterior emission estimate (112 versus 102 Tg CO). From the increment plot, it is observed that apart from a reduction of biomass burning CO emissions in the arc of deforestation, the emissions in the Northwestern part of the Amazon are slightly reduced, indicating that the POET based natural CO emissions might be too high over this region. This can be explained by our assumption of releasing all CO precursors directly as CO, neglecting their atmospheric lifetimes. For the longer lived precursors (like acetone), this results in a CO overestimate.

Apart from assumptions for the prior emissions, model uncertainties also play a role. Recently, Jiang et al. (2011) and Hooghiemstra et al. (2012) showed that in particular the choice of OH field may lead to large differences on both regional and global scales for the inferred emissions. Here we focus on the vertical distribution of the biomass burning emissions. As in our previous study, the biomass burning emissions in the base inversions are released below 2 km. However, what would be the effect on the inferred emissions if we release a fraction of the emissions above the boundary layer? One would expect that those emissions are observed by the satellite earlier which may lead to somewhat lower emission estimates. For this sensitivity study we use an injection height that is defined as follows: 65% is released uniformly below 2 km. Additionally, 25% is released between 2 and 3 km and the remaining 10% is released uniformly between 3 and 6 km altitude. This inversion was performed for the year 2010 and the spatial pattern of the inferred emissions and the total CO emission were very close to the base inversion (not shown). Hence the different injection height has almost no impact on the inversion. The explanation is visualized in Fig. 5.12. In the left panel, the prior modeled CO mixing ratios at different vertical model layers are shown for the base and the sensitivity simulation for a small area dominated by biomass burning emissions. In the sensitivity simulation relatively more CO is injected at higher altitudes and hence, the surface CO mixing ratios decrease in comparison with the base simulation (grey starts and diamond markers). Similarly, due to enhanced injection of CO around 700 hPa in the sensitivity simulation, CO mixing ratios are increased compared to the base simulation (square markers). However, for typical altitudes at which MOPITT is most sensitive, there are no significant differences in the modeled CO mixing ratios for both injection heights (black stars and circular markers)). Hence, the modeled column-average CO mixing ratios in the right panel of Fig. 5.12 are very close to 1:1 line when either the MOPITT averaging kernel is taken into account or not. We acknowledge that for specific situations in which long term accumulation of CO in the boundary layer due to favorable meteorological conditions is suddenly vented out to the free troposphere, the injection height may indeed play a role. In addition,

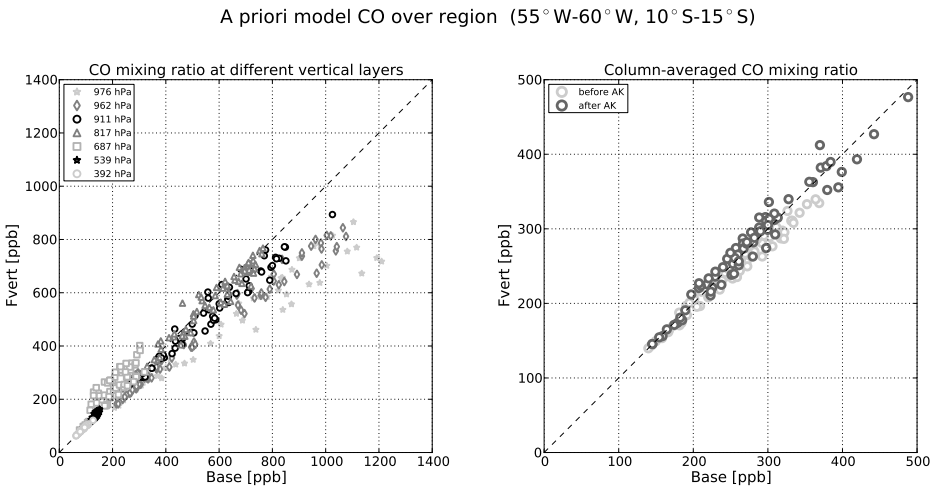

Figure 5.12: *A priori modeled CO mixing ratios for September 2010 over a small region in Mato Grosso. The left panel shows CO mixing ratios for specific vertical model layers for the base injection height versus the altered injection height. The legend indicates the pressure corresponding to the model layers in hPa. The right panel shows column- averaged CO mixing ratios before and after application of the MOPITT averaging kernels. The black dashed line represents the 1:1 relation.*

for a Short Wave Infrared (SWIR) satellite instrument (such as SCIAMACHY, the MOPITT V5 product or the upcoming Tropospheric Ozone Monitoring Instrument (TROPOMI)), with sensitivity to the surface, a different vertical distribution could have effect on optimized CO emissions because these satellite instruments typically view the whole column.

5.7 Appendix B: Comparison with recent work

Our inferred IAV of biomass burning emissions for South America is compared to the posterior emissions derived from a 10 year MOPITT inversion by Fortems-Cheiney et al. (2011). They reported total CO emissions (from fossil fuel and biofuel combustion and biomass burning) for the South American Temperate region, which covers South America south of the Equator. However, we only inverted for the period April to December and hence, we have to make an estimate of the emissions in the period January to March. Also, we have included the NMVOC-CO source in our total emission estimate. In an effort to make a fair comparison we subtract the prior NMVOC-CO emissions for April to December (48 Tg CO) and add the prior anthropogenic and biomass burning emission for January to March (7 Tg CO) and the annual contribution of vegetation for this region (12 Tg CO) to our posterior emission estimates.

The comparison of our results with reported CO emission estimates is shown in the last two columns of Table 5.2. In general our estimates are lower by 10 to 20 Tg CO/yr and even 51 Tg CO lower in 2009. The large 2009 difference is likely caused by the different prior emissions for biomass burning that were used. Fortems-Cheiney et al. (2011) used GFED2 which does not supply biomass burning emission estimates for 2009 and Fortems-Cheiney et al. (2011) used the 2008 prior estimate. However,

the GFED3 prior estimate is significantly lower leading to our posterior estimate of 80 Tg CO in 2009. The remaining discrepancies are likely due to other differences in the inversion setup such as the OH field, the exact treatment of the NMVOC-CO emissions, our inclusion of a bias correction scheme and different spatial model resolution. The interannual variability of the total emissions show similar patterns in which the year 2007 really stands out.

CHAPTER 6

Conclusions and Outlook

6.1 Introduction

This work presented the results from inverse modeling studies to constrain CO emissions using atmospheric observations. Starting point of this research was the TM5-4D-Var version to estimate methane emissions, which has subsequently been transformed to a more generic system, designed to optimize a certain tracer (in our case CO) given a set of first guess emissions and a set of observations. During this research, the system was continuously under development and the three studies reported in this thesis all used different versions of the TM5-4D-Var system. Moreover, the most up-to-date version currently available, is already further developed compared to the system we have used in the latest study in Chapter 5.

The modeling framework was not the only thing that changed, since bottom-up inventories and retrieval methods of atmospheric observations developed as well. For example, in Chapter 3 we have used the Emission Database for Global Atmospheric Research (EDGAR) version 3.2 which was compiled for the year 1995 whereas in the following studies we used version 4.1 (compiled for the year 2004). Currently, EDGARv4.2 is even available, but not yet used in our studies. In addition, the Global Fire Emission Database (GFED) has been updated from version 2 to version 3 (van der Werf et al., 2010).

In the first study we only assimilated observations from the NOAA surface network. Later on, the system was extended to ingest satellite data from MOPITT (version 4, which was released in 2009) and in the final study we assimilated both surface and satellite observations jointly by fitting a bias correction scheme to optimally fit both observational datasets, which was in particular needed for the remote SH. In the most recent version of the system, that has been applied now to four different tracers (CO, CH_3Cl, CH_4 and CO_2), daily emissions fields can be optimized on the (zoom) resolution of the TM5 model.

The remaining part of this thesis describes the main conclusions of our three studies and gives an outlook for future research directions.

6.2 Conclusions

In Sect. 1.7 two main questions were formulated. These have been cut into a series of subquestions which led to the research and findings as described in Chapters 3 - 5. Here we will repeat the main questions and summarize the conclusions in an attempt to answer these questions.

Research question 1

How do CO observations constrain the CO emissions on global and regional scales?

In our first study (Chapter 3) we optimized three CO emission categories: anthropogenic, biomass burning and natural (consisting of direct emissions from plants and the oceans, only) for 2003 and 2004 and we used NOAA surface network observations to constrain these emissions. It was found that in particular European and Asian anthropogenic emissions were underestimated in the prior inventory (EDGARv3.2) by a factor 1.5 and 2, respectively. To assess the information content of the observations, one typically looks at the uncertainty reduction that has been achieved by the inversion. It turned out that the prior uncertainty in anthropogenic emissions in Asia was reduced by a factor 2, whereas the uncertainty reduction for Europe and North America was only small. However, the prior errors were set at 50% of the corresponding emissions for Europe and North America and to 250% for Asia. As outlined in Chapter 2, these settings logically lead to a larger uncertainty reduction for South East Asia. For biomass burning emissions, the uncertainty was reduced for North America, likely due to the high-latitude stations in Alaska and Canada that constrain boreal forest fire emissions well. For South America and Africa, the uncertainty in biomass burning emission was reduced by 60% and 30%, respectively. Again, the high uncertainty reduction (despite poor coverage of the NOAA surface network in the Tropics) can be explained by the large prior errors assigned to the emissions. The natural source, contributing to less than 5% of the budget, was not constrained by the observations. In this study we also optimized the contribution of the oxidation of NMVOCs and methane to CO separately by one global parameter. The spatial distribution of these CO sources was fixed and could only be scaled on monthly time scales. The prior errors on these sources were very small to prevent aliasing and therefore, no significant error reduction was observed for these sources despite the large reduction for NMVOC-CO from prior (812 Tg CO/yr) to posterior (410 Tg in 2004) estimates.

In the next study (Chapter 4), the system was improved to optimize the NMVOC-CO source on the model resolution instead of optimizing this source by monthly global scaling parameters. The NMVOC-CO was added to the natural source and we compared the inferred emissions and their uncertainty reduction for two separate inversions. The first inversion assimilated only NOAA surface network observations and the second assimilated only MOPITT CO columns (Chapter 4). We used an updated bottom-up inventory for the anthropogenic emissions (EDGARv4.1) in comparison with the first study, with somewhat lower anthropogenic emission estimates for Europe and Asia. Therefore, also in this study we found that European and Asian anthropogenic CO emissions were underestimated, both by a factor 2. Moreover, when the posterior emissions from the two inversions are compared, a shift from one category to another was observed on the SH. The NOAA inversion increased the biomass burning CO emissions and to a lesser extent the natural emissions (now including the contribution from NMVOC-CO) compared to the prior. In contrast, the MOPITT inversion decreased biomass burning emissions and increased the natural emissions. This shift was explained by the different spatial and temporal resolution and the vertical sensitivity of the observations. For example, the MOPITT instrument is most sensitive to free tropospheric CO. Because the natural CO emissions are injected much higher up in the atmosphere compared to the biomass burning emissions, the MOPITT based inversion tends to modify the natural source rather than the biomass burning source to fit the observations. For the uncertainty reduction we found a surprising result: The NOAA-only inversion resulted in a comparable or larger uncertainty reduction for Europe and North America compared to the MOPITT inversion. This was likely due to the high density of the NOAA sites at NH mid-latitudes. As expected, the higher spatial resolution and global coverage of the MOPITT instrument compared to the NOAA surface network resulted in higher error reductions for the Tropics and the SH continents.

In this work we explicitly tried to optimize CO emissions divided into several emission categories using the available observations. In general, however, atmospheric observations only constrain the total CO emissions (i.e., the sum of the emission categories) and inverse modeling systems typically

have difficulties separating the sources from one another. Only when individual emission categories have distinct patterns in either space or time specified in the prior information, the system is capable to separate the sources in the inversion. In Chapter 3, we found that the system can not distinguish the anthropogenic and the NMVOC-CO sources well. This was likely due to overlapping spatial patterns combined with similar a priori assumptions on error correlations in time. This resulted in negative posterior correlations between these emissions. Compensating emission increments were also observed: an increase in emissions in one region to fit certain measurements, reduced the fit somewhere else and a different source was adjusted to achieve a good fit with the measurements. Given that the emissions were reported as annual totals, we also found that it was possible to separate the biomass burning source from the other sources, probably due to the the distinct temporal information on the emissions given by the prior. During the last study (Chapter 5), in which we report monthly emission estimates for South America, we found that on monthly time scales, biomass burning and natural (including NMVOC-CO) sources could not be separated due to their partly overlapping prior spatial patterns and no distinct differences in the timing of these emissions during the dry season. Therefore, in this study only the total CO emission was optimized.

A final remark on uncertainty reduction is the presence of model errors. In the TM5-4D-Var system we try to estimate the model errors due to the model resolution, sub-grid scale emission variability and incorporate this error in the observation error. However, no effort has been made to incorporate other uncertainties (e.g., in the prescribed OH field or in model vertical transport) in the model error. Hence, the calculated posterior errors using the CONGRAD method probably underestimate the true errors in the emissions. This was confirmed by the fact that the range of emission estimates we have found for sensitivity inversions with different model settings such as the prescribed OH field or the vertical distribution of biomass burning emissions was larger than our calculated errors. Therefore, we recommend to calculate the posterior errors and the associated uncertainty reduction but to put these numbers in perspective by running appropriate sensitivity inversions.

Research question 2

What is the added value of TIR satellite measurements, compared to surface network observations, in particular for monitoring biomass burning emissions and their variability?

Satellite observations typically have high spatial and temporal resolution compared to the NOAA surface network observations. Moreover, satellite instruments reach global coverage within a couple of days (3 days for MOPITT) and are therefore very useful to constrain CO emissions in the Tropics and the remote SH, regions that are poorly covered by the NOAA surface network. However, satellite retrieved CO columns carry additional uncertainties compared to the high-accuracy laboratory measurements of the surface network. Potential retrieval biases can be harmful to inverse modeling results, because these biases could be projected on the emissions leading to erroneous emission increments. If the satellite and surface observations are not consistent with each other, a satellite bias correction is needed to fit both observational datasets. The separate inversions using either NOAA or MOPITT observations conducted in Chapter 4, pointed in the direction of a positive bias in MOPITT on the mid to high-latitudes of the SH. Indeed, by fitting a bias correction scheme, this bias was confirmed to be 5 ppb between 30 and 50°S.

The available MOPITT observations in combination with NOAA observations and a bias correction scheme, have been used to estimate high resolution CO emissions for South America for the period 2006-2010 (Chapter 5). To our knowledge, this is the first inverse modeling study that estimates CO emission estimates on a 1°x1° resolution using both NOAA and MOPITT observations. The results showed that interannual variability (IAV) in biomass burning CO emissions can be inferred from the atmospheric measurements and shed light on potential deficiencies in GFED. For example, the IAV was smaller than estimated by GFED and biomass burning emissions were overestimated for the dry years 2007 and 2010. For the other years, biomass burning emissions were underestimated in GFED.

The high resolution inversion also marked the importance of waste burning at sugar cane plantations, in particular in São Paulo state, that is currently underestimated in bottom-up inventories. Due to the assimilation of MOPITT observations and the use of the zoom capability of the TM5 we were able to pinpoint this emission underestimate with high spatial accuracy. The spatial localization of emissions is not feasible when only surface observations would have been assimilated. These observations appear capable to constrain emissions only averaged over larger spatial domains. The frequent and high resolution observations of satellite instruments proof therefore valuable to constrain local emissions, despite the fact that the maximum sensitivity of the observation is in the free troposphere and frequent cloud coverage in the Tropics reduces the amount of observations used in the inversion. We showed in Chapter 5 that the exact injection height for biomass burning emissions was not a major issue, at least in the Tropics, where vertical mixing is relatively efficient.

6.3 Outlook

During the research and development of our TM5-4D-Var system in this thesis, some considerations for future CO inverse modeling studies emerged.

First of all, we have seen that it is difficult to separate the CO emission categories on monthly scales, in particular tropical biomass burning and NMVOC-CO emissions. Because these emissions have similar spatial patterns, and the timing of these emissions often overlaps, posterior correlations of -0.8 on monthly scales have been found. To better separate these source categories we propose a multi-species approach in which both CO emissions and emissions of formaldehyde (the precursor of CO from oxidation of methane and NMVOCs) are optimized. Pioneering work on multi-species inversions has been presented by Pison et al. (2009) and Fortems-Cheiney et al. (2011). For example, Pison et al. (2009) optimized emissions of CO, methane, hydrogen, production of formaldehyde and OH concentrations in a 4D-Var system using surface observations of CO, methane, hydrogen and methylchloroform, the latter to constrain OH. Fortems-Cheiney et al. (2011) applied the same system but used MOPITT V4 observations only, just to constrain CO. No observations were used to constrain methane, hydrogen and formaldehyde and hence emissions of these trace gases remained close to the prior estimates. Some recent studies optimized emissions of specific NMVOCs such as isoprene (Stavrakou et al., 2009a,b) and formic acid (Stavrakou et al., 2011). Stavrakou et al. (2009a) calculated formaldehyde production from isoprene using a chemical mechanism. Subsequently, formaldehyde satellite columns were used to constrain the isoprene emissions. In addition, Stavrakou et al. (2011) used satellite derived formic acid columns to optimize formic acid emissions.

A large improvement to our current system would be the optimization of both CO and formaldehyde (emissions and chemical production) in a 4D-Var framework assimilating surface and satellite observations of both trace gases. This is relatively easy to implement in our current framework although it is expected that tuning of the error settings will take some effort. However, since atmospheric production of formaldehyde and CO is a volume source we recommend either to include 3-D emissions in the state vector (as in the study by Fortems-Cheiney et al. (2011)) or to optimize the 2-D emissions that are vertically distributed according to a fixed injection height, for example derived from optimized methane fields. In the former case, the dimension of the state vector will strongly increase and it will be important to have high resolution satellite observations. In the latter case it is important to have proper prior information on the vertical distribution.

A second point of interest is the temporal resolution on which we optimize emissions, in particular, biomass burning emissions. Currently, emissions in our 4D-Var system are optimized on a monthly resolution. However, due to the variable nature of fires, in particular biomass burning emissions vary on much shorter time scales (in the order of hours to days). The GFED inventory is already available

on a daily and even a 3-hourly temporal resolution, and with high resolution satellite observations from the MOPITT V5, IASI and the upcoming TROPOMI instruments, such measurements may be capable to constrain CO emissions on shorter timescales (e.g. daily). The technical implementation of such a system is currently completed and has been applied to the heavy Moscow fires that occurred in the summer of 2010. Figure 6.1 shows preliminary results from the ALANIS (Atmosphere-LANd Integrated Study, see http://www.ileaps.org/multisites/alanis/) project, that aims at a better characterization of boreal fire emissions. The bottom-up emission estimates produced in this project (dashed line) are clearly too small to explain the IASI satellite data that were assimilated to obtain the posterior emissions (solid line). The spatial patterns of the emissions are shown in the right panels, in which the city of Moscow is represented by the black cross in the upper panel. Note that the inversions increases emissions to the southeast of Moscow.

For the anthropogenic emissions, road transport is a dominant source, in particular in North America and Europe. Inclusion of a daily emission profile could better resolve CO maxima due to enhanced emissions in the morning and evening rush hours.

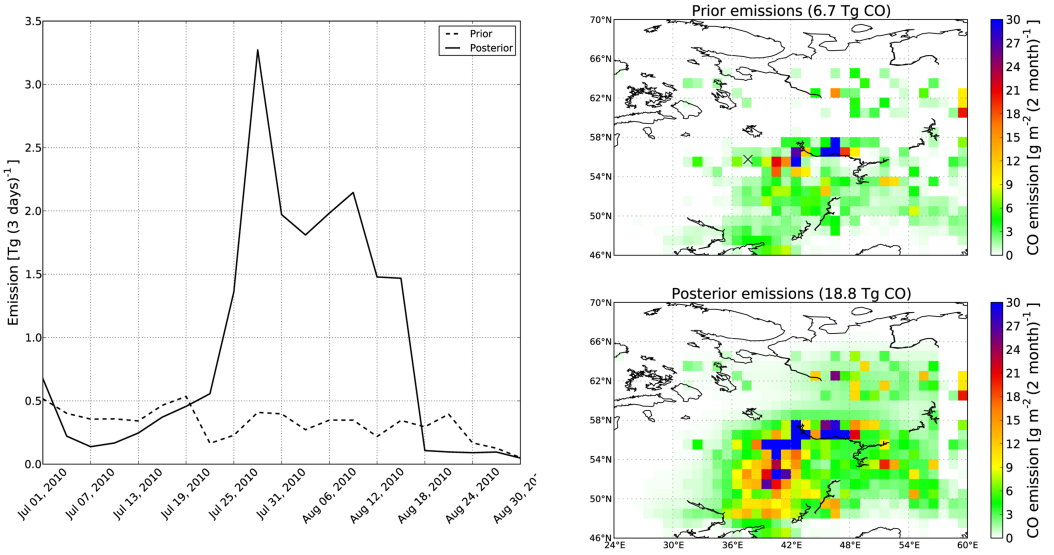

Figure 6.1: *3-Day biomass burning CO emission estimates over the Moscow area for July and August 2010 (left). The prior emissions are shown as a dashed line, the posterior emissions are shown as a solid line. A significant increase in the emissions is shown in the last week of July that pertains for the next 3 weeks. Spatial pattern of cumulative emissions (right). The cross in the upper panel represents the city of Moscow.*

A third point of discussion would be the prescribed OH field. The sensitivity studies presented in this thesis (Chapter 3 and 4), in which we used a different OH field, resulted in significant changes to the CO budget in the NH and the SH. Better constraining OH certainly has the potential to improve CO emissions estimates, for example by a joint optimization of CO and OH as described by Pison et al. (2009) and Fortems-Cheiney et al. (2011). A drawback of this approach is that the model becomes non-linear and hence the CONGRAD optimizer is no longer feasible to compute the approximated posterior errors.

With the development of both atmospheric models and satellite instruments, future applications for 4D-Var systems involve high resolution global and/or regional CO inversions. In our TM5-4D-Var system it is currently possible to define several small regions in which emissions can be optimized at a high spatial resolution of 1°x1°. Although chemistry and transport processes are already better resolved on this resolution compared to the coarse resolution of 6°x4°, an even finer spatial resolution may be favorable in the future. For example, a spatial resolution of 1°x1° leads to grid boxes around the equator of approximately 100 km x 100 km. Fires usually take place on much smaller scales and an improved resolution may therefore lead to better estimates of biomass burning CO emissions. However, such a fine resolution only makes sense if high resolution (both spatial and temporal) satellite observations are assimilated in the system. The upcoming TROPOMI instrument (scheduled for launch in 2015) will meet these requirements and will measure CO in the SWIR at a wavelength of 2.3 µm with a footprint of 7x7 km. Measuring CO at this wavelength ensures sensitivity to the whole column and the fine footprint yields a higher spatial resolution compared to MOPITT (22x22 km) and IASI (circular footprint with 12 km diameter).

The tropics remain a very interesting region for CO emissions. In this work we already focussed on the biomass burning CO emissions and their interannual variability over South America. However, focussing on Southern Africa or Indonesia would also be useful since the emissions in these regions are also highly uncertain. For example, the 4D-Var system could potentially constrain the CO emissions in Southern Africa that are moving from the north-west to the south-east during the dry season (June-October) and may give feedback with respect to deficiencies in bottom-up inventories. Due to ground fires and extensive peat burning in dry years, CO emissions from Indonesia are also uncertain (see Chapter 4) and a high resolution inversion for a time period of 5 or 10 years might be used to detect interannual variability over this region and possibly the effect of deforestation. Apart from the Tropics, the boreal forest fire emissions remain uncertain and high resolution inverse modeling can help to constrain these emissions better. Furthermore, in this work we have shown that in current bottom-up inventories, anthropogenic emissions in India and China are underestimated. Results from inverse modeling studies over the last decade show a large range of estimates for these regions. Therefore, a detailed, high-resolution inverse modeling study focussing on this region may lead to better estimates for CO emissions.

Finally, as already mentioned in the introduction of this thesis, CO is oxidized by OH forming CO_2. In current CO_2 models, the source from CO oxidation is often released directly as CO_2 at the surface. However, with a lifetime of approximately two months (and even more in local winter), this assumption may lead to errors in inferred CO_2 fluxes. Therefore, our inferred CO emissions might be used in CO_2 inverse modeling studies as a source of CO_2.

Bibliography

Andreae, M. O. and Merlet, P. (2001). Emission of trace gases and aerosols from biomass burning. *Glob. Biogeochem. Cy.*, 15:955–966.

Aragão, L. E. O. C., Malhi, Y., Barbier, N., Lima, A., Shimabukuro, Y., Anderson, L., and Saatchi, S. (2008). Interactions between rainfall, deforestation and fires during recent years in the Brazilian Amazonia. *Phil. Trans. R. Soc. B*, 363(1498):1779–1785.

Arellano, Jr., A. F., Kasibhatla, P., Giglio, L., van der Werf, G., and Randerson, J. (2004). Top-down estimates of global CO sources using MOPITT measurements. *Geophys. Res. Lett.*, 31:L01104. doi:10.1029/2003GL018609.

Arellano, Jr, A. F., Kasibhatla, P., Giglio, L., van der Werf, G., Randerson, J., and Collatz, G. (2006). Time-dependent inversion estimates of global biomass burning CO emissions using Measurement of Pollution in the Troposphere (MOPITT) measurements. *J. Geophys. Res.*, 111:D09303. 10.1029/2005JD006613.

Auligné, T., McNally, A. P., and Dee, D. P. (2007). Adaptive bias correction for satellite data in a numerical weather prediction system. *Q. J. R. Meteorol. Soc.*, 133:631–642.

Bala, G., Caldeira, K., Wickett, M., Phillips, T. J., Lobell, D. B., Delire, C., and Mirin, A. (2007). Combined climate and carbon-cycle effects of large-scale deforestation. *PNAS*, 104:6550–6555.

Bergamaschi, P., Frankenberg, C., Meirink, J.-F., Krol, M., Dentener, F., Wagner, T., U.Platt, Kaplan, J. O., Körner, S., Heimann, M., Dlugokencky, E. J., and Goede, A. (2007). Satellite chartography of atmospheric methane from SCIAMACHY on board ENVISAT: 2. Evaluation based on inverse model simulations. *J. Geophys. Res.*, 112:D02304. doi:10.1029/2006JD007268.

Bergamaschi, P., Frankenberg, C., Meirink, J.-F., Krol, M., G.Villani, Houweling, S., Dentener, F., Dlugokencky, E. J., and Engel, A. (2009). Inverse modeling of global and regional CH4 emissions based on recently revised SCIAMACHY retrievals. *J. Geophys. Res.*, 114:D22301. doi:10.1029/2009JD012287.

Bergamaschi, P., Hein, R., Heimann, M., and Crutzen, P. J. (2000). Inverse modeling of the global CO cycle 1. Inversion of CO mixing ratios. *J. Geophys. Res.*, 105(D2):1909–1927.

Bergamaschi, P., Krol, M., Dentener, F., Vermeulen, A., Meinhardt, F., Graul, R., Ramonet, M., Peters, W., and Dlugokencky, E. J. (2005). Inverse modelling of national and Europian CH_4 emissions using the atmospheric zoom model TM5. *Atmos. Chem. and Phys.*, 5:2431–2460. doi:10.5194/acp-5-2431-2005.

Bergamaschi, P., Krol, M., Meirink, J. F., Dentener, F., Segers, A., van Aardenne, J., Monni, S., Vermeulen, A., Schmidt, M., Ramonet, M., Yver, C., Meinhardt, F., Nisbet, E. G., Fisher, R., O'Doherty, S., and Dlugokencky, E. J. (2010). Inverse modeling of European CH4 emissions 2001-2006. *J. Geophys. Res.*, 115(D5):4703–4715.

Blake, N. J., Blake, D. R., Simpson, I. J., Lopez, J. P., Johnston, N. A. C., Swanson, A. I., Katzenstein, A. S., Meinardi, S., Sive, B. C., Colman, J. J., Atlas, E., Flocke, F., Vay, S. A., Avery, M. A., and Rowland, F. S. (2001). Large-scale latitudinal and vertical distribution of nmhcs and selected halocarbons in the troposphere over the Pacific Ocean during the March-April 1999 Pacific Exploratory Misson (PEM-TROPICS B). *J. Geophys. Res.*, 106(D23):32627–32644.

Bousquet, P., Hauglustaine, D. A., Peylin, P., Carouge, C., and Ciais, P. (2005). Two decades of oh variability as inferred by an inversion of atmospheric transport and chemistry of methyl chloroform. *Atmospheric Chemistry and Physics*, 5(10):2635–2656.

Bouttier, F. and Courtier, P. (1999). Data assimilation concepts and methods. Technical report, ECMWF.

Brasileiro de Geografia e Estatistica, I. (2009). Municipal agricultural production. http://www.sidra.ibge.gov.br.

Cardoso, R. S., Özdemir, E. D., and Eltrop, L. (2012). Environmental and economic assessment of international ethanol trade options for the German transport sector. *Biomass Bioenergy*, 36:20–30.

Chevallier, F. (2007). Impact of correlated observation errors on inverted CO_2 surface fluxes from OCO measurements. *Geophys. Res. Lett.*, 34:L24804. doi:10.1029/2007GL030463.

Chevallier, F., Bréon, F.-M., and Rayner, P. J. (2007). Contribution of the Orbiting Carbon Observatory to the estimation of CO2 sources and sinks: Theoretical study in a variational data assimilation framework. *J. Geophys. Res.*, 112:D09307.

Chevallier, F., Fortems, A., Bousquet, P., Pison, I., Szopa, S., Devaux, M., and Hauglustaine, D. A. (2009). African CO emissions between years 2000 and 2006 estimated from MOPITT observations. *Biogeosc.*, 6:103–111. doi:10.5194/bg-6-103-2009.

Davidson, E. A., de Carvalho, C. J. R., Figueira, A. M., Ishida, F. Y., Ometto, J. P. H. B., Nardoto, G. B., Sabá, R. T., Hayashi, S. N., Leal, E. C., Vieira, I. C. G., and Martinelli, L. A. (2007). Recuperation of nitrogen cycling in amazonian forests following agricultural abandonment. *Nature*, 447:995–998. doi:10.1038/nature05900.

de Laat, A. T. J., Gloudemans, A. M. S., Aben, I., and Schrijver, H. (2010). Global evaluation of SCIAMACHY and MOPITT carbon monoxide column differences for 2004Ð2005. *J. Geophys. Res.*, 115:D06307. doi:10.1029/2009JD012698.

de Laat, A. T. J., Gloudemans, A. M. S., Schrijver, H., van den Broek, M. M. P., Meirink, J. F., Aben, I., and Krol, M. (2006). Quantitative analysis of SCIAMACHY carbon monoxide total column measurements. *Geophys. Res. Lett.*, 33:L07807. 10.1029/2005GL025530.

Deeter, M. N. (2009). *MOPITT (Measurements of Pollution in the Troposphere) validated version 4*. National Center for Atmospheric Research, Boulder, CO.

Deeter, M. N., Edwards, D. P., and Gille, J. C. (2007). Retrievals of carbon monoxide profiles from MOPITT observations using lognormal a priori statistics. *J. Geophys. Res.*, 112:D11311. doi:10.1029/2006JD007999.

Deeter, M. N., Edwards, D. P., Gille, J. C., Emmons, L. K., Francis, G., Ho, S.-P., Mao, D., Masters, D., Worden, H., Drummond, J. R., and Novelli, P. C. (2010). The MOPITT version 4 CO product: Algorithm enhancements, validation, and long term stability. *J. Geophys. Res.*, 115:D07306. doi:10.1029/2009JD013005.

Deeter, M. N., Emmons, L. K., Francis, G. L., Edwards, D. P., Gille, J. C., Warner, J. X., Khattatov, B., Ziskin, D., Lamarque, J.-F., Ho, S.-P., Yudin, V., Attie, J.-L., Packman, D., Chen, J., Mao, D., and Drummond, J. R. (2003). Operational carbon monoxide retrieval algorithm and selected results for the MOPITT instrument. *J. Geophys. Res.*, 108:D14. doi:10.1029/2002JD003186.

Derendorp, L., Quist, J., Holzinger, R., and Röckmann, T. (2011). Emissions of H2 and CO from leaf litter of Sequoiadendron giganteum, and their dependence on UV radiation and temperature. *Atmospheric Environment*, 45(39):7520–7524.

Dufek, A. S. and Ambrizzi, T. (2007). Precipitation variability in São Paulo State, Brazil. *Theoretical and Applied Climatology*, 93:167–178.

Duncan, B. N. and Logan, J. A. (2008). Model analysis of the factors regulating the trends and variability of carbon monoxide between 1988 and 1997. *Atmospheric Chemistry and Physics*, 8(24):7389–7403.

Duncan, B. N., Logan, J. A., Bey, I., Megretskaia, I. A., Yantosca, R. M., Noveli, P. C., Jones, N. B., and Rinsland, C. P. (2007). Global budget of CO, 1988-1997: Source estimates and validation with a global model. *J. Geophys. Res.*, 112:D22301. 10.1029/2005JD008459.

Edwards, D., Emmons, L., Gille, J., Chu, A., Attié, J.-L., Giglio, L., Wood, S., Haywood, J., Deeter, M., Massie, S., Ziskin, D., and Drummond, J. (2006a). Satellite-observed pollution from Southern Hemisphere biomass burning. *J. Geophys. Res.*, 111:D14312. 10.1029/2005JD006655.

Edwards, D. P., Pétron, G., Novelli, P. C., Emmons, L. K., Gille, J. C., and Dummond, J. R. (2006b). Southern Hemisphere carbon monoxide interannual variability observed by Terra/Measurements of Pollution in the Troposphere (MOPITT). *J. Geophys. Res.*, 111:D16303.

Eltahir, E. A. B. and Bras, R. L. (1994). Precipitation recycling in the Amazon basin. *Q. J. R. Meteorol. Soc.*, 120:861–880.

Emmons, L. K., Edwards, D. P., Deeter, M. N., Gille, J. C., Campos, T., Nédélec, P., Novelli, P., and Sachse, G. (2009). Measurement of Pollution In The Tropsphere (MOPITT) validation through 2006. *Atmos. Chem. and Phys.*, 9:1795–1803. doi:10.5194/acp-9-1795-2009.

Emmons, L. K., Pfister, G. G., Edwards, D. P., Gille, J. C., Sachse, G., Blake, D., Wofsy, S., Gerbig, C., Matross, D., and Nédélec, P. (2007). Measurements of Pollution in the Troposphere (MOPITT) validation during the summer 2004 field campaigns over North America. *J. Geophys. Res.*, 112(D12S02).

Enting, I. G. (2002). *Inverse Problems in Atmospheric Constituent Transport.* Cambridge University Press, Cambridge.

European Commission, J. R. C. and Netherlands Environmental Assessment Agency (2010). Emission Database for Global Atmospheric Research (EDGAR), release version 4.1. http://edgar.jrc.ec.europa.eu.

Fearnside, P. M. (2001). Soybean cultivation as a threat to the environment in Brazil. *Environmental Conservation*, 28(1):23–38.

Fearnside, P. M. (2005). Deforestation in Brazilian Amazonia: History, Rates, and Consequences. *Conservation Biology*, 19(3):680–688.

Fisher, M. and Courtier, P. (1995). Estimating the covariance matrices of analysis and forecast error in variational data assimilation. Technical report, ECMWF, Shinfield Park, Reading.

Fortems-Cheiney, A., Chevallier, F., Pison, I., Bousquet, P., Carouge, C., Clerbaux, C., Coheur, P.-F., George, M., Hurtmans, D., and Szopa, S. (2009). On the capability of IASI measurements to inform about CO surface emissions. *Atmos. Chem. and Phys.*, 9:8735–8743. doi:10.5194/acp-9-8735-2009.

Fortems-Cheiney, A., Chevallier, F., Pison, I., Bousquet, P., Szopa, S., Deeter, M. N., and Clerbaux, C. (2011). Ten years of CO emissions as seen from Measurements of Pollution in the Troposphere MOPITT. *J. Geophys. Res.*, 116:D05304. doi:10.1029/2010JD014416.

George, M., Clerbaux, C., Hurtmans, D., Turquety, S., Coheur, P.-F., Pommier, M., Hadji-Lazaro, J., Edwards, D. P., Worden, H., Luo, M., Rinsland, C., and McMillan, W. (2009). Carbon monoxide distributions from the iasi/metop mission: evaluation with other space-borne remote sensors. *Atmos. Chem. and Phys.*, 9(21):8317–8330.

Giering, R. and Kaminski, T. (1998). Recipes for Adjoint Code Construction. *ACM Transactions on Mathematocal Software*, 24(4):437–474.

Giglio, L., Randerson, J. T., van der Werf, G. R., Kasibhatla, P. S., Collatz, G. J., Morton, D. C., and DeFries, R. S. (2010). Assessing variability and long-term trends in burned area by merging multiple satellite fire products. *Biogeosciences*, 7:1171–1186. doi:10.5194/bg-7-1171-2010.

Gilbert, J. and Lémarechal, C. (2006). The module M1QN3 version 3.1. Technical report, INRIA.

Gloudemans, A., Krol, M., Meirink, J., de Laat, A., van der Werf, G., Schrijver, H., van den Broek, M., and Aben, I. (2006). Evidence for long-range transport of carbon monoxide in the Southern Hemisphere from SCIAMACHY observations. *Geophys. Res. Lett.*, 33:L16807. 10.1029/2006GL026804.

Gloudemans, A. M. S., de Laat, A. T. J., Schrijver, H., Aben, I., Meirink, J. F., and van der Werf, G. R. (2009). SCIAMACHY CO over land and oceans: 2003–2007 interannual variability. *Atmos. Chem. and Phys.*, 9(11):3799–3813. doi:10.5194/acp-9-3799-2009.

Gloudemans, A. M. S., Schrijver, H., Kleipool, Q., van den Broek, M. M. P., Straume, A. G., Lichtenberg, G., van Hees, R. M., Aben, I., and Meirink, J. F. (2005). The impact of sciamachy near-infrared instrument calibration on ch_4 and co total columns. *Atmospheric Chemistry and Physics*, 5(9):2369–2383.

Gonzi, S. and Palmer, P. I. (2010). Vertical transport of surface fire emissions observed from space. *J. Geophys. Res.*, 115:D02306. doi:10.1029/2009JD012053.

Heald, C. L., Jacob, D. J., Jones, D. B. A., Palmer, P. I., Logan, J. A., Streets, D. G., Sachse, G. W., Gille, J. C., Hoffman, R. N., and Nehrkorn, T. (2004). Comparative inverse analysis of satellite (MOPITT) and aircraft (TRACE-P) observations to estimate Asian sources of carbon monoxide. *J. Geophys. Res.*, 109:D23306. doi:10.1029/2004JD005185.

Hestenes, M. R. and Stiefel, E. (1952). Methods of conjugate gradients for solving linear systems. *J. Res. Nat. Bur. Standards*, 49:409–436.

Hoffmann, W. A., Schroeder, W., and Jackson, R. B. (2002). Positive feedback of fire, climate, and vegetation and the conversion of tropical savanna. *Geophys. Res. Lett.*, 29(22):2052.

Hooghiemstra, P., Krol, M. C., Bergamaschi, P., de Laat, A., van der Werf, G. R., Novelli, P. C., Deeter, M. N., Aben, I., and Roeckmann, T. (2012). Comparing optimized co emission estimates using mopitt or noaa surface network observations. *J. Geophys. Res.*, 117(-):–. Accepted manuscript.

Hooghiemstra, P. B., Krol, M. C., Meirink, J. F., Bergamaschi, P., van der Werf, G. R., Novelli, P. C., Aben, I., and Röckmann, T. (2011). Optimizing global co emission estimates using a four-dimensional variational data assimilation system and surface network observations. *Atmospheric Chemistry and Physics*, 11(10):4705–4723.

Houghton, R. A. (2006). Land-use change and the carbon cycle. *Glob. Change Bio.*, 1:275–287. DOI: 10.1111/j.1365-2486.1995.tb00026.x.

Houweling, S., Dentener, F., and Lelieveld, J. (1998). The impact of nonmethane hydrocarbon compounds on tropospheric photochemistry. *J. Geophys. Res.*, 103(D9):10673–10696.

Hudman, R., Murray, L., Jacob, D., Millet, D., Turquety, S., Wu, S., Blake, D., Goldstein, A., Holloway, J., and Sachse, G. (2008). Biogenic versus anthropogenic sources of co in the united states. *Geophys. Res. Lett.*, 35:L04801. 10.1029/2007GL032393.

Huijnen, V., Williams, J. E., van Weele, M., van Noije, T. P. C., Krol, M. C., Dentener, F., Segers, A., Houweling, S., Peters, W., de Laat, A. T. J., Boersma, K. F., Bergamaschi, P., van Velthoven, P. F. J., Le Sager, P., Eskes, H. J., Alkemade, F., Scheele, M. P., Nédélec, P., and Pätz, H.-W. (2010). The global chemistry transport model TM5: description and evaluation of the tropospheric chemistry version 3.0. *Geoscientific Model Development*, 3(3):445–473. doi:10.5194/gmd-3-445-2010.

IPCC, editor (2007). *Contribution of Working Group I to the Fourth Assessment Report of the Intergovernmental Panel on Climate Change*. Cambridge University Press, Cambridge, United Kingdom and New York, NY, USA.

Jacob, D. J. (1999). *Introduction to Atmospheric Chemistry*. Princeton University Press, Princeton, New Jersey, USA.

Jacob, D. J., Crawford, J. H., Kleb, M. M., Connors, V. S., Bendura, R. J., Raper, J. L., Sachse, G. W., Gille, J. C., Emmons, L., and Heald, C. L. (2003). Transport and Chemical Evolution over the Pacific (TRACE-P) aircraft mission: Design, execution, and first results. *J. Geophys. Res.*, 108:9000.

Jiang, Z., Jones, D. B. A., Kopacz, M., Liu, J., Henze, D. K., and Heald, C. (2011). Quantifying the impact of model errors on top-down estimates of carbon monoxide emissions using satellite observations. *J. Geophys. Res.*, 116(D15306).

Jones, D. B. A., Bowman, K. W., Logan, J. A., Heald, C. L., Liu, J., Luo, M., Worden, J., and Drummond, J. (2009). The zonal structure of tropical O_3 and CO as observed by the Tropospheric Emission Spectrometer in November 2004 Ð Part 1: Inverse modeling of CO emissions. *Atmos. Chem. and Phys.*, 9(11):3547–3562. doi:10.5194/acp-9-3547-2009.

Jones, D. B. A., Bowman, K. W., Palmer, P. I., Worden, J. R., Jacob, D. J., Hoffman, R. N., Bey, I., and Yantosca, R. M. (2003). Potential of observations from the Tropospheric Emission Spectrometer to constrain continental sources of carbon monoxide. *J. Geophys. Res.*, 108(D24). doi:10.1029/2003JD003702.

Kaiser, J. W., Heil, A., Andreae, M. O., Benedetti, A., Chubarova, N., Jones, L., Morcrette, J.-J., Razinger, M., Schultz, M. G., Suttie, M., and van der Werf, G. R. (2012). Biomass burning emissions estimated with a global fire assimilation system based on observed fire radiative power. *Biogeosciences*, 9(1):527–554.

Kaminski, T., Rayner, P. J., Heimann, M., and Enting, I. G. (2001). On aggregation errors in atmospheric transport inversions. *J. Geophys. Res.*, 106(D5):4703–4715.

Kasibhatla, P., Arellano, A., Logan, J. A., Palmer, P. I., and Novelli, P. (2002). Top-down estimates of a large source of atmospheric carbon monoxide associated with fuel combustion in Asia. *Geophys. Res. Lett.*, 29:1900. doi:10.1029/2002GL015581.

Kasischke, E. S., Hyer, E. J., Novelli, P. C., Bruhwiler, L. P., French, N. H. F., Sukhinin, A. I., Hewson, J. H., and Stocks, B. J. (2005). Influences of boreal fire emissions on Northern Hemisphere atmospheric carbon and carbon monoxide. *Global Biogeochem. Cycles*, 19:GB1012. doi:10.1029/2004GB002300.

Kirby, K. R., Laurance, W. F., Albernaz, A. K., Schrotz, G., Fearnside, P. M., Bergen, S., Venticinque, E. M., and da Costa, C. (2006). The future of deforestation in the Brazilian Amazon. *Futures*, 38:432–453.

Konovalov, I. B., Beekmann, M., Kuznetsova, I. N., Yurova, A., and Zvyagintsev, A. M. (2011). Atmospheric impacts of the 2010 russian wildfires: integrating modelling and measurements of an extreme air pollution episode in the moscow region. *Atmospheric Chemistry and Physics*, 11(19):10031–10056.

Kopacz, M., Jacob, D. J., Fischer, J. A., Logan, J. A., Zhang, L., Megretskaia, I. A., Yantosca, R. M., Singh, K., Henze, D. K., Burrows, J. P., Buchwitz, M., Khlystova, I., McMillan, W. W., Gille, J. C., Edwards, D. P., Eldering, A., Thouret, V., and Nedelec, P. (2010). Global estimates of CO sources with high resolution by adjoint inversion of multiple datasets (MOPITT, AIRS, SCIAMACHY, TES). *Atmos. Chem. and Phys.*, 10:855–876. doi:10.5194/acp-10-855-2010.

Kopacz, M., Jacob, D. J., Henze, D. K., Heald, C. L., Streets, D. G., and Zhang, Q. (2009). Comparison of adjoint and analytical Bayesian inversion methods for constraining Asian sources of carbon monoxide using satellite (MOPITT) measurements of CO columns. *J. Geophys. Res.*, 114:D04305. doi:10.1029/2007JD009264.

Krol, M. and Lelieveld, J. (2003). Can the variability in tropospheric OH be deduced from measurements of 1,1,1-trichloroethane (methyl chloroform)? *J. Geophys. Res.*, 108(D3). doi:10.1029/2002JD002423.

Krol, M., Meirink, J., Bergamaschi, P., Mak, J., Lowe, D., Jöckel, P., Houweling, S., and Röckmann, T. (2008). What can ^{14}CO measurements tell us about OH? *Atmos. Chem. and Phys.*, 8:5033–5044.

Krol, M. C., Houweling, S., Bregman, B., van den Broek, M., Segers, A., van Velthoven, P., Peters, W., Dentener, F., and Bergamaschi, P. (2005). The two-way nested global chemistry-transport zoom model TM5: algorithm and applications. *Atmos. Chem. and Phys.*, 5:417–432. doi:10.5194/acp-5-417-2005.

Labonne, M., Bréon, F.-M., and Chevallier, F. (2007). Injection height of biomass burning aerosols as seen from a spaceborne lidar. *Geophys. Res. Lett.*, 34:L11806.

Lanczos, C. (1950). An iteration method for the solution of eigenvalue problem of linear differential and integral operators. *J. Res. Nat. Bur. Stand.*, 45(4).

Lapola, D. M., Schaldach, R., Alcamo, J., Bondeau, A., Koch, J., Koelking, C., and Priess, J. A. (2010). Indirect land-use changes can overcome carbon savings from biofuels in Brazil. *PNAS*, 107(8):3388–3393.

Laurance, W. F. (2007). Switch to corn promotes Amazon deforestation. *Science*, 318:1721.

Lawrence, M. G., Jöckel, P., and von Kuhlmann, R. (2001). What does the global mean OH concentration tell us? *Atmos. Chem. and Phys.*, 1:37–49. doi:10.5194/acp-1-37-2001.

Lelieveld, J., Butler, T. M., Crowley, J. N., Dillon, T. J., Fischer, H., Ganzeveld, L., Harder, H., Lawrence, M. G., Martinez, M., Taraborrelli, D., and Williams, J. (2008). Atmospheric oxidation capacity sustained by a tropical forest. *Nature*, 452:737–740. doi:10.1038/nature06870.

Lewis, S. L., Brando, P. M., Phillips, O. L., van der Heijden, G. M. F., and Nepstad, D. (2011). The 2010 Amazon Drought. *Science*, 331:554. doi:10.1126/science.1200807.

Liu, J., Logan, J. A., Jones, D. B. A., Livesey, N. J., Megretskaia, I., Carouge, C., and Nedelec, P. (2010). Analysis of co in the tropical troposphere using aura satellite data and the geos-chem model: insights into transport characteristics of the geos meteorological products. *Atmospheric Chemistry and Physics*, 10(24):12207–12232.

Logan, J. A., Prather, M. J., Wofsy, S. C., and McElroy, M. B. (1981). Tropospheric chemistry: a global perspective. *J. Geophys. Res.*, 86(C8):7210–7254.

Malhi, Y., Roberts, J. T., Betts, R. A., Killeen, T. J., Li, W., and Nobre, C. A. (2008). Climate Change, Deforestation, and the Fate of the Amazon. *Science*, 319:169–175.

McMillan, W. W., Barnet, C., Strow, L., Chahine, M. T., McCourt, M. L., Warner, J. X., Novelli, P. C., Korontzi, S., Maddy, E. S., and Datta, S. (2005). Daily global maps of carbon monoxide from NASA's Atmospheric Infrared Sounder. *Geophys. Res. Lett.*, 32:L11801.

McMillan, W. W., Evans, K. D., Barnet, C. D., Maddy, E. S., Sachse, G. W., and Diskin, G. S. (2011). Validating the AIRS version 5 CO retrieval with DACOM in situ measurements during INTEX-A and -B. *Geosc. Rem. Sens.*, 49(7):2802–2813.

Meirink, J.-F., Bergamaschi, P., Frankenberg, C., d'Amelio, M. T. S., Dlugokencky, E. J., Gatti, L. V., Houweling, S., Miller, J. B., Röckmann, T., Villani, M. G., and Krol, M. C. (2008a). Four-dimensional variational data assimilation for inverse modelling of atmospheric methane emissions: Analysis of SCIAMACHY observations. *J. Geophys. Res.*, 113:D17301. doi:10.1029/2007JD009740.

Meirink, J.-F., Bergamaschi, P., and Krol, M. C. (2008b). Four-dimensional variational data assimilation for inverse modelling of atmospheric methane emissions: Method and comparison with synthesis inversion. *Atmos. Chem. and Phys.*, 8:6341–6353. doi:10.5194/acp-8-6341-2008.

Michalak, A. M., Bruhwiler, L., and Tans, P. P. (2004). A geostatistical approach to surface flux estimation of atmospheric trace gases. *J. Geophys. Res.*, 109:D14109. doi:10.1029/2003JD004422.

Montzka, S. A., Krol, M., Dlugokencky, E., Hall, B., Jöckel, P., and Lelieveld, J. (2011). Small interannual variability of global atmospheric hydroxyl. *Science*, 331:–. doi:10.1126/science.1197640.

Morton, D. C., DeFries, R. S., Randerson, J. T., Giglio, L., Schroeder, W., and van der Werf, G. R. (2008). Agricultural intensification increases deforestation fire activity in amazonia. *Glob. Biogeoch. Cy.*, 14:2262–2275.

Morton, D. C., DeFries, R. S., Shimabukuro, Y. E., Anderson, L. O., Arai, E., del Bon Espirito-Santo, F., Freitas, R., and Morisette, J. (2006). Cropland expansion changes deforestation dynamics in the southern Brazilian Amazon. *PNAS*, 103:14637–14641.

Mukherjee, C., Kasibhatla, P. S., and West, M. (2011). Bayesian statistical modeling of spatially correlated error structure in atmospheric tracer inverse analysis. *Atmospheric Chemistry and Physics*, 11(11):5365–5382.

Müller, J.-F. and Stavrakou, T. (2005). Inversion of CO and NO_x emissions using the adjoint of the IMAGES model. *Atmos. Chem. and Phys.*, 5:1157–1186. doi:10.5194/acp-5-1157-2005.

Myriokefalitakis, S., Vrekoussis, M., Tsigaridis, K., Wittrock, F., Richter, A., Brühl, C., Volkamer, R., Burrows, J. P., and Kanakidou, M. (2008). The influence of natural and anthropogenic secondary sources on the glyoxal global distribution. *Atmos. Chem. and Phys.*, 8(16):4965–4981. doi:10.5194/acp-8-4965-2008.

Naeher, L. P., Smith, K. R., Leaderer, B. P., Mage, D., and Grajeda, R. (2000). Indoor and outdoor PM2.5 and CO in high- and low-density Guatemalan villages. *Journal of Exposure Analysis and Environmental Epidemiology*, 10:544–551.

Nedelec, P., Cammas, J.-P., Thouret, V., Athier, G., Cousin, J.-M., Legrand, C., Abonnel, C., Lecoeur, F., Cayez, G., and Marizy, C. (2003). An improved infrared carbon monoxide analyser for routine measurements aboard commercial airbus aircraft: technical validation and first scientific results of the mozaic iii programme. *Atmospheric Chemistry and Physics*, 3(5):1551–1564.

Nepstad, D., Soares-Filho, B. S., Merry, F., Lima, A., Moutinho, P., Carter, J., Bowman, M., Cattaneo, A., Rodrigues, H., Schwartzmann, S., McGrath, D. G., Stickler, C. M., Lubowski, R., Piris-Cabezas, P., Rivero, S., Alencar, A., Almeida, O., and Stella, O. (2009). The end of deforestation in the Brazilian Amazon. *Science*, 326:1350–1351.

Nobre, C. A., Sellers, P. J., and Shukla, J. (1991). Amazonian Deforestation and Regional Climate Change. *Journal of Climate*, 4:957–988.

Novelli, P. C. and Masarie, K. A. (2010). Atmospheric Carbon Monoxide Dry Air Mole Fractions from the NOAA ESRL Carbon Cycle Cooperative Global Air Sampling Network, 1988-2009, Version: 2011-10-14. ftp://ftp.cmdl.noaa.gov/ccg/co/flask/event/.

Novelli, P. C., Masarie, K. A., and Lang, P. M. (1998). Distributions and recent changes of carbon monoxide in the lower troposphere. *J. Geophys. Res.*, 103(D15):19015–19033.

Novelli, P. C., Masarie, K. A., Lang, P. M., Hall, B. D., Myers, R. C., and Elkins, J. W. (2003). Reanalysis of tropospheric CO trends: Effects of the 1997-1998 wildfires. *J. Geophys. Res.*, 108(D15):4464. doi:10.1029/2002JD003031.

Olivier, J., Peters, J., Granier, C., Pétron, G., Müller, J., and Wallens, S. (2003). *Present and future surface emissions of atmospheric compounds*. RIVM, Bilthoven. POET report 2, EU project EVK2-1999-00011.

Olivier, J. G. J., Berdowski, J. J. M., Peters, J. A. H. W., Bakker, J., Visschedijk, A. J. H., and Bloos, J.-P. J. (2000). *Applications of EDGAR. Including a Description of EDGAR V3.0: Reference Database with Trend Data for 1970-1995*. RIVM, Bilthoven. NRP report no. 410200 051 / RIVM report no. 773301 001.

Oyama, M. D. and Nobre, C. A. (2003). A new climate-vegetation equilibrium state for Tropical South America. *Geophys. Res. Lett.*, 30(2199).

Palmer, P. I., Jacob, D. J., Jones, D. B. A., Heald, C. L., Yantosca, R. M., and Logan, J. A. (2003). Inverting for emissions of carbon monoxide from Asia using aircraft observations over the western Pacific. *J. Geophys. Res.*, 108(D21):8828. doi:10.1029/2003JD3397.

Palmer, P. I., Suntharalingam, P., Jones, D. B. A., Jacob, D. J., Streets, D. G., Fu, Q., Vay, S. A., and Sachse, G. W. (2006). Using CO_2:CO correlations to improve inverse analysis of carbon fluxes. *J. Geophys. Res.*, 111(D12318):1–11. 10.1029/2005JD006697.

Pan, L., Edwards, D. P., Gille, J. C., Smith, M. W., and Dummond, J. R. (1995). Satellite remote sensing of tropospheric CO and CH_4: forward model studies of the MOPITT instrument. *Applied Optics*, 34(30):6976–6988.

Peters, W., Krol, M. C., Van Der Werf, G. R., Houweling, S., Jones, C. D., Hughes, J., Schaefer, K., Masarie, K. A., Jacobson, A. R., Miller, J. B., Cho, C. H., Ramonet, M., Schmidt, M., Ciattaglia, L., Apadula, F., Heltai, D., Meinhardt, F., Di Sarra, A. G., Piacentino, S., Sferlazzo, D., Aalto, T., Hatakka, J., Ström, J., Haszpra, L., Meijer, H. A. J., Van Der Laan, S., Neubert, R. E. M., Jordan, A., Rodó, X., Morguí, J.-A., Vermeulen, A. T., Popa, E., Rozanski, K., Zimnoch, M., Manning, A. C., Leuenberger, M., Uglietti, C., Dolman, A. J., Ciais, P., Heimann, M., and Tans, P. P. (2010). Seven years of recent European net terrestrial carbon dioxide exchange constrained by atmospheric observations. *Global Change Biology*, 16:1317–1337.

Pétron, G., Granier, C., Khattativ, B., Yudin, V., Lamarque, J.-F., Emmons, L., Gille, J., and Edwards, D. P. (2004). Monthly CO surface sources inventory based on the 2000Ð2001 MOPITT satellite data. *Geophys. Res. Lett.*, 31:L21107. doi:10.1029/2004GL020560.

Pétron, G., Granier, C., Khattatov, B., Lamarque, J.-F., Yudin, V., Müller, J.-F., and Gille, J. (2002). Inverse modeling of carbon monoxide surface emissions using Climate Monitoring and Diagnostics Laboratory network observations. *J. Geophys. Res.*, 107(D24):4761. doi:10.1029/2001JD001305.

Pfister, G., Hess, P. G., Emmons, L. K., Lamarque, J.-F., Wiedinmyer, C., Edwards, D. P., Pétron, G., Gille, J. C., and Sachse, G. W. (2005). Quantifying CO emissions from the 2004 Alaskan wildfires using MOPITT CO data. *Geophys. Res. Lett.*, 32:L11809. doi:10.1029/2005GL022995.

Pison, I., Bousquet, P., Chevallier, F., Szopa, S., and Hauglustaine, D. (2009). Multi-species inversion of CH_4, CO and H_2 emissions from surface measurements. *Atmos. Chem. and Phys.*, 9:5281–5297. doi:10.5194/acp-9-5281-2009.

Prinn, R. G., Huang, J., Weiss, R. F., Cunnold, D. M., Fraser, P. J., Simmonds, P. G., McCulloch, A., Harth, C., Reimann, S., Salameh, P., O'Doherty, S., Wang, R. H. J., Porter, L. W., Miller, B. R., and Krummel, P. B. (2005). Evidence for variability of atmospheric hydroxyl radicals over the past quarter century. *Geophys. Res. Lett.*, 32:L07809.

Rinsland, C. P., Luo, M., Logan, J. A., Beer, R., Worden, H., Kulawik, S. S., Rider, D., Osterman, G., Gunson, M., Eldering, A., Goldman, A., Shephard, M., Clough, S. A., Rodgers, C., Lampel, M., and Chiou, L. (2006). Nadir measurements of carbon monoxide distributions by the tropospheric emission spectrometer instrument onboard the aura spacecraft: Overview of analysis approach and examples of initial results. *Geophys. Res. Lett.*, 33:L22806.

Rodgers, C. D. (2000). *Inverse Methods for Atmospheric Sounding.* World Sci., London.

Rovere, E. L. L., Pereira, A. S., and oes, A. F. S. (2011). Biofuels and sustainable energy development in Brazil. *World Development*, 39(6):1026–1036.

Sala, O. E., III, F. S. C., Armesto, J. J., Berlow, E., Bloomfield, J., Dirzo, R., Huber-Sanwald, E., Huenneke, L. F., Jackson, R. B., Kinzig, A., Leemans, R., Lodge, D. M., Mooney, H. A., Oesterheld, M., Poff, N. L., Sykes, M. T., Walker, B. H., Walker, M., and Wall, D. H. (2000). Global biodiversity scenarios for the year 2100. *Science*, 287(5459):1770–1774.

Sanhueza, E., Dong, Y., Scharffe, D., Lobert, J., and Crutzen, P. (1998). Carbon monoxide uptake by temperate forest soils: the effect of leaves and humus layers. *Tellus*, 50(B):51–58.

Schade, G. and Crutzen, P. J. (1999a). CO emissions from degrading plant matter. *Tellus*, 51(5):909–918.

Schade, G. W. and Crutzen, P. J. (1999b). CO emissions from degrading plant matter (2). Estimate of a global source strength. *Tellus*, 51B:909–918.

Schade, G. W., Hofman, R.-M., and Crutzen, P. J. (1999). CO emissions from degrading plant matter (1). Measurements. *Tellus*, 51B:889–908.

Seinfeld, J. H. and Pandis, S. N. (2006). *Atmospheric Chemistry and Physics: From Air Pollution to Climate Change.* John Wiley and Sons, Hoboken, New Jersey, USA.

Shindell, D., Faluvegi, G., Stevenson, D., Krol, M., and More, M. (2006). Multimodel simulations of carbon monoxide: Comparison with observations and projected near-future changes. *J. Geophys. Res.*, 111:D19306. 10.1029/2006JD007100.

Shukla, J., Nobre, C., and Sellers, P. (2000). Amazonian Deforestation and Climate Change. *Science*, 247(4948):1322–1325.

Sparovek, G., Berndes, G., Klug, I. L. F., and Barretto, A. G. O. P. (2010). Brazilian agriculture and environmental legislation: status and future challenges. *Environ. Sci. Technol.*, 44:6046–6053.

Spivakovsky, C. M., Logan, J. A., Montzka, S. A., Balkanski, Y. J., Foreman-Fowler, M., Jones, D. B. A., Horowitz, L. W., Fusco, A. C., Brenninkmeijer, C. A. M., Prather, M. J., Wofsy, S. C., and McElroy, M. B. (2000). Three-dimensional climatological distribution of tropospheric OH: Update and evaluation. *J. Geophys. Res.*, 105:8931–8980.

Stavrakou, T. and Müller, J.-F. (2006). Grid-based versus big region approach for inverting CO emissions using Measurement of Pollution in the Troposphere (MOPITT) data. *J. Geophys. Res.*, 111:D15304. doi:10.1029/2005JD006896.

Stavrakou, T., Müller, J.-F., De Smedt, I., Van Roozendael, M., van der Werf, G. R., Giglio, L., and Guenther, A. (2009a). Global emissions of non-methane hydrocarbons deduced from sciamachy formaldehyde columns through 2003–2006. *Atmospheric Chemistry and Physics*, 9(11):3663–3679.

Stavrakou, T., M uller, J.-F., Peeters, J., Razavi, A., Clarisse, L., Clerbaux, C., Coheur, P.-F., Hurtmans, D., Maziére, M. D., Vigouroux, C., Deutscher, N. M., Griffith, D. W. T., Jones, N., and Paton-Walsh, C. (2011). Satellite evidence for a large source of formic acid from boreal and tropical forests. *Nature Geosc.*, 5:26–30.

Stavrakou, T., Müller, J.-F., Smedt, I. D., van Roozendael, M., van der Werf, G., Giglio, L., and Guenther, A. (2009b). Evaluating the performance of pyrogenic and biogenic emission inventories against one decade of space-based formaldehyde columns. *Atmos. Chem. and Phys.*, 9:1037–1060. doi:10.5194/acp-9-1037-2009.

Streets, D., Zhang, Q., Wang, L., He, K., Hao, J., Wu, Y., Tang, Y., and Carmichael, G. (2006). Revisiting China's CO emissions after the Transport and Chemical Evolution over the Pacific (TRACE-P) mission: Synthesis of inventories, atmospheric modeling, and observations. *J. Geophys. Res.*, 111:D14306. 10.1029/2006JD007118.

Stroppiana, D., Brivio, P. A., Grégoire, J.-M., Liousse, C., Guillaume, B., Granier, C., Mieville, A., Chin, M., and Pétron, G. (2010). Comparison of global inventories of co emissions from biomass burning derived from remotely sensed data. *Atmospheric Chemistry and Physics*, 10(24):12173–12189.

Tangborn, A., Stajner, I., Buchwitz, M., Khlystova, I., Pawson, S., Burrows, J., Hudman, R., and Nedelec, P. (2009). Assimilation of SCIAMACHY total column CO observations: Global and regional analysis of data impact. *J. Geophys. Res.*, 114:D07307. doi:10.1029/2008JD010781.

Tarr, M. A., Miller, W. L., and Zepp, R. G. (1995). Direct carbon monoxide photoproduction from plant matter. *J. Geophys. Res.*, 100(D6):11403–11413.

Torres, O., Chen, Z., Jethva, H., Ahn, C., Freitas, S. R., and Bhartia, P. K. (2010). Omi and modis observations of the anomalous 2008Ð2009 southern hemisphere biomass burning seasons. *Atmospheric Chemistry and Physics*, 10(8):3505–3513.

Turquety, S., Hurtmans, D., Hadji-Lazaro, J., Coheur, P.-F., Clerbaux, C., Josset, D., and Tsamalis, C. (2009). Tracking the emission and transport of pollution from wildfires using the iasi co retrievals: analysis of the summer 2007 greek fires. *Atmos. Chem. and Phys. Disc.*, 9(2):7413–7455.

Turquety, S., Logan, J. A., Jacob, D. J., Hudman, R. C., Leung, F. Y., Heald, C. L., Yantosca, R. M., Wu, S., Emmons, L. K., Edwards, D. P., and Sachse, G. W. (2007). Inventory of boreal fire emissions for north america in 2004: Importance of peat burning and pyroconvective injection. *J. Geophys. Res.*, 112:D12S03. doi:10.1029/2006JD007281.

Val Martin, M., Logan, J. A., Kahn, D., Leung, F. Y., Nelson, D., and Diner, D. (2009). Smoke injection heights from fires in north america: analysis of 5 years of satellite observations. *Atmos. Chem. and Phys. Disc.*, 9(5):20515–20566. doi:10.5194/acp-10-1491-2010.

van der Werf, G. R., Morton, D. C., DeFries, R. S., Giglio, L., Randerson, J. T., Collatz, G. J., and Kasibhatla, P. S. (2009). Estimates of fire emissions from an active deforestation region in the southern amazon based on satellite data and biogeochemical modelling. *Biogeosciences*, 6:235–249.

van der Werf, G. R., Randerson, J. T., Collatz, G. J., and Giglio, L. (2003). Carbon emissions from fires in tropical and subtropical ecosystems. *Glob. Change Bio.*, 9:547–562.

van der Werf, G. R., Randerson, J. T., Collatz, G. J., Giglio, L., Kasibhatla, P. S., Arellano, Jr., A. F., Olsen, S. C., and Kasischke, E. S. (2004). Continental-scale partitioning of fire emissions during the 1997 to 2001 El Niño/La Niña period. *Science*, 303(5654):73–76. doi: 10.1126/science.1090753.

van der Werf, G. R., Randerson, J. T., Giglio, L., Collatz, G. J., Kasibhatla, P. S., and Arellano, Jr., A. F. (2006). Interannual variability in global biomass burning emissions from 1997 to 2004. *Atmos. Chem. and Phys.*, 6:3423–3441. doi:10.5194/acp-6-3423-2006.

van der Werf, G. R., Randerson, J. T., Giglio, L., Collatz, G. J., Mu, M., Kasibhatla, P. S., Morton, D. C., DeFries, R. S., Jin, Y., and van Leeuwen, T. T. (2010). Global fire emissions and the contribution of deforestation, savanna, forest, agricultural, and peat fires (1997–2009). *Atmospheric Chemistry and Physics*, 10(23):11707–11735.

van Leeuwen, T. T. and van der Werf, G. R. (2011). Spatial and temporal variability in the ratio of trace gases emitted from biomass burning. *Atmospheric Chemistry and Physics*, 11(8):3611–3629.

Walter, A., Dolzan, P., Quilodrán, O., de Oliveira, J. G., da Silva, C., Piacente, F., and Segerstedt, A. (2011). Sustainability assessment of bio-ethanol production in Brazil considering land use change, GHG emissions and socio-economic aspects. *Energy Policy*, 39:5703–5716.

Williams, M. (2003). *Deforesting the Earth: From Prehistory to Global Crisis*. Univ. of Chicago Press, Chicago 60637, USA.

Witte, J. C., Douglass, A. R., da Silva, A., Torres, O., Levy, R., and Duncan, B. N. (2011). Nasa a-train and terra observations of the 2010 russian wildfires. *Atmospheric Chemistry and Physics*, 11(17):9287–9301.

Wooster, M. J., Roberts, G., Perry, G. L. W., and Kaufman, Y. J. (2005). Retrieval of biomass combustion rates and totals from fire radiative power observations: FRP derivation and calibration relationships between biomass consumption and fire radiative energy release. *J. Geophys. Res.*, 110:D24311.

Wooster, M. J. and Zhang, Y. H. (2004). Boreal forest fires burn less intensely in Russia than in North America. *Geophys. Res. Lett.*, 31:L20505. doi:10.1029/2004GL020805.

Xu, L., Samanta, A., Costa, M. H., Ganguly, S., Nemani, R. R., and Myneni, R. B. (2011). Widespread decline in greenness of Amazonian vegetation due to the 2010 drought. *Geophys. Res. Lett.*, 38:L07402. doi:10.1029/2011GL046824.

Yumimoto, K. and Uno, I. (2006). Adjoint inverse modeling of CO emissions over Eastern Asia using four-dimensional variational data assimilation. *Atmos. Env.*, 40:6836–6845.

Yurganov, L., McMillan, W., Grechko, E., and Dzhola, A. (2010). Analysis of global and regional co burdens measured from space between 2000 and 2009 and validated by ground-based solar tracking spectrometers. *Atmospheric Chemistry and Physics*, 10(8):3479–3494.

Yurganov, L. N., Rakitin, V., Dzhola, A., August, T., Fokeeva, E., George, M., Gorchakov, G., Grechko, E., Hannon, S., Karpov, A., Ott, L., Semutnikova, E., Shumsky, R., and Strow, L. (2011). Satellite- and ground-based co total column observations over 2010 russian fires: accuracy of top-down estimates based on thermal ir satellite data. *Atmospheric Chemistry and Physics*, 11(15):7925–7942.

Zepp, R. G., Miller, W. L., Burke, R. A., Parsons, D. A. B., and Scholes, M. C. (1996). Effects of moisture and burning on soil-atmosphere exchange of trace carbon gases in a southern African savanna. *J. Geophys. Res.*, 101(D19):23699–23706.

Dankwoord

Een vierjarig project als dit heb ik natuurlijk niet helemaal alleen en zonder hulp voor elkaar gekregen. Het lijkt me dan ook geen slecht idee om de nodige mensen te bedanken voor hulp, advies, inspiratie (transpiratie) en begeleiding. Ik wil graag beginnen met Maarten Krol, die het 4 jaar geleden aandurfde om die net afgestudeerde wiskundige, die niets wist van de atmosfeer, laat staan chemie, aan te nemen. Het was niet altijd even makkelijk, maar het resultaat, met dit proefschrift als summum mag er wat mij betreft zijn. Altijd kritisch, dat was wel nodig, en het werk is daar alleen maar beter van geworden. Ik hoop dat je met het gebouwde systeem voor CO in de toekomst nog mooie resultaten mag boeken. Dat mag overigens ook een andere tracer zijn.

Ik heb ook veel te danken aan Ilse Aben, die toch maar mooi het voorstel schreef waarop ik ben aangenomen. Enigszins op de achtergrond met betrekking tot dit project, maar de momenten dat we elkaar spraken was je altijd zeer scherp naar de resultaten en conclusies die ik trok. Hiervan heb ik ook geleerd om (nog) beter naar mijn eigen werk te kijken, hoewel dat in de toekomst nog beter moet eigenlijk.

Thomas Röckmann wil ik bedanken voor mijn plaats op het IMAU en in de atmosferische chemie groep. Ik heb daar met veel plezier gewerkt en ik ben heel blij dat mijn werkplek op het IMAU was. Hoewel we niet het meeste contact hebben gehad, was je wel geïnteresseerd in mijn project en hoe het nou ging.

Dan kom ik uit bij mijn collega's, met name op het IMAU. Allereerst Jeroen met wie ik een kamer deelde de eerste 2 jaar. Dat was een mooie tijd, maar achteraf had ik wel iets efficiënter moeten werken in die tijd. Maar we hebben zeker lol gehad. Met Jan Fokke heb ik goed overleg gehad, het was wel jammer dat hij al naar het KNMI vertrok na 1 maand. Ik had nog wel wat langer de tijd willen hebben om vragen te stellen en te leren.

Gelukkig was daar Sourish ineens. Ik mag wel zeggen dat zonder zijn in komst naar Utrecht, het waarschijnlijk allemaal een stuk minder voorspoedig was verlopen. Hoewel ik in het begin wel eens moe werd van het constante gerinkel van de telefoon of binnenlopen voor vragen,

heb ik dit in een later stadium ruimschoots terugbetaald! Ik denk dat we samen (jij wat meer dan ik) een heel mooi systeem hebben gebouwd en ik ben dankbaar dat je de python goeroe wilde zijn.

Internationally there are a number of people I would like to thank. First of all Peter Bergamaschi, who delivered very thoughtful comments throughout the project which have only led to improvements in my work. Therefore, *Grazie mille, Peter, ciao!* We should not forget the people responsible for the observations we have used throughout this thesis. Although there are countless people over the world that have been taking flask samples of air, these samples were measured in the NOAA lab in Boulder and made available by Paul Novelli and his team. *Thanks for Paul for 20 year of data!* In addition I would like to thank the complete MOPITT team at NCAR (also in Boulder) for making available the MOPITT data. Unfortunately there was no more time to use the latest V5 product, but this will be exploited in future research I am sure. I would like to thank Merritt Deeter who has been a helpful colleague in introducing the MOPITT instrument to me. I have read and read your papers and product guides so often, I can dream there content. *Thanks for your help Merritt!*

Tenslotte zijn daar dan nog de mensen in mijn directe omgeving: mijn familie! Maarten, het was een hele mooie tijd, die 5 jaar dat we samen op de Preludeweg hebben gewoond en zo goed gechilled hebben. Dat was ook best wel nodig gegeven dat we allebei soms gefrusteerd thuis kwamen na een dag werken. Bedankt voor al die mooie zondagavonden dat we lekker naar het voetbal zaten te kijken *Ajax!* En niet te vergeten, Jerry, die ineens in Utrecht woonde waardoor ik na mijn werk daar een biertje kon drinken. Wat hebben wij ons ook vermaakt. Het hardlopen was een mooie inleiding van de nodige avondjes doorzakken onder het genot van een stevige bak herrie. Dat moeten we nog eens overdoen. Dan mijn ouders, Ien en Ger, jullie hebben mij altijd gesteund in mijn zoektocht naar meer getallen om mee te rekenen. Ik weet nog een boel voorbeelden, maar met name die tafels (tot 231?) zullen me altijd bijblijven en natuurlijk mijn eerste wiskunde boek in groep 8. Bij jullie kon ik ook terecht in tijden van stress en frustratie en ik ben blij dat we zo goed gepraat hebben en dat jullie me nooit gepusht hebben.

Het laatste stukje is voor maar een iemand, collega, huisgenoot, vriendin, jij bent alles voor mij Leonie! Het meest bijzondere aan mijn werk op het IMAU, waar ik het meest dankbaar voor ben, is dat jij daar ook zat en dat we nu samen zijn. Als geen ander kan jij aanvoelen hoe het met mij is en ook als geen ander snap je alle frustratie. Daarnaast kan ik met jou ook alle successen vieren. Hopelijk gaan we in de toekomst nog vele jaren er heerlijk op uit om alle bergen te beklimmen op de fiets en als we oud zijn doen we het nog, op een elektrische fiets! Bedankt voor je steun!!!

Curriculum Vitae

Pim Hooghiemstra was born on February 10, 1984 in Bergschenhoek, The Netherlands, but grew up in the centre of the 'green hart', Alphen aan den Rijn. He already liked playing around with numbers at an early age. In September 1996 he attended high school in Leiden at the Stedelijk Gymnasium Leiden and graduated in 2002. The love for numbers was not diminished by then and so he went to Delft University of Technology to start a studies Applied Mathematics. After receiving a Bachelor degree in 2005, an internship at the KNMI in 2006 showed that mathematics can be applied in a number of fields, including atmospheric chemistry. A master thesis was conducted in the year 2007 at the National Aerospace Laboratory (NLR) in Amsterdam, the subject again being number crunching. That is, the finite element method was applied to the vector wave equation to optimize the computation of the radar signature of a fighter aircraft. In November 2007, the Master degree was received and a step towards Utrecht was made to join the Netherlands Institute for Space Research (SRON). However, a desk at IMAU was reserved for Pim to conduct his research in the group of Thomas Röckmann under daily supervision of Maarten Krol. The subject was inverse modeling of carbon monoxide emissions from which the results are presented in this thesis.